Diagenesis and fluid-fracture evolution in an intracontinental basin: The Penedès half-graben, western Mediterranean

Diagènesi i evolució de la relació fluid-fractura en una conca intracontinental: la conca del Penedès, oest de la Mediterrània

Vinyet Baqués Almirall

8. APPENDIX

Appendix 1: Principal publications of the thesis

Publication 1

Baqués, V., Travé, A., Benedicto, A., Labaume, P., Cantarero, I., 2010 Relationships between carbonate fault rocks and fluid flow regime during propagation of the Neogene extensional faults of the Penedès basin (Catalan Coastal Ranges, NE Spain). Journal of Geochemical Exploration, 106, 24-33.

Journal of Geochemical Exploration 106 (2010) 24–33

Contents lists available at ScienceDirect

Journal of Geochemical Exploration

journal homepage: www.elsevier.com/locate/jgeoexp

Relationships between carbonate fault rocks and fluid flow regime during propagation of the Neogene extensional faults of the Penedès basin (Catalan Coastal Ranges, NE Spain)

V. Baqués [a,*], A. Travé [a], A. Benedicto [b], P. Labaume [c], I. Cantarero [a]

[a] Dpt. Geoquímica, Petrologia i Prospecció Geològica. Facultat de Geologia. Universitat de Barcelona. c/Martí i Franquès s/n, 08028 Barcelona, Spain
[b] Areva NC, BU Mines. Direction des Géosciences. Tour Areva. 92094 Paris La Défense Cedex. France
[c] Géosciences Montpellier (UMR 5243), Université Montpellier 2, 34095 Montpellier, France

ARTICLE INFO

Article history:
Received 30 April 2009
Accepted 25 November 2009
Available online 5 December 2009

Keywords:
Extensional fault
Fault rock
Tectonic breccia
Karstic breccia
Fracture
Fluid flow

ABSTRACT

Different types of fractures and fault rocks occur within the major normal fault zones bordering the NW of the Neogene Penedès basin (NE Spain). In the southwest part of the basin, the main fault is the Baix Penedès fault that places the Upper Jurassic–Lower Cretaceous dolomicrites of the footwall in contact with the Miocene siliciclastic sediments of the hangingwall. Within the footwall damage zone, different fracture systems and their respective associated breccias and cements have been recognized. Using a combination of structural, petrologic and geochemical analyses, we show that these fracture systems evolved from mainly tectonic to mainly karstic features during the progressive development and upward propagation of the fault. The earlier fractures and associated breccias represent the initial stages of the fault propagation, when the process zone formed around the fault tip was dominated by dilatant fracturing (fractures 1 and dilatant breccias B1). The fluid involved in this early deformation precipitated the dolomite cement C1, in equilibrium with the host-rock in a closed hydrogeological system. Localization of frictional processes generated cataclasites and ultracataclasites along distinct second-order faults (fractures 2). In these fractures, the dolomite cement C2 precipitated in relation to the incipient opening of the hydrological system to percolating meteoric waters. The later fractures and associated breccias represent the late stages of the fault propagation. These structures (fractures 3, fractures 4 and the dilatant breccias B2) were formed when the extensional deformation reached the surface, resulting in an increasingly open hydrogeological system. At these stages, deposition of the dolomitic sediment DS and precipitation of the calcite cements C3, C4 and C5 show the circulation of freshwaters in a vadose meteoric environment, i.e. in karstic conditions.

1. Introduction

In tectonically controlled basins, it is assumed that fluid flow is enhanced along fractures and faults during deformation. Fractures, fault rocks and cements record the interactions between deformation and fluid flow regime during basin development (Knipe, 1993). In that sense, recent works have shown how integrated structural, petrologic and geochemical studies on fractures, cements and host-rocks are a powerful tool to study the interactions between deformation and fluid behaviour both at the fracture and at the basin scale (De Brit, 1989; Travé et al., 1998; Travé and Calvet, 2001; Bitzer et al., 1997; Muchez et al., 1995; Sibson, 2000; Labaume et al., 2004; Micarelli et al., 2005, 2006; Bussolotto et al., 2007; Benedicto et al., 2008; Breesch et al., 2009). This work is a part of a larger project which uses this multidisciplinary approach in the Neogene extensional Penedès basin (Catalan Coastal Ranges, NE Spain) in order to study how major, secondary and minor fractures control fluid flow through the whole basin. The work presented here focuses on the analysis of the main fault bounding the southwest part of the basin, the Baix Penedès fault; more in detail, it focuses on a nice exposure where this fault cross-cuts the carbonaceous Mesozoic series of the basin substratum and where coexist various types of cemented tectonic and karstic breccias in the footwall damage zone. We attempt to unravel the relationships between tectonic features, karstic processes and paleohydrogeological systems during the fault evolution.

2. Geological setting

The Catalan Coastal Ranges (NE Spain) correspond to a system of grabens formed at the NW margin of the Valencia Through (Fig. 1A). This structure results from the superposition of three main tectonic events: (1) a Mesozoic extensional phase from the Late Jurassic to the Early Cretaceous; (2) a Paleogene compressional phase from the

* Corresponding author. Tel.: +34 934031165; fax: +34 934021340.
E-mail addresses: vbaques@ub.edu (V. Baqués), atrave@ub.edu (A. Travé), antonio.benedicto-esteban@areva.fr (A. Benedicto), pierre.labaume@gm.univ-montp2.fr (P. Labaume), i_cantarero@ub.edu (I. Cantarero).

0375-6742/$ – see front matter © 2009 Elsevier B.V. All rights reserved.
doi:10.1016/j.gexplo.2009.11.010

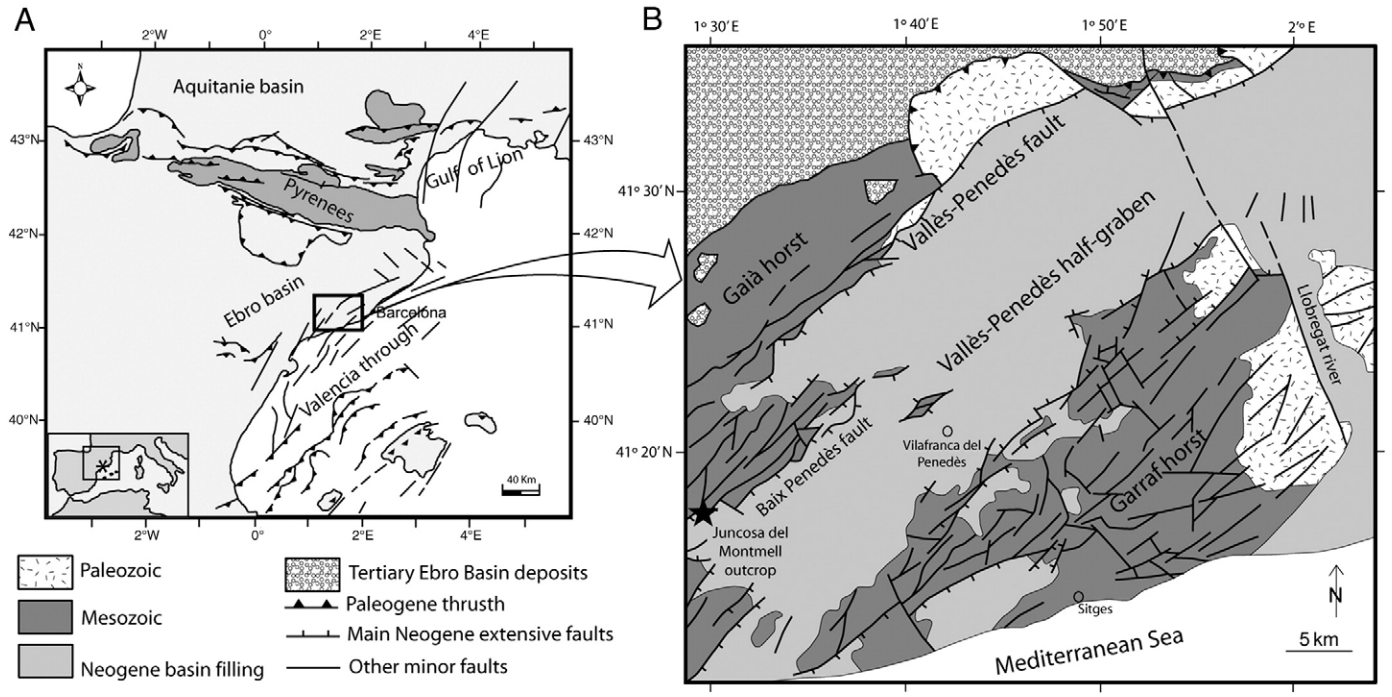

Fig. 1. (A) Simplified geological map of the studied area showing the Catalan Coastal Ranges. (B) Geological map of the central part of the Catalan Coastal Ranges showing the Penedès half-graben and the location of the Juncosa del Montmell outcrop.

Eocene to the early Oligocene, generating the transpressive motion of a major north-west directed basement thrust; and (3) a Neogene extensional phase (late Oligocene?–late Neogene) in association with the Valencia Through opening. During the latter phase, the main compressive structures were reactivated as extensional faults and controlled the location of emergence of extensional faults (Anadón et al., 1985; Amigó, 1986; Guimerà, 1988; Bartrina et al., 1992; Roca et al., 1999; Parcerisa et al., 2007; Marín et al., 2008).

The Penedès half-graben (Fig. 1B) is oriented NE–SW and is up to 50 km long and 10–14 km wide. In its northern part, it is bounded to the northwest by the SE-dipping Vallès-Penedès fault which has a normal displacement of up to 4 km and is probably connected to a detachment at a depth of 13–15 km at the lower/upper crust boundary (Bartrina et al. 1992; Roca, 1994). To the southwest, in the study area, the main displacement is transferred on the Baix Penedès fault. The southeast margin of the Penedès half-graben comprises several minor ENE–WSW-trending normal faults with throws of a few hundreds of meters that compartmentalize the area in minor horsts and grabens (Bartrina et al. 1992). The basin is filled with an up to 4 km thick succession of terrigenous sediments which forms a broad syncline and is cut by normal faults. This succession has been divided into three main lithostratigraphic units which are, from base to top (Cabrera, 1981; Cabrera and Calvet, 1996): (1) a lower continental syn-rift complex, of Aquitanian–early Langhian age, (2) a continental to marine complex, of Langhian age, with reefal carbonate platforms and (3) an upper continental complex, of middle Serravallian–Tortonian age. These three deformed complexes are covered by Pliocene continental to marine deposits which onlap a major Messinian regional erosive surface cutting the underlying deposits.

In the studied outcrop of the Baix Penedès fault zone (Figs. 1B and 2), the Upper Jurassic–Lower Cretaceous dolomites of the footwall are in contact with the conglomerates of the upper continental complex in the hangingwall. We focussed this study on the carbonates of the footwall block, where it is possible to distinguish the spatial and temporal organization of the deformation mechanisms during the fault propagation and the diagenetic features involved during the different deformation stages.

3. Methods and analytical techniques

A detailed structural study was carried out to establish the fault kinematics and the different deformation and diagenetic features. Based on this study, sixteen samples representative of the footwall structures were collected and twenty thin-sections were studied using the optical, cathodoluminescence and scanning electron (with a coupled EDS) microscopes. Some of the thin-sections have been stained with Alizarine Red-S and potassium ferricyanide to distinguish calcite and dolomite and their ferroan equivalents (Dickson, 1966). Cathodoluminescence was carried out on a Technosyn Cold Cathodoluminescence device (model 8200 MkII operating at 15–18 kv and 150–350 μA gun current). The scanning electron microscope used was a QUANTA 200 (FEI Company) with an X-ray microanalysis device (EDAX Genesis).

Forty-five microsamples were prepared after the petrographic study to determine the carbon and oxygen stable isotope ratio of the different cements using the standard technique of Craig and Gordon (1965) and Claypool et al. (1980). The CO_2 was extracted from 60 ± 10 μg of powdered carbonate samples which were reacted with 103% phosphoric acid for 2 min at 70 °C for calcites and 15 min at 70 °C for dolomites. The CO_2 was analysed using an automated Kiel Carbonate Device attached to a Thermal Ionization Mass Spectrometer Thermo Electron (Finnigan) MAT-252. The results are precise to ± 0.02‰ for $\delta^{13}C$ and ± 0.04‰ for $\delta^{18}O$.

Carbon-coated polished thin-sections were used for analyzing minor and trace element concentrations on a CAMECA SX-50 electron microprobe. The microprobe was operated using 20 Kv of excitation potential, a current intensity of 15 nA and a beam diameter of 10 μm. The detection limits are 145 ppm for Mn, 192 ppm for Fe, 130 ppm for Na, 415 ppm for Mg, 190 ppm for Sr ppm and 395 ppm for Ca.

4. Outcrop study and petrography

The Upper Jurassic–Lower Cretaceous dolomites of the footwall of the Baix Penedès fault are composed of 0.3 to 1.5 meters-thick beds of grey dolomites, trending N040 and dipping 10°NW (Fig. 2A and B).

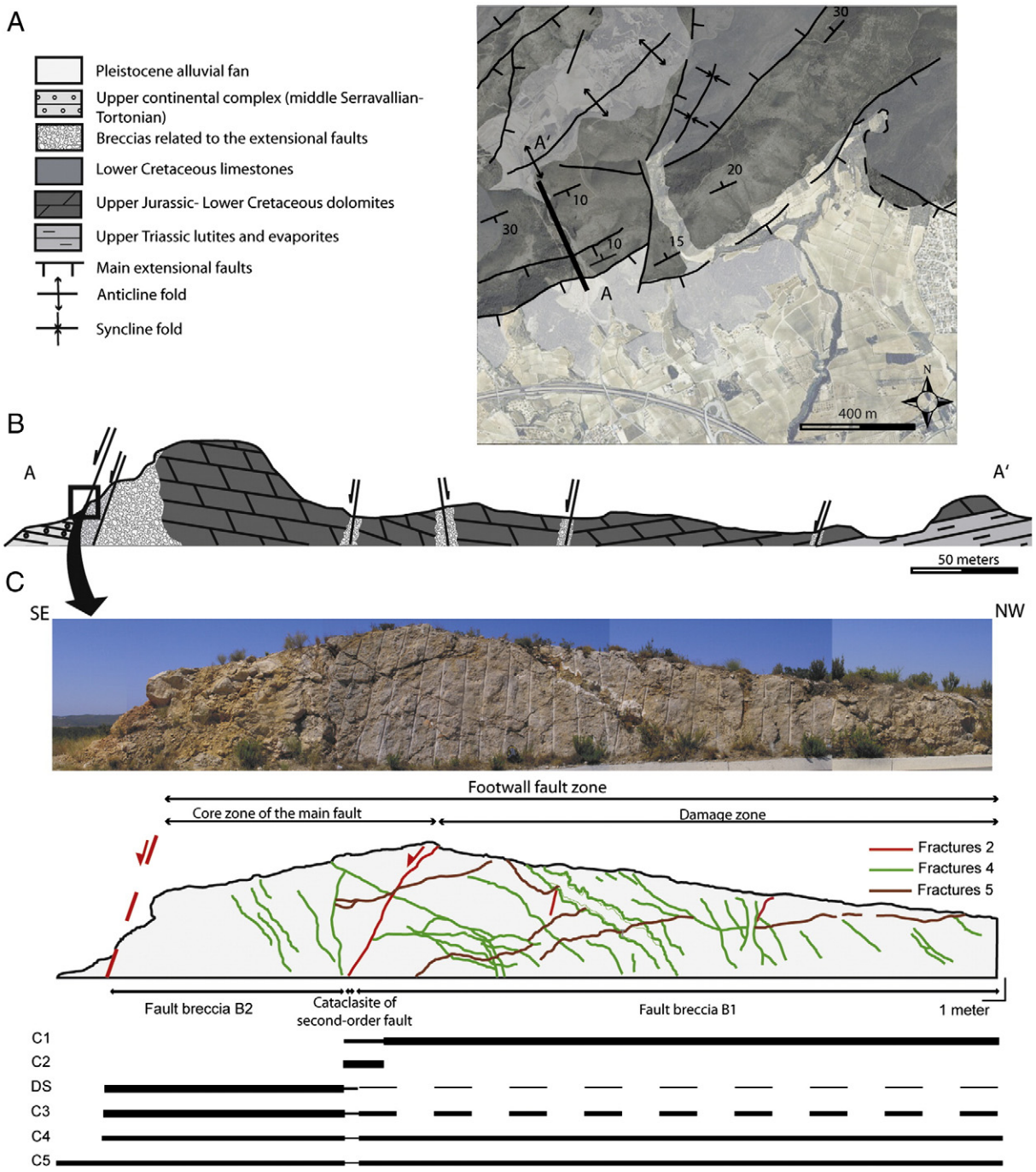

Fig. 2. (A) Schematic geological map, and (B) geological cross-section (A–A′) of the studied area. The square indicates the location of the amplified cross-section (C) showing the distribution of fractures, breccias and cements in the core and damage zone of the footwall block.

The dolomites are composed of dolomicrite to dolosparite featuring anhedral to subhedral dull purple luminescent crystals, 10 to 100 μm in size. These dolomitic rocks correspond to the Garraf Upper Dolomites Formation of Thitonian–Berriasian age (Salas, 1987).

Within this footwall, the main fault is bounded by a damage zone several hundreds of meters wide, which is characterized by intense fracturing and brecciation. Several second-order faults are present within the damage zone. Ten meters-thick core zone is present in the nearest part of the main fault (Fig. 2B and C).

According to the cross-cutting relationships between the different generations of fractures and the main $\delta^{18}O$ and $\delta^{13}C$ signatures of their filling cements, different fracture systems and breccias have been recognized and are described below in a chronologic order.

4.1. Early fractures and breccias

Fractures 1 are mode I (opening) fractures without preferred orientation, 10 to 100 μm thick and with sub-angular walls (Fig. 3A). These fractures are present in the whole footwall damage zone and are filled by the C1 dolomitic cement, which is composed of anhedral dull red luminescent crystals, from 5 to 10 μm in size, growing in optical continuity with the host-rock crystals (Fig. 3B, C).

Fractures 2: are mode II (sliding) second order fractures sub-parallel to the main fault. They are 10 to 100 μm thick and have sharp walls (Fig. 3D). They are filled by the C2 dolomitic cement, constituted by subhedral to euhedral bright orange to bright yellow luminescent crystals, 10 to 100 μm in size (Fig. 3E and F). These crystals precipitated

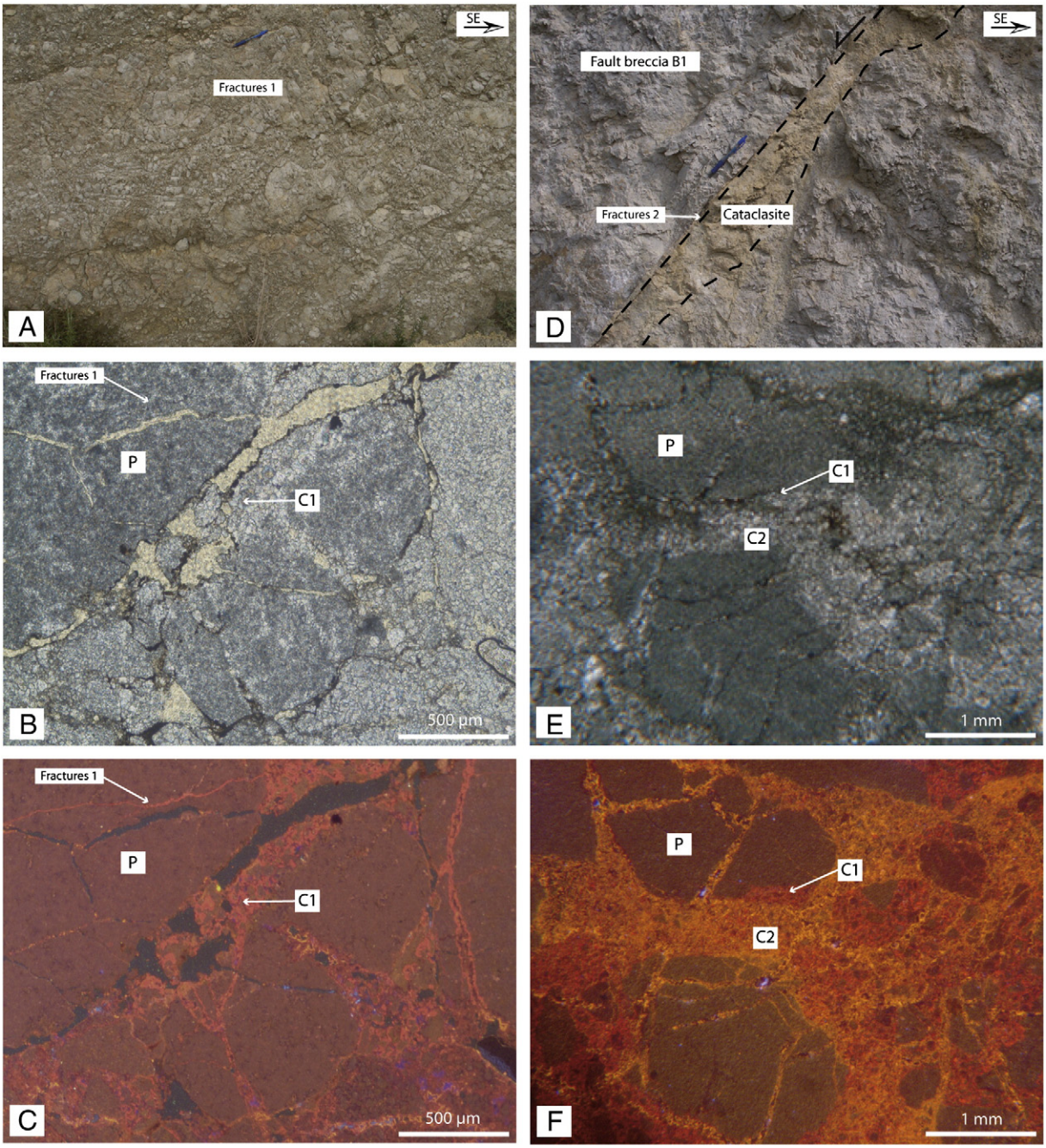

Fig. 3. (A) Outcrop photograph showing fractures 1 affecting the Late Jurassic–Early Cretaceous dolomites of the protolith. Pen as scale; (B and C) Fractures 1, fault breccia B1 and dolomite cement C1 viewed under optical (B) and cathodoluminescence (C) microscope; (D) Outcrop photograph showing the distribution of the dilatant breccia B1 and cataclasite with respect to the fractures 2. Pen as scale; (E and F) Cataclasite and dolomite cement C2 viewed under optical (E) and cathodoluminescence (F) microscope. P: protolith; C1: dolomite cement C1; C2: dolomite cement C2.

as overgrowths over nucleation centres corresponding to micrometric fragments from the protolith or, in some cases, from the dolomitic cement C1. Kaolinite, illite-chlorite and, in lesser amounts, goethite, rutil, apatite and pyrite are present within the dolomite crystals.

According to the textural classification of the fault breccias proposed by Sibson (1977), two types of breccias related to the fractures 1 and 2 have been recognized:

The first type is a moderately cohesive fault breccia B1 formed by angular fragments of dolomitic host-rock, 0.5 to 4 cm in size. This breccia results from opening of fractures 1 and is cemented by the dolomitic cement C1 (Fig. 3B, C and D).

The second type of breccias is a cataclasite formed by subangular fragments of dolomitic rock, up to 0.1 cm in size. Approximately 90% of the fragments correspond to the protolith and 10% to reworked B1 breccia. The fragments float within a matrix of finer fragments resulting from host-rock and B1 breccia comminution. This cataclasite results from sliding along fractures 2 and is cemented by the dolomitic cement C2 (Fig. 3E and F). Inside the cataclasite, the fractures 2 are bounded by ultracataclastic bands due to deformation concentration along the slip surfaces. The ultracataclastic bands have the same composition as their cataclasite matrix and are also cemented by the dolomitic cement C2.

Approaching the fault planes, the cataclasite and the dolomitic cement C2 are more abundant than the fault breccia B1 and the dolomitic cement C1.

4.2. Late fractures and breccias

Three late systems of fractures with related breccias and late cements have been recognized:

Fractures 3 are mode I fractures without preferred orientation, some of them corresponding to the reactivation of pre-existing fractures 1. They are 100 μm to 2 cm thick and have sub-angular walls (Fig. 4A). They contain two phases of filling: a first phase corresponds to a dolomitic sediment DS, constituted by subhedral to euhedral bright orange to bright yellow luminescent dolomitic crystals, 10 to 100 μm in size (Fig. 4A, B and C). The crystal nucleus corresponds to micrometric fragments of the protolith or in some cases C1 cement. Kaolinite, illite–chlorite, quartz and, in lesser amounts, goethite, rutil, apatite and pyrite are associated with this sediment. The dolomitic sediment DS usually shows a thin depositional lamination and fills the lower part of the cavities (Fig. 4D). The second filling phase corresponds to the late C3 calcite cement, constituted by equant non-luminescent crystals, 10 μm to 200 μm in size. This cement can

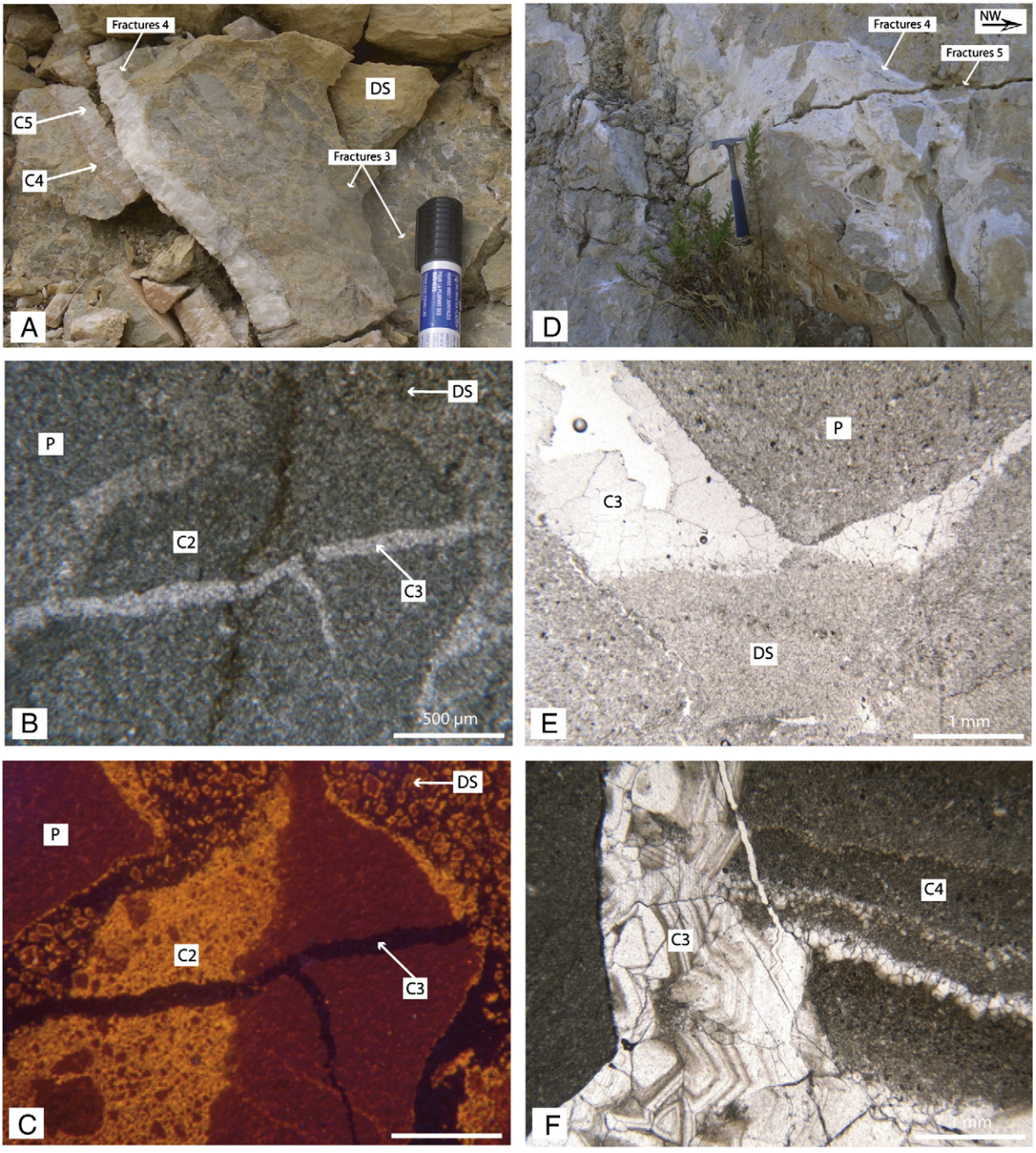

Fig. 4. (A) Outcrop photograph showing the fractures 3 and their related fault breccia B2 with the dolomitic sediment DS, and the fractures 4 with the two stages of filling by the calcite cements C4 and C5. Pen as scale; (B and C) Dilatant breccia B2, dolomitic sediment DS and calcite cement C3 viewed under optical (B) and cathodoluminescence (C) microscope; (D) Laminated dolomitic sediment filling the lower part of the cavities and calcite cement C3 filling the upper part. (E) Fractures 4 showing the associated speleothems and fractures 5. Hammer as scale; (F) Calcite cement C3 and laminated calcite cement C4 with size variations of the calcite crystals. P: protolith; DS: dolomitic sediment; C3: calcite cement C3; C4: calcite cement C4.

incorporate elements of the dolomitic sediment DS (Fig. 4B and C). The calcite cement C3 is also found in the matrix of the fault breccia B1 and in the cataclasites.

Fractures 3 are present in the whole footwall fault zone, increasing in abundance near to the main fault plane.

Fractures 4 are mode I fractures with a general N030 trend and 70–80 NW dip. These fractures are largely open, from 2 to 40 cm wide, and have sub-angular walls (Fig. 4A and E). They contain two phases of filling: the first phase corresponds to the C4 laminated calcite cement constituted of equant non luminescent crystals, 10 to 100 μm in size. The laminations correspond to size variations of the calcite crystals, and in some cases include goethite and dolomitic crystals (Fig. 4F). The second filling phase corresponds to the C5 calcite cement constituted by equant non-luminescent crystals, larger than 200 μm in size. This cement has a palisade texture which can be developed over 30 cm thick (Fig. 4A and E). The fractures 4 are present in the whole footwall fault zone.

Fractures 5 are mode I fractures with a general N030 to N050 trend and 20–30° NW dip. These fractures remained open, from 500 μm to 3 cm wide, and have sub-angular walls. The fractures 5 cut all previous fractures (Fig. 4E).

Forming part of the core zone of the Baix Penedès main fault, a distinct cohesive fault breccia B2 related to fractures 3 occurs in a 10 meters-wide interval (Fig. 2C). It is formed by angular fragments of dolomitic rock, from 0.5 to 4 cm in size. 80% of the fragments correspond to the protolith and 20% to reworked fault breccia B1 and dolomite cement C2. The clasts are surrounded by the dolomite sediment DS and the calcite cement C3 (Fig. 4A, B and C).

5. Geochemistry

Elemental (microprobe) and stable isotopes analyses were performed to compare the protolith and cement compositions, in order to understand the nature of the fluid-rock interactions and the characteristics and evolution of the hydrological system during the development of the fault.

5.1. Elemental analyses

5.1.1. Early fractures and breccias

The Upper Jurassic–Lower Cretaceous dolomites from the protolith contain between 21.3 and 23.7% of Ca, between 12.0 and 13.6% of Mg, and between 535 and 1148 ppm of Sr. The Na content ranges from below the detection limit to 816 ppm, the Mn content ranges from below the detection limit to 188 ppm and the Fe content ranges from below the detection limit to 2306 ppm (Table 1 and Fig. 5).

Within the dolomitic cements C1 and C2, several differences are observed both with respect to the protolith and between them. The dolomitic cement C1 has between 539 and 1036 ppm of Sr, whereas the dolomitic cement C2 has between 364 and 954 ppm of Sr, thus showing a slightly lower concentration in Sr in the second generation of cement. The Na content is slightly lower than in the protolith, being from below the detection limit to 644 ppm for the dolomitic cement C1 and from below the detection limit to 1316 ppm for de dolomitic cement C2, whereas the Mn content is higher, being from below the detection limit to 361 ppm for the dolomitic cement C1, and from below the detection limit to 375 ppm for the dolomitic cement C2. The Fe concentration increases in the successive generations of cements: in the dolomitic cement C1, the Fe content ranges from below the detection limit to 1036 ppm, and in the dolomitic cement C2 from below the detection limit to 5908 ppm.

5.1.2. Late fractures and breccias

The dolomitic sediment DS has similar elemental composition than the earlier dolomitic cement C2, except for the Fe content which, on average, is higher (Table 1 and Fig. 5).

In the case of the calcite cements, the major differences in trace elements with respect to the dolomitic protolith and cements are shown by the Sr and Fe concentrations. The Sr concentration in calcite cements has higher values than the protolith: the calcite cement C3 contains between 846 and 1674 ppm, the calcite cement C4 between 1082 and 1207 ppm, and the calcite cement C5 between 1126 and 1510 ppm. By contrast, the Fe concentration in calcite cements has lower values than the protolith: C3 contains from below the detection

Table 1
Minimum, maximum and average values of the elemental composition of the protolith and dolomite and calcite cements, and calculated Mg/Ca and Sr/Ca molar ratios of the parent fluid applying the distribution coefficient equation.

Filling stage		Ca (%)	Mg (%)	Na (ppm)	Mn (ppm)	Fe (ppm)	Sr (ppm)	Molar ratio Mg/Ca fluid (a)	Molar ratio Mg/Ca fluid (b)	Molar ratio Mg/Ca fluid (c)	Molar ratio Sr/Ca fluid (d)	Molar ratio Sr/Ca fluid (e)
Protolith	Min.	21.30	12.03	<d.l.	<d.l.	<d.l.	535	–	–	–	–	–
$n=49$	Max.	23.68	13.57	816	188	2306	1148	–	–	–	–	–
	Average	22.00	12.83	–	–	–	758	–	–	–	–	–
Dolomite cement C1	Min.	21.35	11.74	<d.l.	<d.l.	<d.l.	539	–	–	–	–	–
$n=30$	Max.	24.65	14.72	644	361	4336	1036	–	–	–	–	–
	Average	22.46	12.91	–	–	–	788	–	–	–	–	–
Dolomite cement C2	Min.	21.27	11.40	<d.l.	<d.l.	<d.l.	364	–	–	–	–	–
$n=99$	Max.	23.89	13.32	1316	375	5908	954	–	–	–	–	–
	Average	22.11	12.65	–	–	–	709	–	–	–	–	–
Dolomite sediment DS	Min.	21.03	11.43	<d.l.	<d.l.	<d.l.	577	–	–	–	–	–
$n=26$	Max.	23.76	13.23	405	379	4134	934	–	–	–	–	–
	Average	22.19	12.37	–	–	–	725	–	–	–	–	–
Calcite cement C3	Min.	38.71	0.03	<d.l.	<d.l.	<d.l.	846	0.114	0.049	0.012	0.016	0.012
$n=101$	Max.	40.37	0.81	712	215	787	1674	2.844	1.219	0.293	0.032	0.024
	Average	39.75	0.29	–	–	–	1234	1.001	0.429	0.103	0.024	0.018
Calcite cement C4	Min.	38.83	0.31	<d.l.	<d.l.	<d.l.	1082	1.084	0.464	0.112	0.021	0.016
$n=4$	Max.	39.43	0.49	163	<d.l.	561	1207	1.728	0.741	0.178	0.024	0.018
	Average	39.15	0.40	–	–	–	1134	1.409	0.604	0.145	0.022	0.017
Calcite cement C5	Min.	38.43	0.19	<d.l.	<d.l.	<d.l.	1126	0.114	0.049	0.066	0.016	0.016
$n=17$	Max.	39.70	0.82	183	<d.l.	1103	1510	2.844	1.219	0.299	0.032	0.022
	Average	39.17	0.46	–	–	–	1291	1.393	0.597	0.166	0.023	0.019

(a) $D^{cc}_{Mg}=0.012$ (25 °C) — Mucci (1987).
(b) $D^{cc}_{Mg}=0.028$ (40 °C) — Mucci (1987).
(c) $D^{cc}_{Mg}=0.1163$ (90 °C) — Katz (1973).
(d) $D^{cc}_{Sr}=0.027$ (25 °C) — Lorens (1981).
(e) $D^{cc}_{Sr}=0.08$ (100–150 °C) — Kinsman (1969).

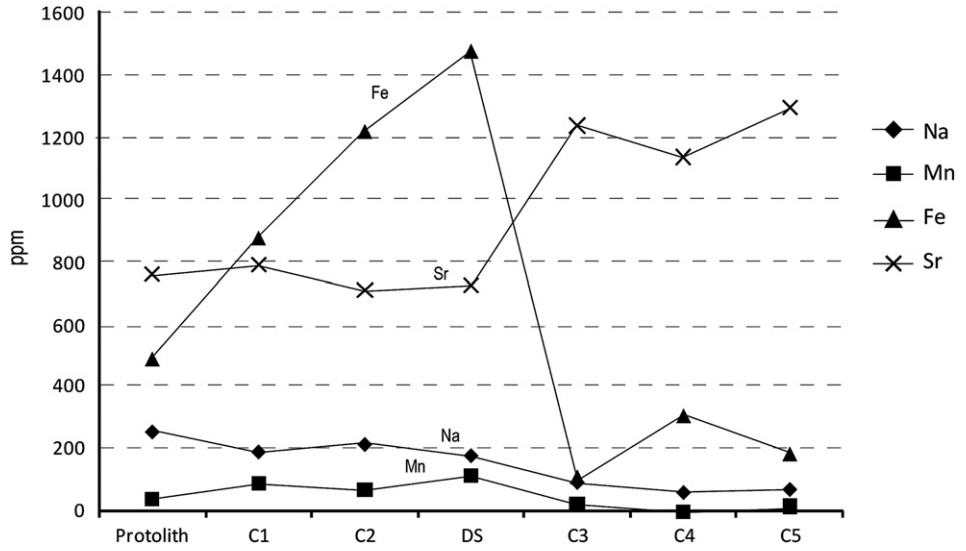

Fig. 5. Average values of the elemental compositions of the protolith, dolomite cements C1 and C2, dolomitic sediment DS and calcite cements C3, C4 and C5. Note: the average has been calculated including the values below the detection limit.

limit to 787 ppm of Fe, C4 from below the detection limit to 561 ppm, and C5 from below the detection limit to 1103 ppm. The Mn concentrations in the calcite cements are lower than in the protolith and dolomitic cements: for C3 they range from below the detection limit to 215, and for C4 and C5, they are always below the detection limit.

5.2. Stable isotopes analyses

The $\delta^{18}O$ values of the protolith range from −2.4 to +1.2‰ VPDB, and the $\delta^{13}C$ values range from −0.5 to +2.2‰ VPDB (Table 2 and Fig. 6). These values are consistent with those of the Jurassic–Cretaceous marine carbonates, which range from −2.5 to +2‰ VPDB for $\delta^{18}O$ and −1.8 to +2‰ VPDB for $\delta^{13}C$ (Veizer et al., 1999).

5.2.1. Early fractures and breccias

Due to the difficulty in sampling, we could pick-up only two microsamples from the dolomitic cement C1 filling fractures 1. This cement has $\delta^{18}O$ values varying between −2.3 and −1.3‰ VPDB and $\delta^{13}C$ values ranging from −0.8 to +0.3‰ VPDB. Although we have the values from two samples, it is shown a similar trend to the values of the protolith. The dolomitic cement C2 filling fractures 2 has $\delta^{18}O$ values varying between +0.1‰ and −0.1‰ VPDB and $\delta^{13}C$ values varying from −3.1‰ to −2.9‰ VPDB, i.e. constant $\delta^{18}O$ values and slightly depleted $\delta^{13}C$ values with respect to C1 and the protolith (Table 2 and Fig. 6).

5.2.2. Late fractures and breccias

The dolomitic sediment DS filling the fractures 3 has $\delta^{18}O$ values varying between −5.8 to −3.9‰ VPDB and $\delta^{13}C$ values ranging from −5.7 to −5.3‰ VPDB. The calcite cement C3 filling the same fractures has $\delta^{18}O$ values varying from −7 to −6.4‰ VPDB and $\delta^{13}C$ from −8.3 to −7.8‰ VPDB. The DS values are thus intermediate between the C2 and C3 values.

The laminated calcite cement C4 filling fractures 4 have $\delta^{18}O$ values around −6.8‰ VPDB and $\delta^{13}C$ values around −8‰ VPDB, similar to those of the calcite cement C3. The palisade calcite cement C5 filling fractures 4 has $\delta^{18}O$ values varying from −7.2 to −6.2‰ VPDB and $\delta^{13}C$ values from −9.6 to −9‰ VPDB, i.e. slightly lower $\delta^{13}C$ values than C3 and C4 (Table 2 and Fig. 6).

Table 2
$\delta^{18}O$ and $\delta^{13}C$ values of the protolith and dolomite and calcite cements.

Filling stage	$\delta^{13}C$‰ VPDB	$\delta^{18}O$‰ VPDB
Protolith	0.7	0.1
Protolith	2.2	0.3
Protolith	2.1	1.2
Protolith	1.5	0.3
Protolith	1.8	0.9
Protolith	2	0.5
Protolith	1.7	0.7
Protolith	0.4	−2.4
Protolith	2.1	−1.7
Protolith	−0.1	−0.9
Protolith	1.2	−0.4
Protolith	−0.5	−1.8
Protolith	1	−1.6
Protolith	1	−1.8
Protolith	0.5	−2.2
Protolith	0.3	−1.5
Protolith	1.1	−1.8
Dolomitic cement C1	−0.8	−2.3
Dolomitic cement C1	0.3	−1.3
Dolomitic cement C2	−2.9	0.1
Dolomitic cement C2	−3.4	−0.8
Dolomitic cement C2	−3.1	−1
Dolomitic cement C2	−2	−0.6
Dolomitic sediment DS	−6.4	−4.8
Dolomitic sediment DS	−5.4	−5
Dolomitic sediment DS	−7.3	−5.2
Dolomitic sediment DS	−8.7	−5.1
Dolomitic sediment DS	−5.3	−3.9
Dolomitic sediment DS	−6.3	−4.2
Dolomitic sediment DS	−5.7	−5.8
Calcite cement C3	−8.2	−7
Calcite cement C3	−8.3	−6.4
Calcite cement C3	−8.1	−7
Calcite cement C3	−8.3	−6.7
Calcite cement C3	−7.7	−6.4
Calcite cement C3	−7.9	−6.9
Calcite cement C4	−8	−6.8
Calcite cement C5	−9.3	−6.2
Calcite cement C5	−9.4	−6.9
Calcite cement C5	−9.6	−7.2
Calcite cement C5	−9.3	−6.8
Calcite cement C5	−9.5	−6.9
Calcite cement C5	−9	−6.7
Calcite cement C5	−9.5	−6.5
Calcite cement C5	−9.4	−7.1
Calcite cement C5	−9.6	−7.2

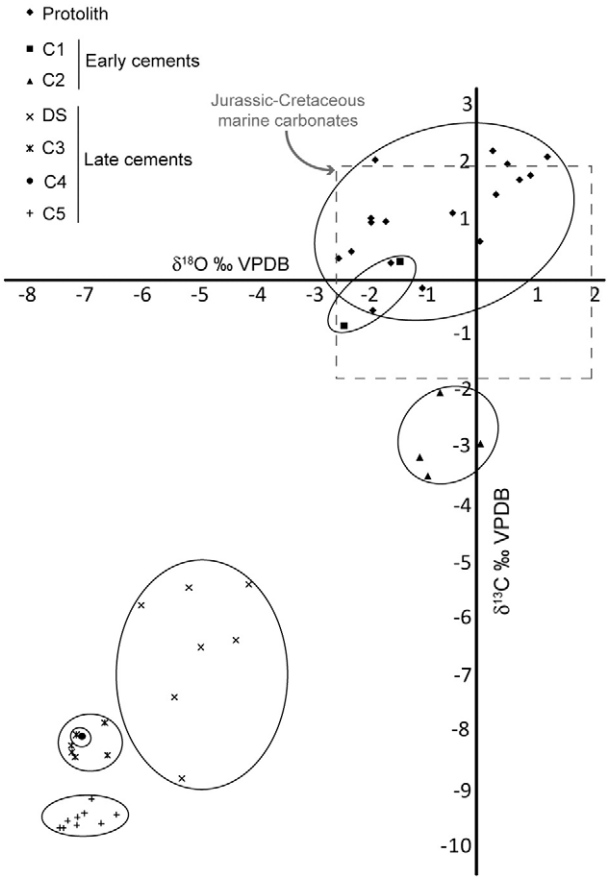

Fig. 6. $\delta^{18}O$ and $\delta^{13}C$ cross-plot of the protolith, dolomitic cements C1 and C2, dolomitic sediment DS and calcite cements C3, C4 and C5.

6. Discussion

The successive deformation stages described above traduce the development of the Baix Penedès footwall fault zone, with an evolution of the regimes (tensile or sliding) and distribution of the deformation. Below, we interpret this evolution in the frame of a model of upward fault-tip propagation similar to those already proposed by Steward and Hancock (1988, 1990) and Labaume et al. (2004) for other examples of major fault zones cutting carbonate rocks in a superficial context. We combine this structural model with the petrographic and geochemical results obtained on the successive cements to highlight the evolution of the hydrologic regime in relation to the fault zone development and propagation.

6.1. Early fractures and breccias

The stable of the protolith, ranging from −2.4 to +1.2‰ VPDB, shows a marine influence during the dolomitization process.

During the initial upward propagation of the fault within the Jurassic dolomites, deformation in the process zone formed around the fault tip was dominated by dilatant fracturing (fractures 1 and fault breccia B1) (Fig. 7A, B). The fluid involved in this deformation, responsible for precipitation of the dolomite cement C1, had an elemental and stable isotopes geochemistry close to that of the protolith, showing that this fluid had a high interaction with the protolith in a closed hydrological system (Travé et al., 1998; Labaume et al., 2004; Benedicto et al., 2008). The $\delta^{18}O$ values, varying between −2.3 and −1.3‰ VPDB, indicates low temperature, which is consistent with the results of thermochronology in the central part of the Catalan Coastal Ranges, which show that maximal burial of the exhumed normal fault footwalls was less than 2 km (Juez-Larré and Andriessen, 2006).

As the fault developed, different second-order incipient faults were formed (fractures 2). The frictional processes along these faults generated the cataclasite and the ultracataclasite bands along the slip surfaces (Fig. 7C). The $\delta^{18}O$ values, varying between +0.1‰ and −0.1‰ VPDB, indicate that the fluid responsible for precipitation of the dolomite cement C2 remained in an essentially closed hydrological system and low temperature of precipitation. The increase in Fe content, the decrease in Mn content, together with the slightly depleted $\delta^{13}C$ of the dolomitic cement C2, is interpreted as the incipient opening of the system, with infiltration of a meteoric fluid carrying soil-derived CO_2 interacting with the host-rock (Travé et al., 1998; Breesch et al., 2009).

6.2. Late fractures and breccias

As the footwall of the fault was uplifted and eroded, the dilatant fractures 3 to 5 were formed in response to the tensional stresses that characterise extensional deformation close to the surface (Figs. 2C and 7D). The fractures 3 and related B2 breccia traduce further localization of the deformation. This breccia shows a significant opening of the hydrologic system to the external fluids responsible of the new

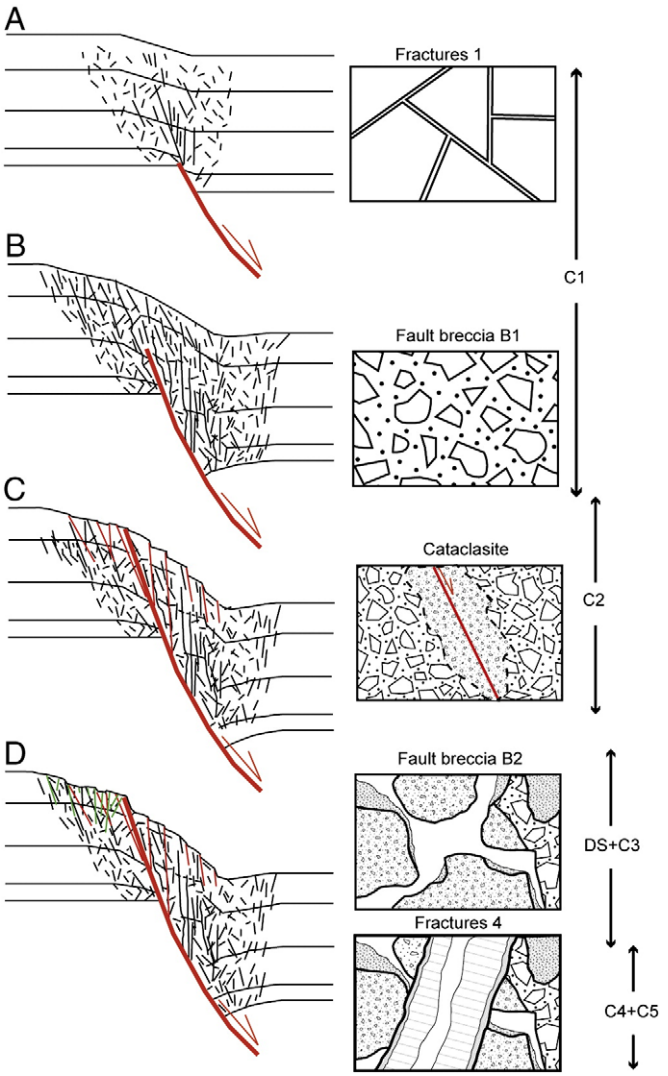

Fig. 7. Model of evolution of the fractures, breccias and cements during upward propagation of the Baix Penedès extensional fault (modified from Steward and Hancock, 1988, 1990, and Labaume et al., 2004).

fillings. The petrography and elemental geochemistry of the dolomitic sediment DS suggests that it results from the reworking of dolomite cement C2 as detritial sediment. The thin depositional lamination of DS and its occurrence in the lower part of the cavities is interpreted as geopetal geometry of the sediment, indicating a deposition in the vadose zone. The increase in Mg and Fe contents with respect to the dolomitic cement C2 also indicates a deposition in an open meteoric regime. The isotopic signal of the dolomitic sediment, intermediate between the C2 and C3 values, is interpreted as resulting from a mixing of these cements. The $\delta^{18}O$ values of C3, varying from −7 to −6.4‰ VPDB, together with the calculated Mg/Ca and Sr/Ca molar ratios (Table 1), show that meteoric waters, which not interacted with the host-rock, were responsible for precipitation of the calcite cement C3.

Formation of the fractures 4 and 5 traduces the generalized tensile deformation of the fault footwall during the final stages exhumation (Figs. 2C and 7D). The $\delta^{18}O$ values of C4 and C5, varying from −7.2 to −6.2‰ VPDB, together with the calculated Mg/Ca and Sr/Ca molar ratios of the fluid (Table 1), indicate precipitation from meteoric waters. The laminated calcite cement C4, which incorporates detritial dolomitic crystals from C2, together with the palisade texture of the calcite cement C5, are interpreted as speleothems covering the fractures walls, in the vadose meteoric environment (Travé and Calvet, 2001). The lower $\delta^{13}C$ of the calcite cement C5 traduces a higher involvement of soil-derived CO_2 (Travé et al., 1998; Breesch et al., 2009).

7. Conclusions

The tectonic fracturing, brecciation and cementation processes observed along the Baix Penedès fault attest to two types of fluid regimes successively involved in the Neogene deformation, and that can be related to successive stages of the fault development and upward propagation: (1) The process zone at the tip of the fault was characterized by dilatant deformation that formed the fault breccia B1. The fluid involved during this initial upward propagation of the fault (precipitating the dolomite cement C1) was in equilibrium with the host-rock in a closed hydrological system. During further development of the fault, localised frictional processes generated cataclasite along distinct second-order faults (fractures 2). Geochemistry of the associated fluid (precipitating the dolomite cement C2) attests to partial opening of the hydrological system. (2) A meteoric fluid regime beginning with further localisation of deformation, with formation of the B2 fault breccia in a tensile tectonic regime close to the main fault planes. The percolation of freshwaters in the vadose meteoric environment, i.e. in karstic conditions, was responsible of the deposition of the dolomitic sediment DS and the precipitation of the calcite cement C3. The last extensive stages, generating fractures 4 and 5, show a prevailing karstic system with precipitation of the laminated calcite cement C4 and the C5 speleothems. This karstic regime developed when the fault reached the surface, where tensional stresses favoured dilatant deformation and complete opening of the hydrological system.

Acknowledgments

We thank Indiana Romaire, Lucas Lamesalles and Sonia Belaid for helping in field works and Ramon Vaquer, Roger Soliva and Eduard Roca for discussions on different geochemical and structural aspects of the faults. We also thank to Luca Micarelli and to the anonymous reviewer of the Journal of Geochemical Exploration for their accurate and constructive reviews of this paper. The isotopic and electron microprobe analyses and the scanning microscope observations were carried out at “Serveis Cientificotècnics” of the Universitat de Barcelona. This research was performed within the framework of DGICYT Spanish Project CGL2006-04860, BES-2007-14935 grant and Grup Consolidat de Recerca “Geologia Sedimentària” (2009SGR-1451).

References

Amigó, J., 1986. Estructura del massís del Gaià. Relacions estructurals amb les fosses del Penedès i del Camp de Tarragona. PhD Tesis, Universitat de Barcelona, Barcelona, Spain.
Anadón, P., Cabrera, L., Guimerà, J., Santanach, P., 1985. Paleogene strike-slip deformation and sedimentation along the southeastern margin of the Ebro Basin. In: Biddle, K.T., Christie-Blick, N. (Eds.), Strike-Slip Deformation, Basin Formation Sedimentation: Special Publication Society of Economic Paleontologists and Mineralogists, vol. 37, pp. 303–318.
Bartrina, M.T., Cabrera, L., Jurado, M.J., Guimerà, J., Roca, E., 1992. Evolution of the central Catalan margin of the Valencia trough (western Mediterranean). Tectonophysics 203, 219–247.
Benedicto, A., Plagnes, V., Vergély, P., Flotté, N., Schultz, R.A., 2008. Fault and fluid interaction in a rifted margin: integrated study of calcite-sealed fault-related structures (southern Corinth margin). In: Wibberley, C.A.J., Kurtz, W., Imber, J., Holdsworth, R.E., Collettini, C. (Eds.), The internal structure of fault zones: implications for mechanical and fluid-flow properties: The Geological Society of London, Special Publication, vol. 299, pp. 1–19.
Bitzer, K., Carmona, J.M., Calvet, F., Travé, A., 1997. Modelling paleohydrological and thermal evolution of distensive basins: application to the Barcelona half-graben (offshore, NE Spain). In: Hendry, J., Carey, P., Parnell, J., Ruffell, A., Worden, R. (Eds.), Geofluids'97 Extended Abstracts. Belfast, Northen Ireland, pp. 352–355.
Breesch, L., Swennen, R., Vincent, B., 2009. Fluid flow reconstruction in hanging and footwall carbonates: compartmentalization by Cenozoic reverse faulting in the Northern Oman Mountains (UAE). Marine and Petroleum Geology 26, 113–128.
Bussolotto, M., Benedicto, A., Invernizzi, C., Micarelli, L., Plagnes, V., Deiana, G., 2007. Deformation features within an active normal fault zone in carbonate rocks: the Gubbio fault (Central Apennines, Italy). Journal of Structural Geology 29, 2010–2037.
Cabrera, L., 1981. Estratigrafía y caracterísitcas sedimentológicas generales de las formaciones continentales del Mioceno inferior de la Cuenca del Vallès-Penedès (Barcelona, Espanya). Estudios Geológicos 37, 35–43.
Cabrera, L., Calvet, F., 1996. Onshore Neogene record in NE Spain: Vallès-Penedès and el Camp half-grabens (NW Mediterranean). In: Friend, P.T., Dabrio, C.T. (Eds.), Tertiary Basins of Spain. Cambridge University Press, Cambridge, pp. 97–105.
Claypool, G.E., Holser, W.T., Kaplan, I.R., Sakai, H., Zak, I., 1980. The age curves of sulphur and oxygen isotopes in marine sulphate and their interpretation. Chemical Geology (Isotope geoscience section) 28, 199–260.
Craig, H., Gordon, I., 1965. Deuterium and oxygen-18 variations in the ocean and marine atmosphere. In: Tongiorgi, E. (Ed.), Stable Isotopes in Oceanographic Studies and Paleotemeratures. Consiglio Nazionale delle Richerche, Laboratorio di Geologia Nucleare, Pisa, Italy, pp. 9–130.
De Brit, T.J., 1989. Timing structural events and basement emplacement using extension veins and cements in the Carboniferous of North Central Ireland. Irish Journal of Earth Science 10, 13–31.
Dickson, J.A.D., 1966. Carbonate identification and genesis as revealed by staining. Journal of Sedimentary Petrology 36, 491–505.
Guimerà, J., 1988. Estudi estrucutal de l'enllaç entre la Serralada Ibèrica i la Serralada Costera Catalana. PhD thesis, Universitat de Barcelona, Barcelona, Spain.
Juez-Larré, J., Andriessen, P.A.M., 2006. Tectonothermal evolution of the northeastern margin of Iberia since the break-up of Pangea to present, revealed by low-temperature fission-track and (U–Th)/He thermochronology: a case history of the Catalan Coastal Ranges. Earth and Planetary Science Letters 243, 159–180.
Katz, A., 1973. The interaction of magnesium with calcite during crystal growth at 25–90 °C and one atmosphere. Geochimica et Cosmochimica Acta 37, 1563–1568.
Kinsman, D.J.J., 1969. Interpretation of Sr^{2+} concentrations in carbonate minerals and rocks. Journal of Sedimentary Petrology 39, 486–508.
Knipe, R.J., 1993. The influence of fault zones processes and diagenesis on fluid flow. In: Horbury, A.D., Robinson, A.G. (Eds.), Diagenesis and Basin Development: AAPG Studies in Geology, vol. 36, pp. 135–151.
Labaume, P., Carrio-Schaffhauser, E., Gamond, J.F., Renard, F., 2004. Deformation mechanisms and fluid-driven mass transfers in the recent fault zones of the Corinth rift (Greece). Comptes Rendus Géoscience 336, 375–383.
Lorens, R.B., 1981. Sr, Cd, Mn and Co distribution coefficients in calcite as a function of calcite precipitation rate. Geochimica et Cosmochimica Acta 45, 553–561.
Marín, M.A., Roca, E., Rosell, O., Marcuello, A., Cabrera, L., 2008. La Falla del Montmell: un ejemplo del control ejercido por las fallas extensivas mesozoicas en la arquitectura cenozoica de las Cadenas Costaneras Catalanas. Geotemas 10, 461–464.
Micarelli, L., Benedicto, A., Invernizzi, C., Saint-Bezar, B., Michelot, J.L., Vergely, P., 2005. Influence of P/T conditions on the style of normal fault initation and growth in limestones from SE-Basin, France. Journal of Structural Geology 27, 1577–1598.
Micarelli, L., Moretti, I., Jaubert, M., Moulouel, H., 2006. Fracture analysis in the south-western Corinth rift (Greece) and implications on fault hydraulic behaviour. Tectonophysics 426, 31–59.
Mucci, A., 1987. Influence of temperature on composition of magnesian calcite overgrowths precipitated from seawater. Geochimica et Cosmochimica Acta 5, 1977–1984.
Muchez, Ph., Slobondik, M., Viaene, W.A., Keppens, E., 1995. Geochemical constraints on the origin and migration of palaeofluids at the northern margin of the Variscan foreland, southern Belgium. Sedimentary Geology 96, 191–200.
Parcerisa, D., Gómez-Gras, D., Roca, E., Madurell, J., Agustí, J., 2007. The Upper Oligocene of Montgat (Catalan Coastal Ranges, Spain): new age constrains to the western Mediterranean Basin opening. Geologica Acta 5, 2–17.
Roca, E., 1994. La evolución geodinámica de la Cuenca Catalano-Balear y áreas adyacentes desde el Mesozoico hasta la actualidad. Acta Geológica Hispánica 29, 3–25.
Roca, E., Sans, M., Cabrera, L., Marzo, M., 1999. Oligocene to Middle Miocene evolution of the central Catalan margin (northwestern Mediterranean). Tectonophysics 315, 209–233.

Salas, R. 1987. El Malm i el Cretaci inferior entre el Massís del Garraf i la Serra d'Espadà. PhD thesis, Universitat de Barcelona, Barcelona, Spain.
Sibson, R.H., 1977. Fault rocks and fault mechanisms. Journal of Geology Society 133, 191–213.
Sibson, R.H., 2000. Fluid involvment in normal faulting. Journal of Geodynamics 29, 469–499.
Steward, I.S., Hancock, P.L., 1988. Normal fault zone evolution and fault scarp degradation in the Aegean region. Basin Research 1, 139–153.
Steward, I.S., Hancock, P.L., 1990. Brecciation and fracturing within neotectonic normal fault zones of the Aegean region. In: Knipe, R.J., Rutter, E.H. (Eds.), Deformation Mechanisms, Rehology and Tectonics: Geological Society Special Publication, vol. 54, pp. 105–112.
Travé, A., Calvet, F., 2001. Syn-rift geofluids in fractures related to the early-middle Miocene evolution of the Vallès-Penedès half-graben (NE Spain). Tectonophysics 336, 101–120.
Travé, A., Calvet, F., Soler, A., Labaume, P., 1998. Fracturing and fluid migration during Palaeogene compression and Neogene extension in the Catalan Coastal Ranges, Spain. Sedimentology 45, 1063–1082.
Veizer, J., Ala, D., Azmy, K., Bruckschen, P., Buhl, D., Bruhn, F., Carden, G.A.F., Diener, A., Ebneth, S., Godderis, Y., Jasper, T., Korte, C., Pawellek, F., Podlaha, O., Strauss, H., 1999. $^{87}Sr/^{86}Sr$, $\delta^{13}C$ and $\delta^{18}O$ evolution of Phanerozoic seawater. Chemical Geology 161, 59–88.

Publication 2

Baqués, V., Travé, A., Roca, E., Marín, M.A., Cantarero, I., 2012. Geofluid behaviour in successive extensional and compressional events: a case study from the south-western end of the Vallès-Penedès Fault (Catalan Coastal Ranges, NE Spain). Petroleum Geoscience, 18, 17-31.

Geofluid behaviour in successive extensional and compressional events: a case study from the southwestern end of the Vallès-Penedès Fault (Catalan Coastal Ranges, NE Spain)

V. Baqués*, A. Travé, E. Roca, M. Marín and I. Cantarero

Geomodels Research Institute, Faculty of Geology, University of Barcelona, c/Martí i Franquès s/n, 08028 Barcelona, Spain

**Corresponding author (e-mail: vbaques@ub.edu)*

ABSTRACT: The structural position of the Upper Jurassic–Lower Cretaceous carbonates located in the central part of the Catalan Coastal Ranges corresponds to the southwestern end of the Vallès-Penedès Fault. This fault was reactivated at different times during successive extensional and compressional events and several generations of fractures and cementations were formed.

Based on petrological and geochemical analyses of this cementation an evolution of the fluids related to the different tectonic stages can be deduced. (1) During the Mesozoic extension, the parent fluids resulted either from a mixing of trapped Upper Jurassic–Lower Cretaceous seawater and meteoric water, or from buffered meteoric waters. (2) Related to the Paleogene compression, the fluids came from the percolation of meteoric waters indicating shallow-depth deformation. (3) During the transitional phase between Paleogene compression and Neogene extension, a karstic dissolution took place and the porosities were infilled by different generations of sediments and cements deposited from meteoric fluids. (4) During the Neogene extension several episodes of meteoric percolations and fracturing processes occurred. The Neogene extensional faults used the earlier karstic system to develop and, later, during the late post-rift stage, a new karstic system occurred, covering the walls of open fractures with speleothems.

INTRODUCTION

In sedimentary basins, deformation and fracturing processes influence the distribution of diagenetic episodes because they are discontinuities that can act as barriers or as conduits for fluid circulations and cause the mobilization of these fluids from reactivation in different episodes of tectonic activity (Sibson 1987; Agosta *et al*. 2007; Breesch *et al*. 2009). Knowing the distribution of fractures, it is possible to predict the potential hydrocarbon and aquifer reservoirs, as well as to assess their quality (Knipe & McCaig 1994; Labaume *et al*. 2004; Géraud *et al*. 2006; Bussolotto *et al*. 2007). The study of fracture-related carbonate precipitates, coupling microstructural, petrological and geochemical analyses, allows one to unravel the origin and pathways of the fluids (De Brit 1989; Muchez *et al*. 1995; Bitzer *et al*. 1997; Travé *et al*. 1998; 2004; 2009; Travé & Calvet 2001; Labaume *et al*. 2007; Micarelli *et al*. 2005; 2006; Benedicto *et al*. 2008; Vilasi *et al.* 2009; André *et al*. 2010). In addition, specific petrophysical properties of the fractured host-rock and the pressure, temperature, origin and behaviour of fluids will control the degree of fluid–rock interaction and precipitation of cements within the fractures. However, these processes depend not only on the lithology; the depth at which the deformation develops is also one of the main factors controlling the diagenetic behaviour of the fractured areas. For example, it is known that the development of fractures in carbonates at shallow crustal depths (<1–3 km) is a very complex process, because of the interaction of mechanical and chemical processes (Sibson 2000; Pili *et al*. 2002; Verhaert *et al*. 2009).

The present study has been focused on characterizing the evolution of fluids within a long basement-involved fault which shows a complex tectonic evolution due to the superposition of successive extensional and compressional events. The case study is the Vallès-Penedès Fault, located in the central part of the Catalan Coastal Ranges, in the northeastern part of Spain. The main aims followed are: (1) to characterize the distribution and chronology of fractures, the timing of diagenetic processes, the type of fault rocks and related cements and the fluids involved during different deformation events; (2) to characterize the differences between the Mesozoic and Neogene extensional events; and (3) to recognize the interference between karstic and tectonic processes. The interest in the study of the karst development and infilling is because the main hydrocarbon reservoirs in Spain are located offshore in the Mediterranean, in Mesozoic reservoirs, equivalent to those studied onshore. For this reason, the diagenetic study can be compared in both areas, and the studied outcrops can be used as analogues of the reservoirs present in the Valencia Trough.

Petroleum Geoscience, Vol. **18**, 2012, pp. 17–31
DOI: 10.1144/1354-079311-017.

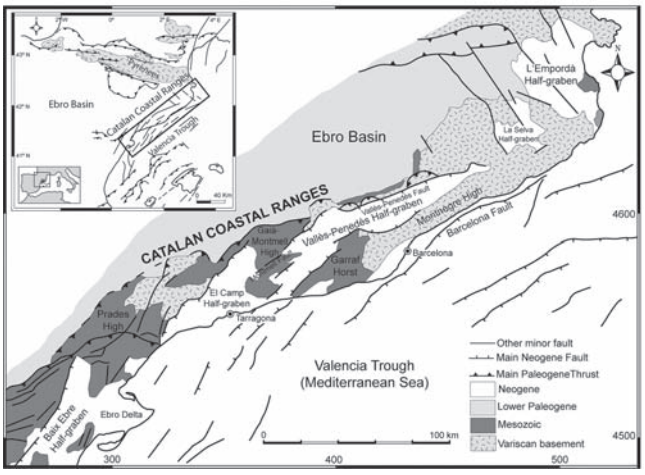

Fig. 1. Simplified geological map of the Catalan Coastal Ranges. Coordinates are in UTM (km).

GEOLOGICAL SETTING

The Catalan Coastal Ranges (CCR), in the NE of Spain, constitute the onshore expression of the northeastern part of the continental margin that separates the thinned crust of the Valencia Trough from the Variscan crust of the Iberian Plate (Dañobeitia *et al*. 1992; Vidal *et al*. 1995). It consists of several ENE- to NE-striking blocks bounded by 50–150 km long basement-involving faults which display a right-stepping *en echelon* arrangement with an ENE–WSW strike (Fig. 1). These faults dip southeastwards and show a reverse and/or normal motion. This double motion of the faults, together with the internal structure of the bounded blocks, reflects a complex evolution in which three main tectonic events can be differentiated: (1) a Mesozoic extensional phase in which several Late Jurassic–Early Cretaceous extensional basins developed along the present-day CCR (Montmell-Garraf, Barcelona, El Perelló and Maestrat Basins; Salas 1987); (2) a Paleocene to middle Oligocene contractional phase that generated an intraplate chain (the Catalan Intraplate Belt) from the emplacement of ENE- to NE-trending thick-skinned thrust sheets bounded by SE-dipping thrusts with a limited left-lateral strike-slip motion (Ashauer & Teichmüller 1935; Llopis-Lladó 1947; Anadón *et al*. 1985; Guimerà 1988, 2004; Roca 1996); and (3) a late Oligocene?–Neogene extensional phase leading to the normal reactivation of some of the main Paleogene faults (Fontboté 1954; Amigo 1986; Gaspar-Escribano *et al*. 2004) which split the area in a set of ENE–WSW blocks mainly tilted toward the NW (Bartrina *et al*. 1992; Roca & Guimerà 1992).

In this regional setting, the study area is placed at the southwestern end of the main outcropping basement fault: the Vallès-Penedès Fault (Fig. 2). This fault is more than 100 km long and has a Neogene extensional displacement that reaches 4 km (Roca *et al*. 1999). It belongs to a long-lived fault that, before this extensional motion, moved as a Paleogene NW-directed thrust (Fontboté 1954) and controlled the northwestern boundary of the Late Jurassic–Early Cretaceous Garraf-Montmell Basin (Salas 1987). The kinematics and structure of the Mesozoic history of the Vallès-Penedès Fault can be inferred from the study of the soft linkage zone that connects this fault with the other CCR major outcropping fault to the El Camp Fault (Fig. 2). This linkage zone is formed by pre-Neogene rocks and includes an ENE–WSW strip of folds and thrusts that, located at the southwestern prolongation of the Neogene Vallès-Penedès Fault, separates two realms with different Mesozoic successions. The

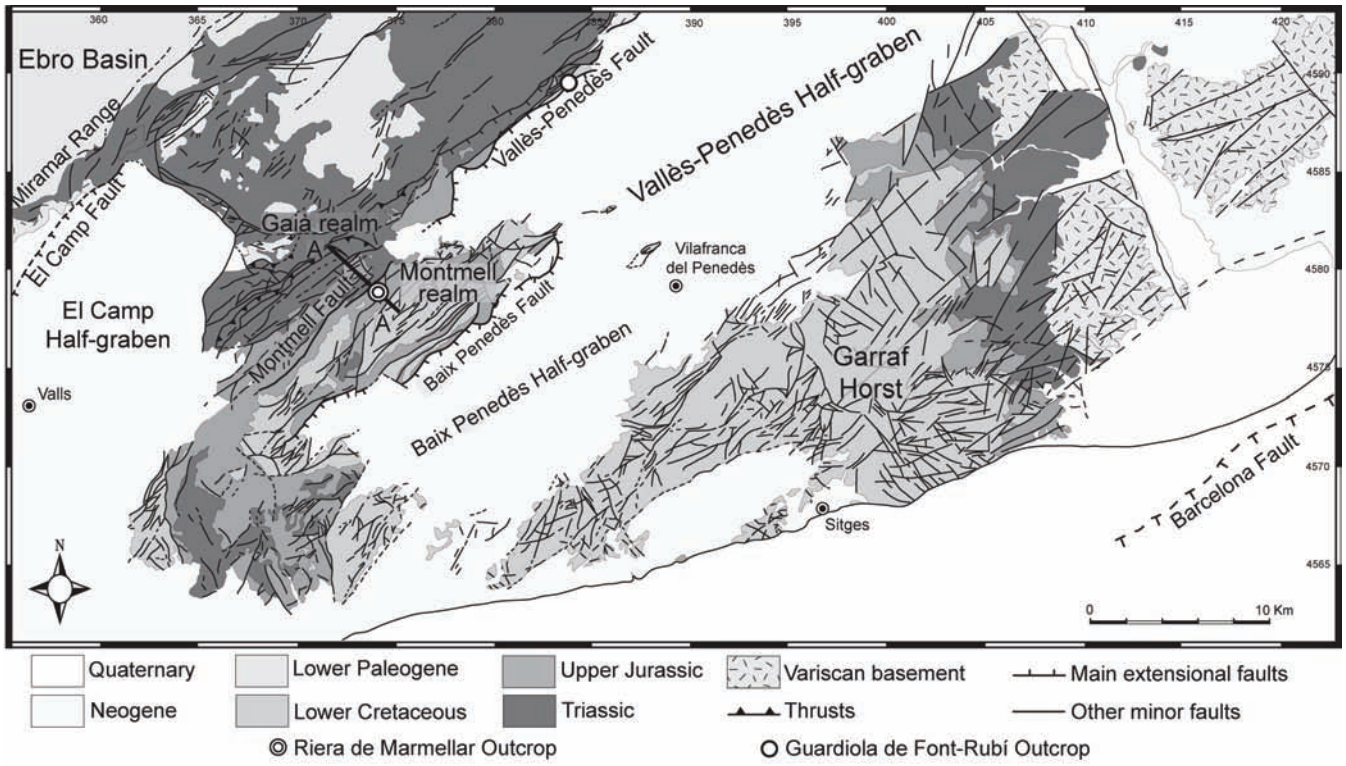

Fig. 2. Geological map of the southwestern segment of the Vallès-Penedès half-graben with location of the studied outcrops and the cross-section depicted in Figure 3. Coordinates are in UTM (km).

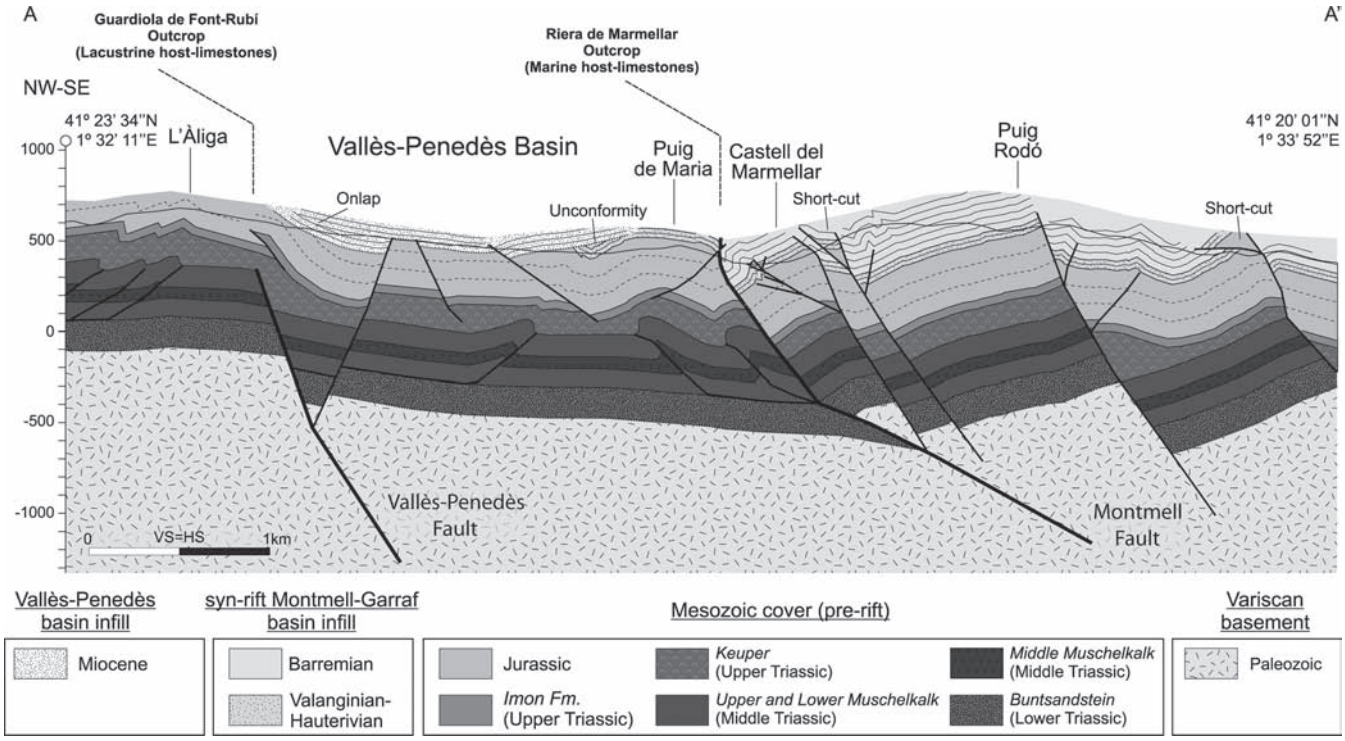

Fig. 3. Geological cross-section through the Vallès-Penedès and Montmell faults. The Riera de Marmellar and Guardiola de Font-Rubí outcrops have been projected to their equivalent structural position.

southern Montmell realm, belonging to the NW margin of the Garraf-Montmell Basin, made up by a complete Mesozoic succession with a thick Upper Jurassic–Lower Cretaceous succession; and the northern Gaia realm in which the Mesozoic is much thinner and represented only by Triassic rocks unconformably covered by lower Paleogene sediments of the Ebro Basin margin (Anadón *et al*. 1979).

A cross-section through the boundary between these two realms (Fig. 3) depicts that the structure of the study area is controlled by the motion of a series of SE-dipping basement extensional faults and by the presence of an Upper Triassic ductile level that decouples the deformation. Among the basement faults the Vallès-Penedès and the Montmell faults are notable. The first one is an extensional fault that, along the presented section, dies out in the Upper Triassic interval and drape folds the overlying Jurassic and Miocene rocks. Growth strata geometries in the Miocene sediments, as well as the fold geometry of the underlying Jurassic rocks, denote that its main extensional motion occurred during the Miocene. The other one, the Montmell Fault, bounds NW of the thick Upper Jurassic–Lower Cretaceous infill of the Garraf-Montmell Basin. It cuts all the Mesozoic successions but not the Miocene basin infill of the Vallès-Penedès half-graben which, northeastwards of the cross-sectional trace (Fig. 2), unconformably overlies the fault. The offset of the fault is extensional on the upper part but contractional on Lower Triassic–Palaeozoic levels. The boundary between these two parts coincides with a concave fault dip change and with the branch line of a hinterland-dipping duplex developed at the footwall block. This geometry is typical in inversion tectonics and corresponds to the contractional reactivation of an extensional fault with a footwall short-cut formation (Cooper *et al*. 1989). Supporting this interpretation, SE of the Montmell Fault, the Jurassic and Lower Cretaceous Garraf-Montmell Basin fill appears deformed by several parallel extensional faults with clear footwall short-cuts and SE-directed thrusts and folds that can be interpreted as buttressing structures developed against the extensional fault (Gillcrist *et al*. 1987). Taking into account that all these structures do not affect the Neogene infill of the Vallès-Penedès half-graben, the extensional motion of the Montmell Fault is attributed to be Late Jurassic–Cretaceous (coeval to the formation of the Garraf-Montmell Basin) and the contractional fault reactivation to the Paleogene (Marin *et al.* 2008).

To ascertain the movement of fluids during the Mesozoic formation and later Cenozoic contractional and extensional reactivations of the major basement faults present in the central part of the Catalan Coastal Ranges, two outcrops have been chosen, one located at the Montmell Fault and the other at the Vallès-Penedès Fault (see Figs 2, 3).

METHODOLOGY

The paragenetic sequence of diagenetic events was deduced from field and petrographic observations. Geochemical characteristics of consecutive diagenetic products then allowed subdividing the paragenesis of fluid flow history into four different stages. Finally, it was possible to link the paragenesis to the kinematic history obtained from the macro- and microstructural study. Diagenetic products (calcite cement and sediments infilling fractures) and the host rocks (marine and lacustrine limestones) were sampled in the two outcrops. Twenty-two samples of the host rock and different generations of veins infilling faults were collected. The samples were cut, polished and 40 thin sections were selected. The thin sections were stained with Alizarine Red-S and potassium ferricyanide to distinguish calcite and dolomite and their ferroan equivalents (Dickson 1966) and later they were studied using optical and cathodoluminescence microscopes. A Technosyn Cold Cathodoluminescence device (model 8200 MkII) operating at 15–18 kV and a 150–350 μA gun current was used.

The calcite cements from the host rock and fractures were sampled for carbon- and oxygen-isotope analysis employing a 500 μm thick dental drill to extract 60±10 μg of powder from polished slabs. The powdered calcite was reacted with 103% phosphoric acid for 2 min at 70ºC. The CO_2 was analysed using an automated Kiel Carbonate Device attached to a Thermal Ionization Mass Spectrometer Thermo Electron (Finnigan) MAT-252. The results are precise to ±0.02‰ for $\delta^{13}C$ and ±0.04‰ for $\delta^{18}O$. The results were corrected using the standard technique of Craig & Gordon (1965) and Claypool *et al*. (1980) and are expressed in ‰ with respect to the VPDB standard.

Sr chromatography was performed using the method described by Pin & Bassin (1992) using Sr resin commercially known as *Sr-Spec* and elaborated by Eichrom. Sr isotope measurements were carried out in a mass spectrometer Finnigan MAT-262 from the Department of Isotope Geochronology and Geochemistry of SGIker of the University of the Basque Country. Samples were loaded on to a Ta filament (99.95%) previously degassed in two stages at 2 A and 4.5 A for 30 minutes. The measurement of isotopic ratios was made in the following conditions: ^{88}Sr beam intensity approx. 4V, acquiring 20 blocks of 10 sweeps, and ^{85}Rb being used to monitor potential isobaric interferences. The analytical data were corrected by linear law mass fractionation using as a constant ratio $^{87}Sr/^{86}Sr = 0.1194$ (Steiger & Jäger 1977).

Carbon-coated polished thin-sections were used to analyse minor and trace element concentrations on a CAMECA SX-50 electron microprobe. The microprobe was operated using 20 kV of excitation potential, a current intensity of 15 nA and a beam diameter of 10 μm. The detection limits are 100 ppm for Mn, 145 ppm for Fe, 100 ppm for Na, 400 ppm for Mg, 90 ppm for Sr and 500 ppm for Ca.

STRUCTURAL AND MICROSTRUCTURAL DATA

Two locations that lie about 15 km apart from each other were selected in accordance with their structural position in the general cross-section through the Montmell and the Vallès-Penedès Faults (Fig. 3): the Riera de Marmellar outcrop (RMO) and the Guardiola de Font-Rubí outcrop (GFRO). The RMO is located within the Montmell Fault hanging wall (central part of the Montmell realm), whereas the GFRO is located in the western sector of the Vallès-Penedès Fault zone. In the RMO the host rocks are Lower Cretaceous marine limestones comprising 1–4 m thick beds, trending NE–SW and dipping 30° to the NW whereas in the GFRO the host rocks are Lower Cretaceous lacustrine limestones comprising 1–3 m thick vertical beds with roof brands and oxides at the strata top, giving a yellowish tinge to the rock (Fig. 4a, b). In both outcrops, the limestones contain metric-scale faults, micro-faults and tension veins filled with calcite cements and numerous stylolite surfaces. The macrostructural data were displayed on stereo-plots and have been grouped in different phases according to their relative chronology (Fig. 5).

- The first phase of deformation is represented by type 1 fractures. These fractures correspond to tension veins that form a complex network. They have been divided into type 1a fractures, which are sub-parallel to bedding, and type 1b fractures, which cut at 30° the type 1a fractures.
- The second phase of deformation has been divided into three sub-groups. In the RMO, fractures type 2a and 2b trend N60 and dip 60–80° to the NW and SE. The type 2b fractures are normal and reverse faults. The normal faults have a general orientation N60/80 NW with 80°W of slip and the reverse faults have a general orientation N70/75 SE with a 70°E of slip. These normal and reverse fault orientations were restored to their original geometry by rotating bedding to horizontal; the reverse faults restore as normal-sense faults, without evidence of reactivation (Wibberley *et al*. 2007). These normal faults have a high angle of dip because of their rotation in close proximity to the Montmell Fault. The last generation is type 2c fractures, trending N15 and dipping 60° to the east. In the GFRO only fracture type 2a is present, trending N150 and dipping 70° to the west.
- The third phase of deformation is characterized by type 3 fractures, which are present in both outcrops. They correspond to reverse faults trending N60 and dipping 70–85° to the SE and NW with 75–90° east and west slickenlines. In the GFRO, these faults are cut by another set of reverse faults trending N55 and dipping 25° to the NW with a slip of 54° to the east.
- The fourth deformation stage is characterized by the type 4 fractures, only present in the RMO. These fractures correspond to sub-vertical tension gashes trending N130 and sometimes displaying a sigmoid morphology consistent with a normal motion. They are recognized at meso- and micro-scale.
- The fifth deformation stage is characterized by the type 5 fractures, only present in the GFRO. They are normal faults trending N–S to NE–SW and dipping 60–70° to the SE and NW with a slip of 25° south for the N–S-trending faults and 70° west for the NE–SW trending faults. Other macro-fractures with the same trend and dip have been recognized; however, the slickenlines are absent.
- Finally the last deformation stage is characterized by the type 6 fractures. They are present in the GFRO and correspond to sub-vertical tension fractures trending NNW–SSE.

PETROLOGY AND GEOCHEMISTRY

The marine host-limestones correspond to wackestone, packstone and grainstone of miliolids, peloids, orbitolines, rudists and ostreids, whereas the lacustrine host-limestones correspond to a wackestone–packstone of charophyta, ostracoda and gasteropoda fragments. In both cases, the intragranular porosity is filled by microsparite cement (C0a) and the luminescence of the limestones is red to orange. Compositional data are summarized in Table 1 and isotopic data are cross-plotted in Figures 6 and 7.

The calcite cement C0a consists of anhedral crystals, 5–10 μm in size, red to orange luminescent. The elemental composition of this cement is similar to the host limestones (see Table 1).

The limestones are brecciated, probably during the initial fluid loss of the sediment, giving weak differences in luminescence and are affected by an incipient process of dolomitization. The dolomitization process is characterized by the presence of individualized rhombohedral crystals (CD1), 100–200 μm in size, non-luminescent, although locally the nucleus shows an orange dull luminescence. The dolomite crystals have been later calcitized (see Table 1).

A partial dissolution of the rock has created moldic and vug porosity. This porosity was partially filled by micrite and the remaining porosity was occluded by the calcite cement C0b showing geopetal disposition. The cement C0b corresponds to euhedric calcite crystals featuring blocky texture, 100–500 μm in size and showing a zoned red to orange luminescence.

Different generation of breccias, cements and sediment infillings have been recognized related to the fractures described in the structural section. These diagenetic products are described following the same chronological order of the different deformations stages.

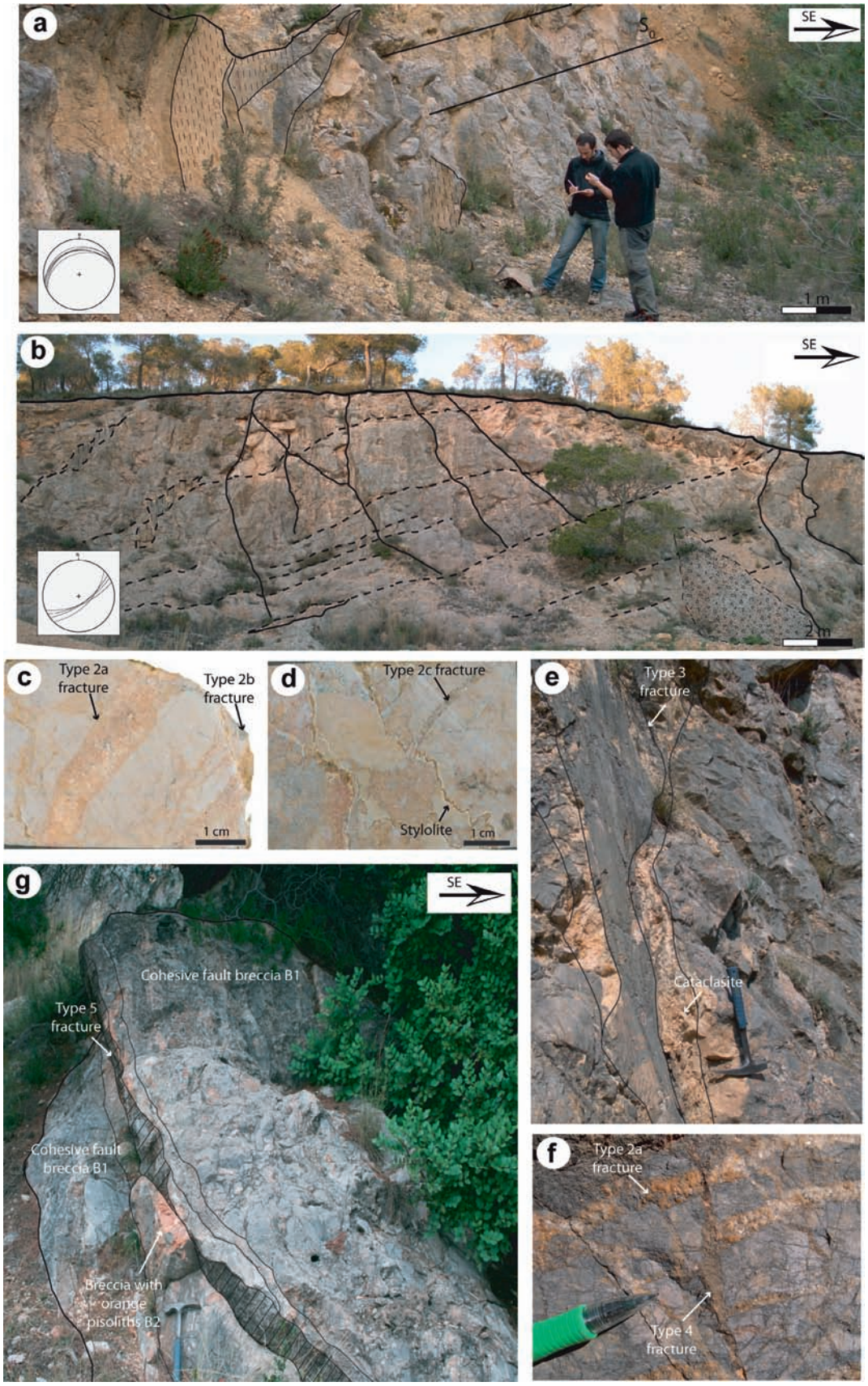

Fig. 4. (**a**) Riera de Marmellar outcrop showing the main normal faults (fractures type 2b) (dashed lines) and bedding planes (continuous lines); (**b**) Guardiola de Font-Rubí outcrop showing the main reverse faults (fractures type 3) (dashed lines) and main normal faults (fractures type 5) (continuous lines); (**c**) hand specimen showing type 2a and 2b fractures; (**d**) hand specimen showing type 2c fractures and random stylolites (stylobreccia); (**e**) slip surface of type 3 fractures and related yellow cataclasite; (**f**) outcrop photograph showing type 2c and type 4 fractures; (**g**) slip surface of type 5 fractures and related cohesive fault breccia B1 and breccia with orange pisoliths B2.

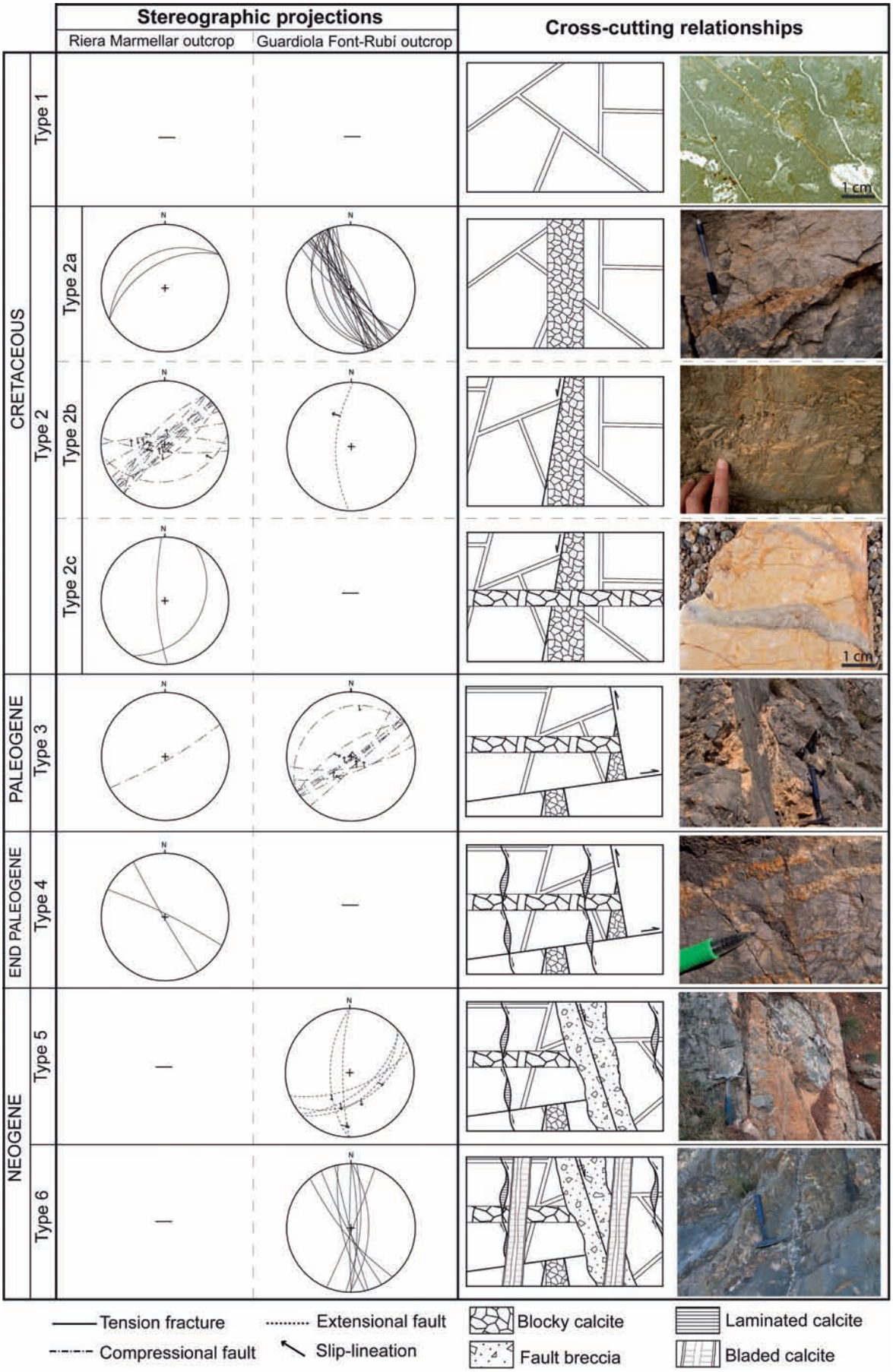

Fig. 5. Stereo-plots of structural and microstructural data from Riera de Marmellar and Guardiola de Font-Rubí outcrops.

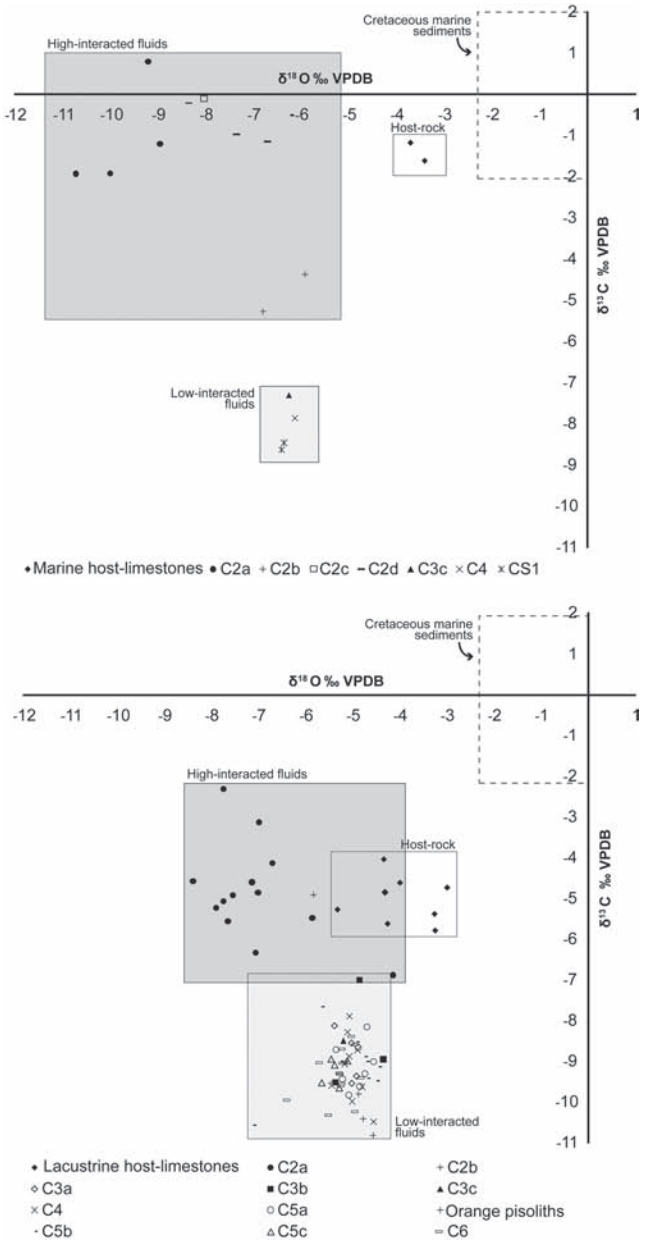

Fig. 6. $\delta^{18}O$ and $\delta^{13}C$ cross-plot of the host limestones and calcite cements and sediments. Range of values for Cretaceous marine sediments after Veizer & Hoefs (1976).

Type 1 fractures and calcite cement C1

Type 1a fractures are 25–50 μm in width and the walls are irregular and enlarged by dissolution. They are filled by two generations of calcite cement. The first generation (C1a) forms a rim, up to 10 μm thick, in one of the fracture walls. The crystals, 5–10 μm in size, are subhedral with c-axes orientated perpendicular to the fracture wall. They are zoned, from non-luminescent to orange bright luminescent. The second cement generation (C1b) is formed by dull-orange luminescent euhedral crystals, 10–15 μm in size, forming a mosaic fabric. Type 1b fractures are filled by the same type of calcite mosaic fabric with dull-orange luminescence (C1b) (Figs 8a, b). The elemental composition of these fillings is variable (see Table 1).

Type 2 fractures and calcite cement C2

Due to the similarities in the geochemistry and structural data, this group includes type 2a, 2b and 2c fractures, each with different types of fillings.

Type 2a fractures and calcite cement C2a and C2b. Type 2a fractures are 500 μm to 5 cm wide and have straight walls (Fig. 4c). They contain two generations of filling: the first corresponds to calcite cement C2a. This calcite has a milky aspect in hand sample and is constituted by subhedric crystals 300 μm to 1.5 mm in size, with a red dull luminescence featuring a drusy texture. The cloudy appearance of these crystals is due to abundant solid inclusions and mechanical twin planes (Figs 8c, d). Locally the crystals are elongated, growing with the c-axis perpendicular to the fracture walls, giving a bladed texture. The second generation of filling corresponds to calcite cement C2b. This calcite is translucent orange in hand sample. The crystals are euhedric, 100 μm to 1.5 mm in size, have a cloudy appearance due to abundant solid inclusions and mechanical twin planes, with a red dull luminescence and have a drusy texture.

Type 2b fractures and calcite cement C2c. The striated calcite cement present along the type 2b fault planes (calcite cement C2c) is constituted by subhedric to euhedric crystals, 100–500 μm in size, featuring a blocky texture. The crystals contain abundant mechanical twin planes and are red dull to red bright luminescent. Closer to the fault plane this calcite becomes a microsparite, 70–100 μm in size, corresponding to the cataclasis of the bigger calcite crystals (Fig. 8e).

Type 2c fractures and calcite cement C2d. Type 2c fractures are open, from 500 μm to 1 cm wide and have sub-angular walls enlarged by dissolution (Fig. 4d). They contain one generation of calcite cement C2d. This calcite has a white translucid aspect in hand sample and is composed of euhedric crystals, 75 μm to 1 mm in size, with a zoned black-orange bright-black luminescence, and a drusy texture (Figs 8a–e).

Type 3 fractures and calcite cement C3

Related to type 3 fractures is a fault zone over 0.5 m thick. The *core zone* is comprised of a yellow cataclasite (Fig. 4e), formed by fragments of the host limestones and earlier cements, 0.1–0.5 cm in size. The cataclasite has two generations of calcite cement: the first generation of cement (C3a) contains anhedric, non-luminescent, microsparite crystals, 4–10 μm in size, featuring blocky texture. The second generation of cement (C3b) surrounds sub-rounded fragments of the cataclasite, 0.1–2 cm in size. This cement consists of euhedric non-luminescent crystals, 10–100 μm in size, featuring blocky texture (Fig. 8f).

Later movements of the reverse faults generated the cataclasis of the earlier cataclasites and cements and a syn-kinematic striated calcite precipitated along the fault planes. This calcite cement (C3c) corresponds to non-luminescent, euhedric crystals, 200–500 μm in size, featuring blocky texture. The crystals are highly deformed and contain abundant mechanical twins planes (Fig. 7f).

Stylolites and breccias

The stylolite system is comprised of mostly open and randomly orientated stylolites (from sub-horizontal to sub-vertical), giving

Table 1. *Summary of oxygen, carbon and strontium isotopic compositions and the trace element composition of the host limestones, calcite sediments and calcite cements. Results of the elemental ratios calculated for fluids which precipitated calcite sediments and cements.*

Filling stage	Luminescence		$\delta^{13}C$ (‰ VPDB)	$\delta^{18}O$ (‰ VPDB)	$^{87}Sr/^{86}Sr$	Mg (%)	Ca (%)	Na (ppm)	Mn (ppm)	Fe (ppm)	Sr (ppm)	Molar ratio Mg/Ca fluid (a)	Molar ratio Mg/Ca fluid (b)	Molar ratio Sr/Ca fluid (c)	Molar ratio Sr/Ca fluid (d)	Molar ratio Ca/Fe fluid (e)
Lacustrine host-limestones (n = 13)	Red to orange	m	−6	−5.3	—	0.11	38.34	< d.l.	< d.l.	< d.l.	341	0.3744	0.0386	0.0151	0.0051	—
		M	−4.0	−3.0	—	0.43	40.25	264	176	3177	941	1.4812	0.1528	0.0396	0.0134	14046.1
		mv	−5.0	−4.0	0.70747	0.28	39.19	—	—	—	533	0.9677	0.0999	0.0230	0.0078	—
Marine host-limestone (n = 5)	Red to orange	m	−1.6	−3.7	—	0.23	38.82	< d.l.	< d.l.	168	403	0.7823	0.0807	0.0172	0.0058	151.8
		M	−1	−3.4	—	0.30	39.7	256	174	714	704	1.0448	0.1078	0.0302	0.0102	659.2
		mv	−1.4	−3.6	0.70728	0.26	39.36	—	—	395	557	0.8917	0.0920	0.0239	0.0081	375.2
Calcite cement C0a (GFRO) (n = 7)	Red to orange	m	—	—	—	0.25	38.89	< d.l.	< d.l.	301	231	0.8656	0.0893	0.0099	0.0034	59.3
		M	—	—	—	0.45	39.84	132	331	1852	605	1.5631	0.1613	0.0257	0.0087	365.1
		mv	—	—	—	0.34	39.35	—	—	1206	445	1.1866	0.1224	0.0191	0.0065	141.8
Calcite cement C0a (RMO) (n = 11)	Red to orange	m	—	—	—	0.10	39.10	< d.l.	< d.l.	< d.l.	200	0.3330	0.0344	0.0086	0.0029	—
		M	—	—	—	0.74	40.16	429	307	1726	1423	2.5972	0.2680	0.0617	0.0208	9096
		mv	—	—	—	0.31	39.54	—	—	—	607	1.0724	0.1107	0.0261	0.0088	—
Calcite cement CD1 (GFRO) (n = 10)	Non-luminescent (orange dull nucleus)	m	—	—	—	0.07	38.82	< d.l.	< d.l.	< d.l.	< d.l.	0.2409	0.0249	—	—	—
		M	—	—	—	0.64	40.06	285	411	2311	471	2.2266	0.2297	0.0199	0.0067	1336.7
		mv	—	—	—	0.26	39.55	—	—	—	—	0.9031	0.0932	—	—	—
Calcite cement C0b (GFRO) (n = 11)	Red to orange zonation	m	—	—	—	0.04	38.62	< d.l.	< d.l.	192	< d.l.	0.1238	0.0128	—	—	52.8
		M	—	—	—	0.42	40.18	217	360	2041	1291	1.4995	0.1547	0.0544	0.0184	584.2
		mv	—	—	—	0.28	39.25	—	—	—	—	0.9778	0.1009	—	—	157.2
Calcite cement C0b (RMO) (n = 13)	Red to orange zonation	m	—	—	—	0.02	39.76	< d.l.	< d.l.	< d.l.	438	0.0769	0.0079	0.0187	0.0063	—
		M	—	—	—	0.34	40.39	95	75	172	1056	1.1865	0.1224	0.0443	0.0150	2942
		mv	—	—	—	0.14	40.06	—	—	—	741	0.4761	0.0491	0.0313	0.0106	—
Calcite cement C1a (GFRO) (n = 12)	Non-luminescent to orange bright zonation	m	—	—	—	0.20	33.96	< d.l.	< d.l.	< d.l.	160	0.6675	0.0689	0.0070	0.0024	—
		M	—	—	—	0.49	40.36	317	524	2977	1031	1.7648	0.1821	0.0443	0.0150	5633.8
		mv	—	—	—	0.32	38.27	—	—	—	531	1.1403	0.1177	0.0233	0.0079	—
Calcite cement C1a (RMO) (n = 15)	Non-luminescent to orange bright zonation	m	—	—	—	0.07	38.99	< d.l.	< d.l.	< d.l.	294	0.2382	0.0246	0.0128	0.0043	—
		M	—	—	—	0.55	40.24	373	449	3118	755	1.9065	0.1967	0.0328	0.0111	1538
		mv	—	—	—	0.21	39.64	—	—	—	486	0.7390	0.0763	0.0208	0.0070	—
Calcite cement C2a (GFRO) (n = 15)	Red dull	m	−6.3	−8.4	—	0.03	38.74	< d.l.	< d.l.	187	< d.l.	0.1107	0.0114	—	—	55.4
		M	−2.3	−5.9	—	0.52	40.10	180	413	1960	2006	1.8267	0.1885	0.0848	0.0286	598.7
		mv	−4.6	−7.3	—	0.33	39.30	—	—	1336	—	1.1641	0.1201	—	—	150.0
Calcite cement C2a (RMO) (n = 3)	Red dull	m	−1.9	−10.7	—	0.09	38.78	< d.l.	< d.l.	473	593	0.2997	0.0309	0.0253	0.0085	34.5
		M	0.8	−9.0	—	0.15	39.7	151	741	3138	759	0.5154	0.0532	0.0332	0.0112	234.3
		mv	−0.9	−9.8	—	0.11	39.27	—	—	1931	672	0.4016	0.0414	0.0290	0.0098	116.6
Calcite cement C2b (GFRO) (n = 29)	Red dull	m	—	—	0.70754	< d.l.	38.79	< d.l.	< d.l.	< d.l.	< d.l.					
		M	—	—	0.70805	0.34	40.44	319	385	1877	1046	1.2063	0.1245	0.0439	0.0148	111002
		mv	−4.9	−5.8	0.70779	—	39.77	—	—	—	—	—	—	—	—	—
Calcite cement C2b (RMO) (n = 7)	Red dull	m	−5.3	−6.8	—	0.02	39.13	< d.l.	< d.l.	< d.l.	297	0.0597	0.0062	0.0125	0.0042	—
		M	−4.4	−5.9	—	0.12	40.46	136	197	3896	583	0.4151	0.0428	0.0244	0.0082	2963
		mv	−4.8	−6.4	—	0.08	39.98	—	—	—	437	0.2855	0.0295	0.0185	0.0062	—
Calcite cement C2c (RM) (n = 2)	Red dull to red bright	m	—	—	0.70752	—	—	—	—	—	—	—	—	—	—	—
		M	—	—	0.70757	—	—	—	—	—	—	—	—	—	—	—
		mv	—	—	0.70755	—	—	—	—	—	—	—	—	—	—	—
Calcite cement C2d (RM) (n = 1)	Black-orange bright-black zonation	m	−1.1	−8.4	—	—	—	—	—	—	—	—	—	—	—	—
		M	−0.2	−6.7	—	—	—	—	—	—	—	—	—	—	—	—
		mv	−0.7	−7.5	0.70757	—	—	—	—	—	—	—	—	—	—	—

Table 1. *(Continued)*

Filling stage	Luminescence		$\delta^{13}C$ (‰ VPDB)	$\delta^{18}O$ (‰ VPDB)	$^{87}Sr/^{86}Sr$	Mg (%)	Ca (%)	Na (ppm)	Mn (ppm)	Fe (ppm)	Sr (ppm)	Molar ratio Mg/Ca fluid (a)	Molar ratio Mg/Ca fluid (b)	Molar ratio Sr/Ca fluid (c)	Molar ratio Sr/Ca fluid (d)	Molar ratio Ca/Fe fluid (e)
Calcite cement C3a (GFRO) (n = 16)	Non-luminescent	m	−9.4	−5.4	—	< d.l.	39.25	< d.l.	< d.l.	< d.l.	< d.l.	—	—	—	—	—
		M	−8.1	−4.9	—	0.18	40.15	447	59	811	375	0.6376	0.0658	0.0160	0.0054	4804.6
		mv	−8.9	−5.1	—	—	39.70	—	—	—	—	—	—	—	—	—
Calcite cement C3b (GFRO) (n = 12)	Non-luminescent	m	−9.5	−5.4	—	< d.l.	39.46	< d.l.	< d.l.	< d.l.	< d.l.	—	—	—	—	—
		M	−7.0	−4.4	—	0.26	40.564	228	312	247	535	0.8995	0.0928	0.0227	0.0077	942
		mv	−8.4	−4.9	—	—	40.00	—	—	—	—	—	—	—	—	—
Calcite cement C3c (GFRO) (n = 5)	Non-luminescent	m	—	—	—	0.09	39.15	< d.l.	< d.l.	< d.l.	< d.l.	0.3049	0.0315	—	—	—
		M	—	—	—	0.20	40.85	128	79	105	293	0.6998	0.0722	0.0125	0.0042	3903.1
		mv	−8.5	−5.2	0.70791	0.15	40.01	—	—	—	—	0.5078	0.0524	—	—	—
Calcite cement C3c (RMO) (n = 1)	Non-luminescent	m	—	—	—	—	—	—	—	—	—	—	—	—	—	—
		M	—	—	—	—	—	—	—	—	—	—	—	—	—	—
		mv	−7.3	−6.3	—	—	—	—	—	—	—	—	—	—	—	—
Calcite cement C4 (GFRO) (n = 13)	Non-luminescent	m	−10.5	−5.5	—	0.11	39.28	< d.l.	< d.l.	< d.l.	< d.l.	0.3734	0.0385	—	—	—
		M	−7.9	−4.6	—	0.41	40.55	108	94	1351	617	1.4234	0.1469	0.0266	0.0090	14034
		mv	−9.2	−5.0	—	0.23	39.92	—	—	—	—	0.7788	0.0804	—	—	—
Calcite cement C4 (RMO) (n = 9)	Non-luminescent	m	—	—	—	0.01	40.14	< d.l.	< d.l.	< d.l.	154	0.0327	0.0034	0.0065	0.0022	—
		M	—	—	—	0.16	40.68	161	141	112	651	0.5391	0.0556	0.0274	0.0092	3903
		mv	−7.9	−6.1	—	0.08	40.35	—	—	—	—	0.2612	0.0270	0.0138	0.0046	—
Calcite sediment CS1 (RMO) (n = 3)	Non-luminescent	m	−8.6	−6.4	—	0.10	39.40	< d.l.	< d.l.	1289	246	0.3557	0.0367	0.0104	0.0035	54.8
		M	−8.5	−6.4	—	0.18	40.24	110	23	2009	382	0.6332	0.0653	0.0162	0.0055	86.5
		mv	−8.5	−6.4	0.70809	0.14	39.84	—	—	1663	308	0.4673	0.0482	0.0131	0.0044	69.6
Calcite cement C5a (GFRO) (n = 25)	Non-luminescent	m	−9.8	−5.4	—	< d.l.	39.13	< d.l.	< d.l.	< d.l.	< d.l.	—	—	—	—	—
		M	−6.9	−4.1	—	0.53	40.499	220	103	1748	578	1.8535	0.1912	0.0245	0.0083	1311
		mv	−8.8	−4.8	—	—	39.63	—	—	—	—	—	—	—	—	—
Orange pisoliths (GFRO) (n = 4)	Non-luminescent	m	−10.8	−4.9	—	0.05	38.96	< d.l.	< d.l.	462	< d.l.	0.1768	0.0182	—	—	52.9
		M	−9.8	−4.6	—	0.16	40.56	150	51	2056	255	0.5649	0.0583	0.0109	0.0037	239.4
		mv	−10.3	−4.7	—	0.11	39.69	—	—	1095	—	0.3952	0.0408	—	—	154.3
Calcite cement C5b (GFR0) (n = 5)	Non-luminescent	m	−10.3	−7.1	—	0.13	40.08	< d.l.	< d.l.	< d.l.	< d.l.	0.4537	0.0468	—	—	—
		M	−8.5	−4.4	—	0.19	40.497	215	175	210	333	0.6677	0.0689	0.0140	0.0047	1561
		mv	−9.2	−5.2		0.17	40.28	—	—	—	—	0.5681	0.0586	—	—	—
Calcite cement C5c (GFRO) (n = 13)	Non-luminescent	m	−9.7	−5.7	—	< d.l.	39.42	< d.l.	< d.l.	< d.l.	< d.l.	—	—	—	—	—
		M	−9.0	−5.1	—	0.25	40.58	160	92	125	332	0.8747	0.0903	0.0139	0.0047	4128
		mv	−9.3	−5.4	0.70825	—	40.13	—	—	—	—	—	—	—	—	
Calcite sediment CS2 (GFRO) (n = 8)	Non-luminescent	m	—	—	—	< d.l.	39.16	< d.l.	< d.l.	124	< d.l.	—	—	—	—	67.5
		M	—	—	—	0.18	39.94	373	77	1643	361	0.6261	0.0646	0.0153	0.0052	898.6
		mv	—	—	—	—	39.60	—	—	677	—	—	—	—	—	383.7
Calcite cement C6 (GFRO) (n = 28)	Non-luminescent	m	−10.2	−6.3	—	0.07	39.50	< d.l.	< d.l.	< d.l.	< d.l.	0.2446	0.0252	—	—	—
		M	−8.4	−4.9	—	0.69	40.577	4246	809	353	500	2.3708	0.2446	0.0213	0.0072	15898
		mv	−9.3	−5.4	—	0.25	40.01	—	—	—	—	0.8673	0.0895	—	—	—

m, minimum value; M, maximum value; mv, mean value; n, number of elemental analysis spots in the same sample; < d.l., below detection limit

[a]KMg = 0.012 at 25°C (Mucci 1987)

[b]KMg = 0.1163 at 90°C (Katz 1973)

[c]KSr = 0.027 at 25°C (Lorens 1981)

[d]KSr = 0.08 at 100–150°C (Kinsman 1969)

[e]KFe = 5 at 25°C (Tucker & Wright 1990)

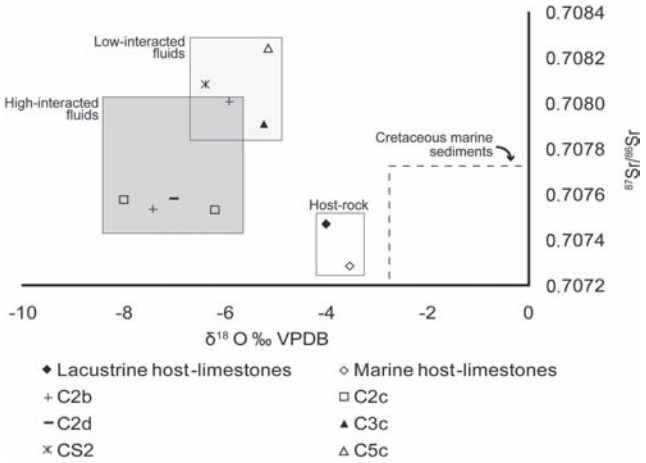

Fig. 7. Cross-plot of strontium ratio versus oxygen isotopic compositions of the host limestones and calcite sediments and cements.

the rock a pseudo-nodular texture, described as stylobreccia (Figs 4d, 8g) (*sensu* Stewart & Hancock 1990).

Type 4 fractures, calcite cement C4 and calcite sediment CS1

Type 4 fractures are 300 μm to 5 cm wide and have sub-angular walls, enlarged by dissolution (Fig. 4f). They contain two generations of calcite fillings. The first generation corresponds to the calcite cement C4 formed by white translucid calcite in hand specimen, comprised of euhedric non-luminescent crystals, 100–200 μm in size, featuring blocky texture. The second generation of filling corresponds to the orange- to pink-laminated calcite sediment CS1. This sediment is comprised of non-luminescent euhedric crystals, 10–50 μm in size, featuring blocky texture. The sediment contains reworked fragments of the host limestone and earlier cements, 0.1–3 cm in size.

Type 5 fractures and calcite cement C5

A different generation of fault breccias were developed in association with type 5 fractures (Fig. 4g). Cohesive fault breccia B1 is formed by angular fragments, between 0.1 cm and 3 cm in size, of host limestone and earlier calcite cements. This breccia is cemented by calcite cement C5a, comprised of non-luminescent anhedral calcite crystals, 10–20 μm in size, featuring blocky texture (Fig. 8h). In the central part of the core zone, there is a breccia with orange pisoliths B2 (Fig. 8i). This breccia is formed from sub-rounded fragments, 1–5 cm in size, of the host rock, calcite cements and cohesive fault breccia B1. Some of the fragments are coated by an orange micrite and between the fragments orange pisoliths are present. These pisoliths are 10–50 μm in size and their nucleus have been totally micritized. The breccia B2 is cemented by the calcite cement C5b. This cement is formed from non-luminescent euhedric crystals, 50–200 μm in size, featuring blocky texture (Fig. 8i).

Later movements of the normal faults caused the cataclasis of breccia B2. Synchronous with the movement of the normal faults, calcite cement C5c was precipitated (Fig. 8j). This cement shows crack-seal structures with inclusion bands of orange pisoliths and locally sigmoidal morphology. C5c is formed from non-luminescent subhedral to euhedral crystals, 250–500 μm in size, featuring blocky texture. The crystals contain abundant mechanical twin planes.

Type 6 fractures, calcite sediment CS2 and calcite cement C6

Type 6 fractures are 5–10 cm in width, with sharp and undulated walls and are partially filled by two generations of calcite sediment and cement. The first generation corresponds to pink-laminated calcite sediment CS2. The sediment is comprised of non-luminescent, subhedral crystals, 10–30 μm in size, featuring blocky texture (Fig. 8k). The second generation of filling is the calcite cement C6. This cement is comprised of non-luminescent bladed crystals, 500 μm to 2 cm in size, with the c-axis perpendicular to the fracture wall (Fig. 8k).

DISCUSSION

Diagenesis of host limestones

If it is assumed that the precipitation of the calcite cement occurred in equilibrium, the chemical composition of the fluid responsible for the calcite precipitation can be determined using the distribution coefficient equation of McIntire (1963). The molar ratios Ca/Fe, Mn/Ca and Sr/Ca of the host marine limestone and the intraparticular cement C0a are consistent with re-equilibration and precipitation from formation waters, whereas the molar ratios of Mg/Ca are consistent with re-equilibration and precipitation from either meteoric or formation waters. The $\delta^{18}O$ values of the host marine limestone are slightly lower than the expected values for limestones precipitated from the Cretaceous seawater (from –2.5 to +1‰ VPDB), whereas the $\delta^{13}C$ and the strontium ratios are in good agreement with those of limestones precipitated from Cretaceous seawater, ranging from –2 to +3‰ VPDB and from 0.7068 to 0.7074, respectively (Veizer & Hoefs 1976; Veizer *et al*. 1997, 1999). These data show that the original marine signal is still recognized for $\delta^{13}C$ and the strontium ratio but it has been moderately overprinted during diagenesis, modifying the $\delta^{18}O$ values. On the other hand, the molar ratios Sr/Ca, Ca/Fe and Mg/Ca and the $\delta^{18}O$ and $\delta^{13}C$ values of the lacustrine host limestone and calcite cement C0a clearly show a meteoric origin for the fluid (from –8 to –2‰ $\delta^{18}O$ VPDB and from –12 to 0‰ $\delta^{13}C$; Veizer & Hoefs 1976). The geochemistry of the intraparticular cement C0a indicates, in both cases, precipitation during the very early stages of diagenesis.

The molar ratios Mg/Ca and Sr/Ca of CD1 and C0b in the marine limestones clearly indicate precipitation from formation waters, whereas in the lacustrine limestones they are consistent with meteoric waters. These values indicate that dissolution, brecciation, incipient dolomitization and subsequent calcitization of the dolomite crystals, as well as precipitation of cement in the vug and moldic porosity, occurred during initial burial of the rock and, therefore, the initial stages of mesogenesis.

Relationships between fracturing events and palaeofluids

Knowing the regional setting of the study area it is possible to correlate the different fracturing stages to the main tectonic events (Knipe & McCaig 1994). The different fractures, breccias

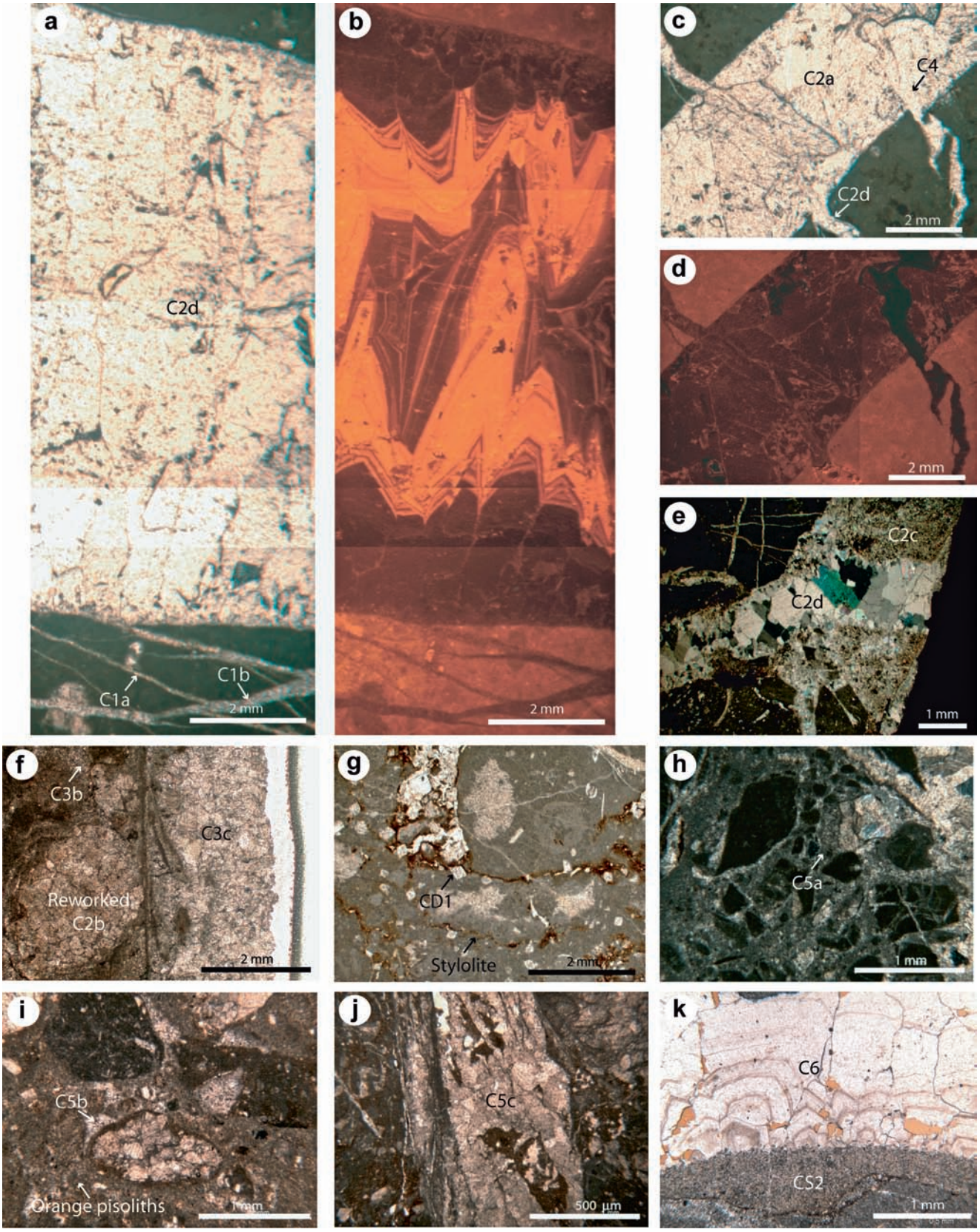

Fig. 8. (**a**), (**b**) Type 1a, 1b and 2c fractures with C1a, C1b and C2d calcite cements under (a) optical and (b) cathodoluminescence microscope; (**c**), (**d**) type 2a, 2c and 4 fractures with C2a, C2d and C4 calcite cements under (**c**) optical and (**d**) cathodoluminescence microscope; (**e**) type 2b and 2c fractures with C2c and C2d calcite cements under optical microscope; (**f**) type 3 fractures with related cataclasite and C3b calcite cement under optical microscope; (**g**) stylobreccia related to type 3 fractures under optical microscope. Detail of the dolomite crystals (CD1); (**h**) cohesive fault breccia B1 related to type 5 fractures with the calcite C5a under optical microscope; (**i**) breccia with orange pisoliths B2 cemented by C5b under optical microscope; (**j**) cataclasite of breccia B2 with the calcite cement C5c under optical microscope; (**k**) type 6 fractures with the calcite sediment CS2 and calcite cement C6 under optical microscope.

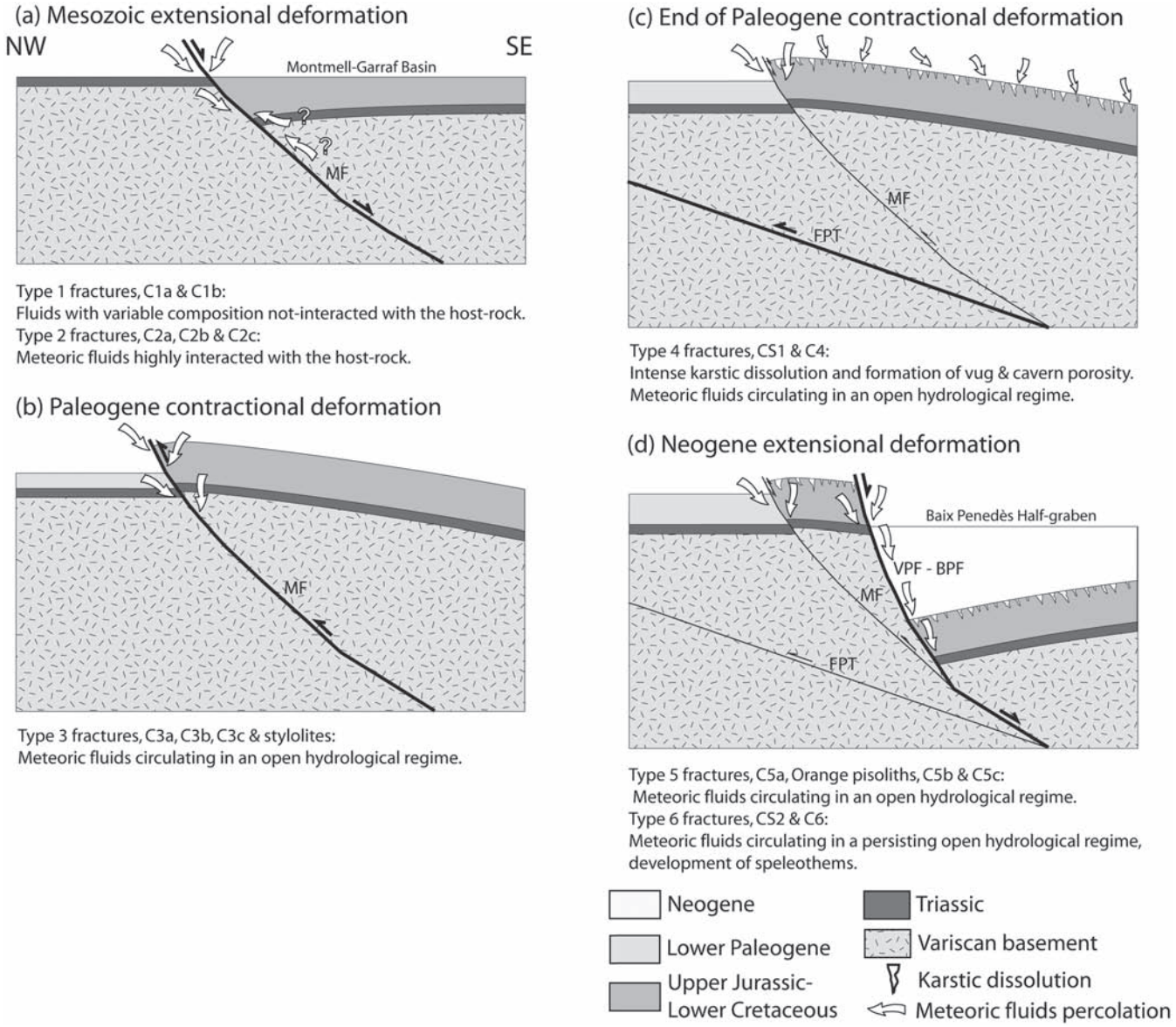

Fig. 9. Evolution of meteoric fluids from Mesozoic to recent within the Vallès-Penedès–Montmell Alpine fault system. MF, Montmell Fault; FPT, Frontal Paleogene Thrust; VPF–BPF, Vallès-Penedès Fault and Baix Penedès Fault.

and cementation processes observed along the NW border of the Penedès Basin attest to different fluids circulating during basin development.

Mesozoic extensional deformation. The complex network of type 1 fractures formed during the initial stage of Mesozoic extension. They represent the process zone formed around the fault tip during its development (Stewart & Hancock 1990). The large elemental composition range of calcite cements C1a and C1b suggests the infiltration of fluids of different compositions and origins, not interacted with the host limestone, during this multistage of fracturing (Fig. 9a).

During the Mesozoic extensional syn-rift stage, the NNW–SSE tension fractures (type 2a) and the NE–SW normal faults (type 2b) were formed. Petrological and geochemical similarities between calcites C2a, C2b and C2c related to type 2a and 2b fractures indicate that they precipitated from a fluid with the same origin. The molar ratios Mg/Ca, Sr/Ca and Ca/Fe of these cements, both in marine and lacustrine limestones, are consistent with precipitation from formation waters. Because fractures in the RMO are from the hanging wall and those of the GFRO are from the footwall of the Montmell Fault, the more negative $\delta^{18}O$ values in the RMO are interpreted as having been precipitated at deeper burial depth. The similarity between the $\delta^{13}C$ values of C2a, C2b, C2c and the host rock is probably due to the buffering of pore-water carbon isotopic composition by extensive dissolution of the host limestones (Marshall 1992). The $^{87}Sr/^{86}Sr$ ratios, together with the $\delta^{13}C$ values, indicate high fluid–rock interaction in a closed palaeohydrological system. On the other hand, type 2c fractures can be related to the post-rift stage. The variations in luminescence of calcite cement C2d attest to a variability of fluid composition during its precipitation. The $\delta^{18}O$ values are consistent either with meteoric or formation waters, whereas the $^{87}Sr/^{86}Sr$ ratio and $\delta^{13}C$ values indicate high fluid–rock interaction in a closed palaeohydrological system.

In summary, cement C2 in type 2 fractures, related to the Mesozoic extensional phase, precipitated from a fluid that strongly interacted with the rock, approaching a closed system.

Paleogene contractional deformation. The reverse faults (type 3) and stylolites formed during the Paleocene to middle Oligocene contractional phase that generated the Catalan Intraplate Belt (Guimerà 2004). The Mg/Ca and Ca/Fe molar ratios, as well as the $\delta^{18}O$ and $\delta^{13}C$ of cements C3a, C3b and C3c in type 3 fractures and related cataclasite, are consistent with precipitation from meteoric water (Fig. 9b).

End of Paleogene contractional deformation. The vertical fractures (type 4) and their later enlargement by dissolution can be related to the subaerial exposure of the Mesozoic horsts and development of a karstic system during the transitional phase between Paleogene compression and Neogene extension (Fig. 9c). The elemental geochemistry and the more radiogenic isotopes of the calcite sediment CS1 indicate low interaction with the host limestone and the opening of the system to meteoric water. The Mg/Ca, Sr/Ca and Ca/Fe ratios, as well as the $\delta^{18}O$ and $\delta^{13}C$ values of the calcite cement C4, indicate precipitation from meteoric waters in an open hydrological system. Similar fractures, sediments and cements related to karstic processes have been described during this transitional phase within the Penedès Basin (Travé *et al*. 1998) and in the neighbouring Amposta offshore oil reservoir (Playà *et al*. 2010).

*Neogene extensional deformation from late Oligocene (?) to late Neogene.*The type 5 fractures corresponding to NE–SW normal faults are attributed to the syn-rift stage of the late Oligocene?–Neogene extensional phase (Roca & Guimerà 1992). The fillings of type 5 fractures are a mixture of tectonic and karstic processes and resulted from multistage movement of the normal faults. The location of frictional processes generated the cohesive fault breccia B1 and the cataclasite during progressive opening of the hydrological system. When the fault reached the surface, karstic features from the vadose and phreatic meteoric environment led to the formation of the red breccias B2, the karstic pisolithic layer and the breccias with pisoliths. Later movements of the normal faults generated the cataclasis of karstic deposits. The $\delta^{18}O$ values of calcite cements C5a, C5b and C5c, varying from –7 to –4.4‰ VPDB, together with the Mg/Ca and Sr/Ca molar ratios and the high radiogenic values of C5c, indicate that meteoric waters, not interacted with the host limestone, were responsible for precipitation of these cements (Fig. 9d).

Finally, the type 6 fractures are attributed to the late post-rift stage of the Neogene extension as a result of generalized tensile deformation of the whole area during the final stages of basin development. The $\delta^{18}O$ values of CS2 and C6 filling type 6 fractures, varying from –6.3 to –4.9‰ VPDB, together with the calculated Mg/Ca and Sr/Ca molar ratios of the fluid, indicate precipitation from meteoric waters. The laminated calcite sediment CS2, together with the palisade texture of the calcite cement C6, are interpreted as speleothems covering the fractures walls, in the vadose meteoric environment, similar to those described in Miocene materials (Travé & Calvet 2001). The low $\delta^{13}C$ of the calcite cement C6 indicates a higher involvement of soil-derived CO_2 (Travé *et al*. 1998; Breesch *et al*. 2009).

This reconstruction of the relationship between fractures and migration of fluids within the Vallès–Penedès extensional basin development has an economic interest because this basin can be used as an analogue for the reservoirs placed offshore of the Valencia Trough (Esteban 1991; Playà *et al*. 2010). These reservoirs correspond to a paleokarst developed over the Mesozoic carbonates during the Paleogene to Neogene transition stage (Vera *et al*. 1988; Esteban 1991). In the Montmell realm, this karstic dissolution and infilling is related to the formation of type 4 fractures which are filled by the carbonate sediments CS1. Knowing in detail the fracturing and diagenesis that occurred in these rocks will help unravel the evolution and migration of the oil during the development of the basin.

CONCLUSIONS

Structural analyses indicate that Mesozoic normal faults were reactivated during the Paleogene as reverse faults. During the Neogene, different normal faults generated the actual disposition of the Catalan Coastal Ranges.

Based on petrological and geochemical analyses of the different generations of calcite cements associated with the different generations of fractures, different types of fluids have been identified: (1) related to the earlier stage of Mesozoic extension, type 1 fractures include a complex network of microscopic fractures filled by calcite cements that precipitated from fluids with variable composition uninteracted with the host rock. (2) During the syn-rift stage of Mesozoic extension, NE–SW- to ENE–WSW-trending normal faults (type 2 fractures) were filled by three generations of calcite cement that precipitated at different burial depths from fluids resulted either from a mixing of trapped Upper Jurassic–Lower Cretaceous seawater and meteoric water, or from buffered meteoric waters highly interacted with the host rock. (3) During the Paleogene contractional deformation, NE–SW reverse faults (type 3 fractures) with a fault gouge cemented by several generations of non-luminescent calcite cements precipitated from meteoric fluids in an open hydrological system. (4) The end of the Paleogene contractional deformation is represented by vertical fractures (type 4 fractures) that favoured dissolution and created vug and cavern porosity. These cavities are filled by calcite cement and sediment precipitated from meteoric fluids related to the subaerial exposure of the basement carbonate rocks during the transitional stage. (5) During the Neogene syn-rift stage, NNW–SSE- and NE–SW-trending normal faults (type 5 fractures) filled by non-luminescent cements precipitated from meteoric fluids. (6) During the late post-rift stage, NNW–SSE open fractures (type 6 fractures) with the walls covered by speleothems indicate a persistent hydrological regime to meteoric open fluids.

We have recognized, in the studied outcrops, a complex fluid history during the two extensional phases, different in the Mesozoic extension than in the Neogene extension. In contrast, the Paleogene compression is characterized by a very simple fluid history characterized by meteoric fluids in small reverse faults.

Finally, two different episodes of karst development have been identified; an early one developed previous to the Neogene extension, which is used by the Neogene faults to develop, and a late one, developed after the Neogene extension, that originated at the expense of the Neogene normal faults.

The isotopic and electron microprobe analyses were carried out at 'Centres Científics i Tecnològics' of the University of Barcelona and the strontium analyses at SGIker Geochronology Department of the Faculty of Science and Technology, University of País Vasco/EHU. We also thank Andrea Billi and the anonymous reviewer of *Petroleum Geoscience* for their accurate and constructive reviews of this paper.

This research was performed within the framework of I+D+I research projects CGL2010-18260 of the Grup Consolidat de Recerca 'Geologia Sedimentària' (2009 SGR-1458), the BES-2007-14935 grant and the CGL2007-66431-C02/BTE of the 'Grup de Recerca de Geodinàmica i Anàlisi de Conques' (2001 SGR-000074).

REFERENCES

Agosta, F., Prasad, M. & Aydin, A. 2007. Physical properties of carbonate fault rocks. Fucino basin, central Italy: implications for fault seal in platform carbonates. *Geofluids*, **7**, 19–32.

Amigó, J. 1986. *Estructura del massís del Gaià. Relacions estructurals amb les fosses del Penedès i del Camp de Tarragona*. PhD Thesis, University of Barcelona, Barcelona, Spain.

Anadón, P., Colombo, F., Esteban, M., Marzo, M., Robles, S., Santanach, P. & Solé Sugrañes, L. 1979. *Evolución tectonoestratigráfica de los Catalánides*. Acta Geológica Hispánica, 14, 242–270.

Anadón, P., Cabrera, L., Guimerà, J. & Santanach, P. 1985. Paleogene strike-slip deformation and sedimentation along the southeastern margin of the Ebro Basin. *In*: Biddle, K.T. & Christie-Blick, N. (eds) *Strike-Slip Deformation, Basin Formation Sedimentation*. Special Publication of the Society of Economic Paleontologists and Mineralogists, 37, 303–318.

André, G., Hibsch, C., Fourcade, S., Cathelineau, M. & Buschaert, S. 2010. Chronology of fracture sealing under a meteoric fluid enviorment: Microtectonic and isotopic evidence of major Cainozoic events in the eastern Paris Basin (France). *Tectonophysics*, **490**, 214–228.

Ashauer, H. & Teichmüller, R. 1935. *Die variszische und alpidische Gebirgsboldung Kataloniens*. Abhandlungen Gesellschaft Wissenschaften Göttingen, Math Phys. Kl, 3F, 16.

Bartrina, M.T., Cabrera, L., Jurado, M.J., Guimerà, J. & Roca, E. 1992. *Evolution of the central Catalan margin of the Valencia trough (western Mediterranean). Tectonophysics*, **203**, 219–247.

Benedicto, A., Plagnes, V., Vergély, P., Flotté, N. & Schultz, R.A. 2008. Fault and fluid interaction in a rifted margin: integrated study of calcite-sealed fault-related structures (southern Corinth margin). *In*: Wibberley, C.A.J., Kurtz, W., Imber, J., Holdsworth, R.E. & Collettini, C. (eds) *The Internal Structure of Fault Zones: Implications for Mechanical and Fluid-flow Properties*. Geological Society, London, Special Publications, 299, 1–19.

Bitzer, K., Carmona, J.M., Calvet, F. & Travé, A. 1997. Modelling paleohydrological and thermal evolution of distensive basins: application to the Barcelona half-graben (offshore, NE Spain). *In*: Hendry, J., Carey, P., Parnell, J., Ruffell, A. & Worden, R. (eds) *Geofluids'97 Extended Abstracts*. Belfast, Northern Ireland, 352–355.

Breesch, L., Swennen, R. & Vincent, B. 2009. Fluid flow reconstruction in hanging and footwall carbonates: Compartmentalization by Cenozoic reverse faulting in the Northern Oman Mountains (UAE). *Marine and Petroleum Geology*, **26**, 113–128.

Bussolotto, M., Benedicto, A., Invernizzi, C., Micarelli, L., Plagnes, V. & Deiana, G. 2007. Deformation features within an active normal fault zone in carbonate rocks: The Gubbio fault (Central Apennines, Italy). *Journal of Structural Geology*, **29**, 2010–2037.

Claypool, G.E., Holser, W.T., Kaplan, I.R., Sakai, H. & Zak, I. 1980. The age curves of sulphur and oxygen isotopes in marine sulphate and their interpretation. *Chemical Geology* (Isotope geoscience section), 28, 199–260.

Cooper, M.A., Williams, G.D. & De Granciansky, P.C. *et al.* 1989. Inversion tectonics – a discussion. *In*: Cooper, M.A. & Williams, G.D. (eds). *Inversion Tectonics*. Geological Society, London, Special Publications, 44, 335–347.

Craig, H. & Gordon, I. 1965. Deuterium and oxygen-18 variations in the ocean and marine atmosphere. *In*: Tongiorgi, E. (eds) *Stable Isotopes in Oceanographic Studies and Paleotemeratures*. Consiglio Nazionale delle Richerche, Laboratorio di Geologia Nucleare, Pisa, Italy, 9–130.

Dañobeitia, J.J., Arguedas, M., Gallart, F., Banda, E. & Makris, J. 1992. Deep crustal configuration of the Valencia trough and its Iberian and Balearic borders from extensive refraction and wide-angle reflection profiling. *Tectonophysics*, **203**, 37–55.

De Brit, T.J. 1989. Timing structural events and basement emplacement using extension veins and cements in the Carboniferous of North Central Ireland. *Irish Journal of Earth Science*, **10**, 13–31.

Dickson, J.A.D. 1966. Carbonate identification and genesis as revealed by staining. *Journal of Sedimentary Petrology*, **36**, 491–505.

Esteban, M. 1991. Paleokarst: practical applications. *In:* Wright, V.P., Esteban, M. & Smart, P.L. (eds) *Palaeokarsts and Palaeokarstic Reservoirs*, **152**, 89–119.

Fontboté, J.M. 1954. *Las relaciones tectonicas de la depresion del Vallès-Penedes con la cordillera prelitoral y con la depresión del Ebro*. Tomo Homenaje a Prof. E. Hernandez-Pacheco. Revista de la Sociedad Espanola de Historia Natural, Madrid, 281–310.

Gaspar-Escribano, J., García-Castellanos, D., Roca, E. & Cloetingh, S. 2004. Cenozoic vertical motions of the Catalan Coastal Ranges (NE Spain): The role of tectonics, isostasy, and surface transport. *Tectonics*, 23, DOI: 10.1029/2003TC001511.

Géraud, Y., Diraison, M. & Orellana, N. 2006. Fault zone geometry of a mature active normal fault: A potential high permeability channel (Pirgaky fault, Corinth rift, Greece). *Tectonophysics*, **426**, 61–76.

Gillcrist, R., Coward, M. & Mugnier, J.L. 1987. Structural inversion examples from the Alpine foreland and French Alps. *Geodinamica Acta*, **1**, 5–34.

Guimerà, J. 1988. *Estudi estrucutal de l'enllaç entre la Serralada Ibèrica i la Serralada Costera Catalana*. PhD thesis, University of Barcelona, Barcelona, Spain.

Guimerà, J. 2004. La Cadena Costera Catalana. *In*: Vera, J.A. (eds) *Geologia de España*. SGE-IGME, Madrid, 603–605.

Katz, A. 1973. The interaction of magnesium with calcite during crystal growth at 25-90ºC and one atmosphere. *Geochimica et Cosmochimica Acta*, **37**, 1563–1568.

Kinsman, D.J.J. 1969. Interpretation of Sr^{2+} concentrations in carbonate minerals and rocks. *Journal of Sedimentary Petrology*, **39**, 486–508.

Knipe, R.J. & McCaig, A.M. 1994. Microstructural and microchemical consequences of fluid flow in deforming rock. *In:* Parnell, J (eds) *Geofluids: Origin, Migration and Evolution of Fluids in Sedimentary Basins*. Geological Society, London, Special Publications, **78**, 99–111.

Labaume, P., Carrio-Schaffhauser, E., Gamond, J.F. & Renard, F. 2004. Deformation mechanisms and fluid-driven mass transfers in the recent fault zones of the Corinth rift (Greece).*Comptes Rendus Géoscience*, **336**, 375–383.

Llopis-Lladó, N. 1947. *Contribución al conocimiento de la morfoestructura de los Catalánides*. Inst. 'Lucas Madalla', C.S.I.C., Barcelona.

Lorens, R.B. 1981. Sr, Cd, Mn and Co distribution coefficients in calcite as a function of calcite precipitation rate. *Geochimica et Cosmochimica Acta*, **45**, 553–561.

Marín, M.A., Roca, E., Rosell, O., Marcuello, A. & Cabrera, L. 2008. La Falla del Montmell: un ejemplo del control ejercido por las fallas extensivas mesozoicas en la arquitectura cenozoica de las Cadenas Costaneras Catalanas. *Geotemas*, **10**, 461–464.

Marshall, J.D. 1992. Climatic and oceanographic isotopic signals from the carbonate rock record and their preservation. *Geological Magazine*, **129**, 143–160.

McIntire, W.L. 1963. Trace element partition coefficients – a review of theory and applications to geology. *Geochimica et Cosmochimica Acta*, **27**, 1209–1264.

Micarelli, L., Benedicto, A., Invernizzi, C., Saint-Bezar, B., Michelot, J.L. & Vergely, P. 2005. Influence of P/T conditions on the style of normal fault initiation and growth in limestones from SE-Basin, France. *Journal of Structural Geology*, **27**, 1577–1598.

Micarelli, L., Moretti, I., Jaubert, M. & Moulouel, H. 2006. Fracture analysis in the south-western Corinth rift (Greece) and implications on fault hydraulic behaviour. *Tectonophysics*, **426**, 31–59.

Mucci, A. 1987. Influence of temperature on composition of magnesian calcite overgrowths precipitated from seawater. *Geochimica et Cosmochimica Acta*, **5**, 1977–1984.

Muchez, Ph., Slobondik, M., Viaene, W.A. & Keppens, E. 1995. Geochemical constraints on the origin and migration of palaeofluids at the northern margin of the Variscan foreland, southern Belgium. *Sedimentary Geology*, **96**, 191–200.

Pili, E., Poitrasson, F. & Gratier, J.P. 2002. Carbon-oxygen isotope and trace element constraints on how fluids percolate faulted limestones form San Andreas Fault system: partitioning of fluid sources and pathways. *Chemical Geology*, **190**, 231–250.

Pin, C. & Bassin, C. 1992. Evaluation of a strontium-specific extraction chromatographic method for isotopic analysis in geological materials. *Analytica Chimica Acta*, **269**, 249–255.

Playà, E., Travé, A., Caja, M.A., Salas, R. & Martín-Martín, J.D. 2010. Diagenesis of the Amposta offshore oil reservoir (Amposta Marino CS well, Lower Cretaceous, Valencia Trough, Spain). *Geofluids*, **10**, 314–333.

Roca, E. 1996. La evolución geodinámica de la Cuenca Catalano-Balear y áreas adyacentes desde el Mesozoico hasta la actualidad. *Acta Geológica Hispánica*, **29**, 3–25.

Roca, E. & Guimerà, J. 1992. The Neogene structure of the esatern Iberian margin: structural constraints on crustal evolution of the Valencia Trough (western Mediterranean). *Tectonophysics*, **203**, 203–218.

Roca, E., Sans, M., Cabrera, L. & Marzo, M. 1999. Oligocene to Middle Miocene evolution of the central Catalan margin (northwestern Mediterranean). *Tectonophysics*, **315**, 209–233.

Salas, R. 1987. *El Malm i el Cretaci inferior entre el Massís de Garraf i la Serra d'Espadà*. PhD thesis, University of Barcelona, Barcelona, Spain.

Sibson, R.H. 1987. Earthquake rupturing as a mineralizing agent in hydrothermal systems. *Geology*, **15**, 701–704.

Sibson, R.H. 2000. Fluid involvment in normal faulting. *Journal of Geodynamics*, **29**, 469–499.

Steiger, R.H. & Jäger, E. 1977. Subcommission on geochronology: convention on the use of decay constans in geo- and cosmochronology. *Earth and Planetary Science Letters*, **36**, 359–362.

Stewart, I.S. & Hancock, P.L. 1990. Brecciation and fracturing within neotectonic normal fault zones of the Aegean region. *In*: Knipe, R.J. & Rutter, E.H. (eds) *Deformation Mechanisms, Rehology and Tectonics*. Geological Society, London, Special Publications, 54, 105–112.

Travé, A. & Calvet, F. 2001. Syn-rift geofluids in fractures related to the early-middle Miocene evolution of the Vallès-Penedès Half-graben (NE Spain). *Tectonophysics*, **336**, 101–120.

Travé, A., Calvet, F., Soler, A. & Labaume, P. 1998. Fracturing and fluid migration during Palaeogene compression and Neogene extension in the Catalan Coastal Ranges, Spain. *Sedimentology*, **45**, 1063–1082.

Travé, A., Labaume, P. & Vergés, J. 2007. Fluid systems in Foreland Fold-and-Thrust Belts: An overview from the Southern Pyrenees. *In*: Lacombe, O., Lavé, J., Roure, F. & Vergés, J. (eds) *Thrust Belts and Foreland Basins. From fold kinematics to hydrocarbon systems*. Springer Verlag, Berlin.

Travé A., Roca, E., Playà, E., Parcerisa, D. & Gómez-Gras, D. 2009. Migration of Mn-rich fluids through normal faults and fine-grained terrigenous sediments during early development of the Neogene Vallès-Penedès half-graben (NE Spain). *Geofluids*, **9**, 303–320.

Tucker, M.E. & Wright, V.P. 1990. *Carbonate Sedimentology*. Blackwell Scientific, Oxford.

Veizer, J. & Hoefs, J. 1976. The nature of O^{18}/O^{16} and C^{13}/C^{12} secular trends in sedimentary carbonate rocks. *Geochimica et Cosmochimica Acta*, **40**, 1387–1395.

Veizer, J., Buhl, D. & Diener, A. *et al.* 1997. Strontium isotope stratigraphy: potential resolution and event correlation. *Palaeogeography, Palaeoclimatology, Palaeoecology*, **132**, 65–77.

Veizer, J., Ala, D. & Azmy, K. *et al.* 1999. *$^{87}Sr/^{86}Sr$, $\delta^{13}C$ and $\delta^{18}O$ evolution of Phanerozoic seawater. Chemical Geology*, **161**, 59–88.

Vera, J.A., Ruiz-Ortiz, P.A., García-Hernández, M. & Molina, J.M. 1988. Paleokarst and related pelagic sediments in the Jurassic of the Subbetic Zone, Southern Spain. *In:* James, N.P. & Choquette, P.W. (eds) *Paleokarst*. Springer, Berlin, 364–384.

Verhaert, G., Muchez, P., Deppens, E. & Sintubin, M. 2009. Fluid impact and spatial and temporal evolution of normal faulting in limestones. A case study in the Burdur-Isparta Region (SW Turkey). *Geologica Belgica*, **12/3**, 59–73.

Vidal, N., Gallart, J., Dañobeitia, J. & Díaz, J. 1995. Mapping the Moho in the Iberian Mediterranean margin by multicoverage processing and mergin of wide-angle and near-vertical reflection data. *In*: Banda, E., Torné, M. & Talwani, M. (eds) *Rifted Ocean Continent Boundaries*. NATO ASI Series Series C, Mathematical and Physical Sciences, 463, 291–308.

Vilasi, N., Malandain, J. & Barrier, L. *et al.* 2009. From outcrop and petrographic studies to basin-scale fluid flow modeling: The use of the Albanian natural laboratory for carbonate reservoir characterization. *Tectonophysics*, **474**, 367–392.

Wibberley, C., Petit, J. & Rives, T. 2007. The effect of tilting on fault propagation and network development in sandstone–shale sequences: a case study from the Lodève Basin, southern France. *Journal of the Geological Society, London*, **164**, 599–608.

Received 1 March 2011; revised typescript accepted 7 November 2011.

Publication 3

Baqués, V., Travé, A., Cantarero, I. Development of successive karstic systems within the Baix Penedès Fault zone (onshore of the Valencia Trough, NW Mediterranean). Geofluids (under review).

GEOFLUIDS

Development of successive karstic systems within the Baix Penedès Fault zone (onshore of the Valencia Trough, NW Mediterranean)

Journal:	*Geofluids*
Manuscript ID:	GFL-2012-051
Manuscript Type:	Geofluids VII: Paris 2012
Date Submitted by the Author:	31-Jul-2012
Complete List of Authors:	Baqués, Vinyet; Facultat de Geologia (UB), Geoquímica, Petrologia i Prospecció Geològica Trave, Anna; Universitat de Barcelona, Geoquímica, Petrologia i Prospecció Geològica Cantarero, Irene; Facultat de Geologia (UB), Geoquímica, Petrologia i Prospecció Geològica
Key words:	meteoric fluids, karstification, normal faults, Neogene, Penedès basin

New Mexico Tech
SCIENCE · ENGINEERING · RESEARCH · UNIVERSITY

Professor A.T rave
Departament de Geoquimica, Petrologia i Prospeccio
Geolo`gica. Facultat de Geologia
Universitat de Barcelona

September 26, 2012

Dear Dr. Trave:

This is to confirm that the manuscript entitled, " Development of successive karstic systems within the Baix Penedès Fault zone (onshore of the Valencia Trough, NW Mediterranean)" by Baques et al. has been submitted to the journal Geofluids and is currently in review.

Sincerely,

Mark Person

Mark Person
Editor-in-Chief, Geofluids

Title: Development of successive karstic systems within the Baix Penedès Fault zone (onshore of the Valencia Trough, NW Mediterranean)

Short running title: Karstic systems of the Penedès area

V. Baqués[2*]: Martí i Franquès s/n, 08028 Barcelona, Spain. Ph.: +34934031165; Fax: +344021340; e-mail: vbaques@ub.edu

A. Travé[2]: Martí i Franquès s/n, 08028 Barcelona, Spain. Ph.: +34934021416; Fax: +344021340; e-mail: atrave@ub.edu

I. Cantarero[2]: Martí i Franquès s/n, 08028 Barcelona, Spain. Ph.: +34934031165; Fax: +344021340; e-mail: i_cantarero@ub.edu

* Corresponding author

[2] Departament Geoquímica, Petrologia i Prospecció Geològica, Facultat de Geologia, Universitat de Barcelona (UB), Martí i Franquès s/n, 08028 Barcelona, Spain

Key words: Karst, extenisonal fault, stable isotopes, strontium isotopes, meteoric diagenesis

ABSTRACT

Four karst episodes have been differentiated based on the field and petrographic observations and geochemical results of the footwall zone of the Baix Penedès Fault (Penedès Half-graben, onshore of Valencia Trough). The footwall zone is constituted by the Upper Jurassic-Lower Cretaceous dolomites which are highly brecciated and fractured. The dolomites were repeatedly modified by dissolution generating different types of karst systems. The first karstic system occurred on top of the Mesozoic rocks due to subaerial exposure after the Paleogene orogeny. The second and third karstic system was favoured by fractures formed during the Miocene syn-rift stage. The latest karst system developed at expenses of N-S fractures formed during the Miocene late post-rift stage, as a consequence of the sea-level fall during the Messinian.

INTRODUCTION

The Valencia Trough is a NE-SW oriented basin located between the Iberian Peninsula and the Balearic Islands. It belongs to the complex system of Neogene basins firstly created in the Mediterranean by the Paleogene compression (early Eocene-late Oligocene). The Valencia Trough was finally developed and settled in the Neogene (early Miocene). An extensive paleokarst system developed over the Mesozoic rocks that surround the Neogene basins (Cabrera 1981, Albaigés et al. 1985, Lomando et al. 1993, Playà et al. 2010, Rodríguez-Morillas

et al. in press). This paleokarst is related to the Tertiary/Mesozoic unconformity which results from subaerial exposure of Mesozoic rocks during the Paleogene orogeny and is recognized along the whole Mediterranean domain (Esteban 1991). The major petroleum system of Iberian Peninsula is located on the offshore Mediterranean, and still considered as one of the most prospective area (Vera et al. 1988, Clavell & Berastegui 1991, Varela et al. 2005, Klimowitz et al. 2005). Besides, during the Messinian (5.96 to 5.35 Ma), the Mediterranean Sea became isolated from the world's oceans resulting in a large drop in sea-level and widespread deposition of evaporites (Krijgsman et al. 1999). This drastic drop in base level affected the local karst systems creating new karst systems or reworking the previous one such as Cretaceous bauxite-filled fissures and caves (Combes 1969, Audra et al. 2004). The influence of the Messinian event has been widely recognized in French (Julian & Nicod 1984, Clauzon et al. 1997) and Italy (Bini et al. 1978, Bini 1994). In addition, several studies attest the development of normal faults in carbonates at shallow crustal depths (< 1-3 km) are a very complex process, because of the interaction of mechanical and chemical processes (Sibson, 2000 and Verhaert et al. 2009). Presented here are the results of an outcrop-based study of the footwall zone of the Baix Penedès Fault, which is very well exposed in the Penedès Half-graben. This basin can serve as an outcrop analogue to the basins existing in the offshore Mediterranean where the oil fields are developed. This study examines the different karstic dissolution and infillings events associated to the different fractures systems that took place in the Penedès Half-graben during its evolution. The objective of this paper is to determine the implication of karstic processes during the development of shallow deformation structures. The results of this study have implications for carbonate hydrocarbon reservoirs analogues subjected to karstic influence, in the Valencia Trough and elsewhere.

GEOLOGICAL SETTING

The Catalan Coastal Ranges (fig.1A) results from the superposition of three main tectonic events: (1) Mesozoic extensional phase which is divided in two rift episodes: the first, Late Permian to Triassic in age, related with the opening of the Neotethys; and the second, latest Oxfordian to Aptian in age, related to the opening of the North Central Atlantic Ocean and the Bay of Biscay (Salas & Casas, 1993, Salas et al. 2001); (2) Paleocene to middle Oligocene compressional phase that generated the Catalan Intraplate Belt (CIB) from the inversion of the Mesozoic rift basins which includes the emplacement of ENE-to-NE-trending thick-skinned thrust sheets bounded by SE-dipping thrusts with a limited left-lateral strike-slip motion (Ashauer & Teichmüller 1935, Llopis-Lladó 1947, Anadón et al. 1985, Guimerà 2004) and (3) late Oligocene?- Neogene extensional phase generating the extensional reactivation of the main

Paleogene reverse faults of the CCR (Fontboté 1954, Gaspar-Escribano et al. 2004) which split the CIB into a set of ENE-WSW blocks mainly tilted toward the NW, constituting the actual horst-and-graben systems present at the north-western Mediterranean (Bartrina et al. 1992; Roca & Guimerà 1992). The Penedès Half-graben is located at the central part of the CCR (fig. 1B). Two major structural highs surround this graben: Gaià-Montmell High and Garraf Horst, which in its turn include minor fault-bounded depressions (Vilanova and Baix Llobregat). The horsts are made up of Mesozoic carbonates and locally siliciclastic and evaporitic rocks overlaying the Variscan basement. Its NW margin is bounded by the Vallès-Penedès Fault, with a vertical slip from 2 to 4 km (Roca et al. 1999) (fig. 1C). Minor faults, up to few hundred meters of slip, make up the present southern boundary, separating the depression from the Garraf Horst. A karstified pre-rift unconformity (late Oligocene-early Miocene) associated with different weathering products (scree deposits, paleosoils), underlies the lowermost Neogene basin infill (Agustí et al. 1985). Three depositional complexes are distinguished filling the basin (Cabrera et al. 1991, Cabrera & Calvet 1996): (1) the lower continental complexes consisting in thick red beds sequences deposited in alluvial fan environment, Aquitanian to early Burdigalian in age; (2) the continental to marine complexes, late Burdigalian to Serravallian in age, with sabhka facies, carbonate platforms facies and siliciclastic and bay facies; and (3) the upper continental complexes, late Serravallian-Tortonian in age, consisting of thick red bed sequences deposited in alluvial fan environments. These sediments are covered by alluvial-fluvial (Gallart, 1981) and/or marine (Martinell, 1988) lower Pliocene units onlaping a deeply entrenched Messinian erosive surface which affected both the basement rocks and the earlier Neogene sequences.

METHODS

The structure, sedimentary fills and macroscopic diagenetic fabrics related to the Baix Penedès Fault and its related karstic features have been measured and mapped onto photomosaics. Twenty-seven samples were collected and thirty-three thin-sections were studied using optical and cathodoluminescence microscopes. The thin-sections were stained with Alizarine Red-S and potassium ferricyanide to distinguish calcite and dolomite and their ferroan equivalents (Dickson 1966). A Technosyn Cold Cathodoluminescence device (model 8200 MkII) operating at 15-18 Kv and 150-350 μA gun current was used. The calcite and dolomite cements and sediments from the host-rock and fractures were sampled for carbon- and oxygen-isotope analysis employing a 500 μm-thick dental drill to extract 60±10 μg of powder from polished slabs. The calcite and dolomite powdered was reacted with 103% phosphoric acid for 10 min at 90º C. The CO_2 was analysed using an automated Kiel Carbonate Device attached to a Thermal Ionization Mass Spectrometer Thermo Electron (Finnigan) MAT-252. The results are precise to

±0.02‰ for $\delta^{13}C$ and ±0.04‰ for $\delta^{18}O$. The results were corrected using the standard technique (Craig & Gordon 1965, Claypool et al. 1980) and are expressed in ‰ with respect to the VPDB standard.

Sr chromatography was performed using the method described by Pin & Bassin (1992) using Sr-resin commercially known as *Sr-Spec* and elaborated by Eichrom. Sr isotope measurements were carried out in a mass spectrometer Finnigan MAT-262. Samples were loaded onto a Ta filament (99.95%) previously degassed in two stages at 2 A and 4.5 A for 30 minutes. The measurement of isotopic ratios was made in the following conditions: ^{88}Sr beam intensity approx. 4V, acquiring 20 blocks of 10 sweeps, and ^{85}Rb being used to monitor potential isobaric interferences. The analytical data were corrected by linear law mass fractionation using as a constant ratio $^{86}Sr/^{88}Sr = 0.1194$ (Steiger & Jäger 1977).

Carbon-coated polished thin-sections were used to analyse minor and trace element concentrations on a CAMECA SX-50 electron microprobe. The microprobe was operated using 20 Kv of excitation potential, a current intensity of 15 nA and a beam diameter of 10 μm. The detection limits are 99 ppm for Mn, 144 ppm for Fe, 103 ppm for Na, 386 ppm for Mg, 89 ppm for Sr ppm and 497 ppm for Ca. Precision on major element analyses averaged 6.32 % standard error at 3 sigma confidence levels.

FIELD OBSERVATIONS

The Baix Penedès fault, well exposed at Castellví de la Marca (Baix Penedès), is a normal fault trending NE-SW and dipping towards SE with a normal displacement accumulated of up to 1 km (fig. 1C). This normal fault corresponds to a neoformed structure related with the Miocene Valencia Trough opening (Roca et al. 1999, Marín et al. 2008) and puts in contact the Mesozoic dolomites of the footwall with the upper continental complex of middle Serravallian-Tortonian age of the hangingwall. Within its footwall, the main fault is bounded by damage zone several hundred meters wide, which is characterized by intense fracturation and brecciation (Baqués et al. 2010). In the fault core zone the karst system is best developed. The architecture of the fractures and the diagenetic products that occur in the karst system and in the fault zone are described in the following sections.

Structure of the fault zone and fractures

We studied three outcrops across the Baix Penedès Fault, all situated within the footwall block. Along this fault, the footwall is constituted by the Garraf Upper Dolomites Formation of Thitonian-Berriasian age (Salas 1987). The Juncosa del Montmell outcrop is located near the

south-west fault termination on a secondary road from La Bisbal del Penedès to La Juncosa del Montmell. The road exhibits one hundred meters-thick fresh section orthogonal to the fault plane, between the undeformed dolomites of the footwall and the main fault plane. The Casetes de Gomila and Castellví outcrops are located along the central part of the fault near to the Castellví de la Marca village. Both outcrops exhibit a fresh section about five to ten meters-thick orthogonal to the fault plane of the footwall block.

In the Juncosa del Montmell are cropping out grey dolomites arranged in 1.5 meters-thick beds trending N40 and dipping 10º north-west. The damage zone is several hundred meters wide and is characterized by random fabric fractures that generate a cemented crackle to mosaic packbreccia (field breccia classification by Morrow 1982) (fig. 2). Various second-order faults are present within the damage zone involving up to fifty centimetres-thick of cemented rubble packbreccia corresponding to their corresponded core zone. At the nearest part of the main fault, the core zone is about ten meters-thick and is characterized by random fractures generating a cemented mosaic floatbreccia with dolomite sediments and calcite cements infilling the fractures. A late fracture system, trending NNW to SSE and dipping 70-80º north-west, cut the Baix Penedès Fault zone. These fractures from 2 to 40 cm with sub-angular walls are partially infilled by calcite sediments and cements.

The Casetes de Gomila and Castellví outcrops are located in a relay zone of two different segments of the Baix Penedès Fault. The Casetes de Gomila outcrop exposes five to ten meters-thick fault zone of Thitonian-Berriasian dolomites unconformably overlapped by the Miocene upper continental complexes (fig. 3A). The dolomites are arranged in 0.2 to 1 meters-thick beds trending N70 and dipping 10º north-west far from the main fault plane and 40º south-east close to the fault plane, forming an anticline forced by the normal motion of the Baix Penedès Fault. The undeformed footwall is not recognized in this outcrop. The damage zone, due to intense fracturation, exhibit a crackle to mosaic packbreccia recognized up to fifty meters away from the main fault plane. Closer to the fault plane, the core zone is arranged into different lentils of cemented rubble floatbreccias with dolomite sediments and cements.

The Castellví outcrop exposes up to thirty meters of the Baix Penedès Fault and five to ten meters-thick fault zone orthogonal to the slip plane (fig.4). The fault plane is curved trending from N60 to N10 and ends towards other fault segment trending N60. This geometry corresponds to a classical connection between two segments of the normal fault generating a relay zone due its propagation (Bellahsen & Daniel 2005). The dolomites are distributed in 0.3 to 1.5 meters-thick beds trending N40 and dipping 10º to the north-west. Nearer to the main fault plane, the bedding dips 10º south-eastwards, forming a slight anticline forced by the

normal motion of the Baix Penedès Fault. As the Casetes de Gomila outcrop, the undeformed footwall is not recognized being the damage zone constituted by the cemented crackle to mosaic packbreccia several meters along to the footwall block and the cemented rubble floatbreccia nearer to the main fault. The core zone architecture is complex, characterized by random fractures partially filled by different types of dolomite sediments and by different layers of breccias parallel to the fault plane, which in its turn are affected by the normal fault. A late fracture system, trending NNW to SSE and dipping 70-88º north-west, cut the Baix Penedès Fault zone.

PETROLOGY AND GEOCHEMISTRY

The mesostructural description of the three outcrops allows us to recognize five different types of common deformation patterns: three different systems of random fractures, NE-SW and NNW-SSE trending normal faults with their related fault rocks (different types of breccias) and karstic fillings (different types of sediments and cements). In this section, we describe the petrologic and geochemical characteristics of those common deformation products and establish their relative chronology with cross-cutting relationships. The figure 5 shows the type of deformation pattern and diagenetic product placed in each outcrop as well as the paragenetic sequence of the fault evolution.

Host-rock (replacive dolomite RD1)

The dolomites are constituted by replacive dolomicrite to dolsparite with penetrative and destructive or non-destructive fabrics (RD1) (fig. 6A). Ooids ghosts of the original limestone are locally recognised. The dolomite crystals are anhedral to subhedral, 10 to 150 μm in size and show dull purple luminescence (fig. 6B). The $\delta^{18}O$ varies from -2.1 to +1.2 ‰ VPDB and the $\delta^{13}C$ varies from +1 to +2.3 ‰ VPDB (fig. 7 & table 1). The $^{87}Sr/^{86}Sr$ ratio is 0.707417 (fig. 8 & table 2) and its elemental composition is between 21.3 and 23.68 % of Ca, between 12.03 and 13.57 % of Mg and between 129 and 1148 ppm of Sr. Na, Mn and Fe content ranges from below the detection limit to 921, 188 and 2306 ppm respectively (table 3).

Dolomitic sediment DS1

The first dissolution process was favoured by the interstrata discontinuities which generated vug porosity sub-parallel to bedding. This porosity is filled by the dolomitic sediment DS1 constituted by dull orange luminescence anehdral dolomite crystals, 25 to 150 μm in size (fig. 6A-B). The $\delta^{18}O$ varies from -1 to -0.6 ‰ VPDB, $\delta^{13}C$ from -3.2 to -2 ‰ VPDB (fig. 7 & table 1) and Ca varies from 21.27 to 24.43 %, Mg from 11.4 to 13.32 % and Sr from 364 to 1228

ppm. The Na, Mn and Fe content ranges from below the detection limit to 1316, 375 and 5906 ppm respectively (table 3).

Breccia type 1, dolomite cement DC1 and replacive dolomite RD2

As mentioned above, along the damage zone the host-rock is highly fractured. The fractures are mode I (opening) without preferred orientation, 10 to 75 μm thick and with sub-angular walls. Due the intensity of fracturing the damage zone is constituted by a cemented crackle to mosaic packbreccia (breccia type 1a) formed by angular fragments of dolomitic rocks, 0,5 to 4 cm in size (fig. 2 & 3B). Both, fractures and breccia are cemented by the dolomitic cement DC1 which is constituted by anhedral dull red luminescence crystals, 5 to 40 μm in size, growing in optical continuity with the host-rock crystals (fig. 6C-D). The $\delta^{18}O$ varies from -2.3 to -0.4 ‰ VPDB, $\delta^{13}C$ from -0.8 to +0.3‰ VPDB (fig. 7 & table 1) and Ca varies from 21.27 to 23.89 %, Mg from 11.4 to 13.32 % and Sr from 314 to 952 ppm. The Na, Mn and Fe content ranges from below the detection limit to 1316, 375 and 5908 ppm respectively (table 3). The core zone of secondary faults (up to 3 to 10 cm thick) is constituted by a cemented rubble packbreccia (breccia type 1b) resulting from comminution of host-dolomite, the breccia type 1a and the dolomitic sediment DS1. Near the main fault plane, mainly on the core zone, the dolomitic cement DC1 is more abundant the host-dolomites are partially replaced by a dolosparite with penetrative and destructive fabric (RD2). The dolomite crystals are subhedral dull to bright red luminescence, 50 to 300 μm in size (fig. 6E-F). The $\delta^{18}O$ varies from -4.6 to -0.7 ‰ VPDB and the $\delta^{13}C$ from -1 to +1 ‰ VPDB (fig. 7 & table 1).

Dolomitic sediment DS2 and dolomitic cement DC2

Random fractures affect the brecciated footwall and the dolomite sediment DS1. They are 75 to 400 μm thick with sub-angular walls and favoured dissolution, generating channel and vug porosity (fig. 3C). This porosity is filled the orange dolomite sediment DS2, constituted by fragments of the host-dolomite, 4 to 100 μm in size (fig. 6). Their $\delta^{18}O$ varies from -1.8 to +0.1 ‰ VPDB, their $\delta^{13}C$ from -4.2 to -2.9 ‰ VPDB (fig. 7 & table 1) and their $^{87}Sr/^{86}Sr$ ratio is 0.708761 (fig. 8 & table 2). The elemental composition is between 21.78 and 24.9 % of Ca, between 10.6 and 13.12 % of Mg and between 177 and 1250 ppm of Sr. Na, Mn and Fe content ranges from below the detection limit to 1130, 364 and 6927 ppm respectively (table 3). The dolomite sediment DS2 is cemented by the dolomitic cement DC2, arranged as a rim position at the fractures walls or surrounding the host-rock fragments (fig. 6). The cement has non-luminescent to orange luminescent zonation and its elemental composition is between 23.68 and 24.71 % of Ca, between 10.61 and 12 % of Mg, between 258 and 476 ppm of Na, between 218

and 2025 ppm of Fe and between 453 and 726 ppm of Sr. Mn content ranges from below the detection limit to 211 ppm (table 3).

Breccia type 2 and dolomitic sediment DS3

The continued dissolution processes favoured by the random fractures locally originated the collapse of fractures walls, producing the cemented rubble floatbreccia (breccia type 2) (fig. 3D & 4A). This breccia is formed by angular centimetric to decametric reworked fragments of host-rock, dolomitic cements and sediments and is cemented by a pink to red dolomitic sediment DS3, contains high amount of iron oxides and locally is laminated (fig. 3C). The sediment is constituted by bright orange luminescent euhedral crystals, 50 to 100 μm in size (fig. 6E-F). The $\delta^{18}O$ varies from -2 to +0.7 ‰ VPDB, the $\delta^{13}C$ varies from -3.1 to +0.1 ‰ VPDB and the $^{87}Sr/^{86}Sr$ ratio is 0.708855 (figs. 7-8 & tables 1-2). The elemental composition is between 22.35 and 24.43 % of Ca, between 10.73 and 12.35 % of Mg and between 237 and 1228 ppm of Sr. Na, Mn and Fe content ranges from below the detection limit to 484, 346 and 2866 ppm respectively (table 3).

Hematite cement H1 and dolomite cement DC3

The hematite and dolomite cements H1 and DC3 respectively are filling the NNW-SSE and NE-SW fractures (fig. 3B). The hematite cement is precipitated at one of the fractures walls and the residual porosity prevailing after the dolomite sediment DS3 (fig. 9A-B). The dolomite cement DC3 corresponds to brown-orange zonated luminescent euhedric crystals, 100 to 500 μm in size, growing with the c-axis perpendicular to the fracture walls (figs. 6A-F & 9A-B). The stable isotopes are -1.2 to +0.1 ‰ for $\delta^{18}O$ VPDB and -2.3 to -1.7 ‰ VPDB for $\delta^{13}C$ (fig. 7 & table 1) and its elemental composition is between 22.52 and 24.49 % of Ca, between 10.95 and 12.19 % of Mg and between 115 and 1071 ppm of Sr. Na, Mn and Fe content ranges from below the detection limit to 611, 406 and 3197 ppm respectively (table 3).

Calcite cement CC1

In the Castellví outcrop, the remaining porosity after the dolomite cement DC3 precipitation is partially infilled by the calcite cement CC1. This cement is constituted by subhedral crystals, 100 to 750 μm, showing black-bright orange-black luminescence zonation and featuring blocky texture (fig. 9a and 9b). The $\delta^{18}O$ varies from -9 to -7.5 ‰ VPDB, $\delta^{13}C$ from -7.5 to -6.7 ‰ VPDB and $^{87}Sr/^{86}Sr$ ratio is 0.708293 (figs. 7-8 & tables 1-2). The elemental composition is between 39.02 and 40.27 % of Ca, between 0.07 and 0.45 % of Mg. Na, Mn, Fe and Sr content ranges from below the detection limit to 330, 210, 273 and 491 ppm respectively (table 3).

Breccia type 3 and calcite cement CC2

In Juncosa del Montmell outcrop, the core zone of the main fault plane is constituted by a 10 meters-thick of mosaic to rubble cemented packbreccia (breccia type 3) (Fig. 2). This breccia consist of subangular fragments, 0,5 to 4 cm in size, of host-dolomite and reworked breccia type 1 and is cemented by two generations of fillings: internal dolomitic sediment (DS4) constituted by subhedral to euhedral bright orange to bright yellow luminescent dolomitic crystals reworked from the previous dolomitic sediments DS3 (fig.9 C-D). This sediment usually shows a thin depositional lamination and fills the lower part of the cavities. The second filling corresponds to the calcite cement CC2, constituted by non-luminescent subhedral crystals, 250 μm to 2 mm in size and featuring blocky texture (fig. 9C-D). The $\delta^{18}O$ varies from -8.5 to -6.4 ‰ VPDB, $\delta^{13}C$ from -8.3 to -6.6 ‰ VPDB (fig. 7 & table 1). The elemental composition is between 39.39 and 40.21 % of Ca, between 0.12 and 0.27 % of Mg. Na, Fe and Sr content ranges from below the detection limit to 312, 255, 273 and 482 ppm respectively. The Mn content is always below to the detection limit (table 3).

Breccia type 4 and hematite cement H2

In Castellví outcrop, overlying the karstified footwall zone occur a particulate rubble floatbreccia (breccia type 4) (fig. 4B). This breccia is formed by angular milimetric to centimetric reworked fragments of host-rock and previous karstic fillings. The matrix contains reworked fragments of the dolomite sediments DS2 and DS3. Surrounding the reworked dolomite crystals the hematite cement H2 is precipitated giving a lateritic aspect to the breccia (fig. 9E). This breccia is cemented by the calcite with the same petrography features and geochemistry signature as the cement CC2.

Breccia type 5 and calcite cements CC3, CC4, CC5, CC6 and CC7

The cemented rubble floatbreccia (breccia type 5) running parallel to the main fault plane is cropping out at Castellví (fig. 4C). This breccia is formed by sub-angular to sub-rounded fragments, 1 to 3 cm in size, of the host-rock, dolomite sediments and breccias of the previous stages. Some of these fragments are surrounded by a rim of bladed calcite cement CC3 (fig. 9F). The $\delta^{18}O$ varies from -8.8 to -8.6 ‰ VPDB, $\delta^{13}C$ from -7.5 to -7.4 ‰ VPDB (fig. 7 & table 1) and the elemental composition from 39.41 to 40.28 % of Ca and from 0.13 to 0.56 % of Mg. Na, Mn, Fe and Sr content ranges from below the detection limit to 262, 253, 655 and 519 ppm respectively (table 3). The fragments are cemented by the calcite cement CC4. This cement is constituted by non-luminescent subhedric crystals with goethite inclusions, 20 to 100 μm in

size, featuring blocky texture (fig. 9F). In the upper part of this layer of breccias the goethite content increase giving a yellow tinge to the rock. The $\delta^{18}O$ is -9.6 ‰ VPDB and the $\delta^{13}C$ is -5.9 ‰ VPDB at the reddish part and from -9.8 to 9.5‰ VPDB for $\delta^{18}O$ and from -5.5 to -5.4 ‰ VPDB for $\delta^{13}C$ the yellow tinge part (fig. 7 & table 1). The elemental composition is between 39.27 and 40.23 of Ca, between 0.14 and 0.45 % of Mg. Na, Mn, Fe and Sr content ranges from below the detection limit to 272, 180, 643 and 668 ppm respectively (table 3). Sigmoidal extensional fractures affect this breccia (fig. 4C) and are filled by three generations of cement: calcite cement CC5, constituted by non-luminescent anhedric calcite crystals, 25 to 50 μm in size, with a rim disposition (fig. 9F). The elemental composition is between 39.05 and 40.13 % of Ca, between 0.07 and 0.42 % of Mg. Na, Mn, Fe and Sr content ranges from below the detection limit to 185, 164, 478 and 455 ppm respectively (table 3). The second cement generation is calcite CC6, which corresponds to a yellow cement, with high amount of goethite inclusions, constituted by non-luminescent blocky subhedric calcite crystals, 50 to 150 μm in size (fig. 9F). The $\delta^{18}O$ is -9.2 ‰ VPDB and the $\delta^{13}C$ is -5.6 ‰ VPDB (fig. 7 & table 1). The elemental composition is between 38.31 and 40.38 % of Ca, between 0.13 and 0.46 % of Mg, between 801 and 6564 ppm of Fe and between 172 and 450 ppm of Sr. Na and Mn content ranges from below the detection limit to 193 and 214 ppm respectively (table 3). The third generation of cement correspond to the calcite cement CC7 formed by non-luminescent blocky euhedric calcite crystals, 100 to 150 μm in size (fig. 9F). The $\delta^{18}O$ is -7.2 ‰ VPDB and the $\delta^{13}C$ is -7.5 ‰ VPDB (fig. 7 & table 1). The elemental composition is between 39.17 and 40.32 % of Ca and between 0.04 and 0.15 % of Mg. Na, Mn, Fe and Sr content ranges from below the detection limit to 327, 160, 541 and 619 ppm respectively (table 3).

Pisoliths, calcite cement CC8 and laminated sediment CS1

Over the breccias type 5, a layer formed by laminated karstic pisoliths is present (fig. 4D). The nucleus of the pisoliths corresponds to fragments of the dolomite sediments, cements and the breccia type 5, all of them cemented by bladed calcite cement CC8 arranged in rim position and surrounded by the laminated calcite sediment CS1. The calcite cement CC8, is constituted by non-luminescent bladed crystals, 300 μm to 1 mm in size. The $\delta^{18}O$ varies from -8.7 to -8.6 VPDB and the $\delta^{13}C$ varies from -7.7 to -7.4 ‰ VPDB (fig. 7 & table 1). The elemental composition is between 39.72 and 40.47 % of Ca, between 0.17 and 0.39 % of Mg. Na, Fe and Mn content ranges from below the detection limit to 253, 216 and 501 ppm respectively. The Mn content is always below to the detection limit (table 3). The calcite sediment CS1 is formed by non-luminescent blocky anhedral calcite crystals, 4 to 10 μm in size. The $\delta^{18}O$ ranges from -8.6 to -8.5 ‰ VPDB and $\delta^{13}C$ from -7.8 to -7.6 ‰ VPDB (fig. 7 & table 1). The elemental

composition is between 39.1 and 40.01 % of Ca, between 0.19 and 0.36 % of Mg, between 212 and 2885 ppm of Fe. Na and Sr content ranges from below the detection limit to 310 and 686 ppm respectively. The Mn content is always below to detection limit (table 3).

Well-rounded pisoliths and calcite cements CC9 and CC10

The upper layer corresponds to a tabular white layer constituted by well-rounded pisoliths (Fig. 4E), 0.5 to 10 cm in size, cemented by the calcite cement CC9 (fig. 4F). This cement is formed by non-luminescent drusy euhedral crystals, 50 μm to 1 mm in size (fig. 9G). The $\delta^{18}O$ varies from -8.8 to -8.1 ‰ VPDB and the $\delta^{13}C$ varies from -7.9 to -7.8 ‰ VPDB (fig. 7 and table 1). The elemental composition is between 38.15 and 40.29 % of Ca and between 0.11 and 1.13 % of Mg. Na, Mn, Fe and Sr content ranges from below the detection limit to 452, 297, 842 and 2146 ppm respectively (table 3). Later movements of the extensional faults generated the cataclasis of the karstic pisoliths (Fig. 4G). This cataclasite is formed by the comminute calcite pisoliths cemented by the calcite cement CC10 (fig. 9G). The $\delta^{18}O$ varies from -8,4 to -8.1 ‰ VPDB, the $\delta^{13}C$ varies from -7.9 to -7.7 ‰ VPDB and the $^{87}Sr/^{86}Sr$ ratio varies from 0.708102 to 0.708253 (figs. 7-8 & tables 1-2).

Laminated calcite sediment CS2 and calcite cement CC11

Dissolution processes enlarged the NNW-SSE fractures up to 5 to 50 cm thick with sharp and undulating walls (fig. 2). These fractures contain two generations of fillings: the first generation corresponds to pink laminated sediment CS2 constituted by, 10 to 100 μm in size, subhedral non-luminescent crystals featuring a blocky texture (fig. 9H). The laminations correspond to size variations of the calcite crystals, and in some cases include goethite and dolomite crystals. The $\delta^{18}O$ is -6.9 ‰ VPDB and $\delta^{13}C$ -8 ‰ VPDB (fig. 7 & table 1). The elemental composition is between 38.83 and 39.43 % of Ca and between 0.31 and 0.49 % of Mg. Na, Fe and Sr content ranges from below the detection limit to 163, 561 and 1207 ppm respectively. Mn content is always below to the detection limit (table 3). The second filling phase corresponds to the CC11 calcite cement constituted by bladed non-luminescent crystals, from 50 to 250 μm in size (fig. 9H). The $\delta^{18}O$ varies from -8.8 to -6.5 ‰ VPDB and $\delta^{13}C$ from -9.6 to -7.8 ‰ VPDB (fig. 7 & table 1). The elemental composition is between 38.59 and 40.23 % of Ca, between 0.11 and 0.82 % of Mg and between 1126 and 1510 ppm of Sr. Na and Fe content ranges from below the detection limit to 211 and 1103 ppm respectively. Mn content is always below to the detection limit (table 3). This cement has a palisade texture which can develop up to 30 cm thick. Sometimes this cement is present filling the remaining fracture porosities form earlier stages.

DISCUSSION

The field characteristics of the three studied fault zones suggest that they are located at different segments of the fault which are been connected during its Neogene development. Below is interpreted the whole evolution of the Baix Penedès Fault and how the different stages of fracturing during the upward fault-tip propagation affect to the dissolution processes. We combine the study of fractures with the petrographic and geochemical results of their infillings to determine from which type of fluid were precipitated or deposited.

Diagenesis of the host-rock

The $\delta^{18}O$ values of the host-rock (RD1) ranging from -2.1 to +1.2 ‰ VPDB, shows a marine influence during the dolomitization process (Budd 1997). These values, together with the $\delta^{13}C$ and $^{87}Sr/^{86}Sr$ suggest that the dolomitization occurred during Upper Jurassic-Lower Cretaceous (Veizer et al. 1999). Nadal (2001) attest the interval from Thitonian to Berriassian age for the dolomitization occurred at the central part of the Catalan Coastal Ranges and neighbouring areas.

Stage A: end of Paleogene

The dolomitic sediment DS1 filling the initial vug porosity, has similar petrographic characteristics and $\delta^{18}O$ values as the host-dolomite RD1 suggesting that this sediment comes from the erosion and reworking of the host rock. However the geochemistry of the dolomitic sediment has values more depleted in $\delta^{13}C$, indicating that the sediment has been further altered by a fluid more enriched with organic CO_2 (Moore 2001). This dissolution event can be related with the extensive dissolution that took place in the area during and after of the uplift of the Catalan Coastal Ranges due the Paleogene compression (Cabrera 1981, Albaigés et al. 1985, Esteban 1991).

Stage B: syn-rift (Aquitanian? to early Burdigalian)

Related to the initial upward propagation of the Baix Penedès fault, deformation was characterized by random fabric fractures cemented by the dolomitic cement DC1. The $\delta^{18}O$ values, varying between -2.3 and -1.3 ‰ VPDB, suggest low temperature (table 1), which is consistent with the results of thermochronology in the central part of the Catalan Coastal Ranges, which show that maximal burial of the exhumed normal fault footwalls was less than 2 km (Juez-Larré and Andriessen 2006). At Castellví and Casetes de Gomila outcrops the host-rock is partially replaced by the dolomite RD2. The petrography and geochemistry of this dolomite suggest that the dolomitization occurred during progressive burial of the Jurassic rocks

(Tucker & Marshall 2004). Moreover, this increasing in fluid flow and in minor magnitude the temperature of fluids (table 1). This replacement can be attributed to the connection of two fault segments in a relay zone (Rowland & Sibson 2004, Cantarero et al. in this volume).

The forced fold related fault formed within the footwall together with the extensive dissolution favoured by randomly fractures formed during folding suggest that the tip of deformation due the propagation of the fault is reaching the surface (Sharp et al. 2000). The $\delta^{18}O$ values of the dolomite sediments and their Sr/Ca molar ratios (table 3) show a similarity with the host-rock. In contrast, the more depleted values of $\delta^{13}C$ indicate the influence of CO_2 derived from the soil suggesting the opening of the system to meteoric waters (Moore 2001). On the other hand, the $^{87}Sr/^{86}Sr$ values are consistent with the marine waters of late Burdigalian-Langhian (Veizer et al. 1999). Similar values are reported for the same type of sediments deposited in the Casablanca oil reservoir (Rodríguez-Morillas et. al 2012). In the following section discusses these values in strontium.

Stage C: Early post-rift (late Burdigalian to Langhian)

The $\delta^{18}O$ and $\delta^{13}C$ together with the Sr/Ca molar ratio values of the dolomite cement DC3 (table 3) are consistent that was precipitated under low temperature marine seawater influence (table 1) (Budd 1997). The similarity values of DC2 which is overgrowing the DS2, the marine signature of $\delta^{18}O$ and $\delta^{13}C$ of DS3 and the $^{87}Sr/^{86}Sr$ values consistent with the marine waters of late Burdigalian-Langhian suggest that the karstic sediments where dolomitized during this stage. Moreover during the late Burdigalian to Langhian the basin was flooded and sabhka carbonate platforms and siliciclastic and bay facies where deposited (Cabrera et al. 1991, Cabrera and Calvet 1996), which are consistent with the upflowing marine waters through faults and the karstic sediments dolomitization (Calvet et al. 2001).

Stage D: Late post-rift (Serravallian to Tortonian)

Normal fault connected to subaerial surface and the calcite cements filling NE-SW normal faults (CC1 to CC10) correspond to a mixture of tectonic and karstic products. The $\delta^{18}O$ values of calcite cements together with the Mg/Ca and Sr/Ca molar ratios, and the high radiogenic values of the calcite cementing the cataclasite of karstic pisoliths indicate that meteoric waters, not interacted with the host-limestone, were responsible for precipitation of the calcite cements. The oscillations in $\delta^{13}C$ values are interpreted that the cements were influenced by the variations of the phreatic level during its deposition (Longman 1980).

Stage E: Late post-rift (Tortonian to Present)

The late NNW-SSE fractures are attributed to the late post-rift stage of the Neogene extension as a result of the generalized tensile deformation of the whole area during the final stages of the basin development. The calcite cement CC11 that covers the fractures walls is interpreted as speleothems formed in the vadose meteoric environment, similar to those described in Miocene materials (Travé & Calvet 2001). The prevailing of the vadose meteoric environment from Tortonian to present is attributed to the Messinian drop of sea level (Julian & Nicod 1984, Clauzon et al. 1997, Bini et al. 1978, Bini 1994).

CONCLUSIONS

The successive deformation stages and related fillings described above allow us to differentiate four different events of karstification:

(1) karstification related to the Paleogene compression and affecting the Mesozoic rocks: characterized by a widespread dissolution and the generation of vug and cavern porosity due to subaerial exposure of the Mesozoic carbonates. The elemental geochemistry of the cements and sediments filling these porosities indicate that comes from the erosion and reworking of the host-rock.

(2) Karstification related to the syn-rift Neogene extension and affecting the Mesozoic rocks: random fractures related to the propagation and evolution of the Neogene faults favoured the dissolution processes. The geochemistry of the different types of dolomite karstic sediments fill the fracture porosity indicates that they were deposited from a meteoric fluid in an open hydrological system. However the $^{87}Sr/^{86}Sr$ radiogenic data suggest that these sediments where further altered by marine dolomitization.

(3) karstification occurred during the transition between syn- and post-rift Neogene extension and affecting some neoformed horsts: the calcite fillings related to the NW-SE normal faults are mixtures of tectonic and karstic processes and resulted from multi-stage movement of the faults during the rifting. The $\delta^{18}O$ values together with the Mg/Ca and Sr/Ca molar ratios of the calcite cements, and the high radiogenic values of the cataclasite of karstic pisoliths indicate that meteoric waters, not equilibrated with the host-limestone, were responsible for precipitation of these cements. The karstic filling of this second event is clearly affected by the normal faults and by the strike-slip faults and therefore developed during the syn- and post-rift stages.

(4) karstification favoured by the NNW-SSE trending fractures related with the late post-rift: calcite sediments and cements interpreted as speleothems covers the fractures walls. The low

$\delta^{13}C$ of the speleothems indicates a higher involvement of soil-derived CO_2 and precipitation in the vadose meteoric environment. The karstic fillings of this third event are not deformed and are attributed to the Neogene post-rift.

ACKNOWLEDGEMENTS

The isotopic and electron microprobe analyses were carried out at "Centres Científics i Tecnològics" of the Universitat de Barcelona and the strontium analyses at SGIker Geochronology department of the Facultad de Ciencia y Tecnologia - Universidad del País Vasco/EHU. We wish to thank Jordi Illa for technical support. This research was performed within the framework of I+D+I research projects CGL2010-18260 of the Grup Consolidat de Recerca "Geologia Sedimentària" (2009 SGR-1458), the BES-2007-14935 grant.

REFERENCES

Agustí J, Cabrera L, Moya S (1985) Sinopsis estratigráfica del Neógeno en la fosa del Vallès-Penedès. *Paleontología Evolutiva*, **18**, 57-81.

Albaigés J, Borbon J, Walker IW (1985) Petroleum isoprenoid hydrocarbons derived from catagenetic degradation of Archaebacterial lipids. *Organic Geochemistry* **8**, 293-297.

Anadón P, Cabrera L, Guimerà J, Santanach P (1985) Paleogene strike-slip deformation and sedimentation along the southeastern margin of the Ebro Basin. In: KT Biddle & N Christie-Blick (editors). Strike-slip deformation, basin formation and sedimentation. *Soc. Econ. Paleon. Min. Sp. Pub*., **37**, 303-318

Ashauer H & Teichmüller R (1935) *Die Variscische und Alpidische Gebirgsbildung Kataloniens*. Abh. Ges. Wiss. Gottingen math-phys. 3 (lo), 115 p. (spanish traduction: Publ. Extr. Geol. Esp. t. 111, CSIC).

Audra P, Mocochain L, Camus H, Gilli E, Clauzon G, Bigot J-Y (2004) The effect of the Messinian Deep Stage on karst development around the French Mediterranean. *Geodin. Acta* **17**, 389-400.

Baqués V, Travé A, Benedicto A, Labaume P, Cantarero I (2010) Relationships between carbonate fault rocks and fluid flow regime during propagation of the Neogene extensional faults of the Penedès basin (Catalan Coastal Ranges, NE Spain). *Journal of Geochemical Exploration*, **106**, 24-33.

Bartrina MT, Cabrera L, Jurado MJ, Guimerà J, Roca E (1992) Evolution of the central Catalan margin of the Valencia trough (western Mediterranean). *Tectonophysics*, **203**, 219-247.

Bini A, Cita MB, Gaetani M (1978) Southern Alpine lakes: Hypothesis of an erosional origin related to the Messinian entrenchment. *Marine Geology,* **27**, 271–288.

Bini A (1994) Rapports entre la karstification périméditerranéenne et la crise de salinité du Messinien : l'exemple du karst lombard, Italie (Relations between perimediterranean karstification and the Messinian crisis: the Lombardy karst example, Italy). *Karstologia,* **23**, 33-53.

Budd DA (1997) Cenozoic dolomites of carbonate islands: their attributes and origin Earth-Science Reviews **42**, 1-47.

Cabrera L (1981) Estratigrafía y características sedimentológicas generales de las formaciones continentales del Mioceno de la cuenca del Vallès-Penedès (Barcelona, España). *Estudios Geol.* **37**, 35-43.

Cabrera L, Calvet F, Guimerà J, Permanyer A (1991) El registro sedimentario miocénico en los semigrabens del Vallès- Penedès i del Camp: organización secuencial y relaciones tectónica sedimentación. *I Congreso del Grupo Español del Terciario. Libro-guía Excursión* 84. 132 pp.

Cabrera L, Calvet F (1996) *Onshore Neogene record in NE Spain: Vallès-Penedès and el Camp half-grabens (NW Mediterranean).* In: PT Friend & C Dabrio (editors). *Tertiary Basins of Spain*. Cambridge University Press, Cambridge, 97-105.

Calvet F, Canals A, Cardellach E, Carmona JM, Gómez-Gras D, Parcerisa D, Bitzer K, Roca E, Travé A (2000) Fluid migration and interaction in extensional basins: application to the Triassic and Neogene rift in the central part of the Catalan Coastal Ranges, NE Spain. *Field Gride III Geofluids Congres*. 58 pp.

Calvet F, Travé A, Bitzer K, Roca E, Tritlla J, Baker J (2001) Dolomitization of detritial deposits related to Neogene extensional faults, Catalan Coastal Ranges (Spain). *Geotemas*, **3** (1), 109-111.

Cantarero I, Travé A, Alías G, Baqués V (this volume) From hydrothermal to meteoric fluid regimes in a segmented fault affecting crystalline and carbonate rocks: case study of the Barcelona Plain (NE Spain). *Geofluids*

Combes P-J (1969) Recherches sur la genèse des bauxitas dans le nord-est de l'Espagne, le Languedoc et l'Ariège (France). *Mémoires du centre d'études et de recherches géologiques et hydrogéologiques. Tomes III-IV,* Université de Montpellier-Faculté des Sciences, 335 pp.

Clauzon G, Rubino JL, Casero P, *1997*. Regional modalities of the Messinian Salinity Crisis in the framework of two phases model. In: Neogene basins of the Mediterranean region: controls and correlation in space and time, *R.C.M.N.S. Inter.-Coll., Catania, Program and Abstracts; 44–46.*

Clavell E & Berastegui X (1991) Petroleum geology of the Gulf of Valencia *Publicación Especial de la Asociación Europea de Geocientíficos Petroleros,* **1**, 355-368.

Claypool, GE, Holser WT, Kaplan IR, Sakai H, Zak I (1980) The age curves of sulphur and oxygen isotopes in marine sulphate and their interpretation. *Chemical Geology (Isotope geoscience section)*, **28**, 199-260.

Craig H & Gordon I (1965) *Deuterium and oxygen-18 variations in the ocean and marine atmosphere*. In: E Tongiorgi (editor) Stable Isotopes in Oceanographic Studies and Paleotemperatures. *Consiglio Nazionale delle Richerche, Laboratorio di Geologia Nucleare, Pisa*, Italy. 9-130.

Dickson JAD (1966) Carbonate identification and genesis as revealed by staining. *Journal of Sedimentary Petrology*, **36**, 491-505.

Esteban M (1991) Paleokarst: case histories. In: Paleokarsts and paleokarstic reservoirs, VP Wright, M Esteban, PL Smart (editors) *Postgraduate Research Institute for Sedimentology, University of Reading Contribution* **152**, 120-146

Fontboté JM (1954) Las relaciones tectonicas de la depresion del Vallès-Penedes con la cordillera prelitoral y con la depresión del Ebro. Tomo Homenaje a Prof. E. Hernandez-Pacheco. *Revista de la Sociedad Española de Historia Natural*, 281-310.

Gallart F (1981) Neógeno superior y Cuaternario del Penedès (Catalunya, España). *Acta Geològica Hispànica* **16**, 151-157.

Gaspar-Escribano J, García-Castellanos D, Roca E, Cloetingh, S (2004) Cenozoic vertical motions of the Catalan Coastal Ranges (NE Spain): The role of tectonics, isostasy, and surface transport. *Tectonics*, **23**, doi:10.1029/2003TC001511.

Guimerà J (1988) Estudi estructural de l'enllaç entre la Serralada Ibèrica i la Serralada Costera Catalana. *PhD thesis, Universitat de Barcelona*.

Guimerà J (2004) La Cadena Costera Catalana. In: JA Vera (editor) *Geologia de España*, SGE-IGME, Madrid, 603-605.

Juez-Larré J, & Andriessen PAM (2006) Tectonothermal evolution of the northeastern margin of Iberia since the break-up of Pangea to present, revealed by low-temperature fission-track and (U-Th)/He thermochronology. A case history of the Catalan Coastal Ranges. *Earth Planet. Sci. Let.* **243**, 159-180.

Julian M, Nicod J (1984) Paléokarsts et paléo-géomorphologie néogènes des Alpes occidentales et régions adjacentes. *Karstologia*, **4**, 11-18

Klimowitz J, Hernández E, Serrano A (2005) A field trip guide book. The Mediterranean Basin (Catalan costal range onshore analogues). In: W Martínez del Olmo (editor). *Asociación de Geólogos y Geofísicos Españoles del Petróleo (AGGEP)-XXV Aniversario*, 187-208.

Krijgsman W, Hilgen FJ, Raffi I, Sierro FJ, Wilson DS (1999) Chronology, causes and progression of the Messinian salinity crisis, *Nature*, **400**, 652-655.

Llopis-Lladó N (1947) Contribución al conocimiento de la morfoestructura de los Catalánides. *Inst. "Lucas Madalla", Barcelona C.S.I.C.* 373 pp.

Lomando AJ, Harris PM, Orlopp DE (1993) Casablanca field, Tarragona Basin, offshore Spain: a karsted carbonate reservoir. In: Paleokarst Related Hydrocarbon Reservoirs RD. Fritz, JL. Wilson, DA.Yurewicz (editors) *Core Workshop, 18, in New Orleans, SEPM 201–25, Tulsa.*

Longman MW (1980) Carbonate diagenetic textures from near surface diagenetic environments. *American Association of Petroleum of Geological Bulletin*, **60**, 601-621.

Marín MA, Roca E, Rosell O, Marcuello A Cabrera L (2008) La Falla del Montmell: un ejemplo del control ejercido por las fallas extensivas mesozoicas en la arquitectura cenozoica de las Cadenas Costaneras Catalanas. *Geotemas*, **10**, 461-464.

Martinell J (1988) An overview of the marine Pliocene of N.E. Spain. *Géol. Méditerran.,* **15**, 227-233.

Moore C (2001) Carbonate reservoirs: porosity evolution and diagenesis in a sequence stratigraphic framework. *Developments in sedimentology*, **55**, 444 pp.

Morrow DW (1982) Diagenesis 2. Dolomite – Part 2: Dolomitization models and ancient dolostones. *Geoscience Canada* **9**, 95-107.

Pin C & Bassin C (1992) Evaluation of a strntium-specific extraction chromatographic method for isotopic analysis in geological materials. *Anal. Chim. Acta*, **269**, 249-255.

Playà E, Travé A, Caja MA, Salas R & Martín-Martín JD (2010) Diagenesis of the Amposta offshore oil reservoir (Amposta Marino CS well, Lower Cretaceous, Valencia Trough, Spain). *Geofluids*, **9**, 1-19.

Roca E & Guimerà J (1992) The Neogene structure of the esatern Iberian margin: structural constraints on crustal evolution of the Valencia Trough (western Mediterranean). *Tectonophysics,* **203**, 203-218.

Roca E, Sans M, Cabrera L Marzo M (1999) Oligocene to Middle Miocene evolution of the central Catalan margin (northwestern Mediterranean). *Tectonophysics* **315**, 209-233.

Rodríguez-Morillas N, Playà E, Travé A, Martín-Martín JD, Guerrero A (in press) Diagenetic processes in a partially dolomitized carbonate reservoir: Casablanca oil field, Mediterranean Sea, offshore Spain, *Geologica Acta*

Rowland JV & Sibson RH (2004) Structural controls on hydrothermal flow in a segmented rift system, Taupo Volcanic Zone, New Zealand. *Geofluids* 4, 259-283.

Salas R, Guimerà J, Mas R, Martín-Closas C, Meléndez A Alonso A (2001) Evolution of the Mesozoic Central Iberian Rift System and its Cainozoic inversion (Iberian Chain). In: PA Ziegler, W Cavazza, AHF Robertson, S Crasquin-Soleau (editors) Peri-Tethys Memoir 6: Peri-Tethyan Rift/Wrench Basins and Passive Margins. *Mém. Mus. nat. Hist. Nat.,* Paris, **186**, 145–185.

Salas R & Casas A (1993) Mesozoic extensional tectonics, stratigraphy and crustal evolution during the alpine cycle of the eastern Iberian Chain. *Tectonophysics,* 228, 33-55.

Sharp IR, Gawthrope RL, Underhill JR, Gupta S (2000) Fault-propagation folding in extensional settings: Examples of structural style and synrift sedimentary response from Suez rift, Sinai, Egypt. *Geological Society of America Bulletin*, **112** (12), 1877-1899.

Sibson RH (2000) Fluid involvement in normal faulting, *J. Geodynamics*, **29**, 469–499.

Steiger RH & Jäger E (1977) Subcommission on geochronology: Convention on the use of decay constants in geo- and cosmochronology. *Earth Planet Sci Lett* **36**, 359-362.

Travé A, Calvet F, Soler A, Labaume P (1998) Fracturing and fluid migration during Palaeogene compression and Neogene extension in the Catalan Coastal Ranges, Spain. *Sedimentology*, **45**, 1063-1082.

Travé A & Calvet F (2001) Syn-rift geofluids in fractures related to the early-middle Miocene evolution of the Vallès-Penedès Half-graben (NE Spain). *Tectonophysics*, **336**, 101-120.

Travé A, Labaume P Vergés J (2005) Fluid systems in Foreland Fold-and-Thrust Belts: An overview from the Southern Pyrenees. In: O Lacombe, J Lavé, F. Roure, J Vergés (editors) *Thrust Belts and Foreland Basins. From fold Kinematics to hydrocarbon systems*. Springer Publications, Berlin.

Varela J, Vicente-Bravo JC, Navarro J, Esteban M, Martinez del Olmo W (2005) The Oil Fields in the Spanish Mediterranean Sea. In: W. Martínez del Olmo (editor). *Asociación de Geólogos y Geofísicos Españoles del Petróleo (AGGEP)-XXV Aniversario*, 121-129.

Veizer J, Ala D, Azmy K, Bruckschen P, Buhl D, Bruhn F, Carden GAF, Diener A, Ebneth S, Goddéris Y, Jasper T, Korte C, Pawellek F, Podlaha OG, Strauss H (1999) 87Sr/86Sr, δ13C and δ18O evolution of Phanerozoic seawater. *Chemical Geology* **161**, 59–88

Vera JA, Ruiz-Ortiz PA, García-Hernández M, Molina JM (1988) Paleokarst and related sediments in the Jurassic of Subbetic Zone, Southern Spain. In: Paleokarst, NP James & J Choquette (editors) Springer-Verlag, New York, 364-384.

Verhaert G, Muchez P, Keppens E, Sintubin M (2009) Fluid impact and spatial and temporal evolution of normal faulting in limestones. A case study in the Burdur-Isparta region (SW Turkey). *Geologica Belgica*, **12**, 59–73.

FIGURE CAPTIONS

Figure 1. A) Regional geological map. B) Geological map of the studied area. C) Cross-section located in B.

Figure 2. Sketch of the Juncosa del Montmell outcrop and fault rocks.

Figure 3. Fault breccias and karstic laminated filling the Casetes de Gomila outcrop.

Figure 4. Fault breccias and karstic features of the Baix Penedès Fault at the Castellví outcrop.

Figure 5. Diagenetic sequence from Mesozoic to Present of the Baix Penedès Fault.

Figure 6. (a & b) Host rock and dolomite sediment DS1 affected by irregular fractures and different fillings. (c & d) Crackle to mosaic packbreccia with dolomite cement DC1. Irregular fractures with dolomite sediments DS2 and DS3 and dolomite cement DC2. (e & f) Replacive dolomite RD2 & fracture filled by DS2, DS3, and DC3.

Figure 7. $\delta^{18}O$ and $\delta^{13}C$ plot of host rocks and cements of the Baix Penedès Fault.

Figure 8. $^{87}Sr/^{86}Sr$ of host rocks and cements. Data from Nadal 2001 and Travé et al. (1998) included.

Figure 9. (a & b) Breccia type 2 (cemented mosaic floatbreccias) with reworked fragments of dolomitic sediment DS2 cemented by DS3. Remaining vug porosity filled by hematite cement H1, DC3 and CC1. (c & d) Breccia type 3 with DS4 and calcite cement CC2. (e) Matrix of breccias type 4 with hematite cement H2. (f) Breccia type 5 with calcite cements from CC3 to CC7. (g) Cataclasite of karstic pisoliths cemented by CC10. (h) Laminated cement CS2 and bladed calcite cement CC11 partially filling N-S fractures.

Figure 10. Evolution of fluids from Mesozoic to Present within the Baix Penedès Fault. MF, Montmell Fault; FPT, Frontal Paleogene Thrust; BPF, Baix Penedès Fault.

TABLE CAPTIONS

Table 1. Oxigen and carbon isotopic compositions of the host rock, sediments and cements placed within the Baix Penedès Fault zone. Results of the temperatures calculated from the isotopic data.

Table 2. Strontium isotopic compositions of the host rock, sediments and cements placed within the Baix Penedès Fault zone.

Table 3. Trace element composition of the host rock, sediments and cements placed within the Baix Penedès Fault zone. Results of the elemental ratios calculated for fluids which precipitated dolomite and calcite sediments and cements.

Figure 1

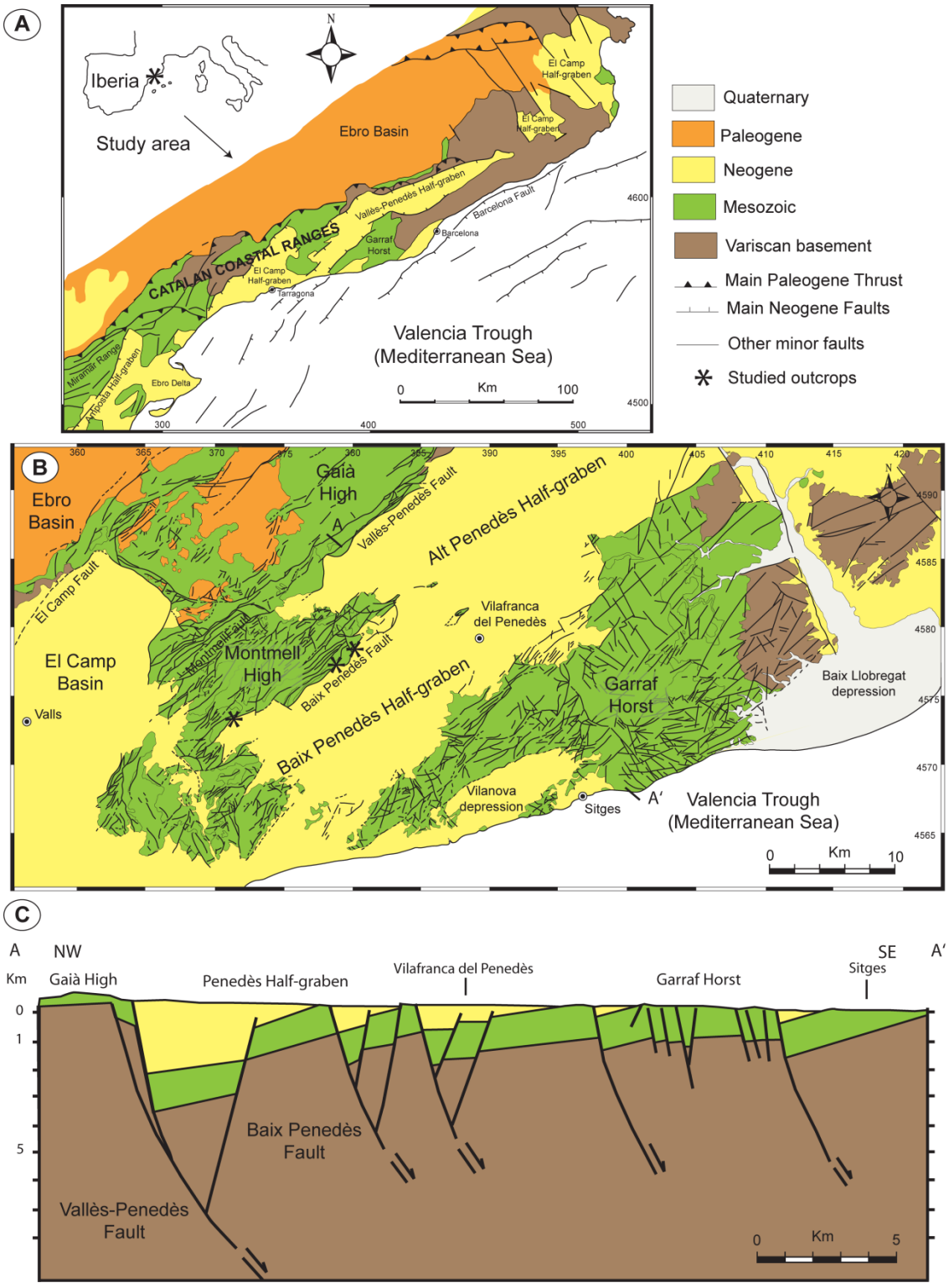
A
Iberia
Study area
N
Ebro Basin
El Camp Half-graben
El Camp Half-graben
Vallès-Penedès Half-graben
Barcelona Fault
CATALAN COASTAL RANGES
Garraf Horst
Barcelona
El Camp Half-graben
Tarragona
Miramar Range
Arnposta Half-graben
Ebro Delta
Valencia Trough
(Mediterranean Sea)
0 Km 100
Quaternary
Paleogene
Neogene
Mesozoic
Variscan basement
Main Paleogene Thrust
Main Neogene Faults
Other minor faults
Studied outcrops
B
Ebro Basin
Gaià High
Vallès-Penedès Fault
Alt Penedès Half-graben
El Camp Fault
Vilafranca del Penedès
Montmell Fault
Montmell High
Baix Penedès Fault
El Camp Basin
Valls
Baix Penedès Half-graben
Garraf Horst
Baix Llobregat depression
Vilanova depression
Sitges
A'
Valencia Trough
(Mediterranean Sea)
0 Km 10
C
A
NW
SE
A'
Km
Gaià High
Penedès Half-graben
Vilafranca del Penedès
Garraf Horst
Sitges
0
1
5
Baix Penedès Fault
Vallès-Penedès Fault
0 Km 5

Figure 2

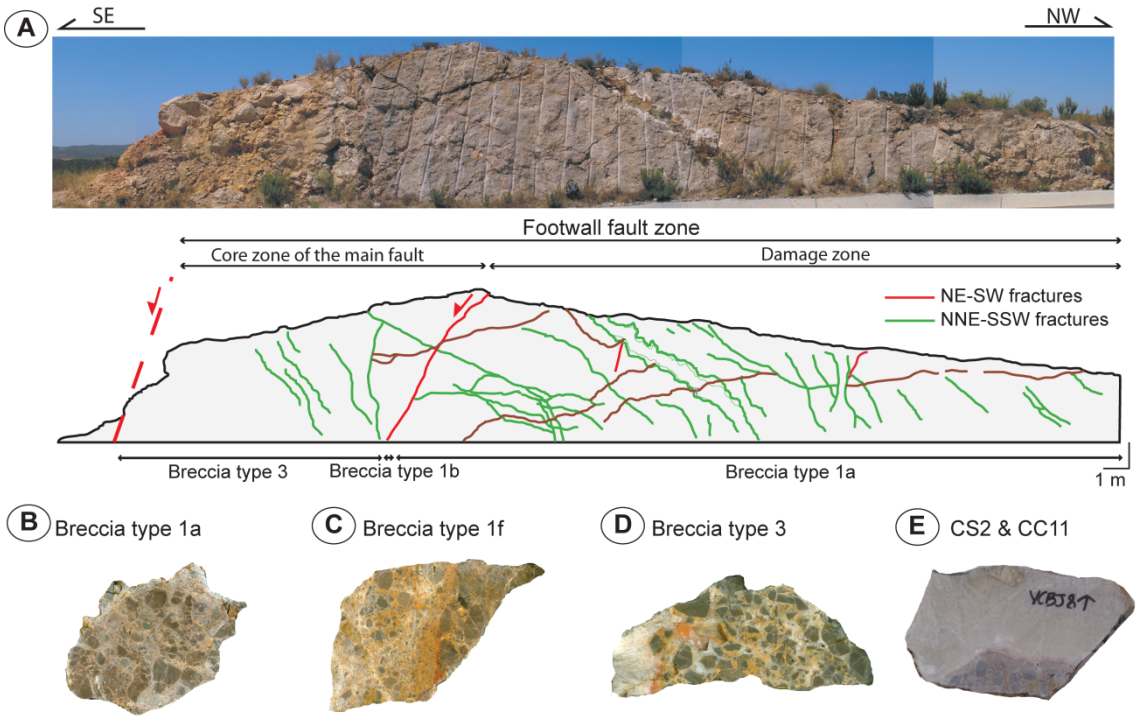
A
SE
NW
Footwall fault zone
Core zone of the main fault
Damage zone
NE-SW fractures
NNE-SSW fractures
Breccia type 3
Breccia type 1b
Breccia type 1a
1 m
B Breccia type 1a
C Breccia type 1f
D Breccia type 3
E CS2 & CC11

Figure 3

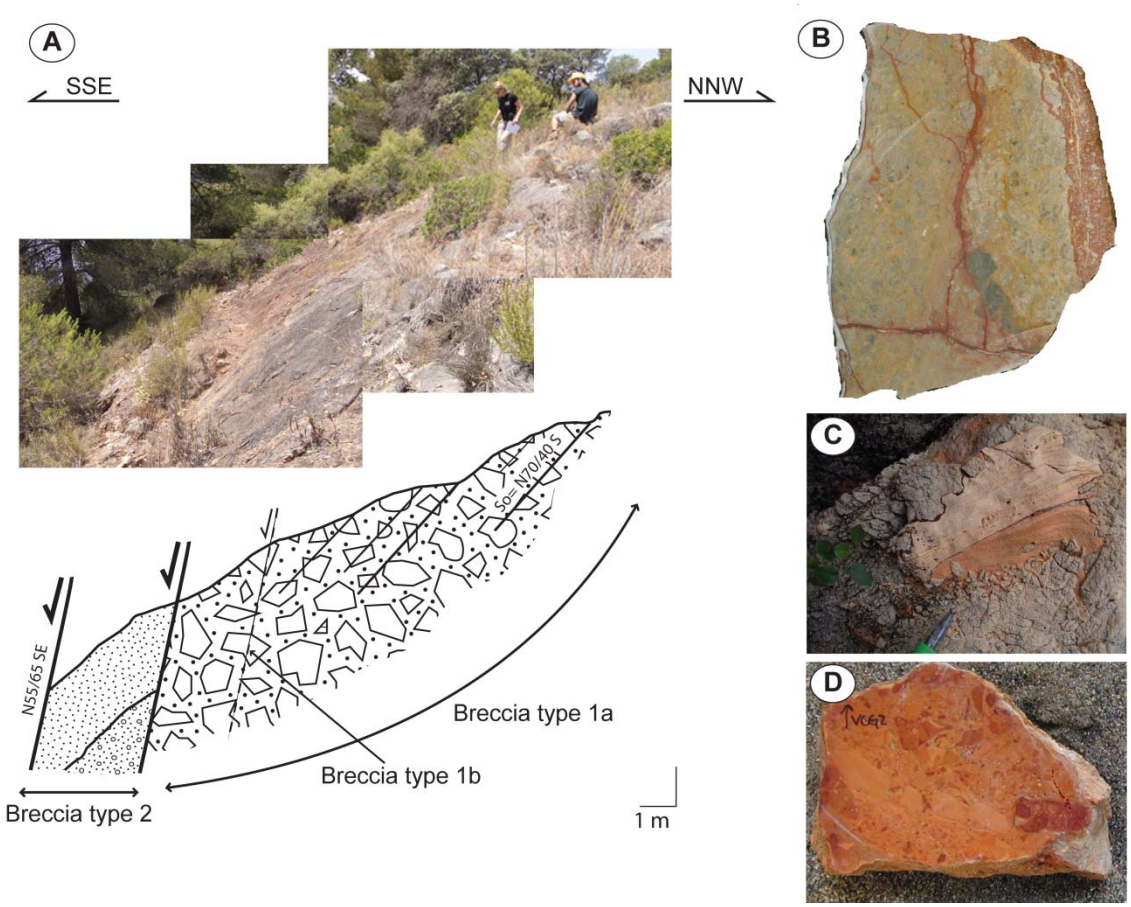
A
SSE
NNW
B
C
D
So= N70/40 S
N55/65 SE
Breccia type 1a
Breccia type 1b
Breccia type 2
1 m

Figure 4

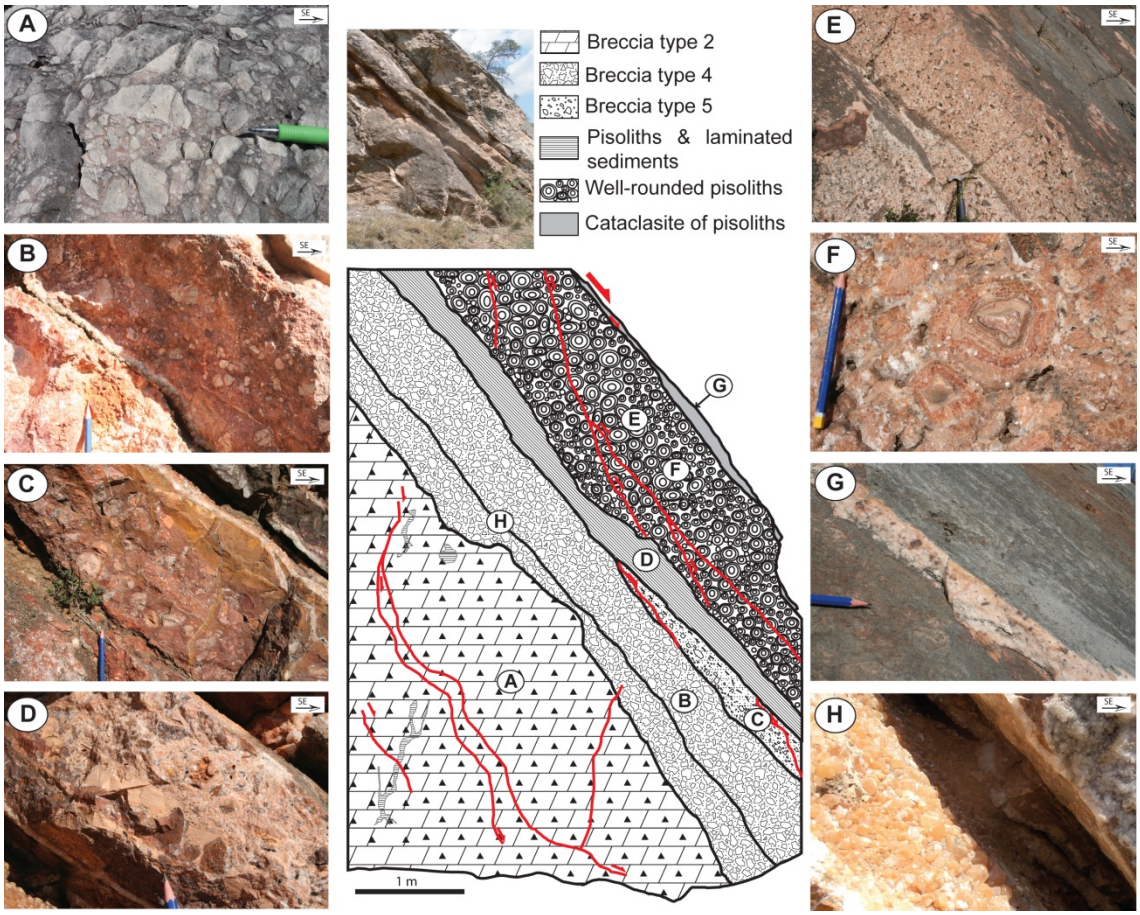
A
B
C
D
E
F
G
H
Breccia type 2
Breccia type 4
Breccia type 5
Pisoliths & laminated sediments
Well-rounded pisoliths
Cataclasite of pisoliths
1 m

Figure 5

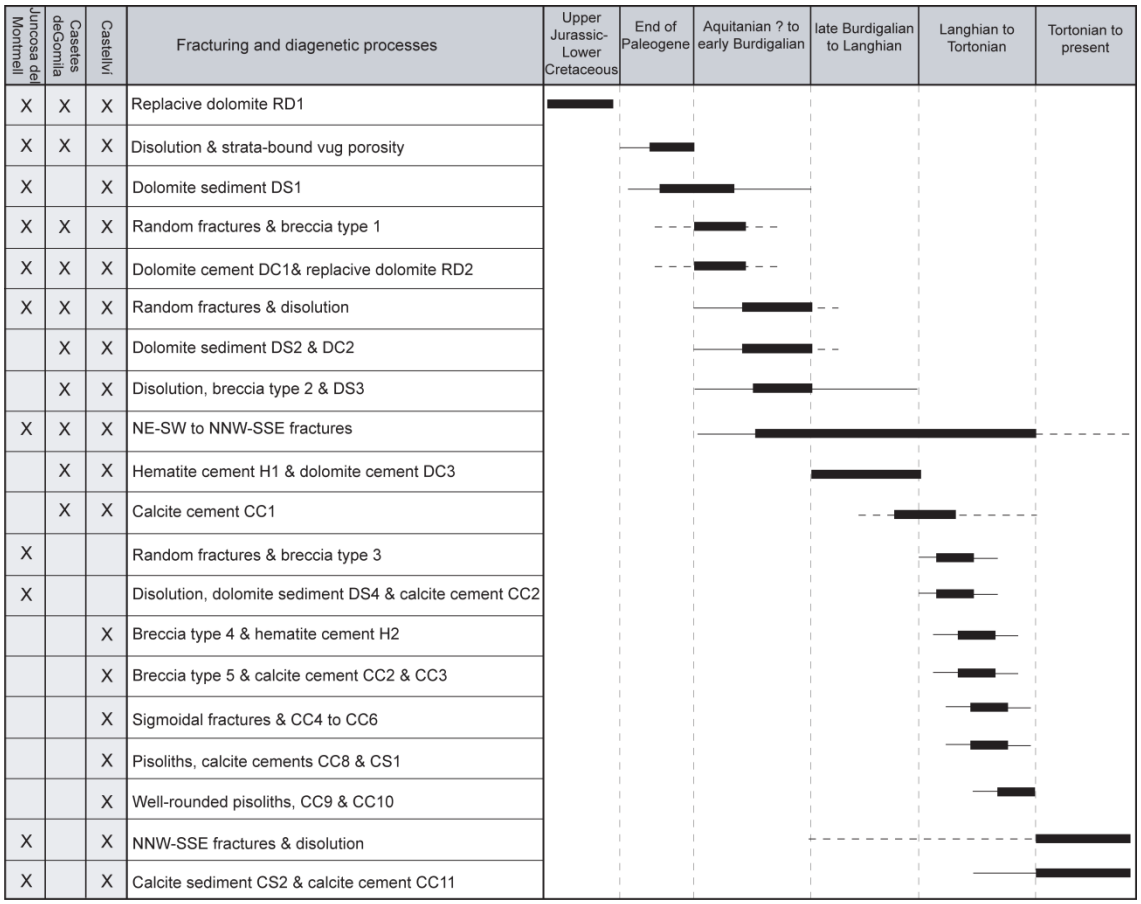

Juncosa del Montmell	Caseles deGomila	Castellví	Fracturing and diagenetic processes
X	X	X	Replacive dolomite RD1
X	X	X	Disolution & strata-bound vug porosity
X		X	Dolomite sediment DS1
X	X	X	Random fractures & breccia type 1
X	X	X	Dolomite cement DC1& replacive dolomite RD2
X	X	X	Random fractures & disolution
	X	X	Dolomite sediment DS2 & DC2
	X	X	Disolution, breccia type 2 & DS3
X	X	X	NE-SW to NNW-SSE fractures
	X	X	Hematite cement H1 & dolomite cement DC3
	X	X	Calcite cement CC1
X			Random fractures & breccia type 3
X			Disolution, dolomite sediment DS4 & calcite cement CC2
		X	Breccia type 4 & hematite cement H2
		X	Breccia type 5 & calcite cement CC2 & CC3
		X	Sigmoidal fractures & CC4 to CC6
		X	Pisoliths, calcite cements CC8 & CS1
		X	Well-rounded pisoliths, CC9 & CC10
X		X	NNW-SSE fractures & disolution
X		X	Calcite sediment CS2 & calcite cement CC11

Figure 6

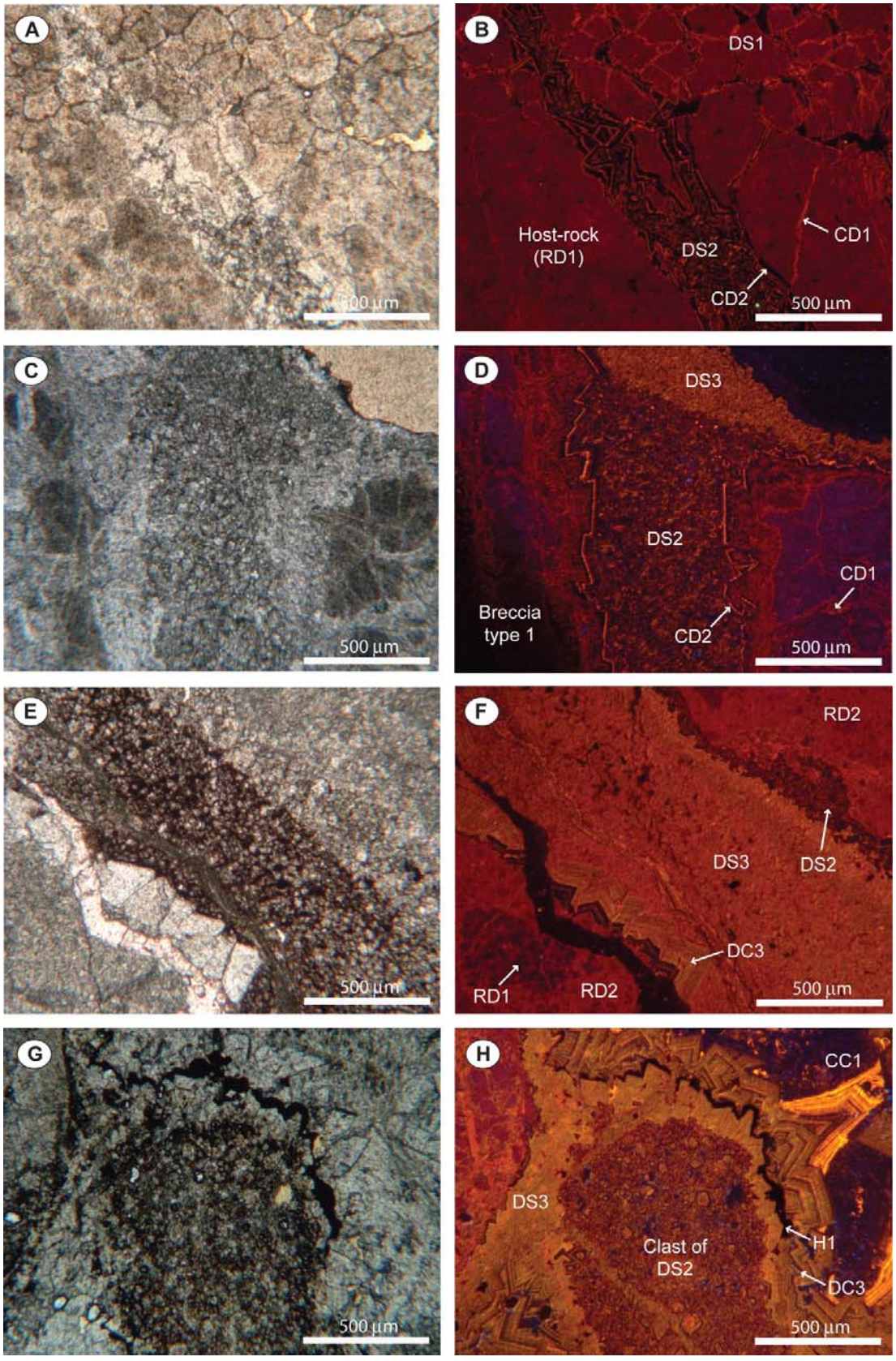
A
500 µm
B
DS1
Host-rock
(RD1)
DS2
CD1
CD2
500 µm
C
500 µm
D
DS3
DS2
CD1
Breccia
type 1
CD2
500 µm
E
500 µm
F
RD2
DS3
DS2
DC3
RD1
RD2
500 µm
G
500 µm
H
CC1
DS3
Clast of
DS2
H1
DC3
500 µm

Figure 7

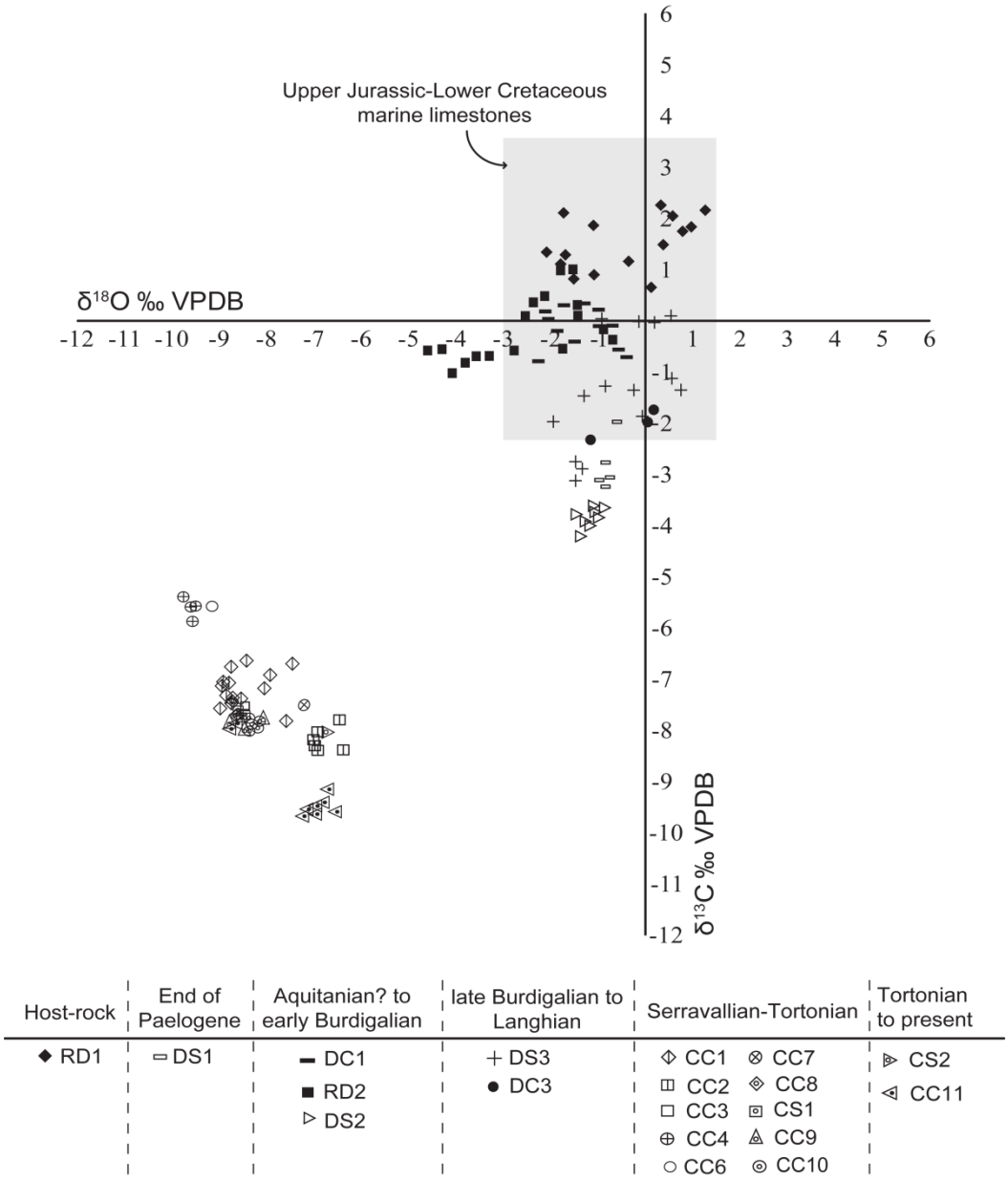
Upper Jurassic-Lower Cretaceous
marine limestones
δ18O ‰ VPDB
δ13C ‰ VPDB
Host-rock
End of Paelogene
Aquitanian? to early Burdigalian
late Burdigalian to Langhian
Serravallian-Tortonian
Tortonian to present
RD1
DS1
DC1
RD2
DS2
DS3
DC3
CC1
CC2
CC3
CC4
CC6
CC7
CC8
CS1
CC9
CC10
CS2
CC11

Figure 8

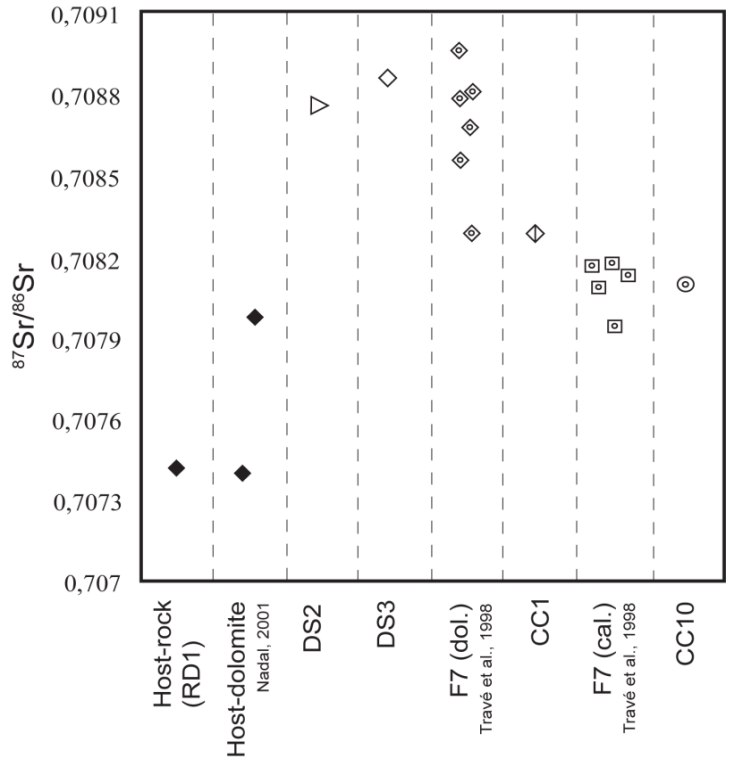
0,7091
0,7088
0,7085
0,7082
0,7079
0,7076
0,7073
0,707
87Sr/86Sr
Host-rock (RD1)
Host-dolomite Nadal, 2001
DS2
DS3
F7 (dol.) Travé et al., 1998
CC1
F7 (cal.) Travé et al., 1998
CC10

Figure 9

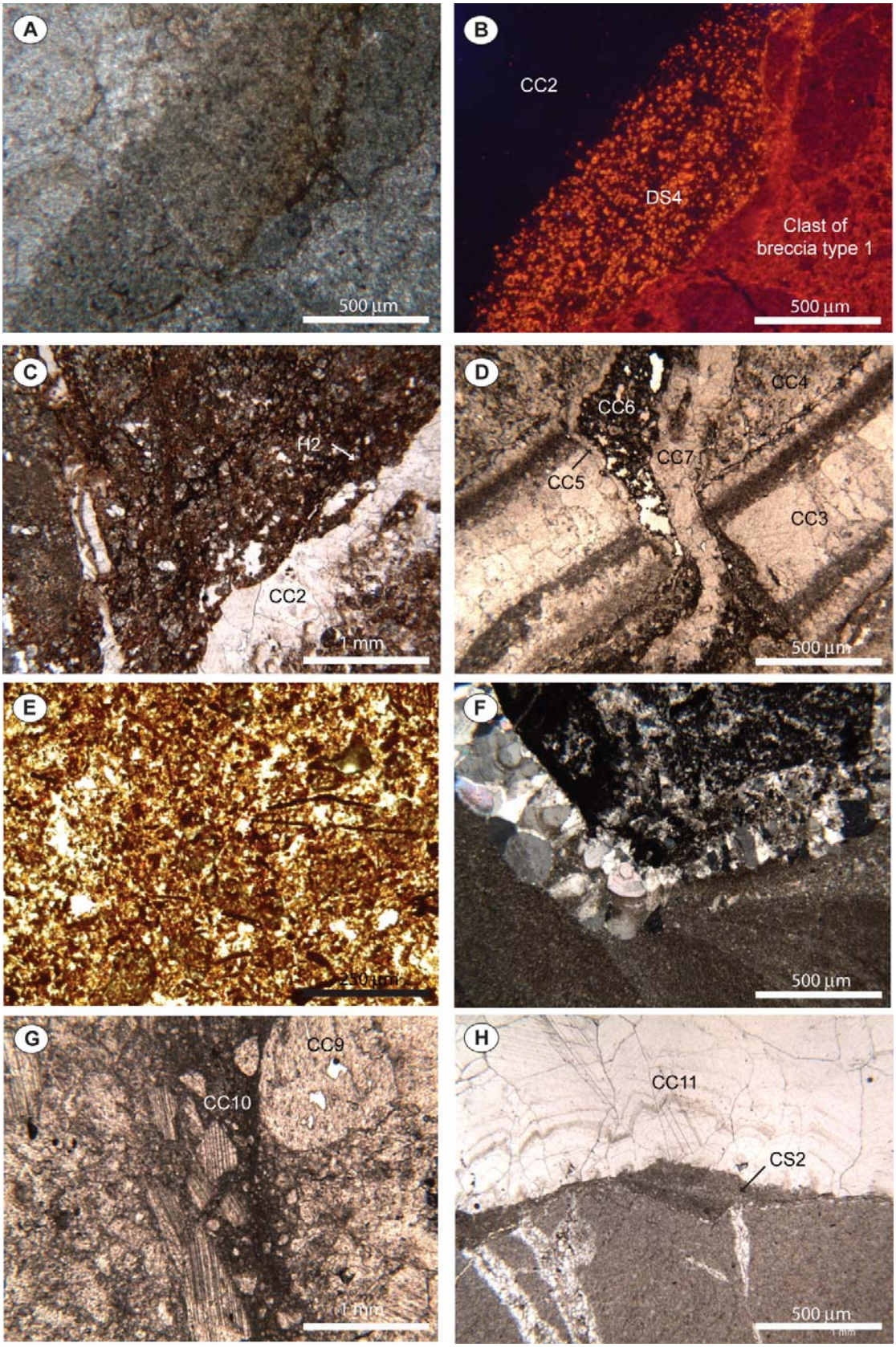
A
500 µm
B
CC2
DS4
Clast of
breccia type 1
500 µm
C
H2
CC2
1 mm
D
CC4
CC6
CC7
CC5
CC3
500 µm
E
250 µm
F
500 µm
G
CC9
CC10
1 mm
H
CC11
CS2
500 µm

Figure 10

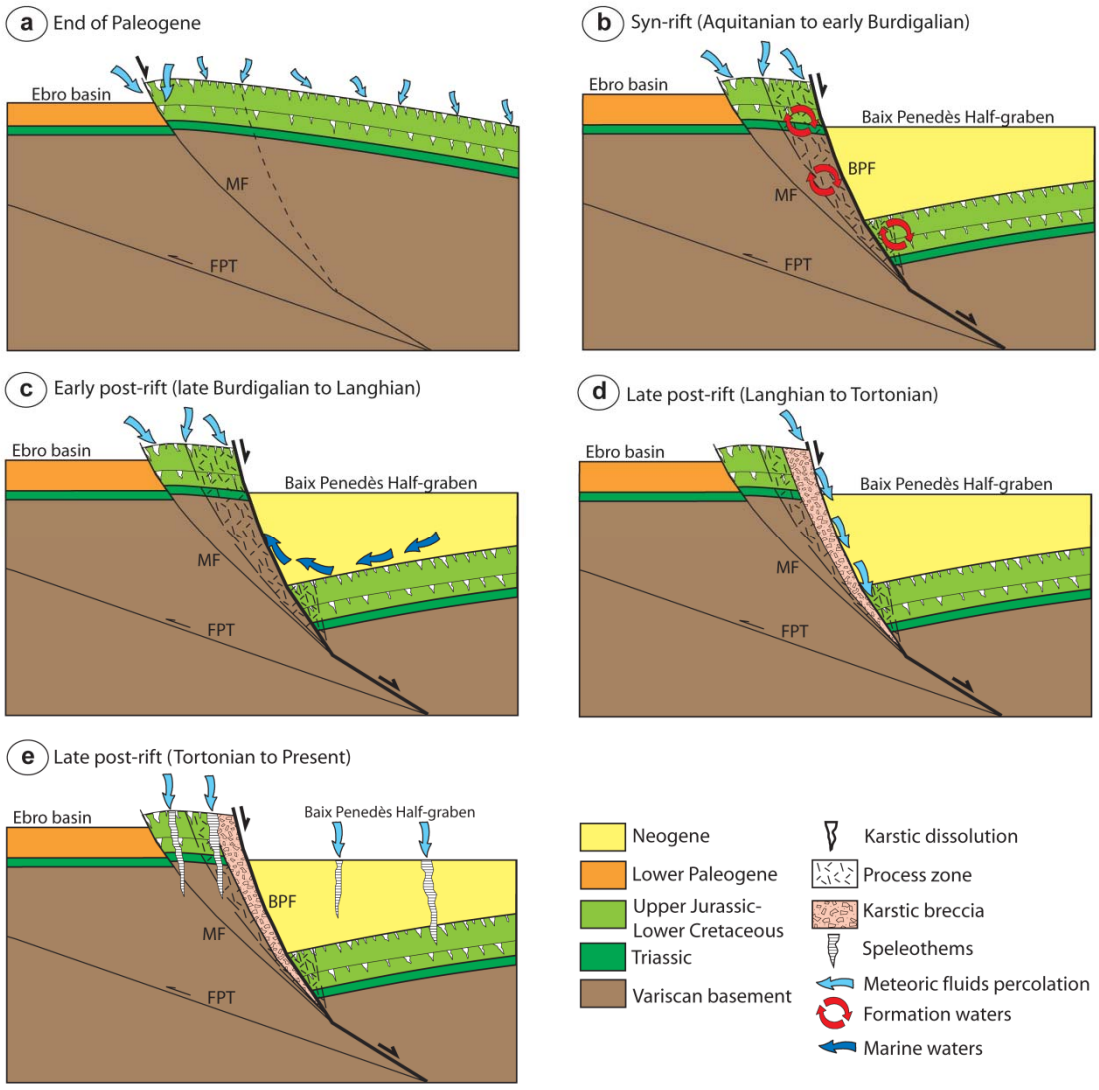
a End of Paleogene
Ebro basin
MF
FPT
b Syn-rift (Aquitanian to early Burdigalian)
Ebro basin
Baix Penedès Half-graben
BPF
MF
FPT
c Early post-rift (late Burdigalian to Langhian)
Ebro basin
Baix Penedès Half-graben
MF
FPT
d Late post-rift (Langhian to Tortonian)
Ebro basin
Baix Penedès Half-graben
MF
FPT
e Late post-rift (Tortonian to Present)
Ebro basin
Baix Penedès Half-graben
BPF
MF
FPT
Neogene
Lower Paleogene
Upper Jurassic-Lower Cretaceous
Triassic
Variscan basement
Karstic dissolution
Process zone
Karstic breccia
Speleothems
Meteoric fluids percolation
Formation waters
Marine waters

Table 1

Filling stage		$\delta^{13}C$ ‰ VPDB	$\delta^{18}O$ ‰ VPDB	$\delta^{18}Ow$ ‰SMOW (Tw=15ºC)	$\delta^{18}Ow$ ‰SMOW (Tw=25ºC)	$\delta^{18}Ow$ ‰SMOW (Tw=40ºC)	$\delta^{18}Ow$ ‰SMOW (Tw=90ºC)
Host-dolomite RD1	Min.	1	-2,1	-4,0	-1,8	1,1	8,2
n = 15	Max.	2,3	1,2	-0,5	1,7	4,5	11,7
	Average	**1,5**	**-0,5**	**-2,3**	**-0,1**	**2,7**	**9,9**
Dolomite sediment DS1	Min.	-3,2	-1,0	-2,8	-0,6	2,2	9,4
n = 5	Max.	-2,0	-0,6	-2,4	-0,3	2,6	9,7
	Average	**-2,8**	**-0,8**	**-2,6**	**-0,5**	**2,4**	**9,5**
Dolomite cement DC1	Min.	-0,8	-2,3	-4,2	-2,0	0,9	8
n = 12	Max.	0,3	-0,4	-2,2	-0,1	2,8	10
	Average	**-0,2**	**-1,4**	**-3,2**	**-1**	**1,8**	**9**
Replacive dolomite RD2	Min.	-1,0	-4,6	-6,6	-4,4	-1,5	6
n = 18	Max.	1,0	-0,7	-2,5	-0,4	2,5	10
	Average	**-0,1**	**-2,5**	**-4,4**	**-2**	**0,7**	**8**
Dolomite sediment DS2	Min.	-4,2	-1,8	-3,7	-1,5	1,4	8,5
n = 11	Max.	-2,9	0,1	-1,7	0,4	3,3	10,5
	Average	**-3,6**	**-1,1**	**-2,9**	**-0,8**	**2,1**	**9,3**
Dolomite sediment DS3	Min.	-3,1	-2,0	-3,9	-1,7	1,2	8,3
n = 14	Max.	0,1	0,7	-1,1	1,1	4,0	11,1
	Average	**-1,4**	**-0,6**	**-2,4**	**-0,2**	**2,6**	**9,8**
Dolomite cement DC3	Min.	-2,3	-1,2	-3,0	-0,9	2,0	9,2
n = 3	Max.	-1,7	0,1	-1,6	0,5	3,4	10,6
	Average	**-2,0**	**-0,4**	**-2,2**	**-0,1**	**2,8**	**10,0**
Calcite cement CC1	Min.	-7,5	-9,0	-9,3	-7,0	-4,0	3,7
n = 10	Max.	-6,7	-7,5	-7,7	-5,5	-2,5	5,3
	Average	**-7,1**	**-8,5**	**-8,8**	**-6,5**	**-3,5**	**4,2**
Calcite cement CC2	Min.	-8,3	-8,5	-8,7	-6,4	-3,5	4,3
n = 8	Max.	-6,6	-6,4	-6,7	-4,4	-1,4	6,3
	Average	**-7,8**	**-7,2**	**-7,4**	**-5,1**	**-2,2**	**5,6**
Calcite cement CC3	Min.	-7,5	-8,8	-9,0	-6,7	-3,8	4,0
n = 2	Max.	-7,4	-8,6	-8,8	-6,6	-3,6	4,2
	Average	**-7,5**	**-8,7**	**-8,9**	**-6,6**	**-3,7**	**4,1**
Calcite cement CC4	Min.	-5,9	-9,8	-10,0	-7,7	-4,7	3,0

Table 1 (continued)

Filling stage		$\delta^{13}C$ ‰ VPDB	$\delta^{18}O$ ‰ VPDB	$\delta^{18}Ow$ ‰SMOW (Tw=15ºC)	$\delta^{18}Ow$ ‰SMOW (Tw=25ºC)	$\delta^{18}Ow$ ‰SMOW (Tw=40ºC)	$\delta^{18}Ow$ ‰SMOW (Tw=90ºC)
n = 4	Max.	-5,4	-9,5	-9,8	-7,5	-4,5	3,3
	Average	**-5,6**	**-9,6**	**-9,9**	**-7,6**	**-4,6**	**3,1**
Calcite cement CC6	Min.						
n = 1	Max.						
	Average	**-5,6**	**-9,2**	**-9,5**	**-7,2**	**-4,2**	**3,6**
Calcite cement CC7	Min.						
n = 1	Max.						
	Average	**-7,5**	**-7,2**	**-7,5**	**-5,2**	**-2,2**	**5,5**
Calcite cement CC8	Min.	-7,7	-8,7	-9,0	-6,7	-3,7	4,0
n = 2	Max.	-7,4	-8,6	-8,9	-6,6	-3,6	4,1
	Average	**-7,5**	**-8,7**	**-8,9**	**-6,6**	**-3,7**	**4,1**
Calcite cement CS1	Min.	-7,8	-8,6	-8,9	-6,6	-3,6	4,1
n = 3	Max.	-7,6	-8,5	-8,8	-6,5	-3,5	4,2
	Average	**-7,7**	**-8,6**	**-8,8**	**-6,5**	**-3,6**	**4,2**
Calcite cement CC9	Min.	-7,9	-8,8	-9,0	-6,7	-3,8	4,0
n = 3	Max.	-7,8	-8,1	-8,3	-6,0	-3,1	4,7
	Average	**-7,8**	**-8,4**	**-8,7**	**-6,4**	**-3,4**	**4,3**
Calcite cement CC10	Min.	-7,9	-8,4	-8,6	-6,3	-3,4	4,4
n = 6	Max.	-7,7	-8,1	-8,4	-6,1	-3,1	4,6
	Average	**-7,8**	**-8,3**	**-8,5**	**-6,2**	**-3,3**	**4,5**
Calcite cement CS2	Min.						
n = 1	Max.						
	Average	**-8,0**	**-6,9**	**-7,1**	**-4,8**	**-1,8**	**5,9**
Calcite cement CC11	Min.	-9,6	-8,8	-9,0	-6,7	-3,8	4,0
n = 11	Max.	-7,8	-6,5	-6,8	-4,5	-1,5	6,2
	Average	**-8,9**	**-7,4**	**-7,7**	**-5,4**	**-2,4**	**5,3**

Table 2

Filling stage	$^{87}Sr/^{86}Sr$
Host-dolomite RD1	0,707417
Dolomite sediment DS2	0,708761
Dolomite sediment DS3	0,708855
Calcite cement CC1	0,708293
Calcite cement CC10	0,708253
Calcite cement CC10	0,708102

Table 3

Filling stage		Mg (ppm)	Ca (ppm)	Na (ppm)	Mn (ppm)	Fe (ppm)	Sr (ppm)	Molar ratio Sr/Ca fluid (a)	Molar ratio Mg/Ca fluid (b)	Molar ratio Mg/Ca fluid (c)	Molar ratio Mg/Ca fluid (d)	Molar ratio Sr/Ca fluid (e)	Molar ratio Sr/Ca fluid (f)	Molar ratio Ca/Fe fluid (g)	Molar ratio Mn/Ca fluid (h)
Host-dolomite RD1	Min.	12,03	21,30	0	0	0	129	0,00763							
n = 88	Max.	13,57	23,68	921	188	2306	1148	0,07425							
	Average	12,80	22,06	243	36	359	727	0,04639							
Dolomite sediment DS1	Min.	11,40	21,27	0	0	0	364	0,02684							
n = 77	Max.	13,32	24,43	1316	375	5908	1228	0,06466							
	Average	12,66	22,12	174	73	1061	729	0,04546							
Dolomite cement DC1	Min.	11,40	21,27	0	0	0	364	0,00573							
n = 49	Max.	13,32	23,89	1316	375	5908	954	0,06836							
	Average	12,68	22,06	169	70	1040	720	0,04264							
Dolomite sediment DS2	Min.	10,60	21,78	0	0	52	177	0,00584							
n = 74	Max.	13,12	24,90	1130	364	6927	1250	0,05316							
	Average	11,71	23,37	297	72	1399	726	0,03166							
Dolomite cement DC2	Min.	10,62	23,68	258	75	218	453	0,01604							
n = 6	Max.	12,00	24,72	476	211	2025	726	0,02595							
	Average	11,36	24,28	396	146	911	574	0,02052							
Dolomite sediment DS3	Min.	10,73	22,35	0	0	76	237	0,00792							
n = 31	Max.	12,35	24,43	484	346	2866	1228	0,06390							
	Average	11,50	23,64	252	73	950	736	0,03016							
Dolomite cement DC3	Min.	10,95	22,52	0	0	16	115	0,004768							
n = 35	Max.	12,19	24,49	611	406	3197	1071	0,039275							
	Average	11,50	23,75	282	112	484	674	0,025944							
Calcite cement CC1	Min.	0,07	39,02	0	0	0	0		0,22712	0,09734	0,02343	0	0	0	0
n = 8	Max.	0,45	40,27	330	210	273	491		1,60043	0,68590	0,16513	0,02083	0,00703	5622	4,79491E-05
	Average	0,28	39,64	142	65	100	222		0,98623	0,42267	0,10176	0,00945	0,00319	2811	1,48245E-05

Table 3 (continued)

Filling stage		Mg (ppm)	Ca (ppm)	Na (ppm)	Mn (ppm)	Fe (ppm)	Sr (ppm)	Molar ratio Sr/Ca fluid (a)	Molar ratio Mg/Ca fluid (b)	Molar ratio Mg/Ca fluid (c)	Molar ratio Mg/Ca fluid (d)	Molar ratio Sr/Ca fluid (e)	Molar ratio Sr/Ca fluid (f)	Molar ratio Ca/Fe fluid (g)	Molar ratio Mn/Ca fluid (h)
Calcite cement CC2	Min.	0,12	39,39	0	0	0	0		0,39780	0,17048	0,04105	0	0	0	0
n = 10	Max.	0,27	40,21	312	35	255	482		0,93569	0,40101	0,09655	0,02074	0,00700	11227	7,98912E-06
	Average	0,18	39,74	100	10	86	203		0,62892	0,26954	0,06489	0,00867	0,00293	5614	2,2091E-06
Calcite cement CC3	Min.	0,13	39,41	0	0	0	0		0,46717	0,20021	0,04820	0	0	0	0
n = 13	Max.	0,56	40,28	262	253	655	519		1,92078	0,82319	0,19819	0,02184	0,00737	9371	0,00006
	Average	0,35	39,73	89	46	153	317		1,21922	0,52252	0,12580	0,01348	0,00455	4685	0,00001
Calcite cement CC4	Min.	0,14	39,27	0	0	45	40		0,50026	0,21440	0,05162	0,00173	0,00058	2436	0
n = 10	Max.	0,45	40,23	272	180	643	668		1,53351	0,65722	0,15823	0,02814	0,00950	175	0,00004
	Average	0,28	39,78	91	61	289	313		0,96284	0,41265	0,09935	0,01332	0,00449	385	0,00001
Calcite cement CC5	Min.	0,07	39,05	13	0	84	49		0,23433	0,10043	0,02418	0,00213	0,00072	1298	0
n = 9	Max.	0,42	40,13	185	164	478	455		1,45286	0,62266	0,14991	0,01921	0,00648	234	0,00004
	Average	0,23	39,64	121	60	238	232		0,81379	0,34877	0,08397	0,00990	0,00334	466	0,00001
Calcite cement CC6	Min.	0,13	38,31	0	0	801	172		0,46618	0,19979	0,04810	0,00761	0,00257	17	0
n = 8	Max.	0,46	40,38	193	214	6564	450		1,57853	0,67651	0,16287	0,01888	0,00637	138	0,00005
	Average	0,29	39,18	100	62	3076	307		1,00618	0,43122	0,10382	0,01328	0,00448	65	0,00001
Calcite cement CC7	Min.	0,04	39,17	0	0	57	59		0,15749	0,06750	0,01625	0,00255	0,00086	208	0
n = 6	Max.	0,15	40,32	327	160	541	619		0,50700	0,21729	0,05231	0,02602	0,00878	1918	0,00004
	Average	0,09	39,90	132	81	223	320		0,30793	0,13197	0,03177	0,01357	0,00458	499	0,00002
Calcite cement CC8	Min.	0,17	39,72	0	0	0	72		0,59045	0,25305	0,06092	0,00307	0,00104	0	0
n = 9	Max.	0,39	40,47	253	139	216	501		1,31784	0,56479	0,13598	0,02098	0,00708	5836	0,00003
	Average	0,26	40,00	78	46	83	320		0,89627	0,38411	0,09248	0,01356	0,00458	2918	0,00001
Calcite sediment CS1	Min.	0,19	39,10	93	0	212	108		0,67280	0,28834	0,06942	0,00468	0,00158	515	0
n = 8	Max.	0,36	40,01	310	128	2885	686		1,24313	0,53277	0,12827	0,02906	0,00981	39	0,00003
	Average	0,28	39,54	174	41	1087	398		0,97950	0,41979	0,10107	0,01707	0,00576	102	0,00001

Table 3 (continued)

Filling stage		Mg (ppm)	Ca (ppm)	Na (ppm)	Mn (ppm)	Fe (ppm)	Sr (ppm)	Molar ratio Sr/Ca fluid (a)	Molar ratio Mg/Ca fluid (b)	Molar ratio Mg/Ca fluid (c)	Molar ratio Mg/Ca fluid (d)	Molar ratio Sr/Ca fluid (e)	Molar ratio Sr/Ca fluid (f)	Molar ratio Ca/Fe fluid (g)	Molar ratio Mn/Ca fluid (h)
Calcite cement CC9	Min.	0,11	38,15	0	0	0	109		0,38671	0,16573	0,03990	0,00484	0,00163	0	0
n = 47	Max.	1,13	40,29	452	297	842	2146		3,84251	1,64679	0,39648	0,09026	0,03046	7900	0,00007
	Average	0,46	39,32	161	69	153	1068		1,59679	0,68434	0,16476	0,04602	0,01553	3950	0,00002
Calcite sediment CS2	Min.	0,31	38,83	0	0	46	1082		1,08379	0,46448	0,11183	0,04690	0,01583	193	0
n = 5	Max.	0,49	39,43	163	0	561	1207		1,72794	0,74054	0,17829	0,05229	0,01765	2374	0
	Average	0,40	39,15	61	0	306	1134		1,40946	0,60406	0,14543	0,04908	0,01656	916	0
Calcite cement CC11	Min.	0,11	38,59	0	0	0	1126		0,38066	0,16314	0,03928	0,04815	0,01625	0	0
n = 19	Max.	0,82	40,23	211	68	1103	1510		2,90118	1,24336	0,29935	0,06631	0,02238	1904	1,5839E-05
	Average	0,39	39,45	83	19	182	1304		1,35186	0,57937	0,13949	0,05606	0,01892	952	4,31801E-06

n, number of analysed spots in the same sample

a: KMg= 0.012 at 25°C (Mucci, 1987)

b: KMg= 0.1163 at 90°C (Katz, 1973)

c: KSr= 0.027 at 25°C (Lorens, 1981)

d: KSr= 0.08 at 100-150°C (kinsman, 1969)

e: KFe= 5 at 25°C (Tucker and Wright, 1990)

Appendix 2: Other relevant publications of the thesis

Publication 4

Baqués, V., Travé, A., Benedicto, A., 2008. Relación entre circulación de fluidos y brechificación tectónica en la cuenca neógena del Penedés (NE Península Ibérica). Geo-Temas 10, 1437-1440.

Relación entre circulación de fluidos y brechificación tectónica en la cuenca extensiva neógena del Penedès (NE Península Ibérica)

Relationship between fluid flow and tectonic brecciation in the extensional neogene Penedès basin (NE Iberian)

V. Baqués[1], A.Travé[1] y A. Benedicto[2]

1 Dpt. Geoquímica, Petrología i Prospecció Geològica. Facultat de Geologia. Universitat de Barcelona. 08028 Barcelona. vbaques@ub.edu, atrave@ub.edu

2 Laboratoire de Tectonique, CNRS/INSU, UMR 7072, Université Paris Sud XI, 91405 Orsay, France. antonio.benedicto-esteban@u-psud.fr

Resumen: El presente trabajo describe los procesos de brechificación tectónica que tienen lugar en la falla mayor del semi-graben del Vallès-Penedès durante la extensión neógena y su relación con los fluidos que intervienen durante la deformación. Se centra en un afloramiento de la falla mayor situado en el sector más occidental del margen NW de la cuenca, donde la falla afecta materiales dolomíticos del Jurásico superior-Cretácico inferior, correspondientes al bloque inferior. Mediante datos petrológicos y geoquímicos se han reconocido cuatro tipos de brechas, dos famílias de fracturas y cuatro generaciones de cementos relacionados con la extensión. Según las diferentes generaciones de cementos, su cronología y su disposición dentro de las fracturas y brechas, se determinan los mecanismos de deformación y la circulación de fluidos dentro de la zona de falla durante su actividad, asi como el comportamiento drenante o barrera de la falla a lo largo de su evolución.

Palabras clave: roca de falla, falla drenante-barrera, brecha tectónica, extensión.

Abstract: *This paper describes the tectonic brecciation processes that took place in the largest fault of the Vallès-Penedès semi-graben during the neogene extension and its relationship with the fluids involved during deformation. It focuses on an outcrop of the main fault in the westernmost NW margin of the basin. In this area the fault affects dolomitic materials of Upper Jurassic-Lower Cretaceous from the footwall block. Petrological and geochemical data allow us to distinguish four types of breccias, two families of fractures and four cement generations related with the extension. According to the different generations of cements, their chronology and their position within fractures and breccias, we have determined the mechanisms of deformation and the fluid flow within the fault zone during its activity, as well as the behaviour of draining or barrier fault behaviour along its evolution.*

Key words: *fault rock, draining-barrier fault behaviour, tectonic brecciation, extension.*

INTRODUCCIÓN Y OBJETIVO

El objetivo del presente trabajo es el estudio de la interacción entre deformación y fluidos a lo largo de la falla mayor de la cuenca, en este caso, la falla extensiva del Vallès-Penedès, situada en el margen NW de la cuenca del Penedès (Fig. 1). Los resultados que aquí se presentan describen los procesos de brechificación tectónica que se observan en la zona de falla afectando a los materiales dolomíticos del Jurásico Superior-Cretácico Inferior correspondientes al bloque inferior y la circulación de fluidos por la misma zona de falla.

DESCRIPCIÓN DE LA ZONA ESTUDIADA

La cuenca del Vallès-Penedès se localiza en las Cadenas Costero Catalanas. Durante la fase compresiva alpina comprendida entre el Eoceno y el Oligoceno inferior, las fallas de dirección NE-SW y ENE-WSW actuaron como fallas direccionales sinistras con trasnpresión local. Posteriormente, durante la extensión Oligocena superior-Miocena inferior, estas fallas fueron reactivadas como fallas normales originando un sistema de horsts y grabens situados al margen NW del Surco de Valencia (Roca *et al*., 1999). El límite NW de la cuenca del Penedès está limitado por la falla Vallès-Penedès, que tiene un salto de 3000 m y una orientación ENE-WSW a NE-SW. El límite SE está formado por diversas fallas de salto hectométrico que la separan de los horsts de Garraf y de Collserola-Montnegre (Bartrina *et al*., 1992).

FIGURA 1. *Localización del área de estudio en su contexto tectónico regional.*

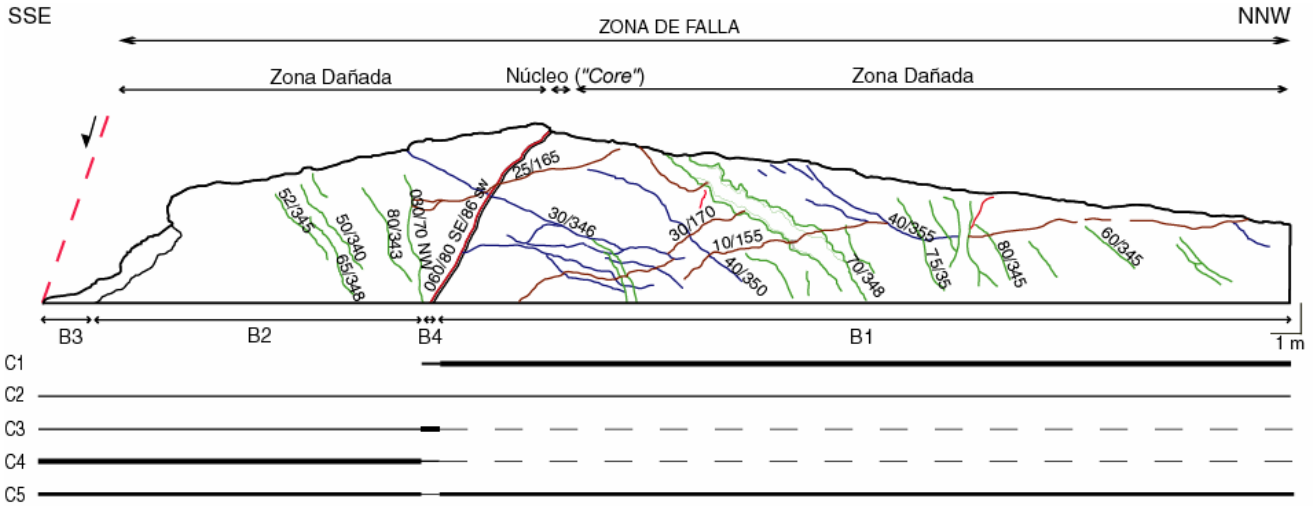

FIGURA 2. *Esquema estructural del afloramiento situado en la carretera de La Bisbal del Penedès a la Juncosa del Montmell. Fracturas 1 en azul, fracturas 2 rojo, fracturas 3 verde y fracturas 4 marrón. En la parte inferior del corte se señalan los distintos tipos de brechas tectónicas (B) y sus cementos asociados (C).*

Se ha seleccionado el afloramiento situado en el sector más occidental del margen NW, en el km. 4 de la carretera TV-2401 que va de la Bisbal del Penedès a la Juncosa del Montmell (Fig. 1). Se trata de una sección transversal a la falla del Vallès-Penedès, que consiste en 275 metros de dolomías Jurásicas altamente fracturadas correspondientes al bloque inferior de la falla. En discordancia sobre estas dolomías es disponen los complejos continentales superiores del Serravaliense superior-Tortoniense (Agustí *et al*., 1991). A pesar de que la zona de fracturación es muy ancha, se ha localizado el estudio en la zona más frontal, justo en el contacto con los sedimentos miocenos.

A nivel de afloramiento se diferencian cinco grupos de fracturas (Fig. 2):

Fracturas 0: fracturas con direcciones aleatorias que afectan a la roca encajante.

Fracturas 1 (color azul en Fig. 2): fracturas de dirección 30-40/340 presentes solo en el sector centro-meridional del afloramiento.

Fracturas 2 (color rojo en Fig. 2): planos de deslizamiento (falla) de dirección N60/80 SE, concordantes con la dirección de la falla mayor. Estos planos tienen estrías verticales que indican movimiento normal.

Fracturas 3 (color verde en Fig. 2): fracturas de dirección N30/70-80 NW que se encuentran abiertas y tapizadas por cementos de calcita con textura en empalizada de grosor hasta 30 cm.

Fracturas 4 (color marrón en Fig. 2): fracturas de dirección 30/165 presentes a lo largo de todo el afloramiento. Se encuentran abiertas cortando a las estructuras anteriores.

PETROLOGÍA Y GEOQUÍMICA

Protolito: se trata de una dolomicirta y doloesparita de color gris con un grado de fracturación elevado. Se dispone en estratos de 30 cm a 1,5 metros de potencia de dirección N40 y buzamiento 10º NW, dando lugar a zonas topográficamente elevadas. Esta dolomicrita está compuesta por cristales de dolomita de morfología anédrica, de tamaño inferior a 10 µm, a subédrica, de tamaño entre 50 y 100 µm. La luminiscencia de los cristales es muy baja, de color morado (Fig. 2A y 2B). Isotópicamente presenta valores entre $\delta^{18}O$ = -0,4 a +1,2 ‰ PDB y $\delta^{13}C$ = +0,7 a +2,2 ‰ PDB. Dicha dolomicirta corresponde a la Fm. Dolomías Superiores del Garraf del Titónico-Berriasiense (Salas, 1987). Se trata de dolomías de reemplazamiento de mudstones y grainstones oolíticos (Nadal, 2001).

Rocas de falla: aplicando los criterios texturales de la clasificación de Sibson (1977), se han diferenciado cuatro tipos de rocas de falla (Fig. 2):

B1- Brecha de falla no cohesiva. Esta roca se caracteriza por tener una fábrica isótropa y tener más de un 30 % de fragmentos visibles respecto a la masa total de la roca. Sus clastos son dolomíticos y angulosos, de tamaño entre 0,5 y 4 cm. Los cristales de dolomita son anédricos a subédricos de tamaño entre 10 y 100 µm y tienen luminiscencia morada. Este tipo de brecha forma parte de la zona dañada por la falla y es la más abundante a lo largo de los 275 m de roca Jurásica fracturada.

B2- Brecha de falla cohesiva. Esta roca se caracteriza por tener una fábrica isótropa y dominar la reducción del tamaño de los clastos debido a la tectónica sobre la recristalización. Tiene un 90 % de fragmentos visibles respecto a la masa total de la roca. Sus clastos son dolomíticos y angulosos, de tamaño entre 0,5 y 4 cm. El 90 % de los clastos están formados por cristales

de dolomita de morfología anédrica a subédrica de tamaño entre 10 y 100 µm y luminiscencia morada. El 10 % restante están formados por cristales subédricos a euédricos entre 100 y 200 µm de luminiscencia naranja brillante. También corresponde a la zona dañada, con una extensión de 10 m de ancho. Está situada en una zona más proximal a la falla mayor. A diferencia de B1 el sellado de calcita está muy desarrollado en estas brechas.

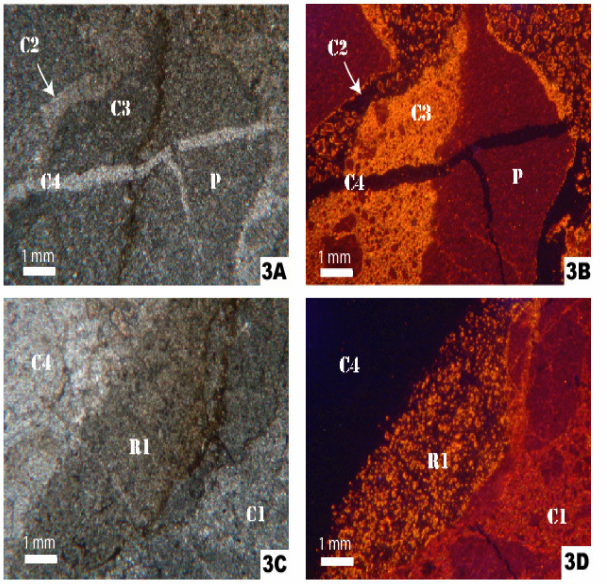

FIGURA 3. *Características petrológicas del protolito y cementos que se disponen entre los clastos de las brechas y fracturas. A-Fotografía de microscopio óptico con el protolito en forma de clasto y tres generaciones de cemento. B-Fotografía de microscopio de catodoluminiscencia con el protolito en forma de clasto y tres generaciones de cemento. C- Fotografía de microscopio óptico con el protolito y el cemento C1 en forma de clasto, el relleno R1 y el cemento C4. D- Fotografía de microscopio de catodoluminescencia con el protolito y el cemento C1 en forma de clasto, el relleno R1 y el cemento C4. Barra de 1 mm.*

B3- Protocataclasita. Esta roca se caracteriza por tener una fábrica isótropa, ser cohesiva y dominar la reducción del tamaño de los cristales debido a la tectónica sobre la recristalización. Tiene un 80 % de fragmentos visibles respecto a la masa total de la roca. Sus clastos son dolomíticos y subangulosos, de tamaño entre 0,1 y 2 cm. El 60 % de los clastos están formados por cristales de dolomita de morfología anédrica a subédrica de tamaño entre 10 y 100 µm y luminiscencia morada. El 40 % restante están formados por cristales subédricos a euédricos entre 100 y 200 µm de luminiscencia naranja brillante. Contiene una matriz rojiza clástica formada por microclastos dolomíticos y arcilla sellada por cemento calcítico micrítico. Esta brecha forma parte de la zona dañada por la falla con una extensión de 2 m de ancho y está situada en la zona más próxima a la falla mayor.

B4- Cataclasita. Esta roca se caracteriza por tener una fábrica isótropa, ser cohesiva y dominar la reducción del tamaño de los clastos debido a la tectónica sobre la recristalización. Tiene un 40 % fragmentos visibles respecto a la masa total de la roca. Sus clastos son dolomíticos y subangulosos, de tamaño inferior a 0,5 cm. El 90 % de los clastos están formados por cristales de dolomita de morfología anédrica a subédrica de tamaño entre 10 y 100 µm y luminiscencia morada. El 10 % restante están formados por cristales subédricos a euédricos entre 100 y 200 µm de luminescencias naranja brillante y roja. Contiene una matriz clástica compuesta por los clastos de las brechas B1 y B2 de color marrón. Esta brecha forma parte de la zona de máxima fracturación, en el núcleo ("*Core*") de la falla y tiene una extensión de 0,30 m de ancho.

Asociados a estas rocas de falla se han observado 5 tipos de cementos:

C1- Cemento dolomítico formado por cristales de morfología anédrica con un tamaño inferior a 10 µm los cuales presentan continuidad óptica con los cristales de la dolomita del protolito. La luminiscencia de los cristales es rojo oscuro. Isotópicamente presenta valores entre $\delta^{18}O$ = -2,3 a -1,3 ‰ PDB y $\delta^{13}C$ = -0,8 a +0,3 ‰ PDB Se dispone entre los clastos de B1 y no se asocia a ninguna de las fracturas reconocidas en el afloramiento (Fig. 2, 3C y 3D).

C2- Cemento dolomítico en disposición rim de luminiscencia naranja brillante a amarillo brillante. Cristales euédricos y zonados de tamaño 10-20 µm. Está asociado a las fracturas 1 que afectan a las brechas B1 y también se reconoce envolviendo los clastos de las brechas B2, B3 y B4 (Fig. 2, 3A y 3B).

C3- Cemento dolomítico tipo blocky de luminiscencia naranja brillante a amarillo brillante. Cristales subédricos de 10 a 100 µm. Isotópicamente presenta valores de $\delta^{18}O$ = +0,1 ‰ PDB y $\delta^{13}C$ = -2,9 ‰ PDB. Se asocia a las fracturas 1 y 2, muy desarrollado en las segundas (núcleo de la falla). Básicamente lo encontramos cementando a B4, aunque también se desarrolla en B1, B2 y B3 (Fig. 2, 3C y 3D).

C4- Cemento calcítico tipo blocky no luminiscente. Cristales euédricos de tamaño 10 µm a 200 µm. Isotópicamente presenta valores entre $\delta^{18}O$ = -7 a -6,4 ‰ PDB y $\delta^{13}C$ = -8,3 a -7,8 ‰ PDB. Se asocia a las fracturas 1, 3 y en menor proporción a las fracturas 2. Lo encontramos a lo largo de todo el afloramiento, cementando a B1, B2, B3 y B4 (Fig. 2 y 3).

C5- Cemento calcítico en disposición rim no luminiscente. Cristales euédricos de tamaño >200 µm. Isotópicamente presenta valores entre $\delta^{18}O$ = -7,2 a -6,2 ‰ PDB y $\delta^{13}C$ = -9,6 a -9,1 ‰ PDB. Se dispone tapizando las paredes de las fracturas 3 localizadas a lo largo de todo el afloramiento, llegando a desarrollar grosores superiores a los 30 cm con textura en empalizada (Fig. 2).

Aparte de los cementos se han reconocido dos tipos de relleno cárstico:

R1- Relleno calcítico de color rosado y laminado. La laminación se debe al crecimiento en bandas de cristales de tamaño 10-50 µm y cristales de tamaño 50-100 µm. Presenta valores de $\delta^{18}O$ = -5,8 ‰ PDB y $\delta^{13}C$ = -5,7 ‰ PDB. Este cemento puede englobar cristales dolomíticos idiotópicos de tamaño de 50 µm y de luminiscencia naranja brillante. El origen de estos cristales es la disgregación del cemento C3 por la fricción generada a partir del movimiento de la falla. Los cristales de dolomita también pueden encontrarse estratificados debido al depósito por gravedad (Fig. 3C y 3D).

R2- Relleno dolomítico con cuarzo y arcilla de color amarillo. Presenta valores de $\delta^{18}O$ entre -1 y -0,8 ‰ PDB y de $\delta^{13}C$ entre -3,4 y -3,1 ‰ PDB. Se encuentra a lo largo de todo el afloramiento aunque su máximo desarrollo se produce en las brechas B2.

DISCUSIÓN Y CONCLUSIONES

Atendiendo a las relaciones espaciales entre fracturas y cementos a nivel macro y microscópico, y basándonos en las relaciones "cross-cutting", se ha establecido la cronología entre las fracturas y cementos (Fig. 4):

1- Generación de las fracturas 0 dando lugar a las brechas B1 y precipitación de C1.

2- Generación fracturas 1 dando lugar a las brechas B2, B3 y precipitación del cemento C2.

3- Generación fracturas 2 (falla) dando lugar a B4 y precipitación del cemento C3.

4- Generación fracturas 3 afectando a las brechas anteriores y precipitación de C4.

5- Karstificación intensa facilitada por los planos de debilidad creados por las fracturas 3 y tapizado de sus paredes por el espeleotema C5 y los rellenos R1 y R2.

6- Generación fracturas 4. No se han observado brechas asociadas.

La brechificación isótropa y dilatante que da lugar a las brechas tipo B1 puede corresponder a una fracturación volumétrica, difusa, precediendo a la creación del plano de falla mayor. Isotópicamente el protólito fracturado y el cemento C1 presentan valores similares, implicando que C1 precipitó a partir de un fluido que estaba en equilibrio químico con la roca de caja e indica un sistema hidrológicamente cerrado. Esta alta interacción entre el fluido y la roca perduró, aunque en menor medida, hasta la precipitación del cemento C3. Posteriormente circuló un fluido meteórico (sistema hidrológico abierto) que dió lugar a C4. Durante este evento, los planos de deslizamiento principales actuaron como barrera, de manera que C4 está casi ausente en el

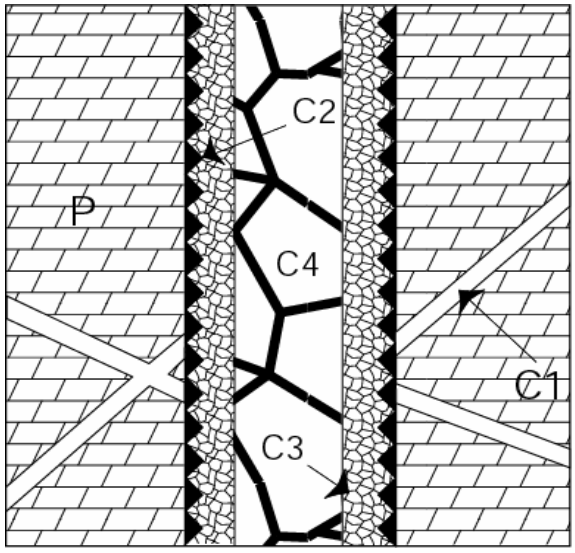

FIGURA 4. *Distribución, geometría y cronología de los cementos descritos.*

núcleo de la falla y es muy abundante entre fracturas y clastos de la zona dañada. Posteriormente y después de una disolución kárstica, precipitó C5 dentro de las fracturas 3 y se depositaron los rellenos R1 y R2.

AGRADECIMIENTOS

Esta investigación esta financiada por el proyecto DGICYT CGL2006-04860, la beca BES-2007-14935 y el *Grup Consolidat de Recerca* "Geologia Sedimentària" (2005SGR-00890).

REFERENCIAS

Agustí, J., Cabrera, L., Calvet, F., Macpherson, J., De Porta, J., Ramos-Guerrero, E. (1991): Registro sedimentario mioceno en las zonas emergidas del sector central de margen catalán. *I Congreso del Grupo Español del Terciario*, 7-10.

Bartrina, M.T., Cabrera, L., Jurado, M.J., Guimerà, J., Roca, E. (1992): Evolution of the central Catalan margin of the Valencia trough (western Mediterranean). *Tectonophysics,* 203: 219-247.

Nadal, J. (2001): *Estudi de la dolomitització del Juràssic superior-Cretaci inferior de la Cadena Ibèrica oriental i la Cadena Costera Catalana: relació amb la segona etapa de rift mesozoica*. Tesis Doctoral, Univ. de Barcelona, 416 p.

Roca, E., Sans, M., Cabrera, L., Marzo, M. (1999): Oligocene to Middle Miocene evolution of the central Catalan margin (northwestern Mediterranean). *Tectonophysics*, 315: 209-233.

Salas, R. (1987): *El Malm i el Cretaci inferior entre el Massís del Garraf i la Serra d'Espadà.* Tesis Doctoral Univ. de Barcelona, 345 p.

Sibson, R.H. (1977): Fault rocks and fault mechanisms. *Journal of the Geological Society of London*, 133: 191-231.

Publication 5

Travé, A., **Baqués, V.**, Benedicto, A., Cantarero, I., Romaire, I., Belaid, S., 2008. Interacciones entre deformación y geofluidos en contexto de tectónica extensiva. Geo-Temas, 10, 1421-1424.

Interacciones entre deformación y geofluidos en contexto de tectónica extensiva

Deformation and geofluid interactions in an extensional tectonic setting

A. Travé[1], V. Baqués[1], A. Benedicto[2], I. Cantarero[1], I. Romaire[2] y S. Belaid[2]

1 Dpt. Geoquímica, Petrologia i Prospecció Geològica. Facultat de Geologia. Universitat de Barcelona. 08028 Barcelona. atrave@ub.edu, vbaques@ub.edu, i_cantarero@ub.edu

2 Université Paris Sud XI, Laboratoire de Tectonique, CNRS/INSU, UMR 7072, 91405 Orsay, France. antonio.benedicto-esteban@u-psud.fr, indiana_romaire@yahoo.fr, belaidsonia@hotmail.com

Resumen: Tomando como ejemplo la cuenca extensiva del Vallès-Penedès, en el NE de la Península Ibérica, se está llevando a cabo el estudio de distintas zonas de falla afectando a materiales distintos (dolomías, calcáreas y sedimentos siliciclásticos) y de edades distintas (Triásico, Jurásico, Cretácico, Mioceno). Los distintos tipos de roca de falla permiten conocer los mecanismos de deformación y la relación con los geofluidos. La cronología entre las distintas fracturas y sus rellenos, principalmente por calcita, permite conocer la evolución de los fluidos durante la deformación. La falla mayor, que limita la cuenca en su borde noroeste, presenta gran variedad de brechas y abundante interacción entre las rocas de falla y procesos cársticos. El borde sureste de la cuenca, caracterizado por fallas de menor tamaño, permite establecer la distribución de las distintas estructuras y rocas de falla en función de la posición dentro de la falla.

Palabras clave: Extensión neógena, geofluidos, deformación.

Abstract: *Taking as example the Vallès-Penedès extensive basin, in the NE of the Iberian Peninsula, a general study of the different fault zones affecting different materials (dolomites, limestones and siliciclastic sediments) and different ages (Triassic, Jurassic, Cretaceous, Miocene) is developing. The different types of fault rocks record the different deformation mechanisms and its relationships with geofluids. The chronology between the different fractures and their infillings, mainly calcite, record the evolution of the fluids during the deformation. The major fault, in the north-western border of the basin, shows a great variability of breccias and a great interaction between the fault rocks and karstic processes. The south-eastern border of the basin, represented by minor faults, shows the distribution of the different structures and different fault rocks as a function of its position within the fault.*

Key words: *Neogene extension, geofluids, deformation.*

INTRODUCCIÓN

En las cuencas sedimentarias, la deformación y los procesos de fracturación influyen en la distribución de los episodios diagenéticos y, por lo tanto, el estudio sobre la relación entre tectónica y la migración de los geofluidos en una cuenca permiten conocer su evolución geodinámica. La migración de los fluidos comporta a menudo alteraciones y cementaciones de los sedimentos y rocas y, por tanto, la formación de nuevos minerales.

La interacción entre fracturación (deformación) y geofluidos depende del contexto tectónico. En concreto, en contextos de tectónica extensiva el incremento de la presión de fluidos puede causar la fracturación de las rocas desde la superfície hasta niveles profundos de la corteza. Esta presión de fluidos controla el comportamiento hidromecánico de las fracturas, lo cual está directamente relacionado con los ciclos sísmicos y los terremotos (Sibson, 2000). De esta forma, la deformación puede estar repartida entre episodios de ruptura co-sísmica y episodios de deformación lenta inter-sísmica. Durante los episodios lentos, la fracturación puede estar asociada a otros mecanismos de deformación en los cuales los fluidos juegan un papel fundamental, en particular la fluencia por disolución bajo esfuerzos (Gratier *et al*., 1999; Labaume *et al*., 2004).

En las cuencas extensivas la circulación de fluidos tiene lugar durante la tectónica (circulación sin-cinemática) o después (post-cinemática). En el primer caso, los fluidos intervienen tanto en la ruptura co-sísmica (presión de fluidos), como en la deformación en las zonas de falla (cambios reológicos y cementación de las rocas de falla y fracturas) o en la diagénesis de los sedimentos sin-tectónicos cercanos a las zonas de falla. Según los mecanismos de deformación y cementación de rocas de falla y de fracturas, las fallas adquieren un carácter barrera o conducto para la circulación post-cinemática de fluidos en la cuenca. Así, el estudio de las zonas de falla, según sus dimensiones, posición estructural, unidades estratigráficas afectadas (litologías afectadas), profundidad, salto, entre otros, es indispensable para establecer un modelo de circulación sin y post-cinemático a la escala de la cuenca.

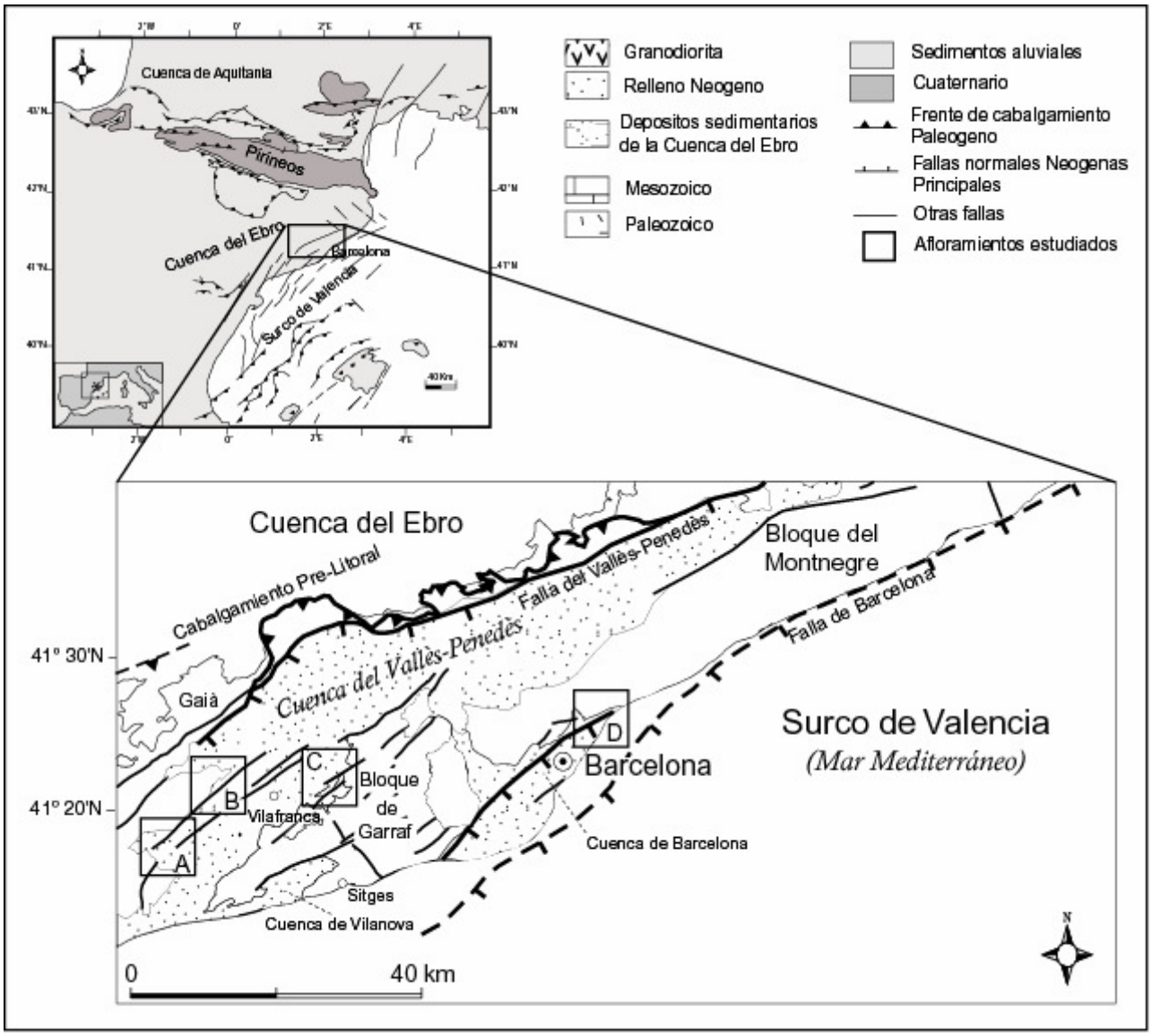

FIGURA 1. *Situación de las cuencas del Vallès-Penedès y del Llano de Barcelona-Badalona-Montgat. Los recuadros representan los afloramientos estudiados, que se presentan de forma separada en los postres realizados por Baqués et al. (A), Belaid et al. (B), Romaire et al. (C), Cantarero et al. (D) a este volumen.*

El estudio de la fracturación y de las rocas de falla en las zonas de falla, así como de sus cementos, permite establecer: la cronología de los diferentes episodios de deformación, el papel de los fluidos en la deformación, las condiciones de la deformación (profundidad, temperatura, presión), las características y el origen de los fluidos (meteóricos, marinos, crustales), los caminos de migración y, en fin, el papel de las fallas en la migración secundaria de fluidos (circulación post-cinemática).

El estudio de los cementos, permite conocer si los fluidos tienen un origen interno o externo a la propia cuenca, si el sistema hidrológico es abierto o cerrado, si el flujo de fluido es rápido o lento, y como todos estos parámetros cambian tanto en el tiempo como en el espacio.

LA CUENCA DEL VALLÈS-PENEDÈS Y EL LLANO DE BARCELONA

El estudio de la relación entre migración de los geofluidos y fracturación se está llevando a cabo en las cuencas extensivas del Vallès-Penedès y del Llano de Barcelona-Badalona-Montgat (Cadenas Costero Catalanas). Ambas cuencas, que forman parte del dominio Catalano-Balear del surco de Valencia, tienen una orientación NE-SW y están limitadas por fallas normales (Fig. 1).

Durante la fase compresiva alpina del Paleógeno, las fallas de dirección NE-SW y ENE-WSW actuaron como fallas direccionales sinistras con transpresión local. Posteriormente, durante la extensión Neógena, fueron reactivadas como fallas normales originando el sistema de horsts y grabens situados en el margen NW del Surco de Valencia (Guimerà, 1988 y Roca *et al*., 1999).

Al NW, la falla que limita la depresión del Vallès-Penedès tiene un salto de 3000 m y una orientación ENE-WSW a NE-SW. Al SE, diversas fallas de salto hectométrico limitan el semigraben del Vallès-Penedès con los horsts de Garraf y de Collserola-Montnegre (Bartrina *et al*., 1992).

RESULTADOS

En el campo se han identificado distintos afloramientos de las zonas de fallas, tanto del borde noroeste, como del borde sureste, y también algunas afectando el relleno mioceno. Se está estableciendo la jerarquía entre las fallas de diferente importancia y la arquitectura de los sistemas de fallas a escala mesoscópica. Se establecen las relaciones temporales y espaciales entre las distintas estructuras de deformación y se realiza un muestreo detallado. Cuando el afloramiento lo permite, y en especial en el borde sur, se realiza la medida de todos los parámetros en cada uno de los segmentos de las fracturas (longitud, desplazamiento, separación en las zonas de relevo, etc.) con el fin de establecer el estado de conexión de los segmentos y su carácter transmisivo con respecto a los fluidos. En el borde norte, la calidad de los afloramientos donde se observan cortes horizontales y paralelos a lo largo de las fallas permite analizar la evolución longitudinal de la deformación (por ejemplo la brechificación y la cementación) y en consecuencia la variación de la transmisividad longitudinal de la falla desde su centro (máximo desplazamiento, máxima deformación) hacia sus extremidades (mínimo desplazamiento, mínima deformación).

En el laboratorio, se realiza el estudio microstructural a escala microscópica (microscopio óptico y de catodoluminiscencia), lo que permite en cada caso reconocer los indicadores cinemáticos y establecer los mecanismos de deformación así como la cronología de la historia diagenética. Se caracteriza cada uno de los cementos y, en función de sus características petrológicas y geoquímicas, se reconoce el origen de los fluidos responsables de la precipitación de cada uno de ellos.

En este mismo congreso presentamos, a modo de pósters, los resultados parciales de la relación entre brechificación y fracturación (A, en Fig. 1; Baqués *et al*.,), la relación entre procesos pedogenéticos y fracturación (D, en Fig. 1; Cantarero *et al*., este volumen), la relación entre procesos cársticos y fracturación (B, en Fig. 1 y Fig. 2; Belaid *et al*.,), los procesos que tienen lugar en las fallas menores del borde sur (C, en Fig. 1 y Fig. 3; Romaire *et al*.,) y, a modo complementario, los resultados obtenidos en el estudio de la fracturación extensiva en el campo de Amposta (Playà *et al*.).

DISCUSION Y CONCLUSIONES

Los resultados obtenidos hasta el momento muestran un comportamiento reológico diferente de los distintos materiales incluso a nivel de una misma litología. Así, por ejemplo, en el borde sureste de la cuenca, las zonas de falla afectando a las calizas miocenas apenas muestran estructuras de deformación ni indicios de fluidos si se las compara con las calcáreas cretácicas en fallas de igual magnitud.

FIGURA 2. *Corte a lo largo de la falla del Vallès-Penedès donde se observa la relación entre los procesos de Karstificación y la fracturación. Situación B en figura 1.*

FIGURA 3. *Corte a lo largo de una de las fallas menores del borde SE de la cuenca del Vallès-Penedès. Situación C en figura 1.*

Las calizas cretácicas, además muestran un comportamiento reológico totalmente distinto durante la extensión neógena y durante la compresión alpina. De manera que la roca de falla es totalmente distinta para cada tipo de fracturas. Así mismo, los fluidos que circularon a través de las fracturas durante la extensión neógena tenían un origen más superficial y lo hicieron en un sistema más abierto que durante la compresión alpina, interactuando menos con la roca encajante.

En el borde noroeste, la falla mayor que limita la cuenca muestra una zona de deformación mucho más importante y caracterizada por distintas rocas de falla, entre las que cabe destacar distintas generaciones de brechas. En todos los casos analizados hasta el momento el tipo de fluido que ha circulado por las fracturas extensivas neógenas es agua de origen

meteórico. Se ha observado además una estrecha relación entre el movimiento de la falla normal y los procesos de carstificación, con un desarrollo muy importante de espeleotemas y rellenos cársticos que fueron progresivamente incorporados a la zona de falla y afectados por ella.

En los estudios realizados en el sector del Llano de Barcelona-Badalona-Montgat, las rocas de falla de las fracturas extensivas afectando a materiales siliciclásticos miocenos están fuertemente obliteradas por procesos pedogenéticos entre los que cabe destacar el *Microcodium*. Este *Microcodium* está a su vez afectado por fracturas de escala milimétrica formadas posiblemente durante los últimos estadios de la extensión.

La abundancia de los procesos ligados a la diagénesis meteórica de superficie, tanto carstificación como procesos pedogenéticos, nos indican posiciones muy superficiales de las zonas de falla estudiadas.

AGRADECIMIENTOS

Esta investigación esta financiada por el proyecto DGICYT CGL2006-04860, las becas BES-2007-14935 y 2008FI_A 00846 y el *Grup Consolidat de Recerca* "Geologia Sedimentària" (2005SGR-00890)

REFERENCIAS

Bartrina, M.T., Cabrera, L., Jurado, M.J., Guimerà, J., Roca, E. (1992): Evolution of the central Catalan margin of the Valencia trough (western Mediterranean). *Tectonophysics,* 203: 219-247.

Gratier J.P., Renard F. y Labaume P. (1999): How pressure solution and fracturing processes interact in the upper crust to make it behave in both a brittle and viscous manner. *Journal of Structural Geology*, 21: 1189-1197.

Guimerà, J. (1988): *Estudi estrucutal de l'enllaç entre la Serralada Ibèrica i la Serralada Costera Catalana*. Tesi Doctoral, Univ. de Barcelona, 600 p.

Labaume, P., Carrio-Schaffhauser, E., Gamond J.F. y Renard. F. (2004): Deformation mechanisms and fluid-driven mass transfers in the recent fault zones of the Corinth rift (Greece), *Comptes Rendus Géoscience*, 336: 375-383.

Roca, E., Sans, M., Cabrera, L., Marzo, M. (1999): Oligocene to Middle Miocene evolution of the central Catalan margin (northwestern Mediterranean). *Tectonophysics,* 315: 209-233.

Sibson, R.H. (2000): Fluid involvement in normal faulting. *Journal of geodynamics*, 29: 469-499.

Publication 6

Belaid, S., **Baqués, V.**, Travé, A., Benedicto, A., Plagnes, V., 2008. El carst de la falla del Vallés-Penedés (NE de España). Geo-Temas, 10, 429-432.

El carst de la falla del Vallés-Penedés (NE de España)

The karst of the Vallés-Penedés fault (NE Spain)

S. Belaid[1], V. Baqués[2], A. Travé[2], A. Benedicto[1] y V. Plagnes[3]

1 Laboratoire de Tectonique, CNRS/INSU UMR 7072. Université Paris Sud 11. 91405 Orsay, Francia. Antonio.benedicto-esteban@u-psud.fr
2 Dpto. Geoquímica, Petrología y Estratigrafía, Facultad de Geología, Universitat Central de Barcelona, 08016 Barcelona, España.
3 Laboratoire Sisyphe, CNRS/INSU UMR 7619. Université Paris VI, 75252 Paris, Francia.

Resumen: En la cuenca neógena extensiva del Vallés-Penedés, numerosas fallas muestran figuras de disolución (cavidades) y relleno de tipo cárstico (sedimento, espelotemas). Estas figuras coexisten con rocas de falla (brechas y cataclasitas) y fracturas bien cementadas (calcita) en la zona de falla. El objetivo de este trabajo es el estudio de las relaciones entre el sistema cárstico como medio de aporte de fluidos meteóricos y la deformación y cementación en una zona de falla afectando rocas carbonatadas. El trabajo aquí presentado se centra en un afloramiento de la falla del Vallés-Penedés, limite occidental del semi-graben del Vallés- Penedés, situado en Castellvi de la marca. En este resumen se presentan los resultados preliminares del estudio estructural de la zona de falla.

Palabras clave: Vallés-penedés, extensión, falla, carst, brecha.

Abstract: *In the extensional neogen Vallés-Penedés basin numerous faults exhibit dissolution and filling patterns of karstic type. These features coexist with well calcite-sealed fault rocks and fault-related fractures in fault zones. The aim of this work is to study the relationships between faults and karstic systems. This work focuses on one outcrop of the Vallés-Penedés fault (Castellvi de la marca). In this abstract, we present the preliminary results of the structural study of the fault zone.*

Key words: *Vallés-penedés, extension, fault, karst, breccia.*

INTRODUCCION Y OBJETIVO

Este estudio se enmarca dentro del proyecto "Interacciones entre deformación y geofluidos en contexto de tectónica extensiva" presentado de forma general en este mismo congreso (Travé *et al*., este volumen. Ver también Baqués *et al*. y Romaire *et al*. en este mismo volumen). Dicho proyecto aborda, entre otros, el estudio de las relaciones entre fracturación y circulación de fluidos, a distintas escalas, en la cuenca neógena del Penedés (Barcelona) (Fig. 1).

Nos focalizamos en el estudio de las relaciones entre las fallas de la cuenca y los sistemas cársticos desarrollados en la serie carbonatada del basamento mesozoico de la cuenca. Varios afloramientos a lo largo de la falla principal, que constituye el borde occidental de la cuenca del Penedés, muestran el desarrollo de modelado y relleno de tipo cárstico en la zona de falla. En este resumen presentamos los resultados preliminares del estudio estructural en curso de un afloramiento de la falla del Vallés-Penedés, localizado en Castellvi de la Marca (Fig. 1). Presentamos el conjunto de resultados de los análisis en curso: análisis petrológicos y geoquímicos de los cementos de las brechas tectónicas y de relleno cárstico, así como de las fracturas en la zona de falla.

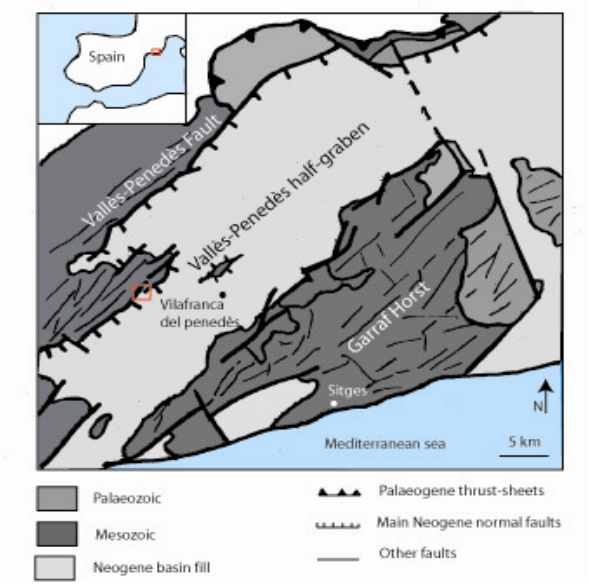

FIGURA 1. *Localización del área de estudio en su contexto tectónico regional.*

CONTEXTO GEOLOGICO

La depresión del Vallès-Penedès, de orientación NE-SW, se localiza en las Sierras Costeras Catalanas (Fig. 1) y tiene su origen ligado a la obertura del surco de Valencia (Roca *et al*., 1999). Rellena de depósitos continentales y marinos miocénicos, la cuenca se instala

sobre un basamento calizo y dolomítico mesozoico estructurado y exhumado durante la compresión alpina (Paleoceno-Eoceno).

Durante la fase compresiva, las fallas de dirección NE-SW y ENE-WSW actuaron como fallas direccionales siniestras e inversas provocando la surrección de las Sierras Costeras Catalanas. Posteriormente, durante la extensión neógena, fueron reactivadas como fallas normales creando el colapso parcial de estas sierras (fosa del Vallés-Penedés). Durante estas fases tectónicas, así como durante la regresión marina mesiniense del Mediterráneo, diferentes episodios cársticos pudieron desarrollarse sobre el basamento calizo controlados por las zonas de facturación.

ANALISIS ESTRUCTURAL DE LA ZONA DE FALLA

En Castellvi de la Marca, el plano de la falla del Vallés-Penedés, de dirección N040-60, aflora a lo largo de una centena de metros y pueden estudiarse varias secciones transversales. La falla pone en contacto un protolito dolomítico jurásico (bloque inferior) y un relleno sedimentario margoso marino miocénico (bloque superior).

El protolito

Se trata de una dolomicrita de color gris con un grado de fracturación elevado. Se dispone en estratos de 0,30 cm a 1,5 metros de potencia ligeramente basculados hacia el oeste. Mineralógicamente esta compuesta por cristales de dolomita de morfología anédrica, de tamaño inferior a 10 µm, a subédrica, de tamaño entre 50 y 100 µm (ver Baqués *et al*., este volumen). Este protolito aparece localmente carstificado.

La zona de falla

En la sección más espectacular (Fig. 2), la zona de falla está constituida, desde el bloque inferior hacia el plano, por:

- Una protocataclasita cohesiva (brecha tectónica) de aspecto masivo, de clastos monogénicos de la dolomía encajante de talla centimétrica (zona A en la Fig. 2). Esta brecha está afectada ella misma por dos sistemas de fracturas secundarias rellenas por varias generaciones de calcita. Las primeras orientadas según la dirección de la falla mayor y las segundas, minoritarias, orientadas ortogonalmente. Estas últimas están cortadas por las primeras indicando su anterioridad (probablemente relacionadas con la compresión alpina). Algunas de las fracturas paralelas à la falla mayor presentan un juego cizallante normal coherente con la extensión miocena. Dicha brecha aparece también afectada por micro-cavidades y conductos de tipo cárstico rellenos de sedimento fino bien cementado y laminado horizontalmente (Fig. 2)

- Una zona de aproximadamente un metro y medio constituida por 4 bandas paralelas (B-E) de espesor decimétrico y sub-paralelas al plano de falla mayor.

La banda B (Fig. 2) esta formada por lo que parece una brecha tectónica cataclástica. Los clastos son angulosos, polygénicos, de talla milimétrica a centimétrica, envueltos en una matriz rojiza. Los clastos presentan marcas de impresión (presión-disolución).

Las bandas C a E (Fig. 2) están constituidas por depósitos de tipo relleno cárstico con granoclasificación desde la base de cada banda hacia su techo. Se trata de brechas sedimentarias de elementos angulosos, de hasta varios centímetros de talla, que pasan progresivamente a de depósitos terrígenos de grano fino, laminados y bien cementados. Los clastos son poligénicos y la mayor parte de ellos están envueltos por concreciones de calcita de cristales automorfos típicas de espeleotemas cársticos. La banda D (Fig. 2) es literalmente un suelo estalagmítico y detrítico de granos redondeados con laminación oblicua.

La banda E (Fig. 2) esta constituida de una espectacular brecha de relleno cárstico con elementos subangulosos, de tamaño centimétrico, envueltos y soldados por varias generaciones de espelotemas y cavidades de tipo geódico.

Excepto la banda B, ninguna otra presenta indicios de deformación mayores. Solo se observan algunas fracturas y fallas normales secundarias discretas de fuerte buzamiento, algunas de ellas rotadas hasta una posición inversa, y fracturas aparentemente tardías de bajo ángulo (Fig. 2). Ambas de dirección coherente con la extensión neógena.

- Por último, una ultracataclasita de 5 a 10 cm de grosor que tapiza el plano de falla, compuesta de algunos granos muy finos, poligénicos, flotando en un cemento calcitico dominante (Fig. 2).

DISCUSION Y CONCLUSIONES

Los resultados preliminares de este estudio muestran la presencia de cuatro tipos de brechas en la zona de falla. La primera es un brecha tectónica de tipo cataclástico (zona A), monogénica, cuyo origen puede relacionarse con la fricción en la zona de falla durante su actividad. La segunda, bandas C a E, es una brecha de relleno cárstico asociada a depósitos de sedimento fino laminado y espeleotemas. La tercera, banda B, es seguramente un deposito de relleno cárstico ligeramente deformado en la zona de falla lo que le da un aspecto de cataclasita (brecha tectónica). La cuarta, F, es una ultracataclasita (brecha tectónica) desarrollada en el plano de falla y a partir de los depósitos de relleno cárstico de las bandas subyacentes.

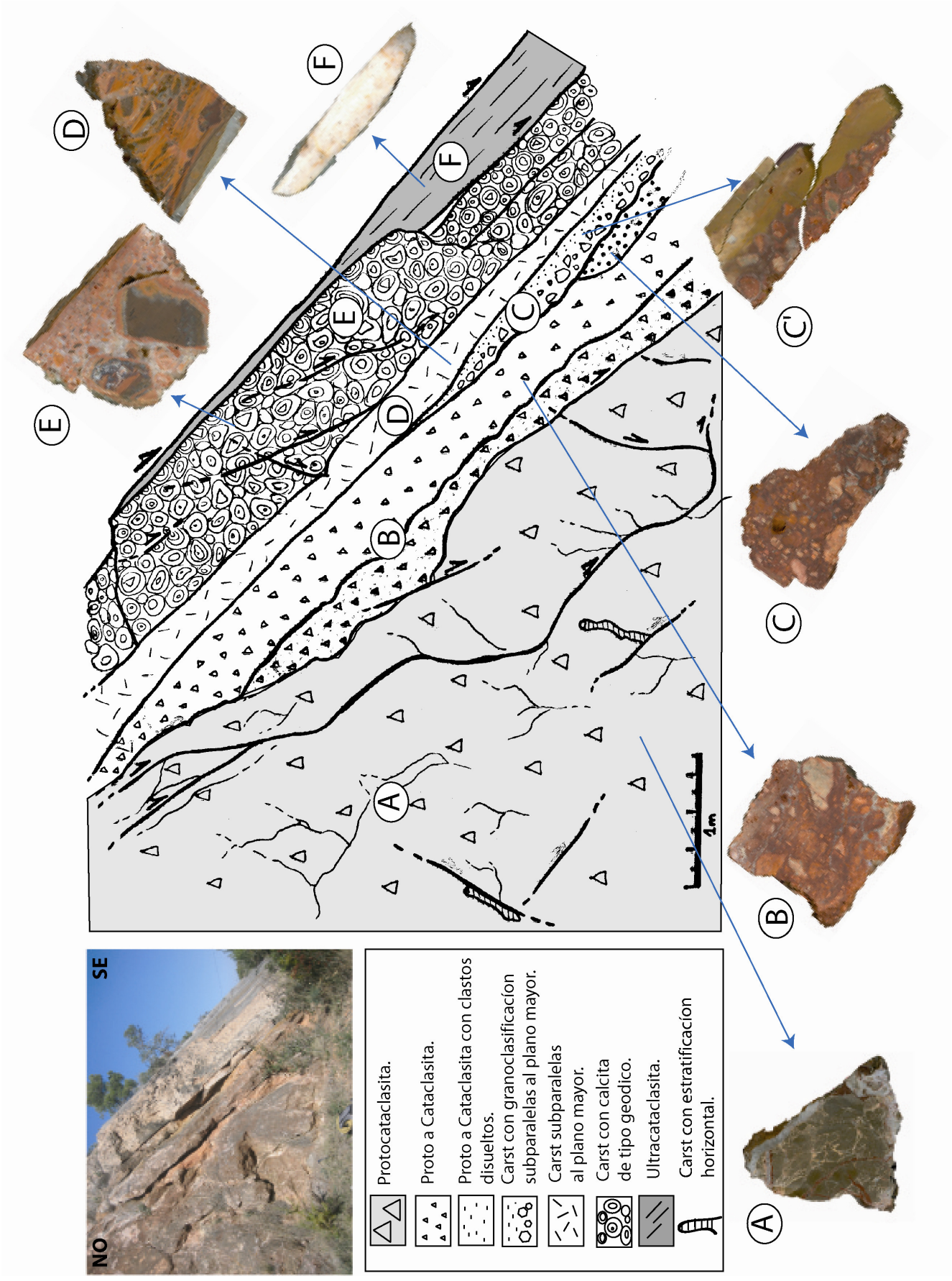

FIGURA 2. *Esquema estructural de la zona de falla de la falla del Vallés-Penedés en Castellvi de la Marca (ver localización en Fig. 1).*

La disposición de la granoclasificación en las bandas de depósitos de relleno cárstico indica la sedimentación de estos materiales horizontalmente, luego anteriormente a su basculamiento en la zona de falla. Así este carst (formación de conductos cársticos y cavidades por disolución) se desarrolló y se rellenó (brechas y sedimentos laminados) con anterioridad a la extensión de la cuenca; probablemente durante la compresión alpina durante el paleoceno.

Al contrario, las cavidades y conductos de tipo cárstico que afectan la brecha tectónica (zona A, Fig. 2) están rellenas de sedimento laminado con disposición horizontal y sin ninguna deformación aparente. Lo que parece indicar la posterioridad de esta carstificación y relleno con respecto a la brechificación tectónica, es decir posterior a la actividad de la falla, carstificación post-tectónica. Esta carstificación post-tectónica puede ser la responsable de la disolución de los clastos de roca encajante y de la formación de cavidades vacías como se observa a lo largo de la zona de falla.

Los análisis petrológico y geoquímico en curso de los diferentes cementos de calcita tanto de las brechas tectónicas como de los espeleotemas y de las fracturas y fallas secundarias nos permitirán un análisis más completo de las relaciones espaciales y temporales entre carstificación y tectónica en este margen fallado de la cuenca.

AGRADECIMIENTOS

Esta investigación esta financiada por el proyecto DGICYT CGL2006-04860, la beca BES-2007-14935 y el *Grup Consolidat de Recerca* "Geologia Sedimentària" (2005SGR-00890) de la Universitat de Barcelona.

REFERENCIAS

Roca, E., Sans, M., Cabrera, L. y Marzo, M. (1999): Oligocene to Middle Miocene evolution of the central Catalan margin (northwestern Mediterranean). *Tectonophysics*, 315: 209-233.

Publication 7

Romaire, I., Benedicto, A., Travé, A., **Baqués, V.,** 2008. Mecanismos de deformación e interacciones fallas-fluidos en contexto extensivo. Geo-Temas, 10, 1205-1208.

Mecanismos de deformación e interacciones fallas-fluidos en contexto extensivo: las fallas del Arboçar, cuenca del Vallès-Penedès (NE de España)

Deformation mechanisms and fault-fluid interactions in extensional settings: the Arboçar faults, Vallès-Penedès basin (NE Spain)

I. Romaire[1], A. Benedicto[1], A. Travé[2] y V. Baqués[2]

1 Laboratoire de Tectonique, CNRS/INSU, Université Paris Sud 11. 91405 Orsay, France. indiana_romaire@yahoo.fr, antonio.benedicto-esteban@u-psud.fr

2 Dpt. Geoquímica, Petrologia i Prospecció Geològica, Facultat de Geologia, Universitat de Barcelona, C/ Martí i Franqués s/n., 08028 Barcelona. atrave@ub.edu, vbaques@ub.edu

Resumen: Se estudian dos fallas normales del margen oriental de la cuenca del Vallès-Penedès: la falla de Mas Ferreny (MFF) y la falla del Arboçar (ArbF). El estudio de estas dos fallas afectando dos litologías calcáreas diferentes, un wackestone del Cretácico (MFF) y una micro-brecha sedimentaria del Mioceno (ArbF), pone de manifiesto dos respuestas distintas a la deformación y un papel diferente de los fluidos durante la deformación. La falla MFF presenta fracturas y rocas de falla de tipo brecha, mientras que la falla ArbF no presenta estructuras de deformación notables. Aquí presentamos el estudio de los mecanismos de la deformación en cada una de las fallas citadas y los resultados de los análisis geoquímicos ($\delta^{18}O$ y $\delta^{13}C$) llevados a cabo en los cementos calcíticos de las fracturas y rocas de falla.

Palabras claves: fallas, fracturas, fluidos, rocas de falla, isótopos.

Abstract: *We study two normal faults of the oriental margin of the Vallès-Penedès basin: the Mas Ferreny fault (MFF) and the Arboçar fault (ArbF). These faults involve two limestone types, a Cretaceous wackestone (MFF) and a Miocene sedimentary micro- breccia (ArbF). Our study points out the different deformation mechanisms and the different role of fluids during the deformation in each case. The MFF has fractures and fault rocks whereas the ArbF does not show relevant deformation patterns. Here, we present the study of the mechanisms of the deformation in both faults and the results of the geochemical analysis (*$\delta^{18}O$ and $\delta^{13}C$*) of calcite cements sealing fractures and fault rocks.*

Key words: *faults, fractures, fluids, fault rocks, isotopes.*

INTRODUCCIÓN Y OBJETIVOS

El testigo de las interacciones entre fallas y fluidos son las mineralizaciones precipitadas en fracturas o los cementos de rocas de falla. Las características petrológicas y geoquímicas de los cementos proporcionan una triple información: sobre la naturaleza y origen de los fluidos (marinos, meteóricos o crustales, e.g. Travé *et al*., 1998), sobre las condiciones de deformación (presión/temperatura o profundidad, e.g. Micarelli *et al*., 2005) y sobre el camino de migración de los fluidos en la cuenca (vertical por las fallas, e.g. Travé y Calvet, 2001).

Por otra parte, la presencia de fluidos durante la deformación modifica el comportamiento mecánico de la falla e influye en los mecanismos de la deformación. La fricción y la presión de fluidos, por ejemplo, son responsables de la fracturación y brechificación de la roca encajante en la zona de falla (Sibson, 2000).

El presente trabajo tiene un doble objetivo: la caracterización de los mecanismos de la deformación en las fallas del margen oriental del semi-graben del Vallès-Penedès (Barcelona) (Fig. 1a), y el estudio de las interacciones entre fallas y fluidos. A continuación se presentan algunos de los resultados del estudio de dos fallas: la falla de Mas Ferreny (MFF) y la falla del Arboçar (ArbF). Estas fallas afectan formaciones de litología y edad diferentes, lo que permite, además, comparar los mecanismos de la deformación según la litología afectada.

CONTEXTO GEOLÓGICO

La cuenca del Vallès-Penedès es un semi-graben orientado noreste-suroeste, de edad neógena (Fig.1) que resulta de la obertura del Mediterráneo occidental con la rotación de las islas Baleares, Córcega y Cerdeña hacia el sureste (Roca *et al*., 1999). El semi-graben está limitado en su borde occidental por una falla principal lístrica y en su borde oriental por un conjunto de horsts y de grabens de pequeña a mediana escala. La falla principal buza hacia el sureste y controla el basculamiento hacia el noroeste del bloque superior formando una estructura en rollover (Bartrina *et al*., 1992, Roca *et al*., 1999) (Fig.1B). El conjunto de horsts y de grabens del margen oriental de la cuenca pueden interpretarse como el resultado del "colapso" de la cresta del rollover (McClay y Ellis, 1987). Las fallas

afectan una serie secundaria triásica a cretácica, principalmente dolomítica y calcárea. El relleno de la cuenca es principalmente detrítico continental y marino con algunos niveles de calizas marinas someras de edad entre Oligoceno superior y Mioceno superior (Roca *et al*., 1999, Travé y Calvet, 2001).

La zona de l'Arboçar, en el borde oriental de la cuenca, esta constituida por fallas normales hectométricas a kilométricas, que afectan materiales calcáreos del Cretácico y del Mioceno (Fig.1).

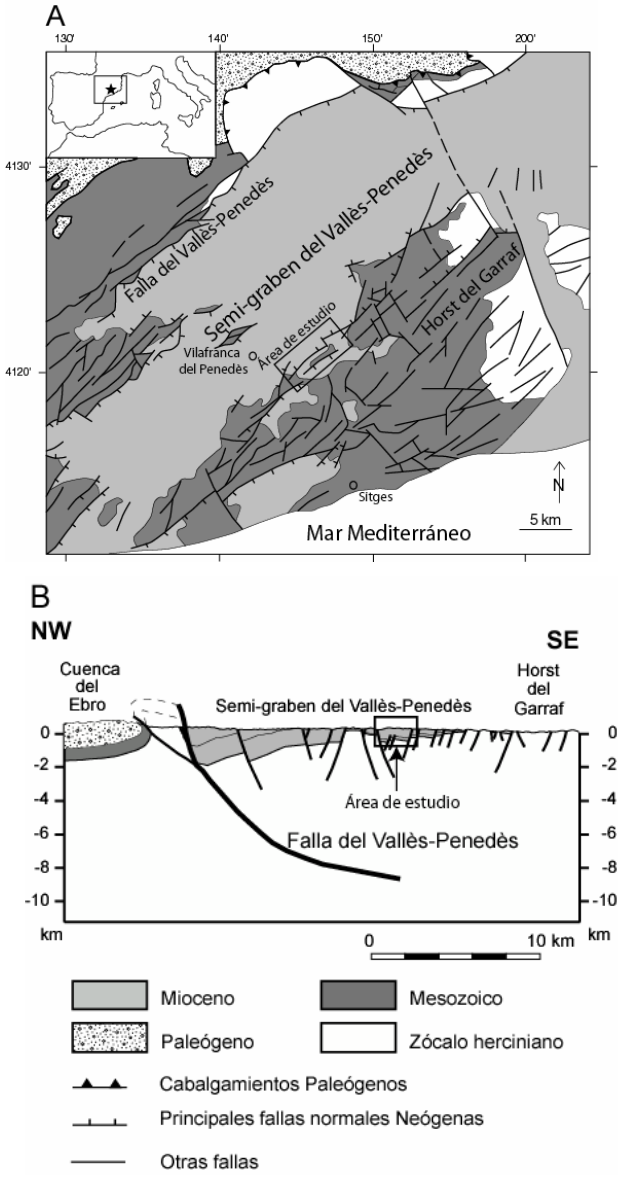

FIGURA.1. *A-Localización del área de estudio. B-Corte geológico a través de la cuenca del Vallès-Penedès indicando la posición estructural de las fallas estudiadas.*

ANÁLISIS DE LA ZONA DE FALLA

Las fallas estudiadas afloran bien y el plano de falla puede seguirse varios centenares de metros.

La falla ArbF

Esta falla afecta las calizas coralinas (micro-brechas) del mioceno sin-tectónico y se le supone un salto de varias decenas de metros.

La zona de falla esta constituida por un conjunto de lentejones, de escala métrica a decamétrica, de brechas tectónicas poco cohesivas (poco o no cementadas). Los clastos son angulosos, de talla centimétrica (>5cm) y flotan en una matriz silto-margosa. Estos lentejones se disponen de manera anastomosada a lo largo de la zona de falla y siempre están limitados por planos de falla netos. No se observan ni fracturas ni otras generaciones de brechas a escala microscópica afectando los clastos. Algunas fracturas poco significativas y sin ningún tipo de relleno (mineralización) se superponen a las brechas. La brechificación a lo largo de la zona de falla parece el único mecanismo de la deformación en esta falla.

La falla MFF

Esta falla afecta las calizas pre-tectónicas del Cretácico. El salto supuesto de esta falla puede alcanzar una o varias centenas de metros. La zona de falla es rica en estructuras tectónicas pre, sin y tardías o post-cinemáticas con respecto a la extensión neógena. Éstas se ven bien sobre el plano principal de falla, algunas de ellas aparecen bien cementadas.

Fracturación. Siete grupos de fracturas pueden observarse sobre el plano falla:

(1) Fracturas de modo I (apertura), rellenas de calcita. Son de grosor comprendido entre 1 y 5mm, y una longitud centimétrica a decimétrica. Su orientación sobre el plano de observación es N80/20S.

(2) Fracturas de modo II (deslizamiento), rellenas de calcita. Son de grosor comprendido entre 1 y 5 mm, con una longitud decimétrica, casi verticales en el plano de observación, de dirección NNW-SSE. Cortan las anteriores desplazándolas con un juego antihorario.

(3) Fracturas de modo I, abiertas. Son fracturas de escala decimétrica a métrica de dirección NNW-SSE.

(4) Fracturas de modo I, rellenas parcialmente de un material de aspecto detrítico amarillento a naranja, probablemente dolomítico. Son fracturas de escala decimétrica a métrica de dirección NNW-SSE.

(5) Fracturas de modo I, rellenas de calcita blanca, de talla métrica y de dirección NNW-SSE.

(6) Fallas normales (fracturas modo II). Son fallas de escala métrica y salto centimétrico con escalones de calcita estriada, de orientación N50/52NW/75S.

(7) Fallas direccionales (fracturas modo II). De escala métrica, poco numerosas y con estrías de orientación N170/54SW/60S.

Las fracturas 1 y 2 son fracturas ante-cinemáticas según sus direcciones y su relleno calcítico (Ca y Cf, ver después) cuyas características geoquímicas corresponden a las fracturas alpinas descritas por Travé *et al*. (1998).

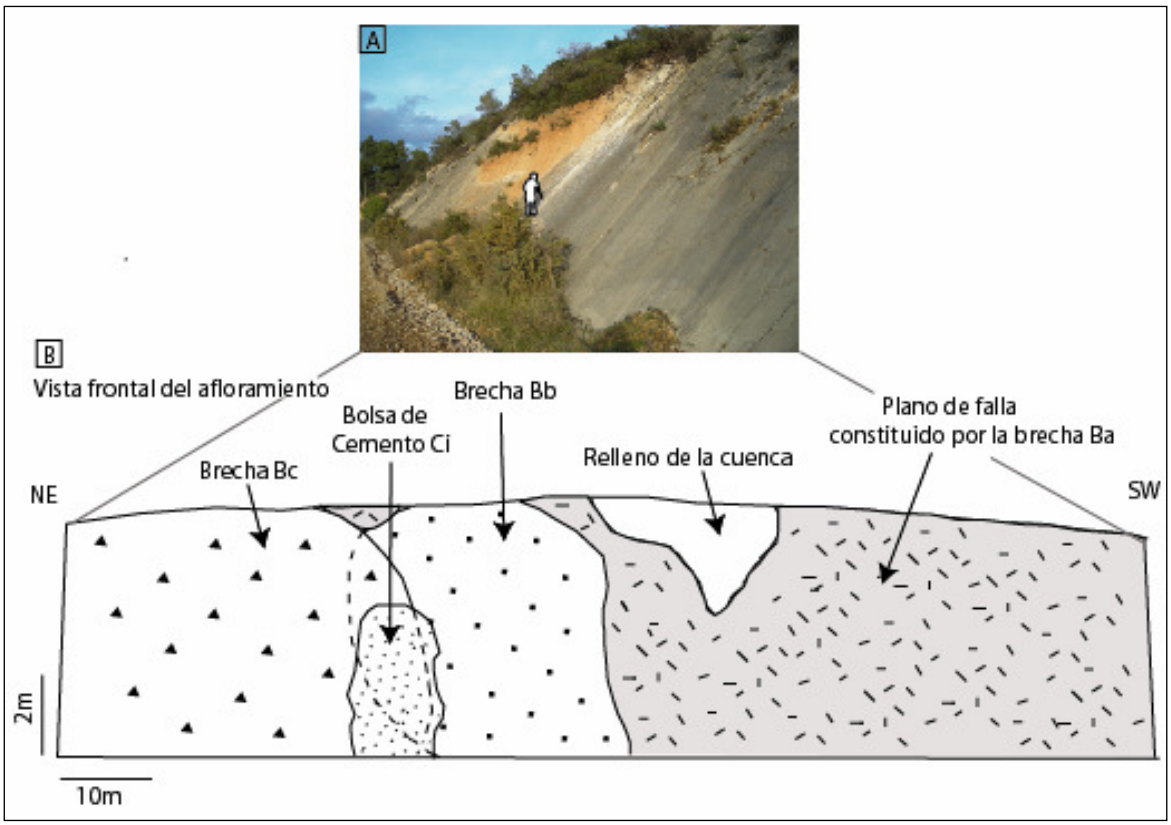

FIGURA 2. A . Fotografía del afloramiento. B. *Esquema de la disposición de las brechas tectónicas sobre el plano de falla MFF.*

Por el contrario, las fracturas 3 a 7 son fracturas tardías o post-cinemáticas ya que afectan las brechas sin-cinemáticas descritas a continuación. Las fallas normales de pich alto (6) y las fallas direccionales (7) están probablemente relacionadas con una reactivación tardía direccional a escala regional.

Brechificación.

La zona de falla está compuesta de tres tipos de brechas sin-tectónicas (Fig.2):

Ba. Brecha cohesiva y compacta caracterizada por una fracturación tridimensional dilatante y bien cementada. Los clastos son angulosos, monogénicos (caliza encajante cretácica), e inferiores a 3 cm. Su textura recuerda un puzzle y se asemeja a una brecha de tipo hidráulico. Los clastos contienen fracturas de tipo F1 y F2 indicando la anterioridad de éstas con respecto a la brechificación. En lámina delgada, esta brecha aparece localmente como una protocataclasita o cataclasita de clastos subangulosos, bastante fracturados y muy próximos entre ellos. El cemento de esta brecha es el descrito más abajo como Cg.

Bb. Brecha cataclástica cohesiva. Los clastos son subangulosos a subredondeados, de 10-15 cm, monogénicos (caliza encajante cretácica). En ellos se reconoce la brecha Ba y las fracturas de tipo 1 y 2 (ante-cinemáticas). Esta brecha está igualmente cementada por el cemento Cg y está afectada por las fracturas tipo 5. Dicha brecha se dispone en capas lenticulares a lo largo del plano de falla.

Bc. Brecha de características similares a la precedente a excepción del cemento que es el descrito más adelante como Ch. Está afectada por las fracturas 5, 6 y 7.

Cementación.

Se han diferenciado ocho tipos de cementos:

Ca. Cemento esparítico con cristales maclados, subanédricos que miden entre 1 y 2 mm. Tienen una luminiscencia variable de negro a rojo.

Cb. Cemento esparítico con cristales maclados, subanédricos que miden entre 1 y 2 mm y equidimensionales. Tienen una luminiscencia marrón rojiza oscura igual a la del encajante.

Cc. Cemento microesparítico anédrico. Los cristales tienen un tamaño medio de 0,1 mm. No maclado. Tienen una luminiscencia marrón rojiza oscura igual a la del encajante.

Cd. Cemento microesparítico con cristales euédricos que miden entre 0,2 y 0,5 mm. No maclado. Estos cristales tienen una luminiscencia de color negro. El cemento no llena toda la porosidad dejando vacios geódicos.

Ce. Cemento microesparítico con cristales anédricos de tamaño inferior a 0,1 mm. No maclado. Su luminiscencia es fuerte, naranja brillante.

Cf. Cemento microesparítico con cristales anédricos de tamaño medio 0,1 mm. No maclado. Su luminiscencia es naranja.

Cg. Cemento microesparítico con cristales anédricos, de

tamaño medio 0,5mm y equidimensionales. Tiene una luminiscencia muy variable de negro hasta naranja. Esta calcita cementa la brecha Ba y Bb.

Ch. Cemento microesparítico con cristales anédricos, de tamaño medio 0,1mm y equidimensionales. Tiene una luminiscencia floja de color marrón. Esta calcita cementa la brecha Bc.

Ci. Se trata de un material de aspecto detrítico amarillento a naranja, probablemente dolomítico (ver Baqués et al., este mismo volumen), a veces laminado, que aparece en forma de bolsas irregulares impregnando tanto la brecha Bb como la Bc. De manera general tapiza las brechas y penetra por los intersticios entre los clastos.

Los cementos **Ca, Cb, Cc, Cd, Ce y Cf** rellenan las fracturas ante-cinemáticas y los cementos **Cg, Ch y Ci** son sin-tectónicos.

ANÁLISIS ISOTÓPICOS DE LOS CEMENTOS

(1) La roca encajante, con una composición mediana de $\delta^{18}O$= -3,1 ‰ PDB y $\delta^{13}C$= +4,2 ‰ PDB, caracteriza el medio marino de sedimentación.

(2) La calcita de los cementos Ca a Cf (fracturas ante-cinemáticas 1 y 2) tienen una composición mediana de $\delta^{18}O$= -8,1 ‰ PDB y $\delta^{13}C$= +2,9 ‰ PDB. Los valores del $\delta^{13}C$ sugieren una fuerte interacción fluido/roca. Los valores del $\delta^{18}O$ caracterizan un fluido de meteórico a profundo.

(3) La calcita de los cementos de las brechas Ba y Bb tienen una composición isotópica de $\delta^{18}O$= -5,2‰ PDB y $\delta^{13}C$= -4,6 ‰ PDB. Estos valores corresponden a un fluido de origen meteórico con una interacción con el encajante muy baja. Podría tratarse de un fluido meteórico subaéreo.

(4) El cemento de la brecha Bc tiene una composición mediana de $\delta^{18}O$= -3,2 ‰ PDB y $\delta^{13}C$= +1,1 ‰ PDB. Estos valores son proximos a los del encajante lo que sugiere un fluido de características marinas (mar mioceno) o una fuerte interacción con la roca (dissolución de las calizas cretácicas).

No se dispone por el momento de datos sobre el cemento dolomítico, pero es muy probable que éste provenga de la disolución de las dolomías jurásicas subyacentes.

CONCLUSIONES

Los mecanismos de la deformación identificados en las dos fallas estudiadas ponen de manifiesto un comportamiento diferente frente a la deformación. La escasa cementación de las brechas en la falla ArbF sugiere una participación escasa de fluidos en la deformación. La brechificación y los planos de deslizamientos netos como únicos mecanismos de la deformación atestan de una deformación frágil de poca profundidad.

En la falla MFF las estructuras de deformación son más complejas. Se han reconocido 2 tipos de fracturas ante-cinemáticas, 3 tipos de brechas tectónicas y 5 tipos de fracturas tardías o post-cinemáticas con respecto a la extensión neógena.

El primer tipo de brecha (Ba) puede corresponder a un primer episodio de brechificación hidráulica que podría haber precedido la propagación de la falla. Los otros dos tipos de brechas cataclásticas (Bb y Bc) estarían asociados con diferentes eventos de deslizamiento y fricción a lo largo de la falla.

Los primeros estadios de brechificación (Ba y Bb) habrían tenido lugar bajo la influencia de un fluido meteórico subaéreo. Mientras que los estadios más tardíos de la brechificación (Bc) habrían ocurrido bajo la influencia de un fluido de posible origen marino en relación con la entrada del mar en la cuenca durante el mioceno superior, o que hubiera interaccionado fuertemente con la roca encajante de origen marino.

Un último evento tectónico habría inducido el ascenso de un fluido dolomítico proveniente de las dolomias jurásicas subyacentes que habría impregnado de manera irregular las brechas Bb y Bc.

AGRADECIMIENTOS

Trabajo financiado por el Proyecto DGICYT CGL2006-04860, la beca BES-2007-14935 y el Grup Consolidat de Recerca “Geologia Sedimentària” (2005SGR-00890).

REFERENCIAS

Bartrina, M.T., Cabrera, L. Jurado, M.J., Guimerà, J. y Roca, E., (1992): Evolution of the central Catalan margin of the Valencia trough (western Mediterranean). *Tectonophysics*, 203: 219-247.

McClay, K. R. y Ellis, P.G. (1987): Geometries of extensional fault systems developed in model experiments. *Geology*, 1: 341-344.

Micarelli, L., Benedicto, A., Invernizzi, C., Saint-Bezar, B., Michelot, J.L. y Vergély, P. (2005): Influence of P/T conditions on the style of normal fault initiation and growth in limestones from SE-Basin, France. *Journal of Structural Geology*, 27 (9): 1577-1598.

Roca, E., Sans, M., Cabrera, L. y Marzo, M. (1999): Oligocene to Middle Miocene evolution of the central Catalan margin (Northwertern Mediterranean). *Tectonophysics,* 315 :209-233.

Sibson, R.H. (2000): Fluid involvement in normal faulting. *Journal of geodynamics,* 29: 469-499.

Travé, A., Calvet F., Soler, A. y Labaume, P. (1998): Fracturing and fluid migration during Palaeogene compression and Neogene extension in the Catalan Coastal Ranges, Spain. *Sedimentology,* 45: 1063-1082.

Travé, A. y Calvet, F. (2001): Syn-rift geofluids in fractures related to the early-middle Miocene evolution of the Vallés-Penedés half-graben (NE Spain). *Tectonophysics,* 336: 101-120.

Publication 8

Baqués, V., Travé, A., Benedicto, A., Labaume, P., 2009. Relationship between fluid flow and tectonic brecciation in the Neogene extensional Vallès-Penedès basin (Catalan Ranges, NE Iberian). Journal of Geochemical Exploration, 101 (1), 4.

Journal of Geochemical Exploration 101 (2009) 4

Contents lists available at ScienceDirect

Journal of Geochemical Exploration

journal homepage: www.elsevier.com/locate/jgeoexp

Relationship between fluid flow and tectonic brecciation in the Neogene extensional Vallès–Penedès basin (Catalan Ranges, NE Iberian)

V. Baqués [a,*], A. Travé [a], A. Benedicto [b], P. Labaume [c]

[a] Dpt. Geoquímica, Petrología i Prospecció Geològica, Facultat de Geologia, Universitat de Barcelona, 08028 Barcelona, Spain
[b] Laboratoire de Tectonique (UMR 7072), Université Paris Sud XI, 91405 Orsay, France
[c] Géosciences Montpellier (UMR 5243), Université Montpellier 2, 34095 Montpellier, France

The diagenetic processes taking place in a sedimentary basin during its evolution are closely linked with the processes of deformation and fracturing. This issue describes the tectonic brecciation processes along the largest fault of the Vallès–Penedès semi-graben and their relationships with the fluids involved in the deformation.

The NE–SW trending Vallès–Penedès basin results from the Late Oligocene–Early Miocene extension related with the opening of the NW-Mediterranean basin. The basin is bordered at the NW by the NE–SW trending Vallès–Penedès master fault, which accumulated 4 km of extensional movement. On the studied outcrop, the Upper Jurassic–Lower Cretaceous dolomites of the footwall are in contact with the Upper Continental Complex of Late Serravallian–Tortonian age in the hangingwall. The footwall protolith comprises grey dolmicrite to dolsparite featuring anhedric to subhedric dull purple luminescent crystals, 10 to 100 μm in size. Their $\delta^{18}O$ varies from −0.4 to +1.2‰ VPDB and $\delta^{13}C$ from +0,7 to +2.2‰ VPDB.

The footwall part of the fault zone, about 100 m wide, features various generations of syn-kinematic fractures and related cements with the following chronology:

Fractures 1 are mode I (opening) fractures without preferred orientation. They are filled by the C1 dolomitic cement, constituted by anhedric dull red luminescent crystals, >10 μm in size, which grew in optical continuity with the host rock crystals. Their $\delta^{18}O$ varies from −2.3 to −1.3‰ VPDB and $\delta^{13}C$ from −0.8 to +0.3‰ VPDB.

Fractures 2a are mode II (sliding) fractures sub-parallel to the master fault. They are filled by the C2 dolomitic cement, featuring a rim habit (C2a) or a blocky texture (C2b). C2 is constituted by subhedric to euhedric bright orange to bright yellow luminescent crystals, 10 to 100 μm in size, with $\delta^{18}O$ about +0,1‰ VPDB and $\delta^{13}C$ about −2.9‰ VPDB.

Fractures 2b are mode I fractures oblique to the master fault. They are filled by the C2a dolomite cement.

Cement C3 is a late filling in fractures 2a and 2b. It is constituted by euhedric non-luminescent crystals, 10 μm to 200 μm in size. Their $\delta^{18}O$ varies from −7 to −6,4‰ VPDB and $\delta^{13}C$ from −8.3 to −7,8‰ VPDB.

Different types of fault rocks breccias are related with these fractures and cements:

Dilatant breccia B1, formed by angular fragments of protolith dolomitic rock, 0,5 to 4 cm in size. This breccia results from opening of fractures 1 and is cemented by C1. It is located in the whole footwall fault zone.

Cataclasite, formed by subangular fragments of dolomitic rock, <0,1 cm in size. The 90% corresponds to protolith fragments and the 10% to reworked B1 fragments. This breccia results from sliding along fractures 2 and is cemented by C2. It forms the core of second-order faults present in the fault zone.

Dilatant breccia B2, formed by angular fragments of dolomitic rock, 0,5 to 4 cm in size. The 90% corresponds to protolith fragments and the 10% to reworked B1 and C2 fragments. This breccia is related to formation of fractures 2 and 3, and is cemented by C2 and mainly C3. It is located in an about 10 m-wide interval along the master fault plane.

Protocataclasite, formed by subangular fragments of dolomitic rock, 0,1 to 2 cm in size. The 60% corresponds to protolith fragments and the 40% to reworked B1 and C2 fragments in a red matrix of calcite, quartz and ankerite. This breccia is related to formation of fractures 2 and 3, and is cemented by C2 and mainly C3. It is restricted to an about 2 m-wide band along the master fault plane.

These various tectonic breccias correspond to the various stages of the fault development. The dilatant fault breccia B1 was formed during the initial upward propagation of the fault. The associated fluid (precipitating the dolomite cement C1) was in equilibrium with the host rock in a closed hydrological system. During the development of the fault, localisation of frictional processes generated the cataclasite along distinct second-order faults. The associated fluid (precipitating the dolomite cement C2) still remained in a closed hydrological system. Further localisation of the deformation led to the formation of the dilatant breccia B2 and the protocataclasite close to the master fault plane. When the propagating fault reached the earth surface, opening of the hydrological system allowed circulation of meteoric water responsible for precipitation of the C3 calcite cement.

* Corresponding author.
E-mail addresses: vbaques@ub.edu (V. Baqués), atrave@ub.edu (A. Travé), antonio.benedicto-esteban@areva.fr (A. Benedicto), pierre.labaume@gm.univ-montp2.fr (P. Labaume).

0375-6742/$ – see front matter
doi:10.1016/j.gexplo.2008.11.006

Publication 9

Baqués, V., Travé, A., Benedicto, A., Labaume, P., 2009. Multi-episodic Fault Movements and karstic Fills along the Vallès-Penedès Fault, Catalan Coastal Ranges, NE Spain. 2nd International Conference on Fault and Top Seals- From Pore to Basin Scale (EAGE). Montpellier (France). EarthDoc. ISBN 978-90-73781-69-6.

P39

Multi-episodic Fault Movements and Karstic Fills Along the Vallès-Penedès Fault, Coastal Catalan Ranges, NE Spain

V. Baqués* (University of Barcelona), A. Travé (University of Barcelona), A. Benedicto (AREVA NC) & P. Labaume (University Montpellier 2)

SUMMARY

We describe different fault rocks within a normal fault bordering the Neogene Vallès-Penedès basin in NE Spain. Through this fault, the Lower Cretaceous limestones of the footwall are in contact with the Miocene siliciclastic sediments of the hangingwall.
In the Lower Cretaceous protolith, cataclasites and breccias are a mixture of tectonic and karstic products resulting from multi-stages movement and development of the fault. The localisation of frictional processes generated a cohesive fault breccia and the cataclasite during the progressive opening of the hydrological system. Later, when the fault reached the surface, meteoric diagenetic processes leaded to the formation of calcretes and karstic features and generating the breccia with the pisolithic matrix.

The diagenetic processes taking place in a sedimentary basin during its evolution are closely linked with the processes of deformation and fracturing. In this paper, we describe the karstic processes that occurred along the largest fault of the Vallès-Penedès semi-graben and their relationships with the evolution of the fault propagation.

The NE-SW trending Vallès-Penedès basin resulted from the late Oligocene-middle Miocene extension related with the opening of the NW-Mediterranean basin. The basin is bordered at the NW by the Vallès-Penedès fault.

On the Montjuïc outcrop (Figure 1), the Lower Cretaceous limestones of the footwall are in contact with the Miocene siliciclastic sediments of the hangingwall.

The Lower Cretaceous limestones are constituted by a packstone of charophyta, ostracoda and gastropoda fragments arranged in meter-thick beds. The $\delta^{18}O$ of this protolith is -4 ‰ PDB and the $\delta^{13}C$ is -4,6 ‰ PDB.

Two families of fractures and related breccias and cataclasites are recognized within the Cretaceous protolith along the main fault:

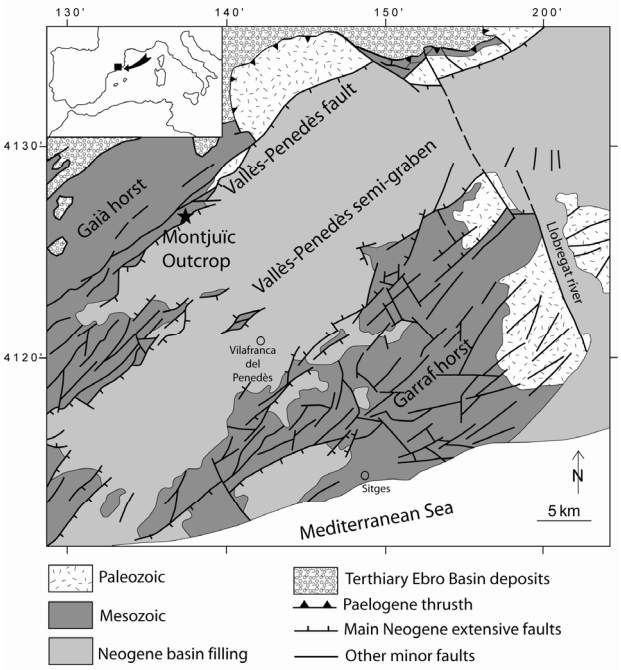

Figure 1 *Simplified geological map of the area.*

Fractures 1, are mode I (opening) trending NNW-SSE. These fractures are filled by the calcite cement **C1** constituted by subhedric-euhedric non-luminescent crystals, 50 to 200 µm in size, showing mechanical twinning planes and with blocky texture. The $\delta^{18}O$ range between -8,4 and -7,0 ‰ PDB and $\delta^{13}C$ range between -6,3 and -4,6 ‰ PDB.

Fractures 2, are mode I and mode II (sliding) trending NE-SW. The fractures mode I are filled by the calcite cement **C2** constituted by euhedric non-luminescent crystals, 25 to 100 µm in size, with a drusy texture. The $\delta^{18}O$ range between -5,3 and -4,9 ‰ PDB and the $\delta^{13}C$ range between -9,5 and -7 ‰ PDB. The fractures mode II are normal faults and strike-slip with a strong normal component faults. Related to these faults, different types of breccias and cements have been recognized (Figures 2 and 3):

Cohesive fault breccia (Figure 2A), formed by angular micro-fragments of protolith limestone rock and cement C1, 100 µm to 1 mm in size. This breccia results from sliding along the normal and strike-slip faults and is cemented by non-luminescent microesparite **C3**. The $\delta^{18}O$ of the microesparite cement range between -5,3 and -4,9 ‰ PDB and the $\delta^{13}C$ is -9,3 ‰ PDB.

Cataclasite (Figure 2B), formed by comminute cohesive fault breccia. This breccia is clast-suppported with pressure-dissolution features and contains a micrite orange matrix.

Breccia with pisolithic matrix (Figure 2C), formed by reworked cohesive fault breccia and cataclasite fragments. The pisolitic matrix is formed by orange micrite pisoliths and is cemented by microesparite cement with a blocky texture (**C4**). The $\delta^{18}O$ of the orange micrite pisoliths is -4,5 ‰ PDB and the $\delta^{13}C$ is -10,8 ‰ PDB, whereas the $\delta^{18}O$ of **C4** range between -6,3 and -5,2 ‰ PDB and the $\delta^{13}C$ range between -9,4 and -8,7 PDB.

Cataclasite of pisolitic matrix (Figure 2D), formed by comminute pisolithic matrix. This cataclasite is cemented by the calcite cement (**C4**) with a bladed and drusy texture.

Figure 2 *Distribution of breccias and cataclasites within one of the faults. D.Z.:Damage zone.*

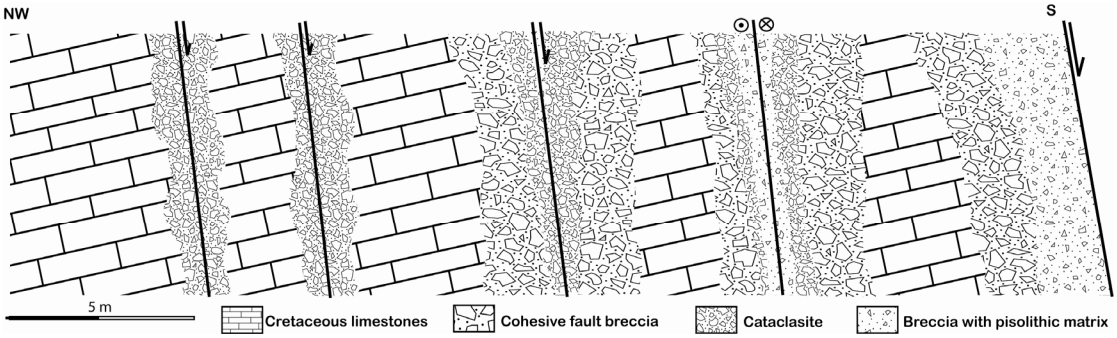

Figure 3 *Synthetic sketch of distribution of breccias and cataclasites within the faults.*

The different cataclasites and breccias are a mixture of tectonic and karstic breccias and resulted from multi-stages movement and development of the fault. The localisation of frictional processes generated the cohesive fault breccia and the cataclasite during the progressive opening of the hydrological system (Figure 4a and 4b), as indicated by the geochemistry of the cements. Later, when the fault reached the surface (Figure 4c), meteoric diagenetic processes leaded to the formation of calcretes and karstic features and generating the breccia with the pisolithic matrix (Figure 4).

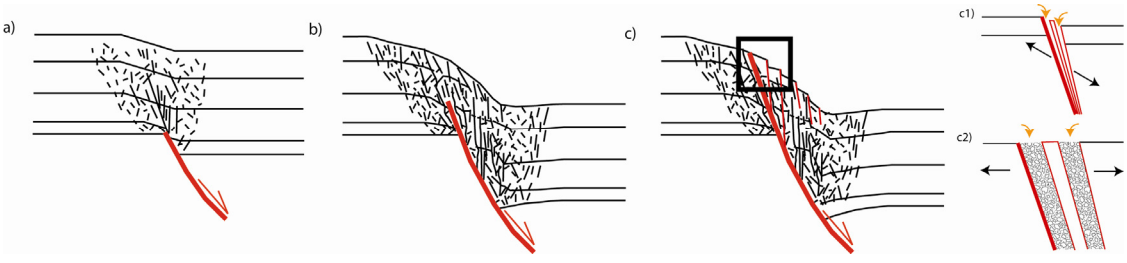

Figure 4 *Propagation fault model.*

ACKNOWLEDGMENTS

This investigation is funded by the DGICYT CGL2006-04860 project, BES-2007-14935 grant and the *Grup Consolidat de Recerca* "Geologia Sedimentària" (2005SGR-00890).

Publication 10

Baqués, V., Travé, A., Benedicto, A., Labaume, P., Cantarero, I., 2010. Diagenetic evolution during progressive development of the Neogene faults (NE Spain). 72nd EAGE Conference & Exhibition incorporating SPE EUROPEC 2010. Barcelona (España). EarthDoc. ISBN 978-90-73781-86-3.

Barcelona '10

J041

Diagenetic Evolution During Progressive Development of Neogene Faults, NE Spain

V. Baques* (University of Barcelona), A. Travé (University of Barcelona), A. Benedicto (Areva), P. Labaume (University of Montpellier) & I. Cantarero (University of Barcelona)

SUMMARY

Different fractures, cements, breccias and karstic sediments identified on the Mesozoic carbonates attest to establish the diagenetic processes that have taken place during the Neogene evolution of the Penedès half-graben.
Six families of fractures are identified. The first generation trending NNW-SSE is compatible with the Alpine compression whereas the fractures 2 to 6 have been attributed to the Neogene extension. The fractures 2, without preferred orientation, generated a fault breccia related to the initial propagation of the Neogene normal faults. The fluid involved during this deformation, shows a high interaction with the host-rock, in a closed hydrological system. The fractures 3, enlarged by the subaerial exposure of the Mesozoic horsts, are filled by different karstic sediments. The geochemistry of the sediments indicates the opening of the system to meteoric water. When the normal faults reached to the surface, fractures 4 to 6 are formed. The fractures fillings are a mixture of tectonic and karstic processes and resulted from multi-stages movement of the normal faults.

Introduction

The study of fractures and related carbonate precipitates coupling microstructural, petrologic and geochemical analyses allows determining the fluid sources, flow pathways and fluid-driven mass transfer through fractures (Travé et al. 1998). The development of normal faults in carbonates at shallow crustal depths (< 1-3 km) is a very complex process, because of the interaction of mechanical and chemical processes (Sibson, 2000 and Verhaert et al. 2009). Here we present different fractures, cements, breccias and karstic sediments identified on the Mesozoic carbonates in order to establish the diagenetic processes that have taken place during the evolution of the Penedès half-graben.

The Penedès half-graben, located at the central part of the Catalan Coastal Ranges (NE Spain), results from the superposition of three main tectonic events: (1) a Mesozoic extensional phase from the Late Jurassic to the Early Cretaceous; (2) a Paleogene compressional phase from the Eocene to the early Oligocene; and (3) a Neogene extensional phase (late Oligocene?- late Neogene) in association with the Valencia Through opening. The Penedès basin is oriented NE-SW and is up to 50 km long and 10-14 km wide. In its northern part, it is bounded by the SE-dipping Vallès-Penedès fault, which has a normal displacement of up to 4 km, and towards the SW by the Baix Penedès fault. The basin is filled with up to 4 km thick succession of terrigenous sediments which forms a broad syncline cut by normal faults.

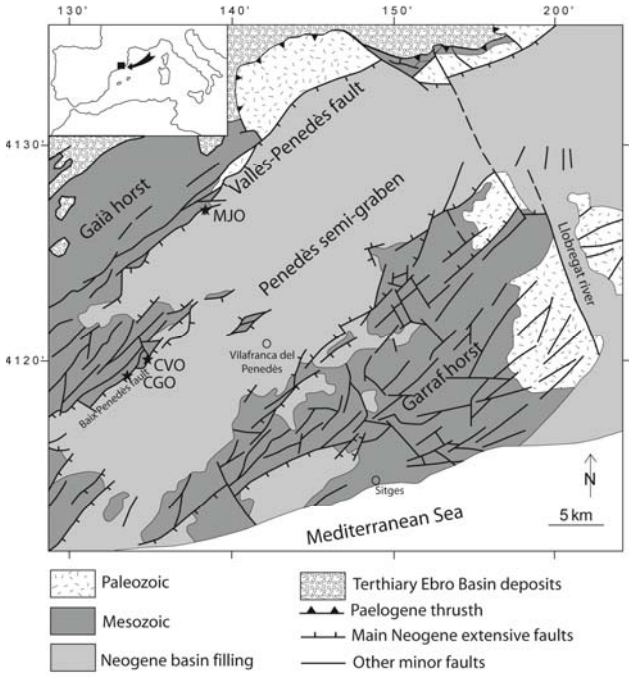

Figure 1. *Simplified geological map of the studied area. CGO: Casetes de Gomila outcrop; CVO: Castellví outcrop; MJO: Montjuïc outcrop.*

Outcrops

Three outcrops have been studied along the northwest border of the Penedès half-graben (Fig.1). Two involve dolomite rocks of Late Jurassic- Early Cretaceous (Casetes de Gomila (CGO) and Castellví (CVO) outcrops) and the other involves limestones rocks of Early Cretaceous age (Montjuïc outcrop (MJO)). In the three outcrops the Mesozoic materials are in contact with the Miocene siliciclastic deposits that fills the basin.

In the CGO and CVO outcrops host-dolomite correspond to a replacive dolosparite with penetrative and non-destructive fabric. The crystals are subhedral, 50 to 300 µm in size and show dull purple luminescence. The isotopic signal of $\delta^{18}O$ varies from -2.1 to -1.1 ‰ VPDB and its $\delta^{13}C$ from -0.4 to +1.9 ‰ VPDB. In the MJO outcrop the host-limestone is constituted by a wackstone of charophyta, ostracoda and gasteropoda fragments. The components have been dissolved and calcite cement fills the moldic porosity. The luminescence of the micrite is orange and the calcite cement is non-luminescent. The oxygen and carbon isotopes range from -5.3 to -3 ‰ VPDB and from -5.8 to -4 ‰ VPDB respectively.

Structure, petrology and geochemistry of the fractures

Different types of fractures, cements and breccias are affecting the Mesozoic carbonates:

Fractures 1, are mode I (opening) NNW-SSE trending, 0.1 to 1 cm thick, with straight walls. These fractures are present in the MJO outcrop and are filled by the **calcite cement C1**, constituted by

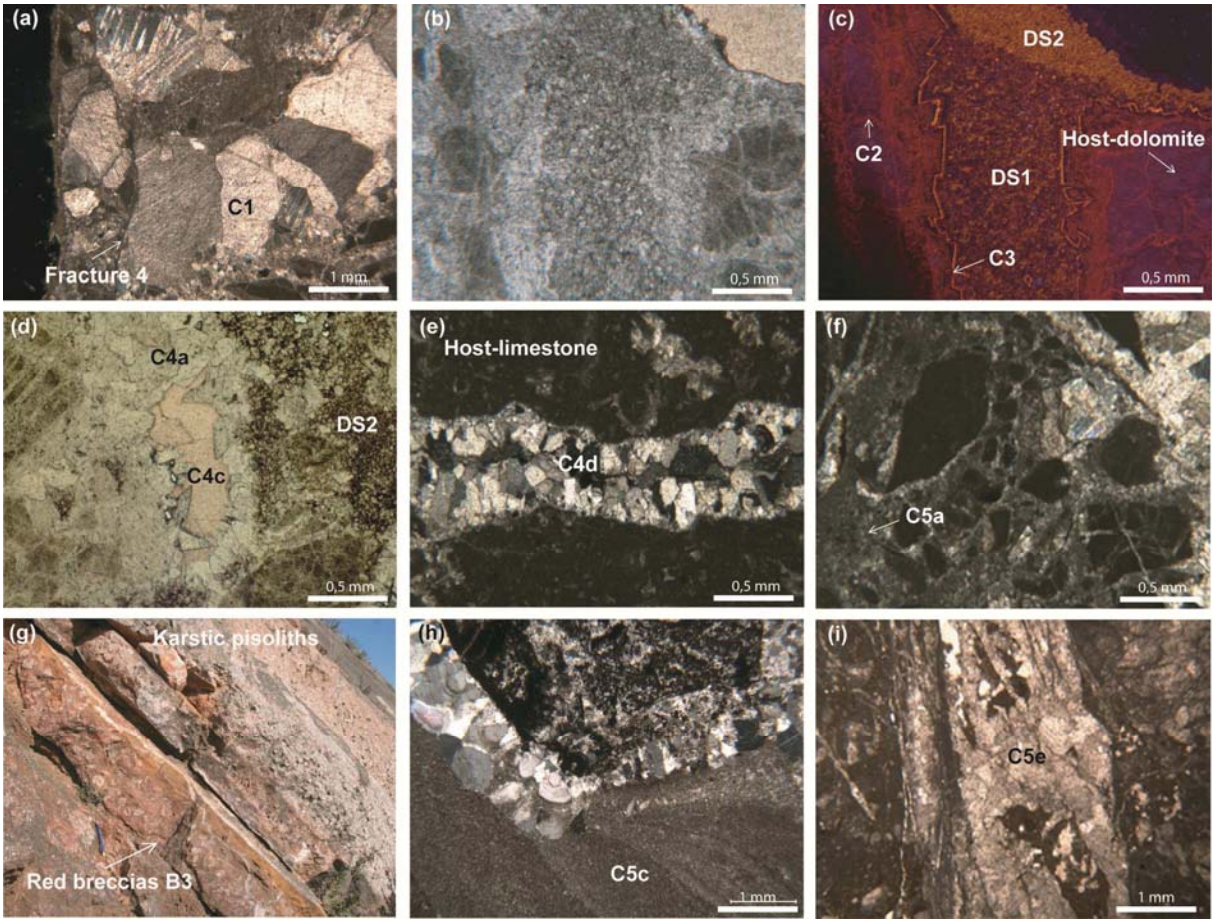

Figure 2. *Petrology of the different fractures fillings and breccias: (a) Calcite cement C1affected by the fractures 4; (b and c) Dilatant breccia B1 and fractures 3 with the dolomite cement C2 and C3 and the dolomite sediments DS1 and DS2; (d) Dolomite cement C4a and calcite cement C4c occluding the vuggy porosity; (e) Fractures 4 filled by the calcite cement C4d; (f) Cohesive fault breccia B2; (g) Red breccias B3 and karstic pisoliths sub-parallel to the fractures 5; (h) Detail of the karstic pisolith cemented by the calcite cement C5c; (i) Cataclasite of the breccia with the orange pisoliths.*

blocky subhedral to euhedral non-luminescent crystals, 50 to 400 µm in size, showing mechanical twinning planes, sometimes curved (Fig. 2a). The oxygen and carbon isotopes range from -8.4 to -5.9 ‰ VPDB and from -6.3 to -3.1 ‰ VPDB respectively (Fig. 3).

Fractures 2, are mode I without preferred orientation, 10 to 25 µm thick, with sharp and undulating walls. These fractures are present in the CGO and CVO outcrops and are filled by the **dolomite cement C2**, which is composed of anhedral dull red luminescent crystals, from 50 to 100 µm in size (Fig. 2b and 2c). The $\delta^{18}O$ varies from -2.1 to -1 ‰ VPDB and its $\delta^{13}C$ from -0.4 to +0.3‰ VPDB. Due to the high amount of fractures, the host-dolomites are totally brecciated and cemented by the dolomite cement C2. The breccia correspond to a **cohesive breccia B1** formed by angular fragments, 0.5 to 4 cm in size and cemented by the dolomitic cement C2.

Fractures 3, are mode I without preferred orientation, 75 to 400 µm thick with sub-angular walls. They are present in the CGO and CVO outcrops. The fractures favoured the dissolution processes, generating channel and vug porosities. Two types of filling are present: the first filling stage is an orange **dolomite sediment DS1**, constituted by fragments the host-dolomite 4 to 100 µm in size. This sediment is cemented by **dolomitic cement C3**, arranged as rim position at the fractures walls or surrounding the host-dolomite fragments. The cement has non-luminescent to orange luminescent zonation. The oxygen and carbon isotopes of the dolomite sediment and cement range from -1.8 to -0.8 ‰ VPDB and from -3.1 to -1.5 ‰ VPDB respectively. The second filling stage is a pink to red

dolomitic sediment DS2, constituted by dolosparite formed by euhedral crystals, 50 to 100 µm in size. The luminescence of the crystals is bright orange, ranging from -2 to 0.7 ‰ VPDB for $\delta^{18}O$ and from -2 to -1.3 ‰ VPDB for $\delta^{13}C$ (Fig. 2d). The dolomitic sediment DS3·contains high amount of iron oxides and locally is laminated. Minor porosity remains even after the deposition of the sediment.

Fractures 4, are mode I NE-SE and NW-SE trending, 0.5 mm to 2 cm thick, with sharp and undulating walls, locally enlarged by dissolution. In the CGO and CVO outcrops the fractures are filled by **dolomite cement C4a** corresponding to euhedric crystals, 100 to 500 µm in size. The crystals grow with the c-axis perpendicular to the fracture walls and have brown-orange luminescence zonation. The isotopic values are -1.2 ‰ VPDB for $\delta^{18}O$ and -2.3 ‰ VPDB for $\delta^{13}C$. C**ement C4b** is hematite cement. **Calcite cement C4c** comprises blocky subhedral crystals, 250 µm to 2 mm in size, no luminescent and ranging from -9 to -7.5 ‰ VPDB for $\delta^{18}O$ and from -7.3 to -6.6 ‰ VPDB for $\delta^{13}C$. On the MJO outcrop these fractures are filled by **the calcite cement C4d**, constituted by drusy euhedral non-luminescent crystals, 25 to 250 µm in size (Fig.2e). The oxygen and carbon isotopes range from -5.5 to -4.6 ‰ VPDB and from -10.5 to -8.2 ‰ VPDB respectively.

Fractures 5, are mode II (sliding) NE-SW to NNE-SSW trending normal faults and strike-slip with a strong normal component faults. In the MJO outcrop, two types of fault breccias have been identified: the **cohesive fault breccia B2** is formed by angular fragments of host-limestone and cement C1, 0.1 to 1 mm in size, cemented by the **calcite cement C5a** (Fig. 2f). This cement is constituted by blocky anhedral non-luminescent crystals, 4 to 10 µm in size. The oxygen and carbon isotopes range from -5.4 to -4.1 ‰ VPDB for $\delta^{18}O$ and from -9.4 to -6.9 ‰ VPDB for $\delta^{13}C$. The **cataclasite** is formed by comminute cohesive fault breccia, clast-supported, with pressure-solution features and contains a micrite orange matrix. In the CVO outcrop, running parallel to the main fault plane, two other types of breccias are present: **red breccia B3,** is formed by sub-angular to sub-rounded fragments, 1 to 3 cm in size, of the host-dolomite, breccias B1, dolomitic sediments and goethite crystals cemented by a blocky **calcite cement C5b** (Fig. 2g). This cement has non-luminescent subhedric crystals, 20 to 100 µm in size and the $\delta^{18}O$ range from -9.7 to -9.2 ‰ VPDB and $\delta^{13}C$ from -5.6 to -5.4 ‰ VPDB. Closer to the main fault plane, a 1 to 1,5 meter-thick tabular layer constituted by **karstic pisoliths** is present. The lower part corresponds to karstic pisoliths cemented by laminated **calcite cement C5c** (Fig. 2h). The laminated cement is a blocky non-luminescent anhedral calcite crystals, 4 to 10 µm in size. The $\delta^{18}O$ ranges from -8.5 to -8.6 ‰ VPDB and the $\delta^{13}C$ from -7.7 to -7.6 ‰ VPDB. The upper part corresponds to white layer with well-rounded non-luminiscent pisoliths, 0.5 to 10 cm in size. The $\delta^{18}O$ ranges from -8.4 to -8.1 ‰ VPDB and $\delta^{13}C$ from -7.9 to -7.7 ‰ VPDB. On the MJO outcrop, this type of breccia consists on reworked cohesive fault breccia, cataclasite fragments and orange micrite pisoliths cemented by **calcite cement C5d** featuring blocky euhedral crystals, 10 to 50 µm in size. The oxygen isotopes range from -7.1 to -4.4 ‰ VPDB and $\delta^{13}C$ from -10.3 to -8.5 ‰ VPDB. Late movements of fractures 4

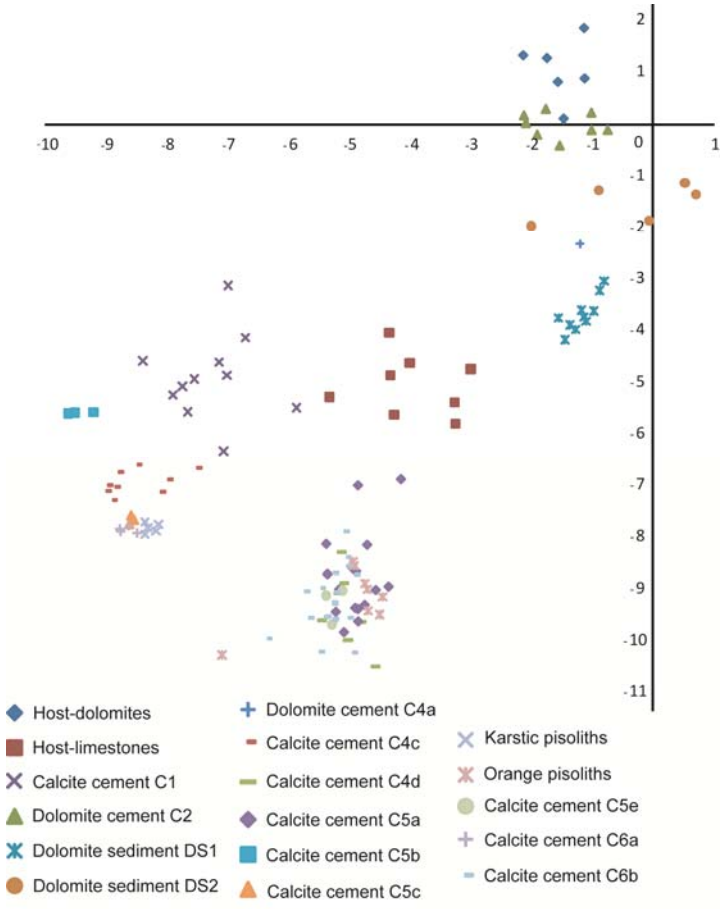

Figure 3. *$\delta^{18}O$ and $\delta^{13}C$ cross-plot of the host-dolomite, host-limestone, dolomite sediments and the dolomite and calcite cements.*

generate a late cataclasite. In the MJO outcrop this late cataclasite is cemented by the **calcite cement C5e** showing crack-seal structures with inclusion bands of the orange pisoliths and corresponds to blocky subhedral to euhedral calcite crystals, 250 to 500 µm in size (Fig. 2i). The oxygen isotopes range from -5.1 to -5.4 ‰ VPDB and $\delta^{13}C$ from -9.8 to -9 ‰ VPDB.

Fractures 6, are mode I with a preferred orientation NNE-SSW, 1 to 4 cm thick with sharp and undulating walls. The fractures remain open and are partially filled by the **calcite cement C6**. This cement is constituted by bladed non-luminescent crystals, 50 to 250 µm in size, with the c-axis perpendicular to the fracture wall. The $\delta^{18}O$ range from -8.9 to -8.5 ‰ VPDB and the $\delta^{13}C$ from -7.9 to -7.8 ‰ VPDB in the CVO outcrop (C6a) and $\delta^{18}O$ range from -5.6 to -4.9 ‰ VPDB and $\delta^{13}C$ from -10.2 to -7.9 ‰ VPDB in the MJO outcrop (C6b).

Discussion and conclusions

The tectonic fracturing, brecciation and cementation processes observed along the northwest border of the Penedès basin attest to different moments during the basin development:

Fractures 1 are compatible with Alpine compression (Travé et al., 1998). The $\delta^{13}C$ values of the calcite cement C1 indicate high interaction between the mineralizing fluid and the host-limestone, whereas the $\delta^{18}O$ can be interpret as precipitated during progressive burial.

Fractures 2, 3, 4 and 5 are attributed to the Neogene extension: fractures 2 and breccia B1 are formed during the initial propagation of the Neogene normal faults. The fluid involved during this deformation, shows a high interaction with the host-dolomite, in a closed hydrological system. Subaerial exposure of the Mesozoic horsts allowed the deposition of dolomitic sediments DS1 and DS2 in karstic environment. The geochemistry of the sediments indicates the opening of the system to meteoric water. This aperture is also indicated by the presence of iron oxides, showing oxic conditions. This type of fractures and sediments has been described in Amposta offshore oil reservoir by Playà et al. (2010). Fractures 4 and 5 fillings are a mixture of tectonic and karstic processes and resulted from multi-stages movement of the normal faults. The location of frictional processes generated the cohesive fault breccia B2 and the cataclasite during the progressive opening of the hydrological system. When the fault reached the surface, karstic features from the vadose and phreatic meteoric environment, lead to the formation of the red breccias B3, karstic pisolithic layer and the breccias with pisoliths. Late movements of the normal faults generated the cataclasis of karstic deposits.

Fractures 6 are the result of the generalized tensile deformation of the all area during the final stages of the basin development. Meteoric waters precipitated speleothems that lining the fractures walls, in the vadose meteoric environment.

References

Playà, E., Travé, A., Caja, M.A., Salas, R. and Martín-Martín, J.D. [2010] Diagenesis of the Amposta offshore oil reservoir (Amposta Marino C2 well, Lower Cretaceous, Valencia Trough, Spain). *Geofluids*, **10**, 1-20.

Sibson, R.H. [2000] Fluid involvment in normal faulting. *Journal of Geodynamics*, **29**, 469-499.

Travé, A., Calvet, F., Soler, A. and Labaume, P. [1998] Fracturing and fluid migration during Palaeogene compression and Neogene extension in the Catalan Coastal Ranges, Spain. *Sedimentology*, **45**, 1063-1082.

Verhaert, G., Muchez, P., Keppens, E. And Sintubin, M. [2009] Fluid impact and spatial and temporal evolution of normal faulting in limestones. A case study in the Burdur-Isparta region (SW Turkey). *Geologia Belgica*, **12**(3), 59-73.

Publication 11

Baqués, V., Travé, A., Cantarero, I., 2010. Evolución diagenética en el sector occidental de la Falla del Vallès-Penedès (Cadenas Costero Catalanas). Geogaceta, 49, 95-98.

Evolución diagenética en el sector occidental de la Falla del Vallès-Penedès (Cadenas Costero Catalanas)

Diagenetic evolution along the occidental part of the Vallès-Penedès Fault (Catalan Coastal Ranges)

Vinyet Baqués, Anna Travé e Irene Cantarero

Departamento de Geoquímica. Petrologia i Prospecció Geològica. Facultat de Geologia. Universitat de Barcelona. c/Martí i Franquès s/n, 08028 Barcelona. vbaques@ub.edu; atrave@ub.edu; i_cantarero@ub.edu

ABSTRACT

From the study of the fracturing, fault rocks, petrology and geochemistry of carbonate cements were established the relative chronology of the different episodes of fracturing and the role of fluids during deformation in the western sector of the Vallès-Penedès Fault. Were recognized different types of fluids and hydraulic regimes during the development of the fault. Thus, during the early stages of fracturing attributed to Paleogene compression, fluids were highly interacted with the host-rock. By contrast, cements that fill the fractures related to the latest stages of deformation have low interaction with the host-rock and can be attributed to: 1) meteoric fluids circulated through the fractures during the latest stages of Paleogene compression or 2) the compressional fractures remained open and were subsequently sealed by cements precipitated from meteoric water. On the other hand, the later stages of fracturing attributed to Neogene extension, the hydrogeological system was opened to the meteoric waters and there was not interacted with the host-rock.

Key words: *Fluids, fractures, cements, Cenozoic, Vallès-Penedès.*

Geogaceta, 49 (2010), 95-98
ISSN: 2173-6545

Fecha de recepción: 15 de julio de 2010
Fecha de revisión: 3 de noviembre de 2010
Fecha de aceptación: 26 de noviembre de 2010

Introducción

Los movimientos de fluidos en cuencas sedimentarias se producen preferentemente durante las etapas de deformación tectónica (Moore y Vrolijk, 1992). A partir del estudio de la fracturación y de las rocas de falla, así como de sus cementos, se puede establecer la cronología relativa de los diferentes episodios de deformación, el papel de los fluidos en la deformación, las condiciones de la deformación (profundidad, temperatura, presión), las características y el origen de los fluidos (meteóricos, marinos, profundos) y el papel de las fallas en la migración de fluidos. El objeto de este estudio es caracterizar el desarrollo de la Falla del Vallès-Penedès basándonos en el estudio petrológico y geoquímico de los distintos productos diagenéticos.

Marco geológico

La cuenca del Vallès-Penedès se localiza en el sector central de las Cadenas Costero Catalanas (Fig.1). Durante la fase compresiva alpina comprendida entre el Eoceno y el Oligoceno inferior, las fallas orientadas NE-SO y ENE-OSO actuaron como fallas direccionales siniestras con transpresión local. Posteriormente, durante la extensión del Oligoceno superior-Mioceno medio, estas fallas fueron reactivadas como fallas normales originando un sistema de horsts y grabens situados en el margen NO del Surco de Valencia (Roca *et al*., 1999). La cuenca del Vallès-Penedès está limitada al NO por la Falla Vallès-Penedès, que tiene un salto de 3000 m y una orientación ENE-OSO a NE-SO. El límite SE está formado por diversas fallas de salto hectométrico que la separan de los horsts de Garraf y de Collserola-Montnegre (Bartrina *et al*., 1992).

Descripción del afloramiento

Se ha seleccionado un afloramiento situado en el sector occidental de la Falla del Vallès-Penedès que corresponde al límite del margen NW de la cuenca del Vallès-Penedès (Fig. 1). El afloramiento consiste en una antigua cantera que muestra una sección transversal de más de 20 metros del bloque inferior de la falla del Vallès-Penedès. En este punto, la falla pone en contacto unas calizas de agua dulce del Cretácico Inferior correspondientes a la Fm. Cantaperdius (Barremiense) con los depósitos continentales superiores del relleno de la cuenca correspondientes a la Fm. Conglomerados de Riudebitlles (Serravalliense-Tortoniense). Estas calizas están falladas, plegadas y basculadas. En la cantera se observan los estratos, con una potencia de 1 a 3 metros, totalmente verticales. A techo de algunos estratos se han identificado marcas de raíces y óxidos que dan una coloración amarillenta a la roca. Discordante con las calizas, en cavidades dentro de ellas, hay un depósito de arenita de color amarillo. Esta arenita está formada por granos angulosos de cuarzo y de calcita y la matriz está formada por una micrita de color marrón. A nivel microscópico se ha observado que este depósito está laminado, siendo subhorizontal e indicando que ha sido depositado posteriormente al plegamiento alpino.

Las calizas cretácicas corresponden a un wackestone-packstone de

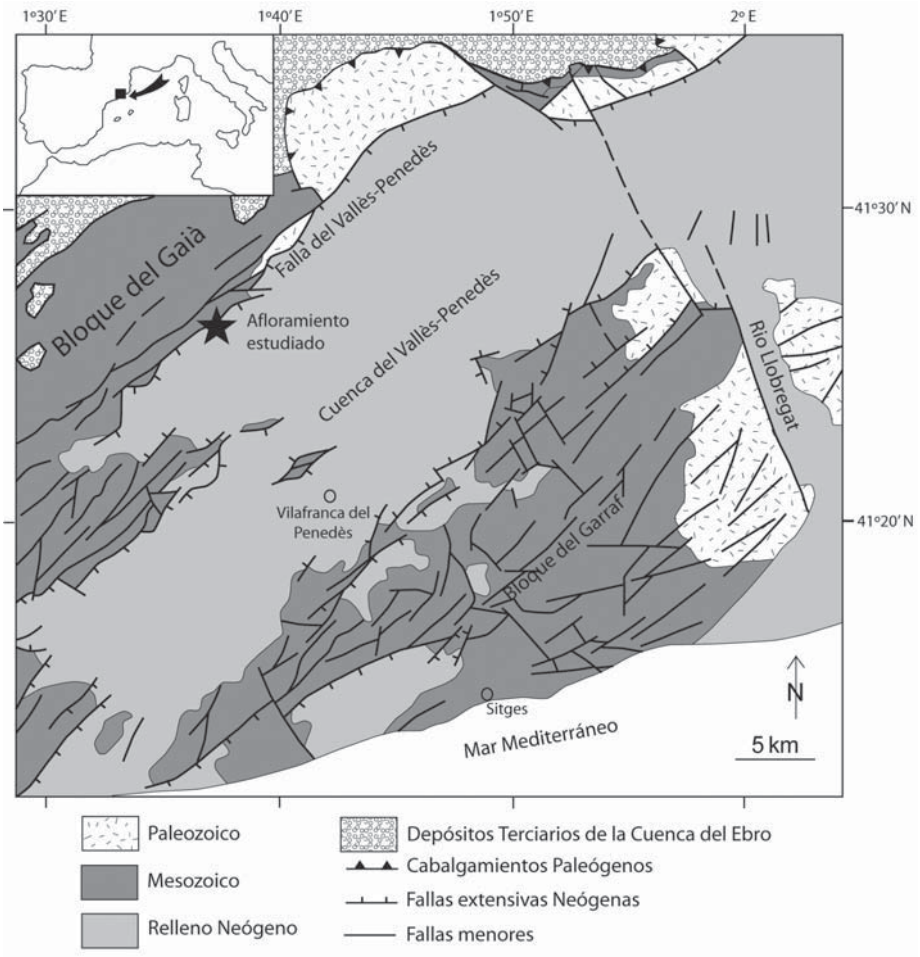

Fig. 1.-Localización del área de estudio en su contexto tectónico regional.

Fig. 1.-Studied area localization in its regional tectonic context.

carofitas, ostrácodos y fragmentos de gasterópodos. La luminiscencia de las calizas es naranja. Los restos fósiles están disueltos dejando una porosidad móldica. Esta porosidad está rellena parcialmente por micrita y por un cemento blocky de calcita (C0) en disposición geopetal. La micrita tiene luminiscencia naranja y la calcita naranja brillante. Puntualmente se observan zonas irregulares de micrita más oscura y micrita más rosada, dando un aspecto sub-nodular a la roca. En los dos tipos de micrita se observan cristales romboédricos de calcita (CD1), de tamaño entre 100 a 200 µm los cuales corresponden a una dolomía de reemplazamiento incipiente que posteriormente ha sido desdolomitizada. Estos cristales generalmente no son luminiscentes, aunque en algunos casos, el núcleo de los cristales presenta luminiscencia naranja. La roca de caja presenta valores entre -5,3 y -3,2 ‰ VPDB para el $\delta^{18}O$ y entre -5,8 y -4,6 ‰ VPDB para el $\delta^{13}C$.

Fracturas y cementos

A partir del estudio macroscópico y microscópico se han diferenciado hasta 8 tipos de fracturas (Fig. 2 y 3). Las relaciones de corte entre las diversas fracturas son complejas, aún así ha sido posible distinguir las distintas generaciones y relacionarlas con las dos grandes fases tectónicas que han tenido lugar en la zona.

Fracturas 1: son irregulares y sub-paralelas a la estratificación. Tienen un grosor entre 10 y 50 µm y están rellenas por un cemento de calcita microesparítico y luminiscencia naranja oscura (cemento C1). Estas fracturas son más abundantes en las zonas de micrita oscura.

Fracturas 2: tienen una orientación general de 150/80 O. Son fracturas con paredes rectas de grosor entre 100 µm y 2,5 cm. Están rellenas por dos generaciones de cemento: cemento de calcita C2a, de color blanco lechoso, tipo drusy y luminiscencia naranja oscura. Los cristales tienen una morfología euédrica de tamaño entre 75 µm y 1 mm. Localmente los cristales son elongados y crecen con el eje c perpendicular a las paredes de la fractura, dando una textura tipo bladed. Presenta valores entre -7,9 y -5,9 ‰ VPDB para el $\delta^{18}O$ y entre -6,3 y -4,1 ‰ VPDB para el $\delta^{13}C$. La segunda generación se trata de un cemento de calcita C2b, de color naranja translúcido, tipo drusy y luminiscencia naranja oscura. Los cristales tienen morfología euédrica de tamaño entre 150 y 750 µm y crecen con el eje c perpendicular a las paredes de la fractura. Presenta valores de -5,8 ‰ VPDB para el $\delta^{18}O$ y -4,9 ‰ VPDB para el $\delta^{13}C$.

Fracturas 3: tienen una orientación general 140/10 SO. Son fracturas de paredes irregulares de grosor entre 200 y 500 µm. Están rellenas por un cemento de calcita tipo blocky no luminiscente (C3). Los cristales son euédricos y nítidos de tamaño entre 100 y 200 µm. Presenta valores entre -5,8 y -4,8 ‰ VPDB para el $\delta^{18}O$ y entre -10 y -4,9 ‰ VPDB para el $\delta^{13}C$.

Fracturas 4: tienen una orientación general de 060/70 SE y corresponden a fallas inversas. El núcleo de la falla es de tan solo 0,5 m de grosor y está constituido por una cataclasita de color amarillento. La cataclasita está formada por microfragmentos de la roca encajante y los cementos descritos anteriormente y está cementada por dos generaciones de cemento: una microesparita no luminiscente (C4a), de cristales anédricos de tamaño entre 4 y 10 µm y con valores entre -5,4 y -4,3 ‰ VPDB para el $\delta^{18}O$ y entre -9,5 y -7 ‰ VPDB para el $\delta^{13}C$. La segunda generación corresponde a un cemento tipo blocky no luminiscente (C4b), de cristales euédricos de tamaño entre 10 y 50 µm, con valores entre -5,4 y -4,4 ‰ VPDB para el $\delta^{18}O$ y entre -9,5 y -7 ‰ VPDB para el $\delta^{13}C$.

Fracturas 5: tienen una orientación general de 054/25 NO con un cabeceo de 54ºE y corresponden a fallas inversas. Asociada a las fallas se ha identificado una cataclasita similar a la cataclasita amarilla, con fragmentos del mismo origen y cementada por la microesparita C4a y el cemento de calcita blocky C4b. Las estrías de la falla inversa, se desarrollaron sobre una calcita blocky deformada (C5), con los cristales entre 200 y 500 µm no luminiscentes. Presenta valores de -5,2 ‰ VPDB para el $\delta^{18}O$ y -8,5 ‰ VPDB para el $\delta^{13}C$.

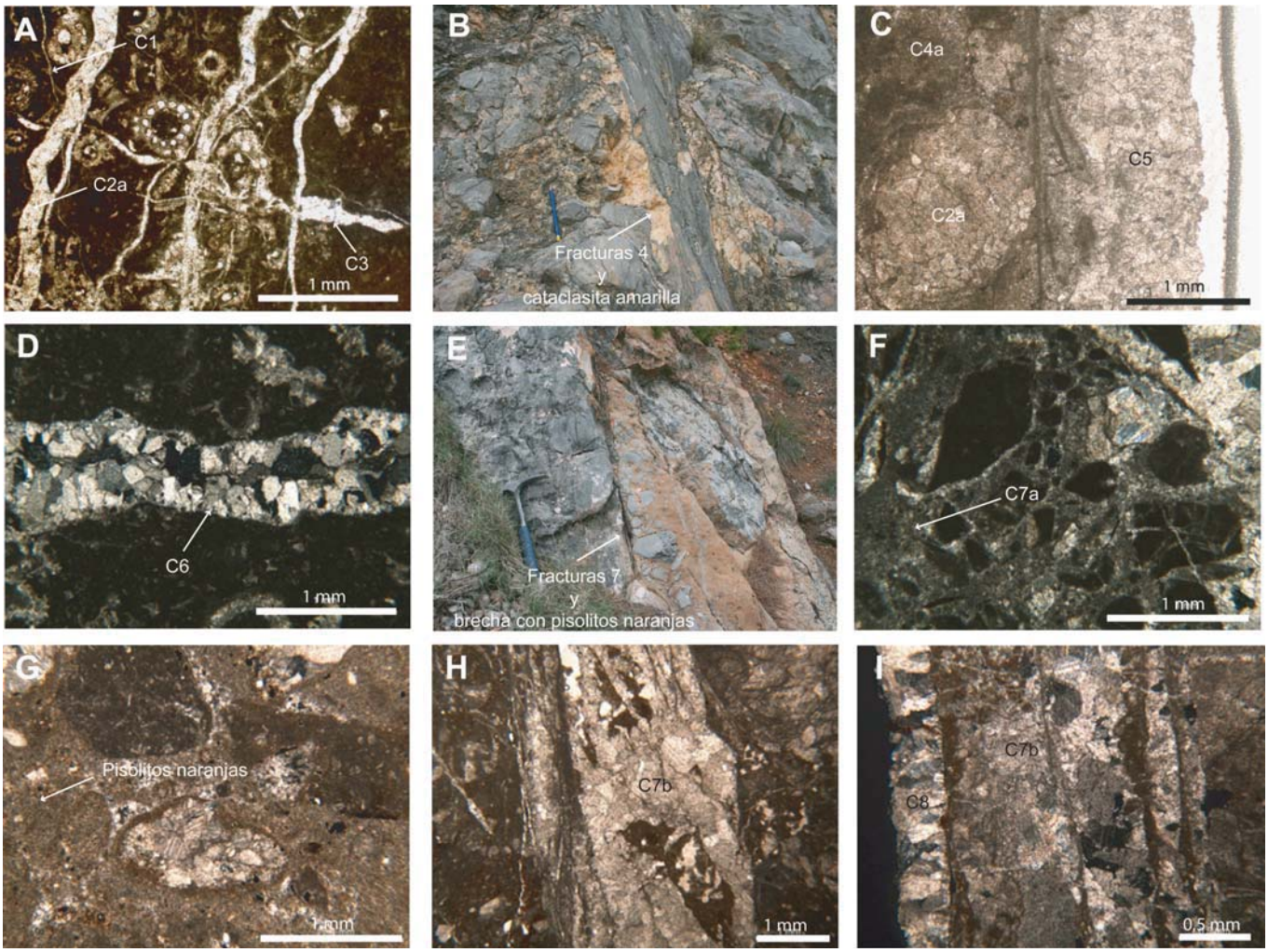

Fig. 2.- Características petrológicas de la roca de caja y cementos descritos para cada familia de fracturas. A-Wackestone-packstone de carofitas afectado por las fracturas 1, 2 y 3 y los correspondientes cementos C1, C2 y C3. B-Fallas inversas relacionadas con la familia de fracturas 4. En la zona del núcleo de la falla se encuentra la cataclasita amarilla. C- Fracturas 5 con los cementos C4a y C5. D- Fracturas 6 rellenas por el cemento C6. E-Fallas normales relacionadas con la familia de fracturas 7. En la zona del núcleo de la falla se encuentran las brechas con los pisolitos naranjas. F- Brecha de falla cementada por el cemento C7a. G-Detalle de los pisolitos naranjas. Se puede observar fragmentos de cementos anteriores que tienen una envuelta pisolítica. H-Catáclasis de la brecha con los pisolitos naranjas y cemento sintectónico C7b. I-Cemento C7b y el cemento en empalizada C8.

Fig. 2.- Petrological characteristics of the host-rock and cements described for each family of fractures. A-Wackestone-packstone of charophyte affected by fracture 1, 2 and 3 and their related cements C1, C2 and C3. B-Thrust faults related to the family of fractures 4. In the core zone there is the yellow cataclasite. C- Fractures 5 with C4a and C5 cements. D-Fractures 6 filled by cement C6. E-Normal faults related to the family of fractures 7. In the core fault zone there is the breccia with the orange pisoliths. F-Fault breccia with cement C7b. G-Breccia of orange pisoliths. H-Cataclasite of orange pisoliths with the syntectonic cement C7b. I-Cement C7b and cement C8.

Fracturas 6: tienen una orientación general de 080/30 S a 060/30 NO. Son fracturas de paredes rectas y de grosor entre 100 y 700 µm. Están rellenas por un cemento de calcita tipo drusy no luminiscente (C6). Los cristales son euédricos de tamaño entre 25 y 250 µm y crecen con el eje c perpendicular a la pared de la fractura. Presenta valores entre -5,4 y -4,6 ‰ VPDB para el $\delta^{18}O$ y entre -10,5 y –7.9 ‰ VPDB para el $\delta^{13}C$.

Fracturas 7: tienen una orientación general de 060/60 SE y corresponden a fallas normales. Asociado a las fallas se han reconocido distintos tipos de brechas de falla:

Brecha de falla cohesiva: formada por clastos angulosos, de tamaño entre 0,1 y 3 cm correspondientes a la roca de caja y los cementos descritos anteriormente. Esta brecha está cementada por cristales microesparíticos de 10 a 20 µm no luminiscentes (C7a). Presenta valores entre -5,4 y -4,1 ‰ VPDB para el $\delta^{18}O$ y entre -9,8 y -6,8 ‰ VPDB para el $\delta^{13}C$.

Pisolitos naranjas: en el núcleo de las fallas se ha observado una brecha de falla donde los fragmentos están sustentados por unos pisolitos micríticos de color naranja. Algunos de los fragmentos de la brecha tienen también una envuelta pisolítica naranja grisácea en los que el núcleo no se reconoce. En general, esta brecha está afectada por procesos pedogenéticos que dan lugar a vacuolas y fracturas muy irregulares rellenas por una microesparita gris. Estos pisolitos presentan valores entre -7,1 y -4,4 ‰ VPDB para el $\delta^{18}O$ y entre -10,3 y -8,5 ‰ VPDB para el $\delta^{13}C$.

Cataclasis de los pisolitos naranjas: los últimos movimientos de la falla provocan la catáclasis de los pisolitos naranjas. Se han observado sigmoides con cementos de calcita precipitados sintectónicamente (C7b). Esta calcita presenta valores entre -5,6 y -5,1 ‰ VPDB para el $\delta^{18}O$ y entre -9,8 y -9 ‰ VPDB para el $\delta^{13}C$.

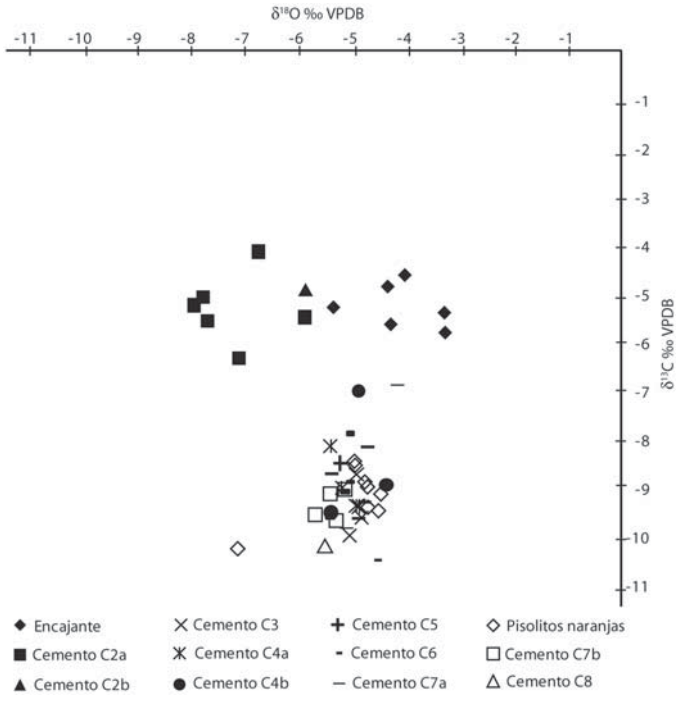

Fig. 3.- Representación gráfica de los valores isotópicos de C y O de la roca de caja y cementos.

Fig. 3.- Cross-plot of oxygen and carbon stable isotopic composition of host-rock and cements.

Fracturas 8: son fracturas de orientación NNO-SSE, de paredes rectas y grosor entre 5 y 10 cm. Las paredes de las fracturas están tapizadas por un cemento de calcita tipo empalizada (C8). Los cristales son elongados de 500 µm a 2 cm no luminiscentes. Presenta valores de -5,5 ‰ VPDB para el $\delta^{18}O$ y -10,2 ‰ VPDB para el $\delta^{13}C$.

Discusión

Las fracturas 1, 2, 3, 4 y 5 son compatibles a nivel estructural con la compresión Paleógena. Los cementos relacionados con las fracturas 2 muestran una alta interacción con el encajante. Además, la señal empobrecida en oxígeno indica que este cemento precipitó durante el enterramiento máximo de la roca. Por el contrario, las calcitas relacionadas con las fracturas 3, 4 y 5 muestran una baja interacción con el encajante, y precipitación a partir de aguas meteóricas. Las fracturas 6, 7 y 8 se atribuyen a la extensión neógena. Los distintos cementos, brechas y pisolitos relacionados con las fracturas extensivas neógenas son una mezcla de procesos tectónicos y kársticos. La interferencia entre la tectónica y los procesos kársticos relacionada a fallas normales ha sido descrita por varios autores en fallas superficiales que afectan carbonatos (Sibson, 2000; Verhaert *et al*., 2009). Los valores isotópicos de C y O indican que en esta fase el sistema hidrológico estuvo abierto a la entrada de aguas meteóricas.

Trabajos realizados en la zona muestran alta interacción con la roca encajante durante la compresión paleógena y entrada de aguas meteóricas durante la extensión neógena (Travé *et al*., 1998). En el afloramiento estudiado, las fracturas 3, 4 y 5 son fracturas claramente compresivas y, a pesar de ello, los cementos que las rellenan fueron precipitados a partir de aguas meteóricas que interaccionaron poco con la roca de caja. Los resultados actuales pueden indicar dos posibles hipótesis: 1) La entrada de aguas meteóricas a través de las fracturas, sin interacción con la roca de caja, se podría haber producido ya en los últimos estadios de la compresión o, 2) Durante los últimos estadios de la compresión, si circularon fluidos, éstos no dejaron registro y los cementos que se encuentran en las fracturas compresivas 3, 4 y 5 precipitaron posteriormente, durante la extensión neógena, a partir de fluidos meteóricos.

Conclusiones

Se han reconocido distintos tipos de fluidos y distintos regímenes hidrológicos durante el desarrollo de la Falla del Vallès-Penedès:

1- Fluidos con una alta interacción con la roca de caja relacionados con las fracturas 2.

2- Fluidos con baja interacción con la roca de caja relacionados con las fracturas 3, 4 y 5. Los cementos que rellenan las fracturas abren la posibilidad de dos hipótesis: 2a) En los últimos estadios de la compresión se produjo la entrada de fluidos meteóricos. 2b) Las fracturas compresivas permanecieron abiertas y fueron selladas posteriormente por cementos precipitados de aguas meteóricas.

3- Fluidos que provocaron una baja interacción con la roca de caja, indicando un sistema hidrológico abierto a las aguas meteóricas durante la formación de las fracturas 6, 7 (fallas normales) y 8.

Agradecimientos

Esta investigación está financiada por el proyecto CGL2010- 18260, la beca BES-2007-14935 y el *Grup Consolidat de Recerca* «Geologia Sedimentària» (2009 SGR-1458).

Referencias

Bartrina, M.T., Cabrera, L., Jurado, M.J., Guimerà, J. y Roca, E. (1992). *Tectonophysics,* 203, 219-247.

Moore, J.C y Vrolijk, P. (1992). *Review of Geophysics*, 30, 113-135.

Roca, E., Sans, M., Cabrera, L. y Marzo, M. (1999). *Tectonophysics,* 315, 209-233.

Sibson, R.H. (2000). *Journal of Geodynamics*, 29, 469-499.

Travé, A., Calvet, F., Soler, A. y Labaume, P. (1998). *Sedimentology*, 45, 1063-1082.

Verhaert, G., Muchez, P., Keppens, E. y Sintubin, M. (2009). *Geologia Belgica*, 12(3), 59-73.

Publication 12

Baqués, V., Travé, A., Benedicto, A., Cantarero, I., 2012. The meteoric fluids circulation during the Miocene rifting of the Penedès half-graben, NE Iberian Peninsula. Geo-Temas, 13 (ISSN: 1576-5172).

The meteoric fluids circulation during the Miocene rifting of the Penedès Half-graben, NE Iberian Peninsula

La circulación de fluidos meteóricos durante la apertura Miocena del Semi-graben del Penedès, NE de la Península Ibérica

V. Baqués[1], A. Travé[1], A. Benedicto[2] and I. Cantarero[1]

1 Dpt. Geoquímica, Petrologia i Prospecció Geològica. Facultat de Geologia. Universitat de Barcelona (UB). 08028 Barcelona (Spain). vbaques@ub.edu; atrave@ub.edu; i_cantarero@ub.edu
2 Areva Mines. Direction des Géosciences. Tour Areva. La Défense Cedex. 92094 Paris (France). antonio.benedicto@areva.fr

Abstract: The structural features of faults and fractures formed within the Penedès Half-graben during the Miocene have allowed identified three deformational phases. The first, during the syn-rift phase, is characterised by three successive stages of NE-SW normal faults. The second, during the early post-rift phase, consists of a minor compression phase which developed two successive stages of fractures agree with a dextral directional sense. The third, during the late post-rift phase, is characterised by two successive stages of N-S trending fractures. The fluids circulating during the Miocene rifting are meteoric in origin. The meteoric fluids related with the syn- and early post-rift stage were consistent with the fluids that cemented and altered the Miocene host-rocks, but latter, during the late post-rift, the fluids were characterised by higher involvement of soil-derived CO_2 because of the vadose meteoric flow origin.

Key words: meteoric fluids, fractures, diagenetic, Miocene, Penedès Half-graben.

Resumen: *Las características de estructurales de fallas y fracturas formadas dentro del Semi-graben del Penedès durante el Mioceno han permitido identificar tres fases de deformación. La primera, durante la fase syn-rift, se caracteriza por tres etapas sucesivas de las fallas normales NE-SO. La segunda, durante el post-rift inicial, consiste en una fase de compresión menor, la cual desarrolla dos etapas sucesivas de fracturas con movimiento direccional dextro. La tercera, durante el post-rift tardío, se caracteriza por dos etapas sucesivas de fracturas de dirección N-S. Los fluidos que circularon durante el rifting Mioceno son de origen meteórico. Los fluidos meteóricos relacionados con el syn- y post-rift inicial eran compatibles con los fluidos que cementaron y alteraron las rocas de caja de edad Miocena. En cambio, los fluidos relacionados con el post-rift tardío se caracterizan por una mayor influencia del CO_2 derivado del suelo debido a la circulación dentro del medio meteórico vadoso.*

Palabras calve: *fluidos meteóricos, fracturas, diagénesis, Mioceno, Semi-graben del Penedès.*

INTRODUCTION

In tectonically controlled basins, it is assumed that fluid flow is enhanced along fractures during deformation. Fractures, fault rocks and cements record the interaction between deformation and fluid flow regime during basin development (Knipe, 1993). This work is part of a larger project which uses a multidisciplinary approach in the Neogene extensional Penedès basin (Catalan Coastal Ranges, NE Spain) in order to study how major, secondary and minor fractures control fluid flow through the whole basin. The work presented here focuses on the analysis of the minor faults that affect the Miocene basin infillings. We attempt to unravel the different stages of fracture development and the successive fluid circulation episodes during the Miocene rifting.

The Penedès Half-graben (Fig. 1), located at the central part of the Catalan Coastal Ranges (NE Spain), results from the superposition of three main tectonic events: (1) a Mesozoic extensional phase from the Late Jurassic to the Early Cretaceous; (2) a Paleogene compressional phase from the Eocene to the early Oligocene; and (3) a Neogene extensional phase related to the Valencia Through opening. The Penedès basin is trending NE-SW belongs up to 50 km and has a wide between 10 and 14 km. In its NW margin is bounded by the Vallès-Penedès Fault, with a vertical slip larger than 3 km. Minor faults, up to few hundred meters of slip, make up the present southern boundary, separating the depression from the Garraf Horst. The basin is filled up by 4 km of sediments divided into three depositional complexes (Cabrera & Calvet, 1996): (1) syn-rift lower continental complexes consisting in thick red beds sequences deposited in alluvial fan environments, Aquitanian to lower Burdigalian in age; (2) an early post-rift Continental to marine complexes, upper Burdigalian to Langhian in age, with sabhka facies, carbonate platforms facies and siliciclastic and bay facies; and (3) late post-rift upper continental complexes, middle Serravallian-Tortonian in age,

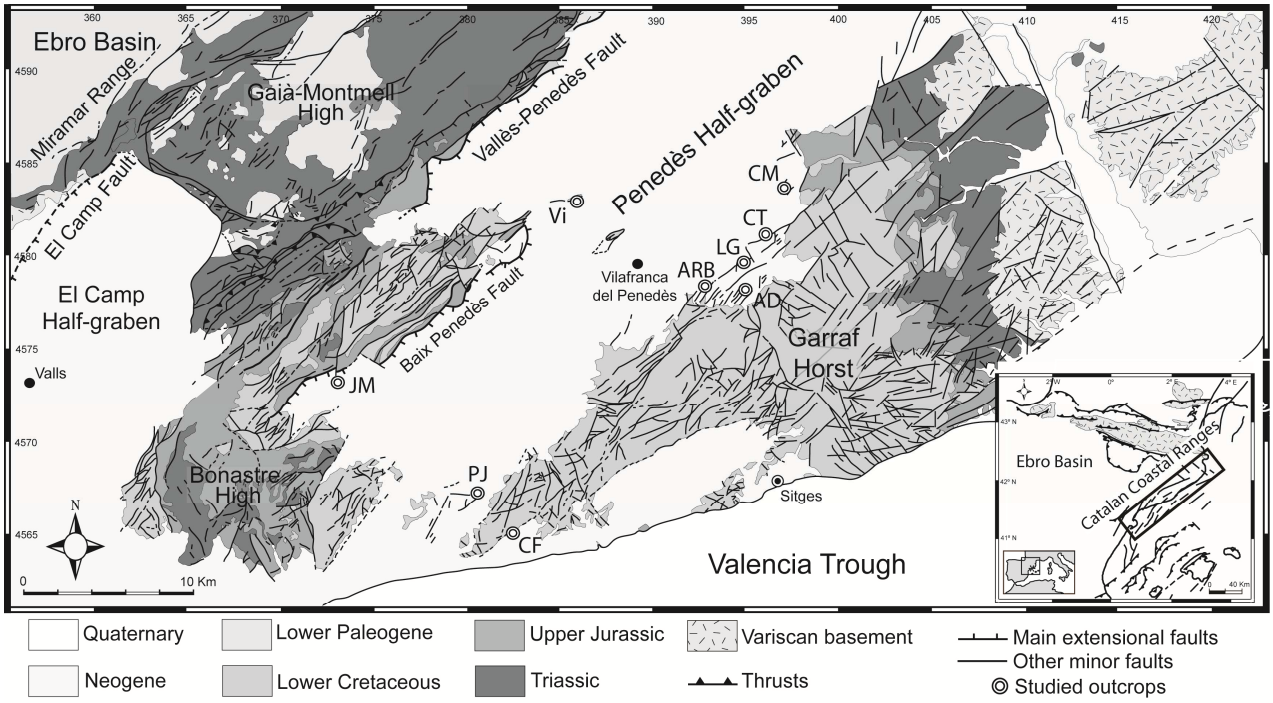

FIGURE 1. *Geological map of the Penedès Half-graben with the location of the studied outcrops. AD: Arboçar de Dalt; LG: Les Gunyoles; Vi: Vilobí; PJ: Pedrera Juliana; CF: Calafell; ARB: Arboçar; CT: Cantallops; CM: Can Mata; JM: Juncosa Montmell;*

consisting of thick red bed sequences deposited in alluvial fan environments.

STUDIED OUTCROPS

The study was performed on nine outcrops located at different position within the Miocene sequences (Figs. 1 y 2):

(1) The Arboçar de Dalt (AD), Les Gunyoles (LG) and Vilobí (Vi) outcrops are located on the lower continental complexes. In the three outcrops, the host rocks consist of subhoritzontal stratified clast-supported conglomerates. The clasts are heterometric, 1 to 60 cm in size, sub-rounded, and consist of wackestones and packstones with orbitolinids, miliolids, peloids, bivalves and dasycladales eroded from the Lower Cretaceous and dolomitic clasts eroded from the Jurassic. The $\delta^{18}O$ of the Cretaceous carbonate clasts varies from -5,4 to -2,7 ‰ Viena Pee Dee Belemnite standard (VPDB) and their $\delta^{13}C$ varies from -2,1 to +4,5 ‰ VPDB. The conglomerate matrix contents spherulites of microcodium. The conglomerate is cemented by 25 to 50 µm in size anhedral calcite crystals to 100 to 500 µm in size euhedral calcite crystals both featuring a blocky texture (calcite cement Cc1). This calcite cement is orange bright luminescent and its $\delta^{18}O$ varies from -5,4 to -4,5 ‰ VPDB and the $\delta^{13}C$ varies from -5,4 to -3,3 ‰ VPDB.

(2) The Pedrera Juliana (PJ) and Calafell (CF) outcrops are located on the Continental to transitional complexes where the faults affect the Bellvei facies. These facies are constituted by white mudstone, wackestone and packstone of corals, rhodolits, oysters, bivalves and gastropods. This rock has variable porosity, from 20 to 30%, and low permeability, displaying a chalky character. The rock became more cemented near the fault planes. The values of $\delta^{18}O$ range from -4,2 to -3,2 ‰ VPDB and the $\delta^{13}C$ varies from -4,9 to -2,8 ‰ VPDB. The Arboçar (ARB), Cantallops (CT) and Les Gunyoles (LG) outcrops are also located on the Continental to transitional complexes but where faults affect the Castellet facies. These facies correspond to well-cemented white packstones of corals, rhodolits, oysters, bivalves and gastropods. The values of $\delta^{18}O$ range from -6,2 to -4 ‰ VPDB and the $\delta^{13}C$ varies from -5,3 to -1,4 ‰ VPDB. The Can Mata (CM) outcrop is located on the same complexes but where faults affect the Torrelletes facies. These facies correspond to cemented wackestone and packstones of oysters, bivalves and gastropods with high amount of detritic sediments and display a yellow to grey colour, locally reddish. The $\delta^{18}O$ is -7,6 ‰ VPDB and the $\delta^{13}C$ is -5,7 ‰ VPDB.

(3) The Juncosa del Montmell (JM) outcrop is located on the upper continental complexes. The host rock consist on 0,5 to 3 meter-thick conglomerate beds, trending NNE-SSW and dipping 45º to the northwest. The conglomerates are matrix-supported. The clasts are heterometric, 0,5 to 80 cm in size, sub-angular and correspond to reworked fragments from Upper Jurassic- Lower Cretaceous dolostones. The $\delta^{18}O$ of the dolomitic clasts varies from -1,8 to +1,2‰ VPDB and the $\delta^{13}C$ varies from -0,5 to +2,3 ‰ VPDB. The matrix consists on calcite, quartz, hematite, kaolinite, illite and interstratified illite-smectite. The conglomerate is cemented by anhedral calcite crystals 25 to 50 µm in

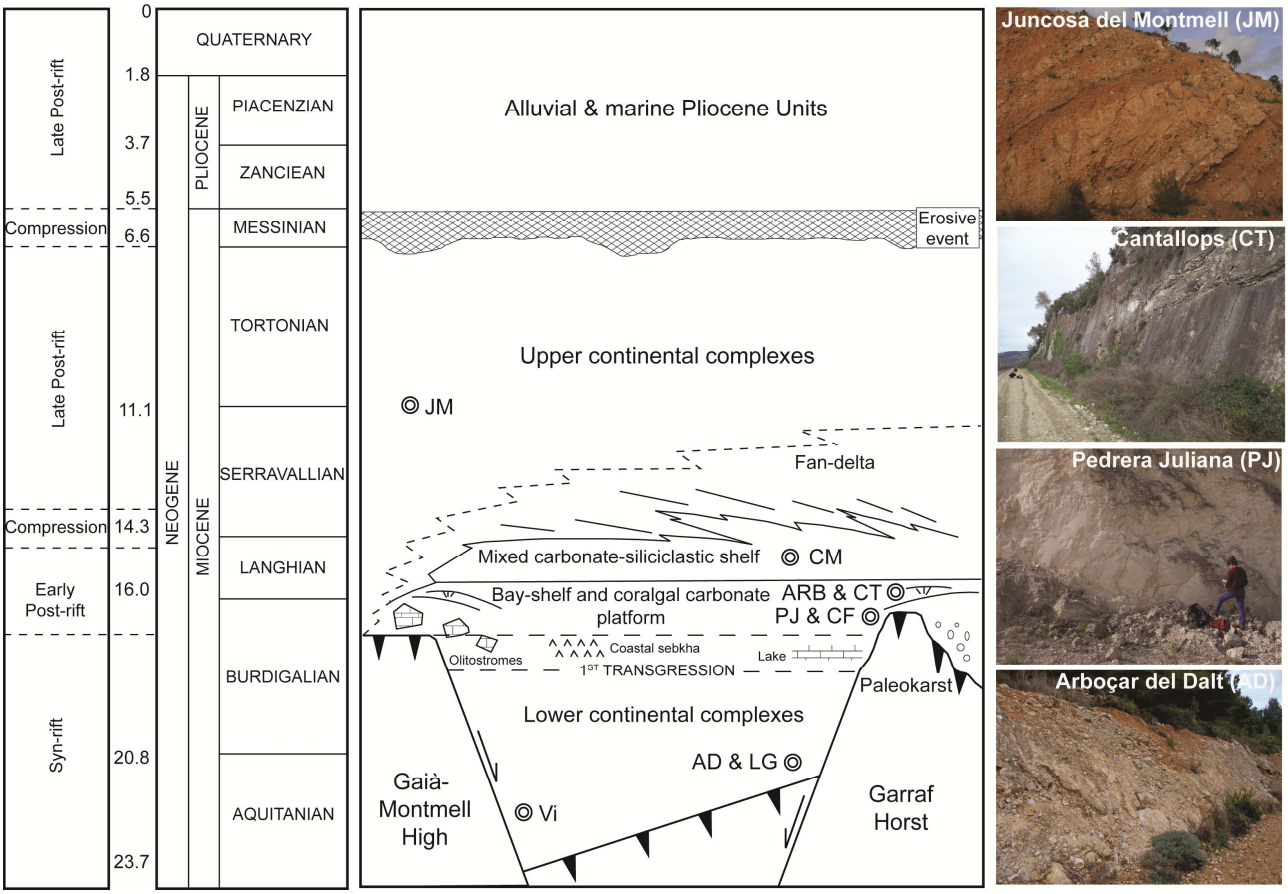

FIGURE 2. *Conceptual sketch of the Neogene sedimentary record in the Penedès Half-graben (modified from Cabrera & Calvet, 1996), where have been approximately located the studied outcrops and field images of the different Miocene sequences that fill the basin. AD: Arboçar de Dalt; LG: Les Gunyoles; Vi: Vilobí; PJ: Pedrera Juliana; CF: Calafell; ARB: Arboçar; CT: Cantallops; CM: Can Mata; JM: Juncosa Montmell.*

size to euhedral calcite crystals 100 to 500 µm in size featuring a blocky texture (calcite cement Cc2). The $\delta^{18}O$ of the calcite cement varies from -6,2 to -4,8‰ VPDB and the $\delta^{13}C$ varies from -10,1 to -9,3 ‰ VPDB.

Deformation features

According to the cross-cutting relationships between fractures and the stratigraphic position of the outcrops, three different stages of fault development have been differentiated.

The first stage, attributed to the syn-rift, consists of three successive normal faulting trending NE-SW. The first faulting (1a) separates the Mesozoic horst from the Miocene basin infill. The fault plane is characterised by a well cemented, up to 2 meter-thick, fault breccia (fault cement Fc1a) in the JM and Vi outcrops resulting from a mixture of tectonic and karstic processes. The $\delta^{18}O$ values of the calcite cement varies from -7 to -6,4 ‰ VPDB and the $\delta^{13}C$ varies from -8,3 to -7,7 ‰ VPDB. The second faulting (1b) consists of normal faults affecting the Miocene conglomerates close to the major faults 1a and are cemented by striated calcite cement (fault cement Fc1b) in the AD, Vi, ARB, CT and CM outcrops. The values of $\delta^{18}O$ varies from -7 to -3,4 ‰ VPDB and the $\delta^{13}C$ varies from -6,1 to -2,5 ‰ VPDB. The third faulting (1c) is cemented by striated iron oxides (fault cement Fc1c) in the AD, Vi, ARB, CT and CM outcrops. The mineralogy of the striated oxides is quartz, goethite, calcite and in less amount palygorskite, psilomelane, hematite and illite. Locally, the striated calcite cement and the iron oxides develop within a single fault plane.

The second stage, attributed to the early post-rift consists of a minor compression phase which developed two types of fracture sets. The first set is characterised by dextral directional faults striking NW-SE and NE-SW respectively. Theses faults are cemented by striated calcite and produce a highly cementation of the host rock, which decreases far from the fault (fault cement Fc2) in the PJ and CF outcrops. The values of $\delta^{18}O$ and $\delta^{13}C$ are -4,5 ‰ VPDB and -6.1 ‰ VPDB respectively. The second set is characterised by open fractures within the previously formed NE-SW normal faults giving a dextral directional sense in the Vi, ARB, CT and CM outcrops.

The third stage, attributed to the late post-rift, consists of two successive fractures trending N-S. The first fracture type is characterised by normal faults cemented by calcite cement (fault cement Fc3a) in the Vi, LG and JM outcrops, or dolomite cement (fault cement Fc3b) in the Vi outcrop. The values of $\delta^{18}O$ and $\delta^{13}C$ of the calcite cement are -5,1 ‰ VPDB and -11.3

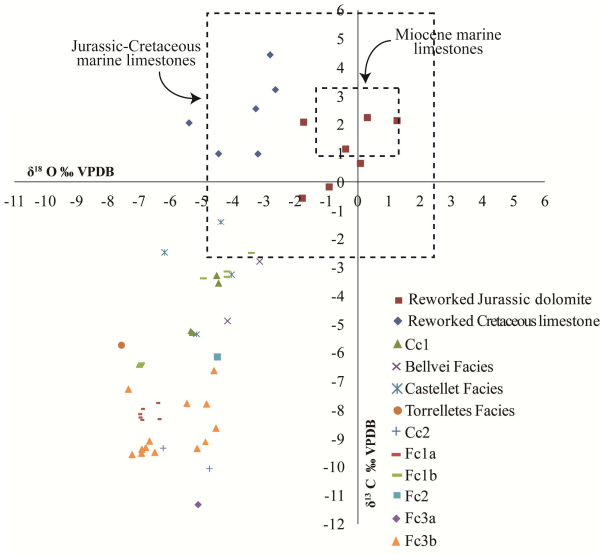

FIGURE 3. *Cross-plot of the oxygen and carbon isotopes.*

‰ VPDB respectively. The second fracture type is characterised by fractures filled with laminated calcite cement interpreted as speleothems (fault cement Fc3c) in the AD, Vi, CM and JM outcrops. The $\delta^{18}O$ varies from -7,4 to -4,6 ‰ VPDB and the $\delta^{13}C$ varies from -9,6 to -6.6 ‰ VPDB.

DISCUSSION

The stable isotopes of the reworked Mesozoic clasts within the Miocene conglomerates are in agreement with its marine origin (Veizer et al., 1999) (Fig. 3). In contrast, the isotopic values of the Miocene marine facies (Bellvei, Castellet and Torrelletes Facies), depleted in $\delta^{18}O$ and $\delta^{13}C$ respect to the expected values for the Miocene seawater (Veizer et al., 1999), indicate that the marine limestones were completely re-equilibrated under the meteoric diagenetic environment. The similarity between the isotopic values of the Miocene limestones and those of the Cc1 cement suggests that the same meteoric fluid formed the cement and diagenetically altered the marine host limestone. The isotopic values of the Cc2 cement indicate that the cement precipitated from a meteoric fluid more influenced by the soil-derived CO_2 than the previous one.

The different fluids related to the successive deformation stages recognized during the Miocene rifting have the common feature of its meteoric origin. The $\delta^{18}O$ and $\delta^{13}C$ values from syn-rift and early post-rift fracture cementations (Fc1b and Fc2) are similar to their correspondent diagenetically re-equilibrated host-limestones. These values are consistent with a meteoric fluid which highly interacted with the host rock. The striated oxides from the fractures 1c indicate that reduced Fe^{2+}-rich fluids circulated through the faults during their movement. When these fluids encountered oxidizing conditions and then precipitated goethite and hematite concretions (Busigny and Dauphas, 2007). The $\delta^{18}O$ and $\delta^{13}C$ values of the calcite cement filling the late post-rift fractures (Fc3a and Fc3b) are successively more depleted in $\delta^{13}C$ indicating higher involvement of soil-derived CO_2, probably due to their precipitation at the vadose meteoric zone.

CONCLUSIONS

The structural features of faults and fractures formed within the Penedès Half-graben during the Miocene rifting have allowed identified three deformational phases. The first, during the syn-rift phase, is characterised by three successive stages of NE-SW normal faults. The second, during the early post-rift phase, consists of two types of fracture sets: one characterised by dextral directional faults striking NW-SE and NE-SW respectively and other characterised by open fractures within the previously formed NE-SW normal faults giving a dextral directional sense. The third, during the late post-rift phase, is characterised by two successive stages of N-S fractures. The fluids circulating during the Miocene rifting are meteoric in origin. The meteoric fluids related with the syn- and early post-rift stage were consistent with the fluids that cemented and altered the Miocene host-rocks, but latter, during the late post-rift, the fluids were characterised by higher involvement of soil-derived CO_2 because of the vadose meteoric flow origin.

ACKNOWLEDGEMENTS

This work was funded by the Spanish Government Project CGL2010-18260, the "Grup Consolidat de Recerca Geologia Sedimentària" 2009SGR-1451 and the grant BES-2007-14935.

REFERENCES

Busigny, V. and Dauphas, N. (2007): Tracing paleofluid circulations using iron isotopes: A study of hematite and goethite concretions from the Navajo Sandstone (Utah, USA). *Earth and Planerary Science Letters*, 254: 272-287.

Cabrera, L. and Calvet, F. (1996): Onshore Neogene record in NE Spain: Vallès-Penedès and el Camp half-grabens (NW Mediterranean). In: *Tertiary Basins of Spain*. (P. Friend y C. Dabrio, eds.). Cambridge University Press, Cambridge, 97-105.

Knipe, R.J. & McCaig, A.M. (1994): Microstructural and microchemical consequences of fluid flow in deforming rock. In: *Geofluids: Origin, Migration and Evolution of Fluids in Sedimentary Basins.* (J. Parnell, eds.). Geol. Soc. Lond. Spec. Publ., 78, 99-111.

Veizer, J., Ala, D., Azmy, K., Bruckschen, P., Buhl, D., Bruhn, F., Carden, G.A.F., Diener, A., Ebneth, S., Godderis, Y., Jasper, T., Korte, C., Pawellek, F., Podlaha, O. & Strauss, H. (1999): $^{87}Sr/^{86}Sr$, $\delta^{13}C$ and $\delta^{18}O$ evolution of Phanerozoic seawater. Chemical Geology, 161, 59-8.